

**Millimeter-Wave Galaxy Spectroscopy: SuperSpec
On-Chip Spectrometer Technology Development and
ALMA Observations of Molecular Gas in the Arp 220
Nucleus**

by

Jordan Wheeler

M.S., University of Colorado Boulder, 2015

A thesis submitted to the
Faculty of the Graduate School of the
University of Colorado in partial fulfillment
of the requirements for the degree of
Doctor of Philosophy
Department of Astrophysical and Planetary Sciences
2019

This thesis entitled:
Millimeter-Wave Galaxy Spectroscopy: SuperSpec On-Chip Spectrometer Technology
Development and ALMA Observations of Molecular Gas in the Arp 220 Nucleus
written by Jordan Wheeler
has been approved for the Department of Astrophysical and Planetary Sciences

Prof. Jason Glenn

Prof. Julie Comerford

Prof. James Green

Prof. Nils Halverson

Date _____

The final copy of this thesis has been examined by the signatories, and we find that both the content and the form meet acceptable presentation standards of scholarly work in the above mentioned discipline.

Wheeler, Jordan (Ph.D., Astrophysical and Planetary Sciences)

Millimeter-Wave Galaxy Spectroscopy: SuperSpec On-Chip Spectrometer Technology Development and ALMA Observations of Molecular Gas in the Arp 220 Nucleus

Thesis directed by Prof. Jason Glenn

This dissertation is comprised of two components: millimeter-wave spectrometer technology development and millimeter-wave observations and interstellar medium modeling of the nucleus of an ultra luminous galaxy. SuperSpec is an on-chip spectrometer developed for multi-object, moderate resolution ($R = 300$), large-bandwidth survey spectroscopy of high-redshift galaxies for the 1.0 to 1.5 mm atmospheric transmission window. SuperSpec targets the CO ladder in the redshift range of $z = 0$ to 4, the [C II] 158 μm line from $z = 5$ to 9, and the [N II] 205 μm line from $z = 4$ to 7. SuperSpec employs a novel architecture in which detectors are coupled to a series of resonant filters along a microwave feedline instead of using dispersive optics. This construction allows for the creation of a spectrometer occupying only a few cm^2 of silicon, a reduction in volume of several orders of magnitude when compared to grating spectrometers. This small profile will enable the production of future multi-object spectrometers.

Results from the characterization of SuperSpec test devices are presented. In particular, spectral response profiles, filterbank efficiency, and detector noise equivalent powers are presented. The design motivation and implementation for science-grade SuperSpec spectrometers based on these test results are also presented.

In the second part of the thesis, ALMA observations of Arp 220 using $^{12}\text{CO } J = 3 \rightarrow 2$, and $^{13}\text{CO } J = 4 \rightarrow 3$, where J is the angular momentum quantum number, are analyzed. Arp 220 is an ultra-luminous infrared galaxy in the late stages of a merger between two gas-rich galaxies, with a high nuclear star formation rate and an extremely large dust optical depth, exhibiting strong evidence for a molecular outflow. Observations are compared to gas

excitation and non-LTE radiative transfer models created using the Line Modeling Engine for simple gas dynamics, yielding insight into how parameters such as rotational velocity, velocity dispersion, temperature, outflow velocity, and gas mass can reproduce the observed kinematic features. Together, these observational and technological aspects of the thesis demonstrate the power of millimeter-wave spectroscopy for understanding galaxy evolution.

Dedication

For my father, who taught me by example how to work hard.

Acknowledgements

I would not have been able to accomplish all that I did without the help of others. First, I would like to thank my family. Though I strived to work hard in graduate school, I never achieved the level of hard work my father carried out for his children. My mother taught me an appreciation for art which has taught me that data visualizations can be beautiful as well as informative. My first ever astronomical instrumentation job was working for my brother at a position that he made possible. My brother blazed the trail for my career, propelling my work beyond what I could have accomplished without his aid. The knowledge gained from his perseverance over struggles, and passed onto me, allowed me to navigate difficult obstacles with confidence. I owe him a debt that a younger sibling may never be able to repay.

Second, I would like to thank my colleagues. Throughout my graduate career, I enjoyed working with many different individuals almost all of whom were helpful and encouraging. I know that without the aid of many different people, of which there are too many to mention, I would not have been able to accomplish as much as I did. I especially would like to thank my advisor for always putting the advancement of my career first. In addition, while many people advised me in my graduate career, I would like to specifically thank Dr. Steven Hailey-Dunsheath, who took the time to train me in astronomical instrumentation and always found the time to discuss issues in detail.

Finally, my wife Laura. Laura potentially contributed to the success of my graduate career more than anyone else, both professionally and personally. Professionally, no one will

ever spend as much time reading my scientific written work as Laura. She has spent countless hours tirelessly helping proof and edit all of my written work with only a minimal amount of complaining. Personally, she has been supportive, understanding, and has prevented me from disappearing completely into my work by organizing and planning some of my life's greatest adventures. She has truly been a partner in every sense of the word and there is no way to thank her enough for all that she has done.

The work in this thesis was made possible by the funding of NASA Space Technology Research Fellowship, Grant NNX15AQ09H.

Contents

Chapter	
1	1
1.1	1
1.2	4
1.3	8
1.4	11
1.4.1	13
1.4.2	16
1.4.3	20
1.5	21
1.6	23
2	25
2.1	25
2.1.1	26
2.1.2	28
2.2	31
2.2.1	31
2.2.2	36
2.2.3	40
2.3	45

3	SuperSpec Test Results: Ultra Low Volume TiN Kinetic Inductance Detectors	47
3.1	Tc Variations for TiN KIDs: Characterization and Coping Strategy	47
3.2	Readout Frequency Targeting and Predicted Collisions	55
3.3	TiN NEP and Noise	57
3.3.1	NEP 9 Cubic Micron Detectors	61
3.3.2	NEP 2.6 Cubic Micron Detectors	63
3.3.3	White Noise	64
3.3.4	1/f Noise	68
3.4	Time Constants	71
3.5	Summary	74
4	SuperSpec Test Results: Filterbank Performance	75
4.1	Filterbank Testing Procedure	75
4.2	SuperSpec Millimeter-wave Profiles and Model Fitting	80
4.3	Spectral Profiles	81
4.4	Millimeter-Wave Resonator Frequency Scatter	84
4.5	Dielectric Loss	86
4.6	Response	87
4.7	Antenna/Lens Performance	89
4.7.1	First Generation Dual-Bowtie Antenna	90
4.7.2	Second Generation Dual-Bowtie Antenna	91
5	SuperSpec Demonstration Instrument	94
5.1	Design Optimization for a Full Filterbank	94
5.2	Readout Software Development	100
5.2.1	KID Resonance Location	105
5.2.2	Tone Power Optimization	107
5.3	SuperSpec on the Large Millimeter Telescope	113

5.3.1	SuperSpec Cold Readout Optimization	116
5.4	SuperSpec Observational Strategies	118
6	Arp 220: New Observational Insights into the Structure and Kinematics of the Nuclear Molecular Disks and Surrounding Gas	125
6.1	Introduction	125
6.2	Observations and Data Reduction	126
6.3	Observed Morphology and Kinematics	127
6.3.1	$^{12}\text{CO } J = 3 \rightarrow 2$	131
6.3.2	$\text{SiO } J = 8 \rightarrow 7$	133
6.3.3	$^{13}\text{CO } J = 4 \rightarrow 3$	134
6.3.4	$\text{HCN } J = 5 \rightarrow 4$	135
6.4	Arp 220 Extended Emission	138
6.5	$^{12}\text{CO } J = 3 \rightarrow 2$ Outflow	139
6.6	LIME Modeling	143
6.6.1	Arp 220 Eastern Nucleus	144
6.6.2	Arp 220 Western Nucleus	148
6.7	Discussion	157
6.8	Conclusions	161
7	The Path Forward	164
7.1	Future of SuperSpec Technology	164
7.1.1	SuperSpec for Orbital Platforms	166
7.2	Future ALMA Observations of Arp 220 and High-Redshift Galaxies	167
7.3	Outlook of Future Millimeter and Submillimeter Spectroscopy	169

Bibliography	170
---------------------	------------

Appendix

A LIME Parameter Dependencies	187
-------------------------------	-----

Tables

Table

4.1	Fitted Parameters for SuperSpec Filterbank	83
5.1	SuperSpec Demonstration Instrument Coaxs	119
6.1	Arp 220 Continuum and Line Measurements	128
6.2	Arp 220 Outflow Measurements	141
6.3	Parameters for Arp 220 East Asymmetric Disk LIME Model	149
6.4	Parameters for Arp 220 West LIME Model	156

Figures

Figure

1.1	Cosmic Backgrounds	2
1.2	Negative K-Correction for Submillimeter Observations	5
1.3	Star Formation History	5
1.4	PDR Structure Diagram	14
1.5	CO Ladder Excitation versus Temperature and Density	17
1.6	CO Ladder Excitation versus Galaxy Type	18
2.1	X-Spec Multi-Object Spectrometer Concept	27
2.2	TIME-Pilot Experiment	30
2.3	Filterbank Schematic	32
2.4	SuperSpec Filter Spacing Examples	34
2.5	SuperSpec Filter Spacing NEP Dependence	35
2.6	Single Filterbank Channel Response	39
2.7	Filterbank Oversampling Factor Examples	41
2.8	KID Readout Example	43
2.9	SuperSpec Test Device Diagram	46
3.1	T_c Fitting Example	50
3.2	T_c Fits for SuperSpec Devices	51
3.3	2-Dimensional T_c Fits for SuperSpec Devices	52

3.4	T_c Variation Effects on Resonator Frequency Placement	54
3.5	Fit to Resonator Readout Frequency Scatter	55
3.6	Collision Prediction for SuperSpec Detectors	58
3.7	NEP 9 Cubic Micron Detectors	62
3.8	NEP 2.6 Cubic Micron Detectors	63
3.9	Noise versus Array Temperature	67
3.10	Noise versus Loading	69
3.11	1/f Noise Transition Temperature Scaling	71
3.12	Detector Time Constants	73
4.1	SuperSpec Test Structure Diagram	77
4.2	SuperSpec Filterbank Spectral Profiles with Model Fit	82
4.3	Millimeter-wave Frequency Placement Scatter Fit	85
4.4	Millimeter-wave Frequency Placement 300 Channel Prototype	85
4.5	50 Channel Response	88
4.6	SuperSpec Antenna Types	90
4.7	First Generation Dual-Bowtie Antenna Beam Maps	91
4.8	Broadband Antenna Spectral Response	92
4.9	Second Generation Dual-Bowtie Antenna Beam Maps	93
5.1	SuperSpec Full Filterbank NEP as a Function of Q_c and Q_i	96
5.2	SuperSpec Full Filterbank Resolution Optimization	97
5.3	SuperSpec Full Filterbank Optical Response Model	101
5.4	SuperSpec Full Filterbank NEP	102
5.5	SuperSpec Full Filterbank NEP Q_c and Q_i Variation Sensitivity	103
5.6	Readout Circuit Diagram	104
5.7	Non-linearity of a Kinetic Inductance Detector	108
5.8	Multitone Tone Power Optimization Software	111

5.9	Multitone Tone Power Optimization Software Output	112
5.10	SuperSpec Demonstration Instrument CAD Model	114
5.11	SuperSpec Optical Design for the LMT	115
5.12	SuperSpec Demonstration Instrument Cut Away	117
5.13	SuperSpec Sensitivity Landscape on the LMT	121
5.14	SuperSpec 2 mm Redshift Selection	123
6.1	Continuum Subtracted CO Line Profiles in Arp 220 Nuclei.	131
6.2	Channel Maps for $^{12}\text{CO } J = 3 \rightarrow 2$	132
6.3	346.5 GHz Continuum Emission, Moments 0, 1, and 2 for $^{12}\text{CO } J = 3 \rightarrow 2$, and Moment 0 of SiO $J = 8 \rightarrow 7$	135
6.4	Channel Maps for $^{13}\text{CO } J = 4 \rightarrow 3$	136
6.5	427.8 GHz Continuum Emission, Moments 0, 1, and 2 for $^{13}\text{CO } J = 4 \rightarrow 3$, and Moment 0 of HCN $J = 5 \rightarrow 4$	136
6.6	Arp 220 Extended Emission	139
6.7	Arp 220 Outflow	142
6.8	LIME Models for Arp 220 East	150
6.9	Preferred Model for Arp 220 East	151
6.10	Preferred Model for Arp 220 West	153
6.11	Schematic of Arp 220 System	158
6.12	Flux Density versus Dust Temperature in the Arp 220 Nuclei	161
A.1	Parameter Degeneracy: Turbulent Velocity, Circular Velocity, and Disk Inclination Angle	188
A.2	Parameter Degeneracy: Gas Temperature, Disk Thickness, Gas Mass, and Disk Inclination Angle	189

Chapter 1

Millimeter-wave and Submillimeter-wave Astrophysics

1.1 Motivation for Submillimeter and Millimeter Observations

Submillimeter and millimeter radiation is a powerful tool for understanding our Universe. Submillimeter light contains a substantial fraction of the cosmic infrared background (CIB), of which the integrated flux was found by the COBE mission to rival the power of all ultraviolet (UV) and visible radiation in the Universe (Dole et al., 2006), Figure 1.1. The CIB is light from infrared galaxies at high redshift. Surveys using SCUBA, MAMBO, LABOCA, AzTEC, and PACs and SPIRE on-board Herschel showed that the luminosity of galaxies at submillimeter and millimeter wavelengths is ~ 1000 times that of the local universe (Coppin et al., 2006; Greve et al., 2008; Weiß et al., 2009; Austermann et al., 2010; Glenn et al., 2010). This indicates that the massive amount of energy produced by star formation and black hole accretion in the early universe is being largely absorbed and re-emitted by dust in the far-infrared. In fact, approximately half of all starlight ever produced has been reprocessed by dusty galaxies (Hauser and Dwek, 2001). Herschel has revealed thousands of bright galaxies per square degree (Glenn et al., 2010). This stresses the importance of submillimeter and millimeter radiation to study high-redshift galaxies. Without far-infrared and submillimeter observations, half of all the energy produced by star formation could not be measured.

Submillimeter observations have historically lagged behind its UV and optical counterparts. This is for two reasons. The first is that observations at submillimeter wavelengths become increasingly more difficult the shorter the wavelength due to atmospheric absorp-

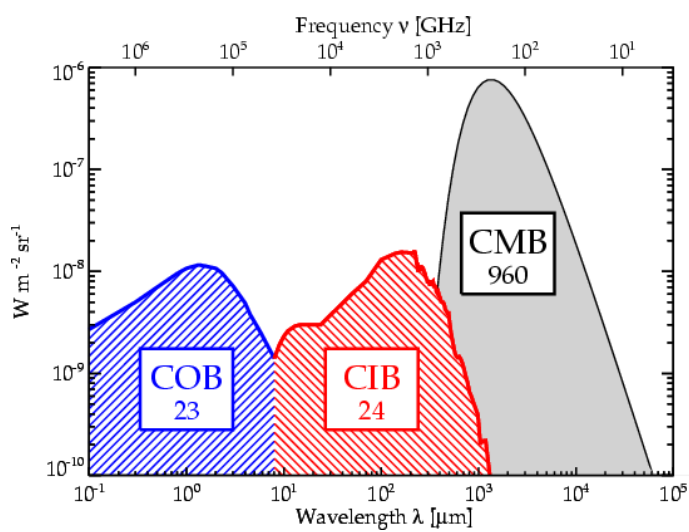


Figure 1.1: A Plot of the relative intensities of three of the major radiation backgrounds in astrophysics, the cosmic optical background, the cosmic infrared background, and the cosmic microwave background. Figure from Dole et al. (2006).

tion mostly from water vapor; so much so, that shorter far-infrared wavelength observations are entirely impossible from the ground. This restricts submillimeter observations to the highest elevations and the driest environments, such as the Atacama Desert in Chile or the South Pole. The second reason the submillimeter field is playing catch-up is due to a lack of sensitive detector technology. Where infrared and visible detector technology has been fueled by significant defense and industry interest, submillimeter detectors are often purpose-built by the astronomical community to carry out astronomical observations. Only recently has the detector technology become sensitive enough to be background limited from the best ground-based observation sites. For space-based observations, background-limited sensitivity is still an area of ongoing development and growth. Even with background-limited sensitivity achieved, significant efforts are still being made to increase the pixel count in millimeter and submillimeter cameras to provide efficient mapping over large areas of the sky. In particular, efforts are being made to create large detector arrays using sustained, straight-forward fabrication procedures.

It is not without hope though. This is because observing in the millimeter and submillimeter does have its advantages, especially for high-redshift objects. For continuum dust emission, submillimeter observations benefit from negative K-correction with redshift. This is because the location of the peak of the dust blackbody spectral energy distribution (SED) and the shape of the SED results in high-redshift objects being just as easy to observe as low-redshift objects. For a 30 K dust temperature, the dust blackbody peaks at 100 μm . As the redshift of an object increases, the peak of the blackbody spectrum is moved to longer submillimeter wavelengths. Thus, the brightest part of the blackbody spectrum is moved into submillimeter bands. In particular, at wavelengths longer than the dust blackbody SED peak, the SED is in the Rayleigh-Jeans regime where the intensity $S_\nu \propto \nu^{2+\beta}$. β is the dust emissivity index $\sim 1.5 - 2$. Hence, the flux density will go as $S_\nu \propto \nu^{2+\beta}/4\pi D_L^2$. D_L is the luminosity distance. $\nu^{2+\beta} \propto \nu_{rest}^{2+\beta}(1+z)^{2+\beta}$ and $D_L \propto (1+z)$ indicates that the flux density goes as $S_\nu \propto (1+z)^{2+\beta}/(1+z)^4 \propto (1+z)^{\beta-2}$ (Casey et al., 2014). Since $\beta \sim 1.5 - 2.0$,

the flux density in the Rayleigh-Jeans regime of the dust blackbody is roughly constant with redshift. This is shown in graphical form for a selection of different observational wavelengths in Figure 1.2. This effect makes submillimeter and millimeter wavelengths arguably one of the best wavelength regimes to observe high-redshift galaxies.

Beyond the CIB the millimeter and microwave are very important for probing the Cosmic Microwave Background (CMB). The applications of the science and study of the CMB are profound; however, they are not the main topics of the science for this thesis and thus are only discussed briefly. As noted in Section 2.1.2, the technology detailed in this thesis has significant implications for study in this wavelength regime as well.

1.2 Star Formation History of the Universe

Over a period spanning seven to eleven billion years ago, the Universe changed dramatically. Over half of the stars we can observe today were formed during this time, with a star formation rate density in the Universe 30 times higher than observed in the current universe (Figure 1.3). This is the crux of one of the major outstanding questions in astrophysics: What physical processes gave rise to the shape of the Universe's star formation history? In particular, what processes led to the rise of the star formation rate to its peak at $z \sim 2$ and what process then caused the subsequent decline in star formation rate to the rates currently observed in the Universe?

To this day the astrophysical community lacks a complete theoretical model that can trace galaxy evolution and star formation from early times to the present while accounting for the broad range of current observations. In order to understand star formation history and the underlying physics governing star formation rate, three things are required:

1. an unbiased measure of star formation rate for a large number of galaxies,
2. correlation of star formation rate with other physical tracers allowing insight into the underlying physics occurring in galaxies that dictates the rate of star formation, and
3. accurate redshifts to determine when in cosmic history a particular star formation rate is

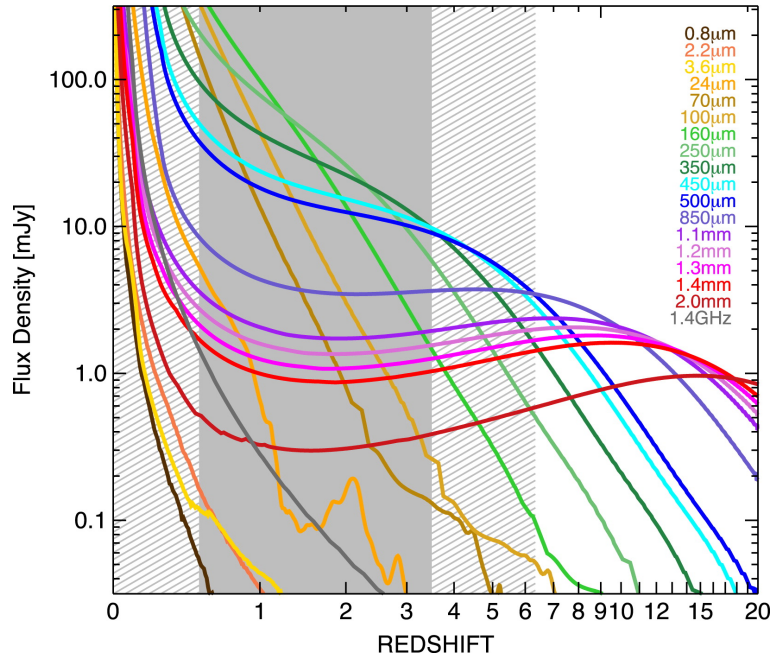


Figure 1.2: Plot showing how the flux density of continuum dust radiation scales with redshift for several different observational wavelengths. This is for a composite submillimeter galaxy dust SED from Pope et al. (2008) scaled to a $10^{12.5} L_{\odot}$ galaxy. Note that at $850 \mu\text{m}$ and longer (up to 2 mm) high-redshift galaxies are equally if not more easily observed at high redshift for redshifts > 1 . Figure from Casey et al. (2014).

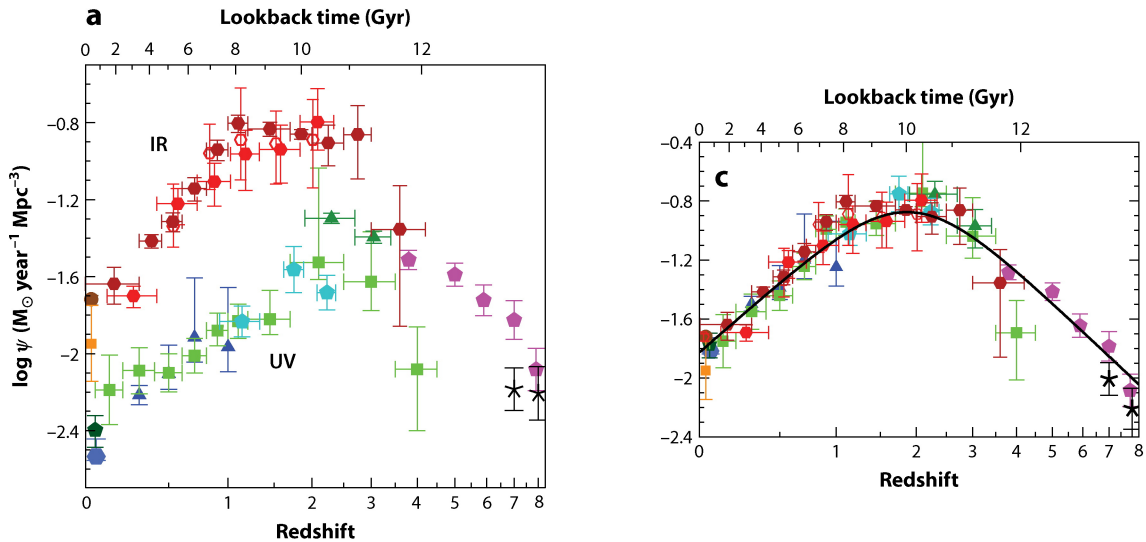


Figure 1.3: Left: Plot of measured star formation rate densities uncorrected for dust attenuation. Right: Star formation rate in solar masses per year per co-moving cubic megaparsecs. Figure from Madau and Dickinson (2014).

occurring.

The power of millimeter and submillimeter observations to measure star formation rate is well demonstrated in Figure 1.3. UV measurements are an ideal tracer of star formation because UV observations directly probe the emission of young hot stars. Unfortunately, UV studies suffer from highly uncertain dust-extinction corrections which must be utilized to back-out star formation rates (Madau and Dickinson, 2014). However, the reason it is difficult to measure star formation rates in the UV, dust extinction, is the reason why submillimeter and millimeter radiation is such a good tool for measuring star formation. This is because the total-IR radiation from 8 to 1000 μm is the reradiated energy produced by these dust-absorbed UV photons, and the majority of the total-IR luminosity is from either dust heated by star formation or by Active Galactic Nuclei (AGN). Given a way to distinguish AGN luminosity from star formation driven luminosity, the total-IR emission yields an unbiased direct measure of the star formation rate. Thanks to the negative K-correction discussed in the previous section, IR emission is easy to measure at high redshift in the submillimeter and millimeter bands. Ultimately, the best understanding of the star formation history of the Universe will come from multi-wavelength studies that include UV, submillimeter, and other wavelengths. However, in this thesis, the focus is on the power of millimeter and submillimeter spectroscopy.

While dust continuum measurements constrain the total star formation rates that are currently ongoing in a galaxy, this does not provide the whole picture of star formation processes in galaxies. In particular, dust continuum traces the output of stars, yet it is also desirable to understand what drives the actual formation of stars. In order to study this, the fuel for star formation, cool gas, must also be observed. In this way, spectroscopic measurements of cool molecular gas, such as CO, inform astronomers about the available gas in galaxies to form stars. Furthermore, resolved CO spectroscopy measurements can show exactly where in a galaxy star formation is occurring. Very high-resolution spectroscopic measurements of the gas yield its kinematic properties in galaxies, revealing the dynamics

of the gas. Furthermore, the kinematics can directly search for high-velocity gas outflows tracing feedback that may inhibit continued star formation.

Spectral lines probe the internal physical conditions within galaxies. This is because different spectroscopic transitions will trace different gas densities and gas temperatures as well as different ionization environments. For example, AGN lead to higher ionization than star formation regions, meaning higher ionization energy atomic transitions tend to trace AGN activity versus star formation. In particular, the [O IV] at $25.89 \mu\text{m}$, ionization potential of 54.9 eV, and [Ne V] at $14.32 \mu\text{m}$ and at $24.3 \mu\text{m}$, ionization potential of 97.1 eV, are strong indicators of AGN (LaMassa et al., 2012). Whereas, [Ne II] $12.8 \mu\text{m}$, ionization potential of 21.6 eV, is an indicator of star formation (Ho and Keto, 2007; Dale et al., 2009). Using the ratio of these lines can provide a measure of AGN luminosity contribution fraction.

Perhaps most importantly, spectroscopy provides a direct measure of the redshift of an object with an accuracy that cannot be obtained by continuum measurements. Of the now many thousands of galaxies detected in submillimeter and millimeter bands, only a small percentage of them have determined redshifts (Casey et al., 2018). This is because the most commonly utilized spectroscopic redshift identifier lines are in the UV and visible wavelength ranges. However, multi-wavelength follow-up of submillimeter and millimeter sources in these wavelength ranges can be very difficult. This is for two reasons. First, the large beams of submillimeter and millimeter single-dish survey telescopes do not constrain the location of the sources with the required accuracy for UV or visible follow-up. A single beam could contain as many as 10 individual visible sources (Casey et al., 2014). The second is that extinction for these sources in the UV and visible wavelength range is extreme (Chapman et al., 2005). To this day, there remain many bright submillimeter detected galaxies that have failed to uncover an optical counterpart, and not from lack of effort (e.g. HDF850.1 (Serjeant and Marchetti, 2014)). This makes direct spectroscopic follow-up in the millimeter and submillimeter the preferred method of obtaining redshifts for these sources. This is because there is no source location ambiguity when observing in the same band for

which the source was detected; and additionally, these sources are expected to have bright submillimeter and millimeter emission lines.

Spectroscopic measurements yield all the information needed to unravel the cosmic star formation history. Continuum observations combined with spectroscopic measurements of different ionization energy fine structure lines (to decouple star formation luminosity from AGN luminosity) allow for an unbiased measure of the total star formation rate. Spectroscopic measurements of molecular gas both trace the fuel for star formation as well as feedback from outflows that can inhibit star formation. This gives insight into the processes that facilitate and prevent star formation. Finally, spectroscopic measurements of redshifts provide the absolute best way to measure how far away a galaxy is; and thus, when in cosmic history a particular object is being observed. Combining all of the measurements together will allow astronomers to obtain the best understanding of how the cosmic star formation history has evolved from CMB fluctuations into the present day structure we observe in the modern universe.

1.3 Galaxy Evolution

In addition to understanding how star formation rate has evolved over cosmic time, it is desirable to understand what has driven this star formation. In particular, a detailed understanding of what physical processes dictate star formation is needed. To accomplish this an understanding of galaxy evolution is imperative. Galaxies are the fundamental star containing unit in the Universe, and cosmic star formation is dictated by galaxy evolution. Thus to really understand cosmic star formation, we must understand the internal physics that dictate the growth of structure in galaxies through star formation and black hole growth.

It is believed that galaxies are formed and evolve over time due to three mechanisms: (1) in situ star formation, (2) major and minor mergers with other galaxies, and (3) cold gas accretion from the intergalactic medium (Conselice, 2014). Astronomers have a general idea of what this galactic evolutionary process looks like. Gas is drawn to galactic dark matter

halos surrounding galaxies. If the dark matter halo is very massive, $> 10^{12} M_{\odot}$, then gas is shock-heated and will take a long time to cool and enter a galactic disk. For less massive halos, which are more abundant at high redshift, less cooling is required and the gas can enter the galaxy more quickly (Tumlinson et al., 2017). This gas then adds to a galaxy's mass and over time collapses within the galaxies to form stars. During this process, the formation of stars and AGN activity within the galaxies will drive feedback that directly impacts the formation of stars (Naab and Ostriker, 2017). This feedback can have both positive and negative effects on star formation. In particular, it can both heat the star-forming gas and drive outflows that push gas out of the disks of galaxies. Heating of gas can create thermal pressure that prevents the gravitational collapse necessary to form stars. It can also inhibit the cooling required to accrete gas onto galaxies. In addition, strong outflows can deplete the galaxy of the necessary gas to form stars. On the other hand, outflows can enrich the circumgalactic medium around the galaxies with metals created by star formation. Since metals are a dominant cooling mechanism for gas, these metals can allow the accreting gas to more efficiently cool and enter the galaxy enhancing the star formation rate (Tumlinson et al., 2017). While this is ongoing, galaxies additionally interact with each other by colliding and merging together. This merging process can involve either major mergers, where two galaxies that differ in mass by no more than a factor of 4 collide, or minor mergers, where small galaxies are captured by larger galaxies. The merging of galaxies causes a temporary increase to the star formation rate and facilitates the coalescence of super-massive black holes. Most of these mechanisms operate together to cause galaxies to form stars at a quasi-steady state rate. Finally, in some cases, galaxies evolve to form large elliptical galaxies for which star formation is almost nonexistent. In this situation, some mechanism has quenched the ongoing star formation.

While this paints an informative picture of the processes involved in galaxy evolution, many of the details of these interactions are still poorly understood. Is galactic star formation dominantly triggered by merger events or by gas accretion from extragalactic halos? Why is

super-massive black hole growth so well correlated with star formation and galaxy evolution (Heckman and Best, 2014)? In particular, what governs the growth of super-massive black holes at the center of galaxies and how are they connected to the evolution of the galaxy as a whole? Does feedback from AGN enhance or inhibit star formation in a galaxy? What are the main drivers that cause some galaxies to form stars faster than others? What causes the quenching of star formation in the large elliptical galaxies observed throughout the Universe (Tumlinson et al., 2017)? Is shock-heating of the accreting gas for massive dark matter halos to blame, or is feedback from luminous AGN heating the circumgalactic gas? Finally, how exactly does feedback from AGN and star formation impact future star formation? In particular, a decrease in SFR efficiency for high luminosity galaxies is observed. In an effort to explain this, it is often proposed that star formation is inhibited by feedback from winds and outflows driven by AGN (King and Pounds, 2015). The outflow depletes a galaxy of the necessary gas to produce stars. However, somewhat contrary to this theory, there is a clear correlation between AGN mass and galaxy central bulge mass suggesting that AGN activity might enhance the formation of stars in the central bulge (Ferrarese and Merritt, 2000).

Submillimeter and millimeter-wave observations cannot answer all of these questions, but they do help answer some of them and form an important wavelength regime in a multi-wavelength effort to fully understand galaxy evolution. As discussed above, submillimeter spectroscopy is very sensitive to the cool gas in galaxies that are forming stars. Thus, these observations can show us the morphology and physical conditions of the cool star-forming gas. Kinematically resolved spectroscopy allows for the detection of both inflowing (Rangwala et al., 2015) and outflowing gas (Barcos-Muñoz et al., 2018) in galaxies. Comparison of fine structure lines in galaxies constrain the ionization environment and thus the importance of AGN feedback. At the same time, spectroscopy of fine structure lines can measure the metal content of the gas, the presence of which is essential to enabling the cooling and accretion of gas into galaxies. For example, $[\text{O III}]/[\text{N III}]$ can be used as a measure of metallicity above 0.2 solar (Groves et al., 2004) and Ne to S ratios can also be used going back to a

redshift of $z = 4$ (Fernández-Ontiveros et al., 2016). Certainly, millimeter and submillimeter spectroscopy will play an important role in developing our understanding of galaxy evolution throughout cosmic history.

1.4 Millimeter and Submillimeter Spectroscopy and Spectral Lines

In order to understand galaxy evolution and the formation of stars, measurements of the cool gas that acts as the fuel for star formation is needed. The most abundant molecular gas molecule that dominates the gas within galaxies is H_2 . H_2 , however, is a diatomic molecule that is made up of two identical nuclei and thus does not have a permanent dipole moment. As such, the transitions in the electronic ground state are forbidden. In addition, its quadrupole transition has a high excitation temperature and weak Einstein A coefficient, making it difficult to observe. For this reason, observations of tracer molecules are used to infer the total gas mass content within galaxies. One of the tracer molecules that is most commonly utilized is CO. This is because CO is the most abundant molecule after H_2 , it is easily excited in cool gas, and the lowest transition is observable with ground-based telescopes via the 3 mm atmospheric window.

For any linear polar molecule the angular momentum is $L = n\hbar$. The rotational energy levels then are defined by $E_{rot} = L^2/2I$, where I is the moment of inertia of the molecule. Together this gives $E_{rot} = n^2\hbar/2I = J(J+1)/2I$, where the change in J is only allowed to be $\Delta J = \pm 1$ to conserve angular momentum. Thus, the difference in energy levels between transitions is $\Delta E = [J(J+1) - (J-1)J]\hbar/2I = \hbar J_{upper}/I$, where J_{upper} corresponds to the higher energy level (Carilli and Walter, 2013). Fortunately, the moment of inertia, I , changes with higher rotational energy levels due to centrifugal forces stretching the linear molecules apart. This acts as a small modifier on the energy levels of each transition for a given J_{upper} . This small modification means the separation in energy levels of any two transitions for a given molecule is unique. This, in turn, allows for unambiguous redshift determination if any two transitions are simultaneously measured.

An important metric when thinking about spectral transitions is the critical density, n_{crit} . The critical density is the density at which collisional excitation is balanced by spontaneous radiative decay. The collisional excitation rate is dependent on the density and temperature of the colliding partner, in cool molecular gas this will be dominantly H_2 . Whereas, the spontaneous radiative decay rate is based purely on the internal properties of the emitting molecule or atom. For molecular rotational transitions, this is proportional to the dipole moment squared, μ^2 . In general, but not always, emission is most prevalent when gas has densities in excess of the critical density of a particular line. Different lines have different critical densities and thus can be used to trace different density environments. For instance, HCN has a very strong dipole and thus a very fast spontaneous radiative decay rate, which in turn drives it to have a very high critical density of $\sim 2.6 \times 10^6 \text{ cm}^{-3}$ for the $J = 1 \rightarrow 0$ transition compared to CO $\sim 2.1 \times 10^3 \text{ cm}^{-3}$. Thus, HCN should preferentially trace much denser gas than CO, whose emission will be more widespread throughout a galaxy. Some other important commonly observed dense gas tracers are CS and HCO^+ .

In addition to molecular lines, atomic fine structure lines are important for cool interstellar gas. This is because their radiation represents a dominant path for cooling gas at slightly warmer temperatures than the coldest molecular gas. In particular, the [C II] fine structure transition from $^3P_{3/2} \rightarrow ^3P_{1/2}$ is one of the most important coolants. [C II] is a dominant coolant because it is easy to ionize (ionization potential of 11.26 eV) and easy to excite (excitation potential of only 91 K). Fine structure lines are forbidden and thus generally optically thin. Therefore, they avoid line trapping and allow radiation to escape, thus allowing for net cooling to occur. The regions in which different species exist and are important for cooling is demonstrated in Figure 1.4. Other important fine structure lines in ionized gas are the [N II] 205 μm and 122 μm lines and the [O III] 88 μm and 52 μm lines. The [N II] 122 μm / [O III] 88 μm ratio is very sensitive to the radiation field. This is because both lines have very similar critical densities, 300 and 500 cm^{-3} in molecular gas and 48 and 50 cm^{-3} in ionized gas, yet very different ionization potentials, 14.5 eV versus

35 eV. The [C II] 158 μm and the [N II] 205 μm lines both have critical densities of $\sim 50 \text{ cm}^{-3}$ in ionized gas. This, along with their ionization potentials that are more and less than hydrogen, means that their ratio can give the fraction of ionized to neutral gas (Oberst et al., 2006; Ferkinhoff et al., 2011; Decarli et al., 2012). This, of course, does require an assumed C/N abundance ratio.

1.4.1 CO Molecular Lines

As stated above, because of the difficulty in observing H_2 , CO has become the workhorse of the astronomical community in measurements of cool star-forming gas. The CO molecule has a relative abundance to H_2 of around 2×10^{-4} , a critical density of $\sim 10^3 - 10^4 \text{ cm}^{-3}$, and a low excitation potential of only 5.5 K for the $J = 1 \rightarrow 0$ transition. All of this makes CO rotational transitions luminous tracers of molecular gas. As such, astronomers use the CO line luminosity to predict the total gas mass present in H_2 via a CO line luminosity to H_2 mass conversion factor. A CO luminosity to H_2 mass conversion factor works because of the principles detailed in the following paragraph.

The CO $J = 1 \rightarrow 0$ line is almost always optically thick for giant molecular clouds. Since these clouds are optically thick, their luminosity in CO scales as the line width of the CO line observed such that,

$$L_{CO} \propto T_B \sigma R^2, \quad (1.1)$$

where T_B is the brightness temperature of the CO, σ is the 1-D line dispersion, and R is the radius of the giant molecular cloud. For giant molecular clouds that are self-gravitating, the line width increases as the square root of the size of the cloud (Larson, 1981) such that,

$$\sigma \propto R^{0.5}. \quad (1.2)$$

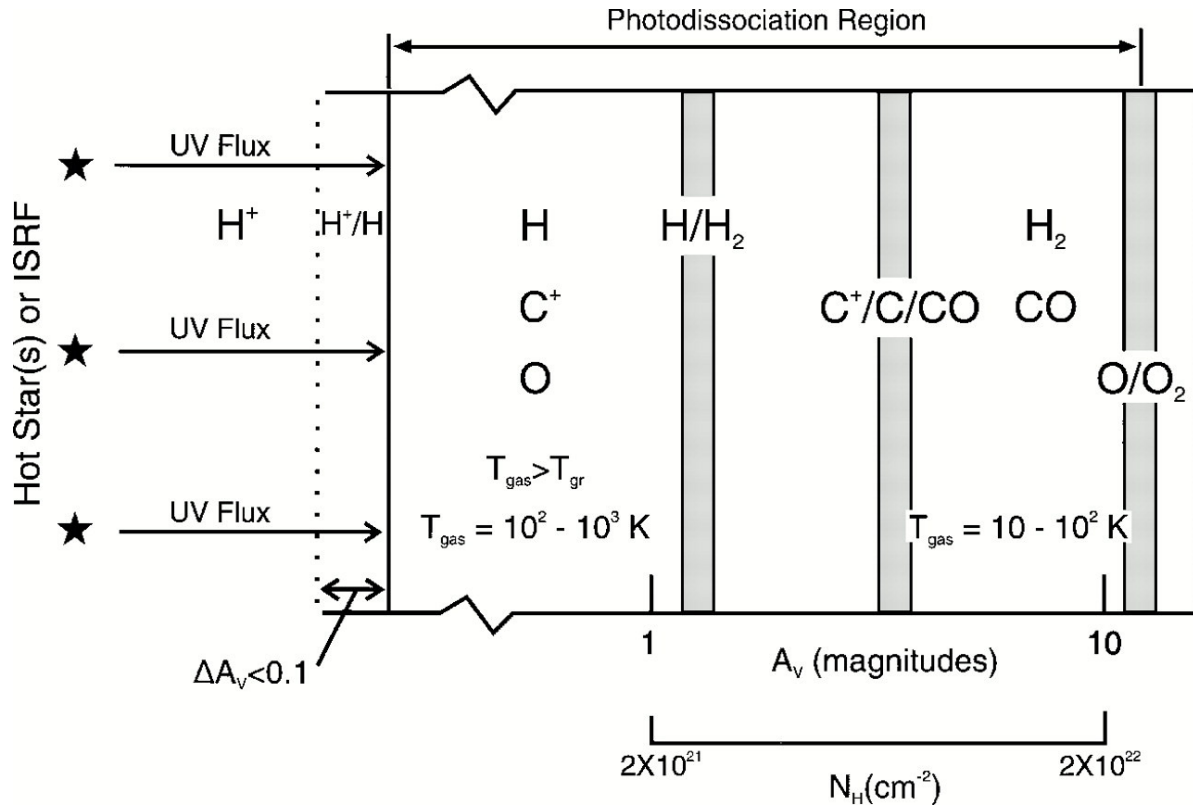


Figure 1.4: Diagram showing the structure of a photon-dominated region (a.k.a. photodissociation region). Presence of different atomic/molecular species and their ionization states is dictated by the ability of UV flux from young hot stars to penetrate cool gas clouds. For different temperature gas, different species will dominate the radiation and thus the cooling of the gas. H⁺ and C⁺ are H II and C II as commonly referred to throughout this thesis. Figure from Hollenbach and Tielens (1999).

Thus Equation 1.4.1 becomes

$$L_{CO} \propto T_B \sigma^5 \Rightarrow \sigma \propto (L_{CO}/T_B)^{1/5}. \quad (1.3)$$

Therefore, the mass of a virialized cloud is

$$M_{vir} \propto R \sigma^2 \propto \sigma^4 \propto (L_{CO}/T_B)^{4/5}. \quad (1.4)$$

From this, it can be seen that the mass of a giant molecular cloud is almost linearly related to the line luminosity, modulo a weak dependence on the brightness temperature of the CO. Using this idea, a relationship can be established such that we have the following equation (Bolatto et al., 2013):

$$M_{mol} = \alpha_{CO} L_{CO}, \quad (1.5)$$

where $\alpha_{CO} = 4.0 M_{\odot} (\text{K km/s pc}^2)^{-1}$. L_{CO} can be calculated from a measured flux density from

$$L'_{CO} = 3.25 \times 10^7 \times I \times \nu_{obs}^{-2} \times D_L^2 \times (1+z)^{-3}, \quad (1.6)$$

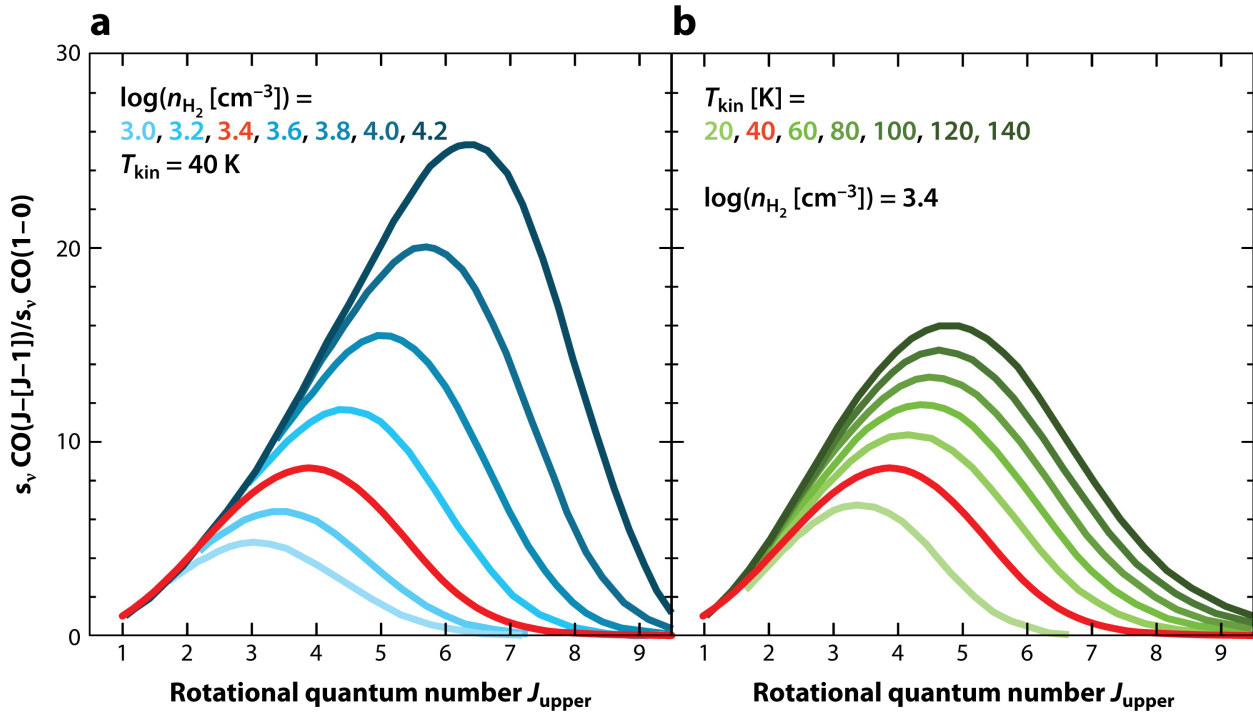
where I is in Jy km/s, ν_{obs} is in GHz, and D_L is in Mpc (Solomon et al., 1992). The value of $\alpha_{CO} = 4.0 M_{\odot} (\text{K km/s pc}^2)^{-1}$ is empirically derived based on the Milky Way and nearby “normal” galaxies (Bolatto et al., 2013). This conversion factor should still be valid for entire galaxies as long as multiple giant molecular clouds do not occupy the same sightline. When the assumption that the dynamics of the molecular gas are representative of virialized clouds

is not correct, this relationship breaks down and the constant must be modified. This is the case for starbursting galaxies like Arp 220, in which the gas kinematics are dominated by other mechanisms such as the rotation of the two central nuclei. For galaxies undergoing a starburst, a conversion factor of $\alpha_{CO} = 0.8 M_{\odot} (\text{K km/s pc}^2)^{-1}$ is recommended (Bolatto et al., 2013). This relation is valid for CO $J = 1 \rightarrow 0$ but not necessarily for higher transitions. For high-redshift galaxies, higher J transitions are often the only lines measurable. In these cases, it is common to try to scale a higher J line luminosity to predict the line luminosity in the $J = 1 \rightarrow 0$ transition so that the above relation can still be used. This, however, is not always straight-forward and merits careful consideration.

Beyond using CO as a way to predict the total molecular mass, if multiple CO transitions are obtained the excitation of the CO ladder, often referred to as the CO SLED, can be modeled. The results of this modeling can then be used to predict the density and temperature of the CO observed. This is demonstrated in Figure 1.5, where the CO SLED is shown for several different temperatures and densities. In order to model the CO excitation, one must assume that the different CO transitions are probing the same component of gas, which for very different transitions, high J versus low J , is not likely. Thus, as often as not, multiple gas components are used to model a single CO SLED (Kamenetzky et al., 2017). Besides extracting the temperature and density of the CO gas, CO ladder excitation can be used to differentiate between different galaxy populations. This is demonstrated in Figure 1.6. Most noticeably, it can be seen that the QSOs, which are known to host AGN, have the highest excitation, peaking at the highest J CO transitions. In this way, the CO ladder can be used to distinguish between galaxy populations and potentially can be used as a metric to detect the presence of an AGN.

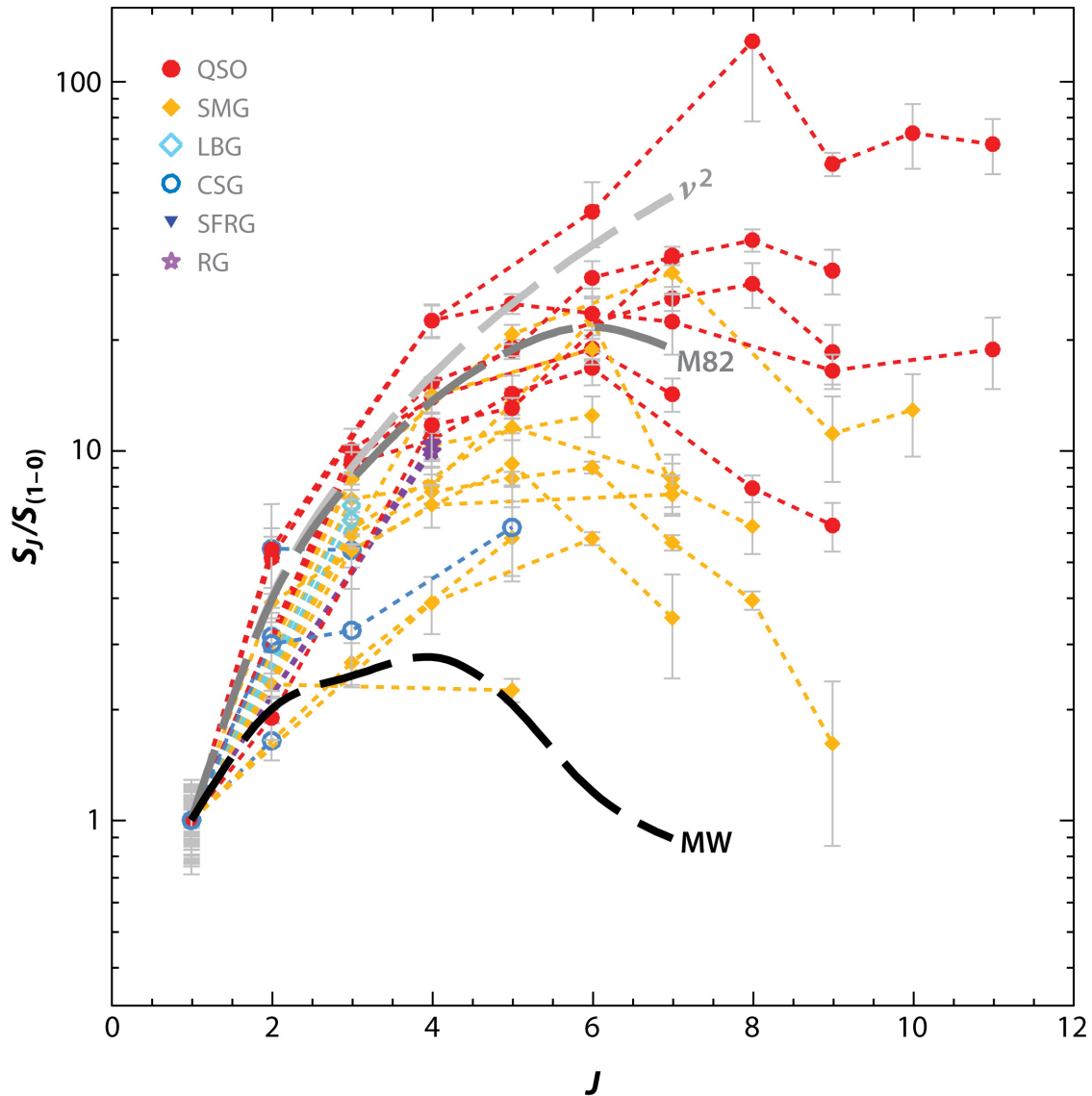
1.4.2 The [C II] Fine Structure Line

Carbon is the fourth most abundant element in the Universe. It is the strongest line in star-forming regions throughout radio and far-IR wavelengths, with a line flux that is often



A Carilli CL, Walter F. 2013.
R Annu. Rev. Astron. Astrophys. 51:105–61

Figure 1.5: Left: Plot showing the CO excitation ladder as a function of J for different densities. Right: Plot showing the CO excitation ladder as a function of J for different temperatures. Increasing excitation towards higher J_{upper} is degenerate with both increasing density and increasing temperature. However, increasing temperature leads to a broader ladder due to the Boltzmann velocity distribution for collisions. Thus, given enough transitions, this degeneracy can be broken. Observationally, it can be difficult to obtain many transitions for a single source at a single redshift. Figure from Carilli and Walter (2013).




 Carilli CL, Walter F. 2013.
 Annu. Rev. Astron. Astrophys. 51:105–61

Figure 1.6: Plot showing the CO excitation ladder as a function of J for different galaxies. QSOs are quasi-stellar objects, bright galaxies known to host an AGN. SMGs are submillimeter galaxies which are galaxies that are bright in submillimeter continuum emission (see Section 1.5). LBGs are Lyman break galaxies. CSGs are color selected galaxies, selected via their optical or near-IR colors. SFRGs are radio-selected galaxies, and RGs are radio galaxies identified in centimeter radio surveys. Figure from Carilli and Walter (2013).

1000 times higher than CO $J = 1 \rightarrow 0$ in star-forming galaxies (Carilli and Walter, 2013). Carbon has an ionization energy of 11.3 eV, compared to hydrogen’s ionization energy of 13.6 eV. This means UV photons produced by young hot stars can penetrate un-ionized gas and ionize the atomic carbon present there. The atomic form of carbon will also be present in this environment because the dissociation energy of the CO molecule is also lower than hydrogen’s ionization energy at 11.2 eV. Since carbon is easily excited, has a modest critical density, and is optically thin, C II can radiate the heat away from these regions. All of this makes [C II] one of the dominant coolants of the interstellar medium in galaxies. So much so, that the [C II] line luminosity can comprise from 0.1 to 1 % of the total-IR luminosity of the whole galaxy (Stacey et al., 1991). This incredible brightness of [C II] means that if only a single line is detected for a source at high redshift then, more often than not, it can be safely assumed to be the [C II] 158 μm line.

Spectral lines do not benefit from the negative K-correction from which submillimeter continuum observations benefit. As such, it becomes increasingly difficult to detect CO emission in high-redshift sources. Thus, in order to obtain redshifts and complete spectroscopy of cool gas at high-redshift, the [C II] line is quickly becoming the workhorse of high-redshift spectroscopy. Not only is it much brighter than CO, but for high-redshift objects, the 158 μm line is redshifted into atmospheric windows so that it becomes observable from the ground with telescopes such as ALMA and the LMT. In particular, for galaxies from $z = 5$ to 9, [C II] falls in the 1 mm atmospheric window where it can be observed using current SuperSpec technology.

[C II] has now been detected using ALMA in several 10s of galaxies (Gullberg et al., 2015; Carniani et al., 2018; Lagache et al., 2018) and references within. In local star-forming galaxies, the ratio of the $L_{[CII]}/L_{FIR}$ is 0.1 to 1 % (Stacey et al., 1991). Yet, it seems that even at high redshift the $L_{[CII]}/L_{FIR}$ remains high (Stacey et al., 2010; Carniani et al., 2018; Lagache et al., 2018). Furthermore, $L_{[CII]}$ seems to correlate well with the total SFR for a galaxy (De Looze et al., 2011; Stacey et al., 2010; Lagache et al., 2018) (albeit with large

scatter and some dependency on metallicity). This does mean though, with a large statistical sample of [C II] measurements at high redshift, the star formation rate can be determined from this line.

1.4.3 The [N II] Fine Structure Line

The singly ionized nitrogen ground state is split into three levels producing two fine structure transitions: the ${}^3P_2 \rightarrow {}^3P_1$ 122 μm line, with a excitation potential of 188 K and a critical density of 310 cm^{-3} , and the ${}^3P_1 \rightarrow {}^3P_0$ 205 μm line, with a excitation potential of 70 K and a critical density of 48 cm^{-3} (Carilli and Walter, 2013). [N II] has an ionization potential of 14.5 eV compared to hydrogen’s 13.6 eV. As such, it mostly exists in ionized gas not shielded from UV light by neutral hydrogen. Since it occurs in an ionized environment, its critical density corresponds to collisions with electrons rather than H_2 . The [N II] 205 μm line is particularly interesting to the SuperSpec collaboration because it allows for the detection of high redshift galaxies in the range $z = 3.5$ to 6.5 for the 1 mm atmospheric window. In particular, this fills a sensitivity gap from $z = 3.5$ to 5 where SuperSpec struggles to detect CO lines and cannot detect the [C II] line.

The [N II] line is important in and of itself because it traces the gas in H II regions. As discussed above, examining the [N II]/[C II] ratio allows for one to quantize exactly how much of the [C II] emission is arising from neutral versus ionized gas. The ratio of both the 205 μm to 122 μm [N II] lines provides a measure of the electron density (Goldsmith et al., 2015). The [N II] line is roughly ten times weaker than the [C II] line causing it to be more difficult to detect (Decarli et al., 2014). As such, [N II] has only been detected by ALMA in a handful of high-redshift galaxies (Ferkinhoff et al., 2015; Béthermin et al., 2016; Pavesi et al., 2016; Lu et al., 2017, 2018). However, these observations will only continue to grow and [N II] line luminosities will prove invaluable for the interpretation of the more commonly detected [C II] line. In addition, the [N II] line coupled with the [O III] line may provide one of the best ways to detect the presence of AGN in high-redshift dusty galaxies.

1.5 Arp 220 as a Local Case For High-Redshift Galaxies

Submillimeter galaxies (SMGs) are galaxies that have continuum detections of ≥ 1 mJy detected in the wavelength range from 250 μm to 2 mm (Casey et al., 2014). Historically, they refer to SCUBA detections at 850 μm with fluxes of at least 5 mJy (Hughes et al., 1998; Barger et al., 1998). They exhibit incredibly high luminosity and thus have incredibly high inferred star formation rates on order 100-1000 $M_{\odot} \text{ yr}^{-1}$. Understanding the origin of these bright SMGs at high redshift is of particular importance in order to better understand how they are formed and what their evolution will be. Of particular importance, is determining if they represent short-lived periods of enhanced star formation or if they represent a longer sustained method of star formation. This will then determine their contributonal importance in creating the structure we observe in the Universe today, i.e. does SMG star formation represent 1%, 10%, or more of the total star formation. Furthermore, the assumption of whether SMGs are starbursts or not directly impacts which CO line luminosity to gas mass conversion factor astronomers should choose for these galaxies, which could lead to incorrect estimates of the gas mass by almost an order of magnitude for these galaxies.

The usefulness of Arp 220 and other local ULIRGs as an analog for high-redshift ULIRGs and HyLIRGs is a question that is still very much under debate. In particular, are bright submillimeter galaxies (SMGs) the result of gas-rich mergers like ULIRGs are in the local universe, and can our knowledge of local ULIRGs be utilized for high-redshift systems? Early resolved measurements of SMGs found their morphologies to be disturbed indicative of mergers (Engel et al., 2010). This led to the conclusion that bright SMGs are formed by gas-rich mergers. Yet studies also found SMG sizes were larger than that of local ULIRGs, which in turn led to the conclusion that they are scaled up versions of local ULIRGs such as Arp 220. Supporting this, some simulation work suggests that mergers of galaxies with higher gas fractions will indeed produce more extended gas emission (Mihos, 1999). In this case, because of the higher gas fraction, there is more star formation and less disk stability. This

results in a more knotted distributed star formation rather than just a central coalescence of star-forming gas. On this side of the debate, SMGs are indeed merging systems but it is still unclear whether local ULIRG conditions will be valid at high redshift.

Alternatively, it is proposed that SMGs are simply normal disk galaxies accreting cold gas from their dark matter halos with high efficiency. This theory is in part fueled by the difficulty, due to the short timescale of merger events, in reproducing the number counts observed for SMGs, i.e. merging events should be a relatively rare occurrence on the sky (Davé et al., 2010). In this situation SMGs are simply just the high-mass end of a normal star-forming galaxy main sequence (Hayward et al., 2012). The galaxy main sequence is the empirical observation that most galaxies for a given redshift lie on a tight relationship between star formation rate and stellar mass (Noeske et al., 2007). This effect is caused because star formation correlates well with gas accretion rates which in turn is well correlated with halo mass (Faucher-Giguère et al., 2011). In this picture, SMGs are not starburst systems triggered by mergers but rather they represent the final stages before quenching, as a galaxy moves along the galactic main sequence. This, in fact, was the conclusion from the analysis of two SCUBA-2 surveys (Koprowski et al., 2016; Michałowski et al., 2017) for 80 sources down to an 850 μm depth of 0.25 mJy and 651 sources at a depth of ~ 1 mJy respectively. This is additionally supported by a continuum survey carried out by ALMA for 708 galaxies (Scoville et al., 2017a). These results are also theoretically supported by simulations from Narayanan et al. (2015).

Based on these observations, it seems that the majority of SMGs are normal main sequence galaxies with only a small subset of galaxies exhibiting enhanced star formation that places them off of the main sequence. In particular, it is believed that $\sim 5\%$ of the population would be considered high-redshift starburst galaxies and that this population is responsible for 8 to 14% of the total cosmic star formation density (Sargent et al., 2012). It remains to be determined if these high-redshift starburst galaxies are indeed analogs to the mergers seen in local ULIRGs or if they are powered by some other mechanism such

as enhanced gas accretion or minor mergers. Our ability to distinguish between these two mechanisms will continue to grow with more surveys that increase the statistical significance of the detected SMG population and with more morphologically and kinematically resolved observations that determine if the gas dynamics are perturbed by interactions. It may be ultimately found that more than one mechanism is responsible for the observed populations.

Ultimately, the understanding of SMGs at high redshift is still evolving. However, if we are to decide whether or not these galaxies are similar to low-redshift ULIRGs, a detailed understanding of local ULIRGs is needed. Local studies have most definitely contributed to our understanding of high-redshift objects, and I believe they will continue to provide invaluable insights into these interesting objects. Even if SMGs are not scaled up versions of ULIRGs, a comprehensive understanding of local ULIRGs is needed to make this distinction. In addition, detailed study of these local ULIRGs will undoubtedly yield insight into our understanding of star formation within extreme conditions, informing high-redshift observations. Yet, caution is warranted when applying results for low-redshift galaxies to higher-redshift galaxies where the physical conditions are different.

1.6 Thesis Organization

Following this chapter, in Chapter 2, I first present the required background for why on-chip spectrometers are motivated and the general knowledge required to understand how to construct an on-chip filterbank. In Chapters 3 and 4 I divide up the testing results of SuperSpec filterbanks into two Chapters. In Chapter 3, I discuss the testing results of the SuperSpec kinetic inductance detectors, and in Chapter 4, I discuss the filterbank performance. The testing results are decoupled because the results for the detectors themselves are in general applicable to any instrument that utilizes kinetic inductance detectors. The filterbank performance is in many ways applicable to any on-chip filterbank regardless of the detector choice. I was the primary person responsible for all of the testing and data analysis for SuperSpec prototype devices over the course of 3 years. This included characterizing

devices for almost 20 separate cryogenic cooldowns. Throughout this thesis, when I show the characterization of a device, I generally only show the results of one device at a time; however, for every plot characterizing a SuperSpec device that is shown there are 10 others like it that are stashed away on the SuperSpec wiki. The results of the test data shown in this thesis have helped the SuperSpec collaboration move forward from one iteration to the next at each step bringing us closer to a field deployable instrument. While the choices on how to proceed were not solely decided by myself, but rather by the collective intelligence of the entire SuperSpec collaboration, my opinion and data analysis had a significant impact on the direction and success of the SuperSpec project. Finally, to wrap up the instrument development portion of this thesis, in Chapter 5, I present how the test results have informed the designs and observational strategies for a SuperSpec demonstration instrument on the Large Millimeter Telescope.

Following the instrument development portion of the thesis, in Chapter 6, I present ALMA observations of the local ULIRG Arp 220 in $^{12}\text{CO } J = 3 \rightarrow 2$ and $^{13}\text{CO } J = 4 \rightarrow 3$. The observations are described and interpreted. In addition, I present non-LTE radiative transfer models for the two nuclei in this merging system. The implications of the observed and modeled parameters with relation to Arp 220 and its applicability as a high-redshift analog are then discussed. Finally, in Chapter 7, the prospects for future SuperSpec applications and technology development are briefly discussed along with the potential impact of future ALMA observations of Arp 220 and high-redshift galaxies.

Chapter 2

SuperSpec On-Chip Spectrometer Concept

2.1 Motivation for an On-Chip Spectrometer

In the astronomical world where scientific measurements are often very uncertain, astronomers cannot appreciate a technology proposal unless you propose to do something at least 10 times better than before. If you propose a new more sensitive detector technology, you had best argue that it will be 10 times more sensitive than the current best. Any number less than 10 and an astronomer will round to 1 and consider it equivalent to previous technology. The state of the art for a millimeter/sub-millimeter spectrometer is Z-Spec (Bradford et al., 2004; Glenn et al., 2007). For SuperSpec we are not building a spectrometer that is more sensitive than Z-Spec but building a spectrometer that is much smaller. By building a spectrometer on a chip with a microstrip feedline and resonant microstrip filters a spectrometer that is 100 to 1000 times smaller than the state-of-the-art spectrometer can be built. This reduction in size means that an instrument can be built that contains 100 to 1000 more spectrometers. 100 to 1000 more spectrometers allows for 100 to 1000 times more efficient observing for mapping the sky or obtaining observations of many sources at once. Ultimately, this enables the creation of an instrument that is effectively 100 to 1000 times more efficient than the current state-of-the-art. A 100 to 1000 times improvement in efficiency can be appreciated by any astronomer, not just a CMB astronomer. Thus, a reduction in size of this magnitude is really exciting because of the future technology it can enable, and in-turn, future scientific observations that can be obtained. In the following

sections, we discuss two of the potentially groundbreaking instrument types that could be enabled by SuperSpec technology.

2.1.1 Multi-Object Spectrometer

Imaging arrays at submillimeter and millimeter wavelengths are exponentially growing in pixel counts and will soon map the entire sky to deeper and deeper sensitivities. These surveys will reveal many thousands of galaxies. Spectroscopic follow-up of these sources has been and will remain a bottleneck. Without redshifts for these sources, we cannot know when and where in the Universe these sources are, and without this information, we cannot understand the history of our Universe as discussed in Section 1.2. This motivates the development of large array spectroscopy instruments to provide efficient spectroscopic follow-up of sources.

When considering a submillimeter spectroscopic instrument today, one must consider how to best utilize a spectrometer in the era of ALMA. The Atacama Large Millimeter/submillimeter Array is an interferometric observatory in the Atacama Desert in Chile. Using heterodyne instrumentation, ALMA can complete high-resolution spectroscopic measurements on single sources with a sensitivity that no single dish telescope/instrument combination can even hope to rival. However, as an interferometric telescope, ALMA's field of view is quite small and thus can only observe single sources at a time. While over its lifetime ALMA will provide measurements of 100s of infrared galaxies, in order to statistically constrain star formation rates and galaxies' properties, 10,000s of observations will be required. In this way, the ALMA observatory necessitates the accompaniment of a survey instrument.

A single spectrometer on a single-dish telescope could never hope to achieve the sensitivity of ALMA. However, by building a multi-object spectrometer that can simultaneously observe 100s of galaxies at once, an instrument that can survey galaxies faster than ALMA can be created. While for a single source, a single spectrometer may be 10 times slower than ALMA, if one builds an instrument that can observe 100 sources at once, this instrument

will be 10 times faster than ALMA. At the same time, a multi-object spectrometer does not just become competitive with respect to ALMA but rather synergistic. After accurate redshifts are determined for many galaxies, that information can be used to more efficiently target ALMA’s heterodyne instrumentation for kinematically resolved follow-up for the most interesting sources. In fact, ALMA’s observing time is arguably too valuable to be used to carry out inefficient blind spectral surveys.

One example of such an instrument would be a ~ 100 spectrometer SuperSpec style instrument installed on the Large Millimeter Telescope, see Section 5.4. Another example of such an instrument was the X-Spec concept for the CCAT observatory shown in Figure 2.1. The X-Spec concept would achieve similar speeds, at 6 times faster than ALMA, for spectroscopic redshift follow-up of submillimeter galaxies (Bradford et al., 2014). Ultimately, building a multi-object spectrometer is the only way in which we can further our spectroscopic knowledge of bright submillimeter galaxies beyond that of which ALMA is capable.

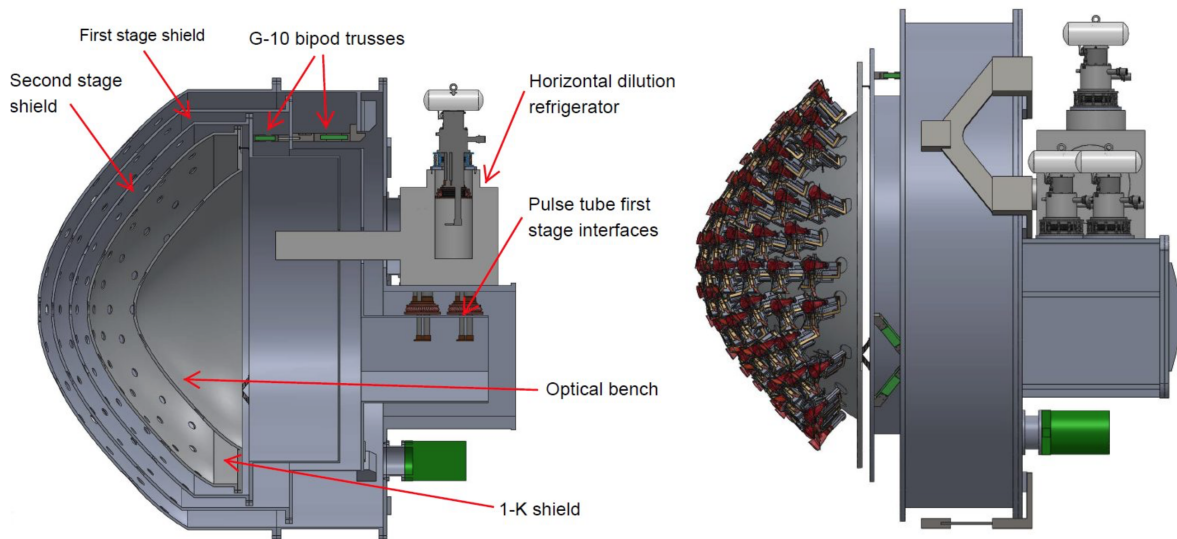


Figure 2.1: A concept cryostat for multi-object spectrometer concept instrument developed for the CCAT observatory. This shows 84 spectrometers, each sensitive to two polarizations. Not shown are periscopic positioners to steer the beams on the sky. The cylindrical vacuum shell of this instrument has a diameter of 260 cm. Figure from Bradford et al. (2014)

2.1.2 Imaging Spectrometer for [C II] Tomographic Mapping

A multi-object spectrometer can measure many luminous galaxies to unprecedented levels. At the same time, the emission from less luminous galaxies must also be measured. This can be accomplished via the measurement of the total luminosity function of galaxies through intensity mapping. Intensity mapping is simply mapping the total intensity of an emission mechanism over some area of the sky. For each spatial pixel on the sky, the total cumulative emission is measured of all sources along that sight line; including sources that are too faint to be individually resolved. These faint sources are of significant importance, and it may, in fact, be that the faint sources actually dominate the total photon output.

2D intensity mapping missions have been most successfully applied in mapping and constraining signals in the CMB. However, tomographic mapping of continuum radiation to measure the linear and non-linear clustering of submillimeter galaxies has also been completed using Herschel continuum bands (Viero et al., 2013). These studies demonstrate the power and ability to utilize the tomographic mapping technique for 2D data sets. However, the real power of this technique for understanding galaxies is revealed when spectral information is included that allows for the distinguishing of signal with redshift. This allows for disentangling the faint signal at high redshift from bright low redshift sources. Also, in terms of just mapping sources across the sky, spectroscopic information in intensity mapping breaks the degeneracy with redshift that causes source confusion, making the extraction of individual sources impossible. An example of this is the source confusion experienced by the Herschel Space Observatory. For the 250 μm imaging array on-board Herschel only 15% of the total luminosity can be resolved into individual galactic sources regardless of increased integration time (Oliver et al., 2010).

[C II] is a particularly good candidate for line intensity mapping. As described in Section 1.4.2, [C II] is a very bright line and a modulus for the total star formation rate of a galaxy. A 3D (2 spatial and 1 spectral dimension) [C II] intensity data cube across

an area of the sky can be made using an imaging spectrometer. This 3D data cube can then be analyzed to produce a 3D power spectrum. This 3D power spectrum contains the linear clustering signal of galaxies, which is proportional to the total [C II] intensity of all galaxies. This total [C II] signal can then be used to constrain the total luminosity function of all galaxies. Combined with observations from single source spectroscopic measurements, this will allow for the determination of the faint end of the galactic luminosity function. Once the [C II] signal is detected, it can be cross-correlated with HI intensity maps to reveal information about the size of ionization bubbles during the epoch of re-ionization. [C II] provides a complementary measurement to neutral HI intensity mapping and acts as a sanity check on those measurements. Where HI will reveal the signature of the neutral un-ionized universe at high redshift, [C II] probes the sources responsible for ionization, producing the inverse image of the neutral universe measurement. Not only will [C II] intensity mapping help constrain the total galaxy luminosity function, and thus star formation rates through cosmic history, but it will also have significant impacts toward understanding the epoch of re-ionization.

The TIME collaboration and current TIME-Pilot experiment intend to pioneer these measurements (Crites et al., 2014; Staniszewski et al., 2014; Bradford et al., 2016; Hunacek et al., 2016a,b, 2018). The TIME-Pilot instrument is shown in Figure 2.2. The current iteration of the TIME experiment utilizes 32 grating spectrometers (16 pixels) laid out in a single linear array. The experiment will achieve 2 spatial dimensions by scanning the linear array of spectrometers across a section of the sky. The utilization of grating spectrometers is necessary as my collaboration increases the technological maturity of lithographic on-chip spectrometers. However, the implications for the incorporation of SuperSpec technology into future TIME missions is evident. At the same resolution as the current TIME-Pilot instrument, 100 lithographically patterned SuperSpec style spectrometers could be incorporated onto a single 6-inch silicon wafer. The increase in pixels of almost an order of magnitude would mean reduced mapping time, allowing much larger portions of the sky to be mapped

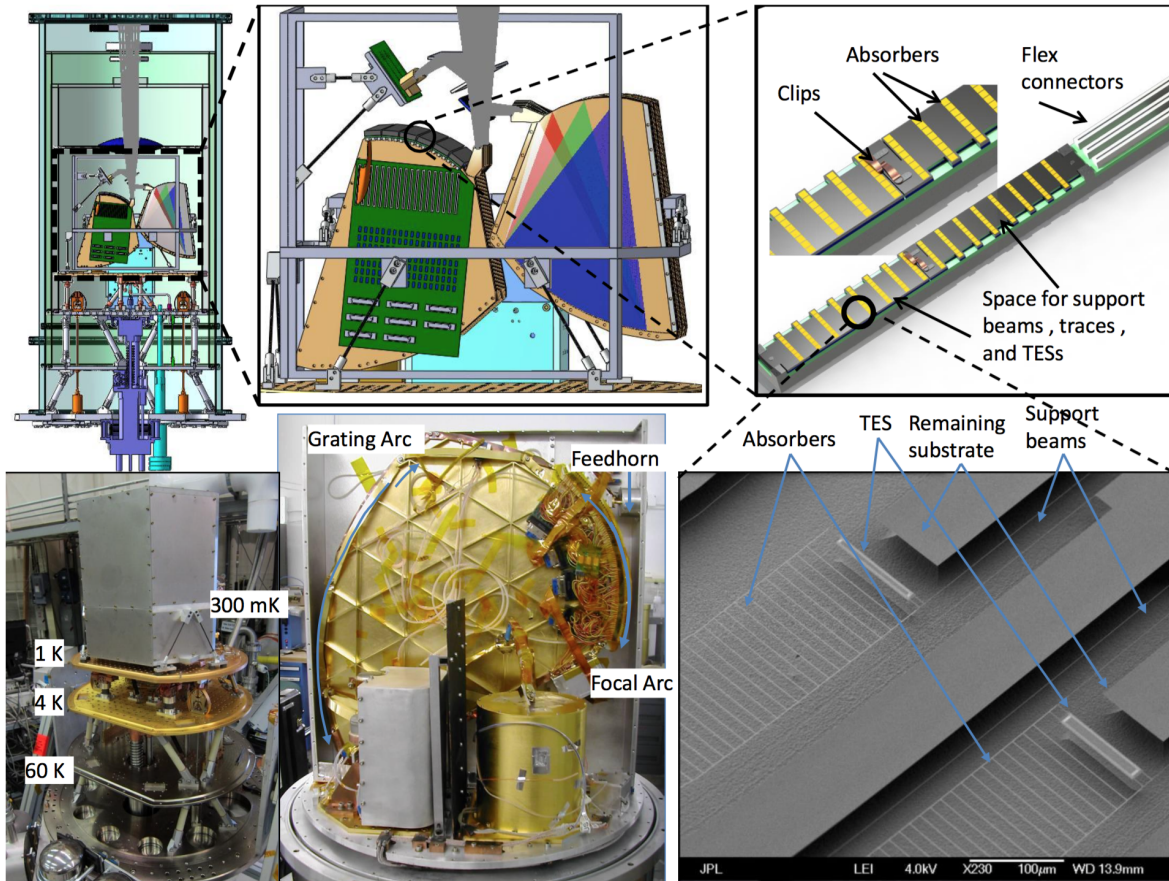


Figure 2.2: The TIME-Pilot experiment. The experiment consists of 32 grating spectrometers (16 spatial pixels with two polarizations). Grating spectrometers require a large cold volume and mass. Incorporation of SuperSpec technology could enable more spatial pixels while at the same time reducing the size and cryogenic requirements. Figure from Crites et al. (2014).

or mapping smaller regions to much deeper sensitivity levels. The SuperSpec technology has the ability to significantly improve this measurement technique, allowing for a significant increase in the understanding of the total galaxy luminosity function and the epoch of re-ionization.

2.2 The SuperSpec Concept

2.2.1 Filterbank Principle

The SuperSpec concept is described in full detail in Barry et al. (2012); Kovács et al. (2012); Shirokoff et al. (2012). The idea of a filterbank is shown in schematic form in Figure 2.3. The SuperSpec design is a filterbank much like those used in radio astronomy but at much higher frequencies. The signal propagates down a feedline that is coupled to N_c resonant filters that consist of $\lambda/2$ transmission lines, where λ is the central wavelength of radiation absorbed by each filter. Each of the resonating filters is then coupled to a detector (in this case a kinetic inductance detector).

Somewhat intuitively, the filters are spaced at $\lambda/4$ or $3\lambda/4$ so that any power that is reflected off of the next filter is in phase when it arrives back at the first filter. However, $\lambda/4$ or $3\lambda/4$ is not a strict requirement. This is because not only is reflection off of the first resonator important, but reflection off the next few, as well as the preceding few, resonators will impact the total response. In fact, with $\lambda/4$ spacing, the second resonator is at $\lambda/2$, which is optimally bad for achieving constructive interference upon reflection. Thus when considering the filterbank as a whole, slightly better performance is achieved with spacings that are smaller than $\lambda/4$ or $3\lambda/4$. This will actually produce more reflections that interfere constructively rather than destructively. In practice, achieving spacing smaller than $\lambda/4$ while maintaining strong coupling is not practical in terms of chip layout. While $\lambda/4$ is not a perfect optimum, $\lambda/2$ is very strongly the least optimum spacing. In this case, all of the resonators are spaced perfectly for destructive interference. A few examples of different

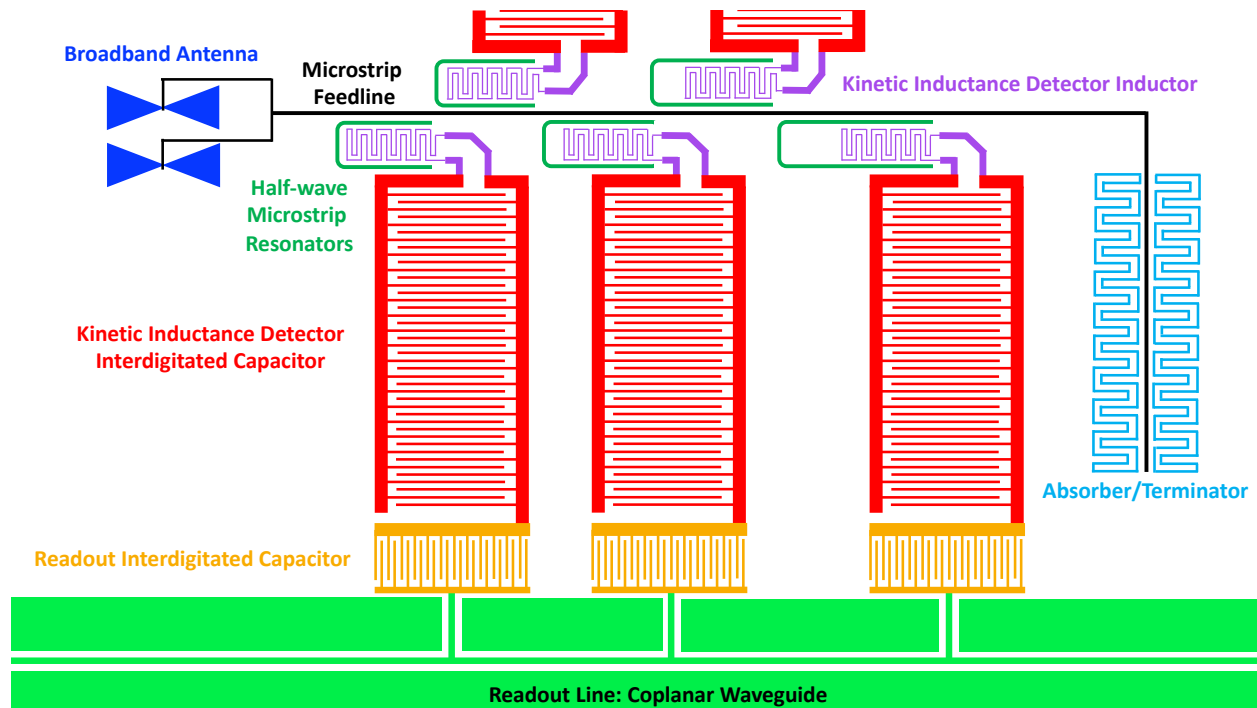


Figure 2.3: Filterbank spectrometer concept: Broadband radiation enters the filterbank through the broadband antenna and then propagates down a microstrip transmission line to the right. Half-wave resonators spaced at roughly quarter wavelength separations are coupled via proximity to the transmission line. Each one extracts one spectral output channel, which in turn are coupled via proximity to power detectors (kinetic inductance detectors). Kinetic inductance detectors are then read out using a coplanar waveguide transmission line. Any power remaining after transmission through the filterbank is terminated with a broadband absorber.

spacing choices are shown in Figure 2.4. The optimum spacing is examined in detail for a 300 channel filterbank in Figure 2.5.

Following the filterbank, SuperSpec has 20 linear centimeters of broadband absorbers that absorb any power that makes it through the filterbank. One could consider having the filterbank terminate in an open circuit so that radiation is reflected and has a second chance to pass through the filterbank. However, this would cause a standing wave pattern in the filterbank that would reduce efficiency at specific frequencies. In addition, current SuperSpec filterbanks are designed so that very little in-band radiation makes it through the filterbank. This means a second pass would result in only trivial amounts of increased efficiency. Having the absorber at the end of the filterbank prevents any out-of-band radiation from reflecting and being re-emitted by the antenna where, it could scatter and be re-absorbed by the detectors directly. In this way, the rear absorber helps minimize stray light.

SuperSpec implements this filterbank architecture using superconducting inverted microstrip lines. There are several reasons that the SuperSpec collaboration decided to use microstrip versus other transmission line technologies. One is that the microstrip ground plane provides a means of shielding the resonator inductors from directly coupling to stray light that might enter the chip directly above the inductors. Another is that microstrip versus coplanar waveguide (CPW) has less of a tendency to radiate modes into the substrate. Indeed, DESHIMA, a CPW on-chip spectrometer, estimates from models that 13% of the radiation in one of their 50 channel filterbanks is lost via radiation into the substrate (Endo et al., 2019). Not only will radiated energy reduce efficiency but it will also lead to inter-channel cross-talk. On the other hand, the disadvantage of microstrip versus CPW is that microstrip requires the deposition of a dielectric layer in between the strip and the ground plane. If this dielectric layer is not sufficiently low-loss it will hurt the filterbank efficiency. In fact, dielectric loss from SiN is the dominating factor in determining SuperSpec's current filterbank efficiency. This is not completely solved by CPW lines. This is because CPW lines require bridges to connect the two sides of the CPW line or vias to a lower ground plane

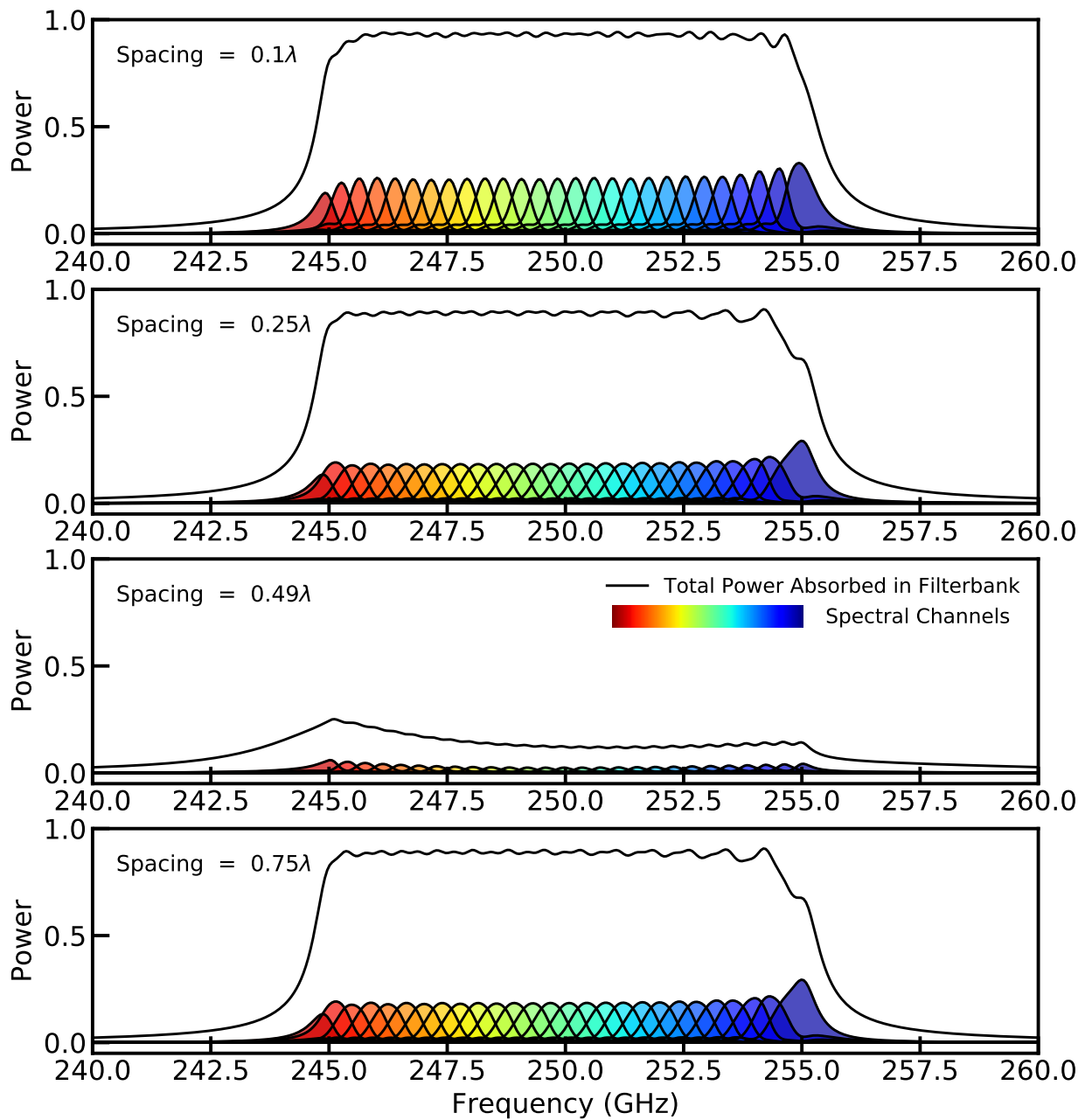


Figure 2.4: A few examples of different spacing choices between mm-wave resonant filters. This is for a lossless, $Q_{loss} = \infty$, $Q_i = Q_c = 700$, and $\Sigma = 2$ filterbank from 245 to 255 GHz. 0.1λ spacing is the best, but not necessarily realizable given the physical size constraints when fabricating. For a lossless filterbank, 0.25λ and 0.75λ are good spacing choices. A spacing of 0.49λ is optimally bad in terms of creating the most deconstructive interference on the filterbank.

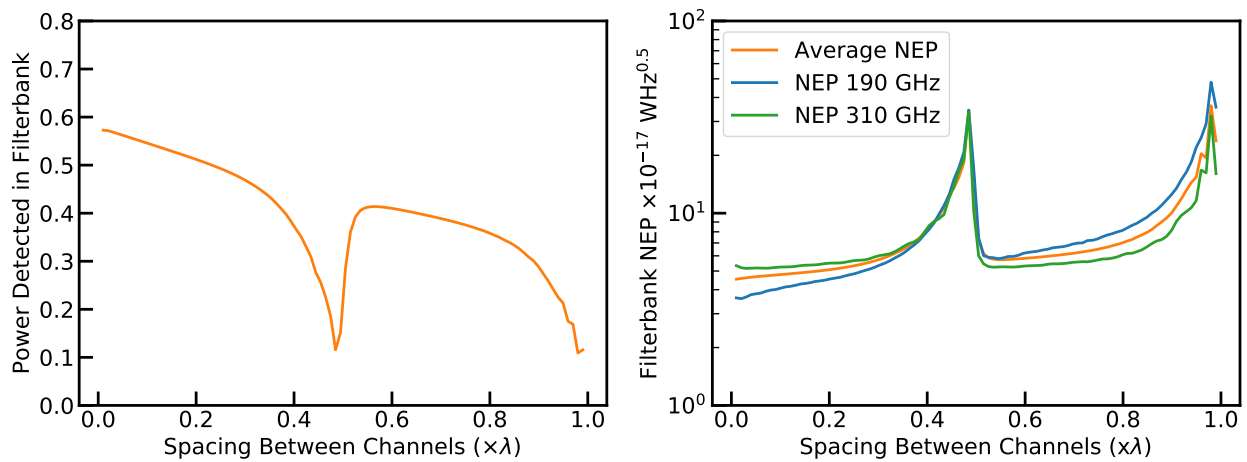


Figure 2.5: The effect of mm-wave resonant filter spacing on filterbank efficiency. Left: The total power detected in the filterbank. Right: The effect of spacing choice on filterbank NEP. This is for a 185 - 315 GHz 300 channel filterbank with $Q_i = Q_c = 700$ and $Q_{loss} = 1200$. This is the same filterbank shown in Figure 5.3 and 5.4. Total power detected in the filterbank decreases with increasing spacing due to dielectric loss.

separated by a dielectric and both of these structures can also introduce loss.

Given a transmission line architecture, a low loss conductor must be chosen to construct the feedline. At these frequencies conductor loss in normal conductors is substantial. Thus, superconducting transmission lines are used to propagate the mm-wave signal. Superconducting lines are approximately lossless to radiation frequencies with energies less than the superconducting gap energy. This cutoff frequency is given by the following equation.

$$f_{gap} = 3.52 \frac{k_b T_c}{h}. \quad (2.1)$$

SuperSpec uses a niobium transmission line that has a T_c of 9.2 K, resulting in $f_{gap} = 672$ GHz. Thus, losses in the conductor should be negligible for current SuperSpec target frequencies of 200 to 300 GHz. Pushing on-chip spectrometers to higher frequencies requires higher T_c superconductors such as NbTiN (Endo et al., 2019).

2.2.2 Filterbank Spectral Channels

For a single isolated resonant channel, the resolution is set by the following equation.

$$\frac{1}{R} = \frac{1}{Q_r} = \frac{1}{Q_c} + \frac{1}{Q_i} + \frac{1}{Q_{loss}}. \quad (2.2)$$

The Qs in this equation are all quality factors. A quality factor is a dimensionless parameter that quantizes a resonator's bandwidth with respect to its center frequency, such that $Q = f/\Delta f$, where Δf is the FWHM bandwidth of the resonator. In particular, Q_r is the total Q of a spectral channel, Q_c describes the coupling strength of the resonator to the feedline, Q_i describes the dissipation of radiation from the resonator into the detector, and Q_{loss} describes the dissipation of the radiation from the resonator into other loss mechanisms (mostly the dielectric for SuperSpec). This is the single most important equation for on-chip

spectrometers and thus this thesis, so take a moment to memorize it or write it down. Many of the SuperSpec design choices spawn from the optimization of this equation.

Q_c represents the coupling strength between the feedline and the resonant staples. Coupling is achieved through proximity by placing the half-wave microstrip resonator close to the microstrip feedline. This couples the resonator both inductively and capacitively to the feedline, though mostly inductively. In order to achieve strong coupling, it is best to have a coupling length of approximately $\lambda/4$. This is accomplished by bending the microstrip resonator into a “U” shaped staple with approximately half of the staple adjacent to the microwave feedline. The coupling strength is then tuned by increasing or decreasing the distance between the staple and the feedline. This coupling strength can be calculated analytically or can be simulated using EM simulation software, but in practice, we have found that the calculations must be empirically tuned based on real measurements.

Q_i represents the coupling strength from a resonator into a detector. For our kinetic inductance detectors, discussed in the following section, this is also accomplished by proximity. The coupling, in this case, is mostly capacitive. The active area of the kinetic inductance detector is placed inside the staple so that it can couple from two sides at the same time, Figure 2.9 Panel D. Simulations indicate the majority of the coupling occurs near the ends of the resonator. This means that strong coupling can still be achieved with only filling a subset of the resonator staple (Shiu, 2015). This allows for smaller inductor volumes for the kinetic inductance detectors, which enables more sensitive detectors.

Q_{loss} represents the dissipation of radiation in the resonator that is not coupling into the detector. This could be conductor losses on the niobium microstrip, radiation into the substrate, or losses in the microstrip dielectric. For the current SuperSpec devices, the dominant loss mechanism is loss in the microstrip dielectric and thus Q_{loss} and dielectric loss is often referred to interchangeably. Q_{loss} can be equated to a more commonly quoted

measurement, the loss tangent ($\tan \delta$). through the equation:

$$\tan \delta = 1/Q_{loss}. \quad (2.3)$$

SuperSpec utilizes a SiN (Cataldo et al., 2012) dielectric because it is relatively easy to deposit and etch but has better loss performance than commonly used SiO (Gao et al., 2009).

Given the choice of Q_c and Q_i , a single resonator can be in a few different regimes. When Q_c is dominant, i.e. $Q_c < Q_i$ and Q_{loss} , reflection from a single filterbank channel is maximized, Figure 2.6 Bottom Left. Transmission, on the other hand, is maximized when Q_i is dominant, i.e. $Q_i < Q_c$, Figure 2.6 Top Right. Maximum coupling to the detector occurs for a lossless resonator when $Q_c = Q_i$, Figure 2.6 Top Left. A single isolated filterbank channel can at most have a peak coupling efficiency into the detector of 50%. High-redshift galaxies are, by their namesake, quite far away and thus they are also not incredibly bright. This means absorbing only 50% of the radiation in your filterbank is unacceptable. This is somewhat easily remedied by adding in more spectral channels at similar frequencies. If one channel absorbs 50% of the radiation, then two channels could absorb 75% and so on. In practice, we do not use spectral channels at the same frequency to increase the total efficiency of the filterbank but rather resonant channels are log spaced with a density described by an overdensity factor Σ . The total number of channels for a given R , Σ , and band can be calculated from the following equation (Shirokoff et al., 2012).

$$N_c = \Sigma R \ln(f_u/f_l). \quad (2.4)$$

Here f_u and f_l are the highest and lowest frequency spectral channel in a filterbank. Given N_c , f_u , and f_l the filterbank is constructed by starting with the highest frequency channel f_u

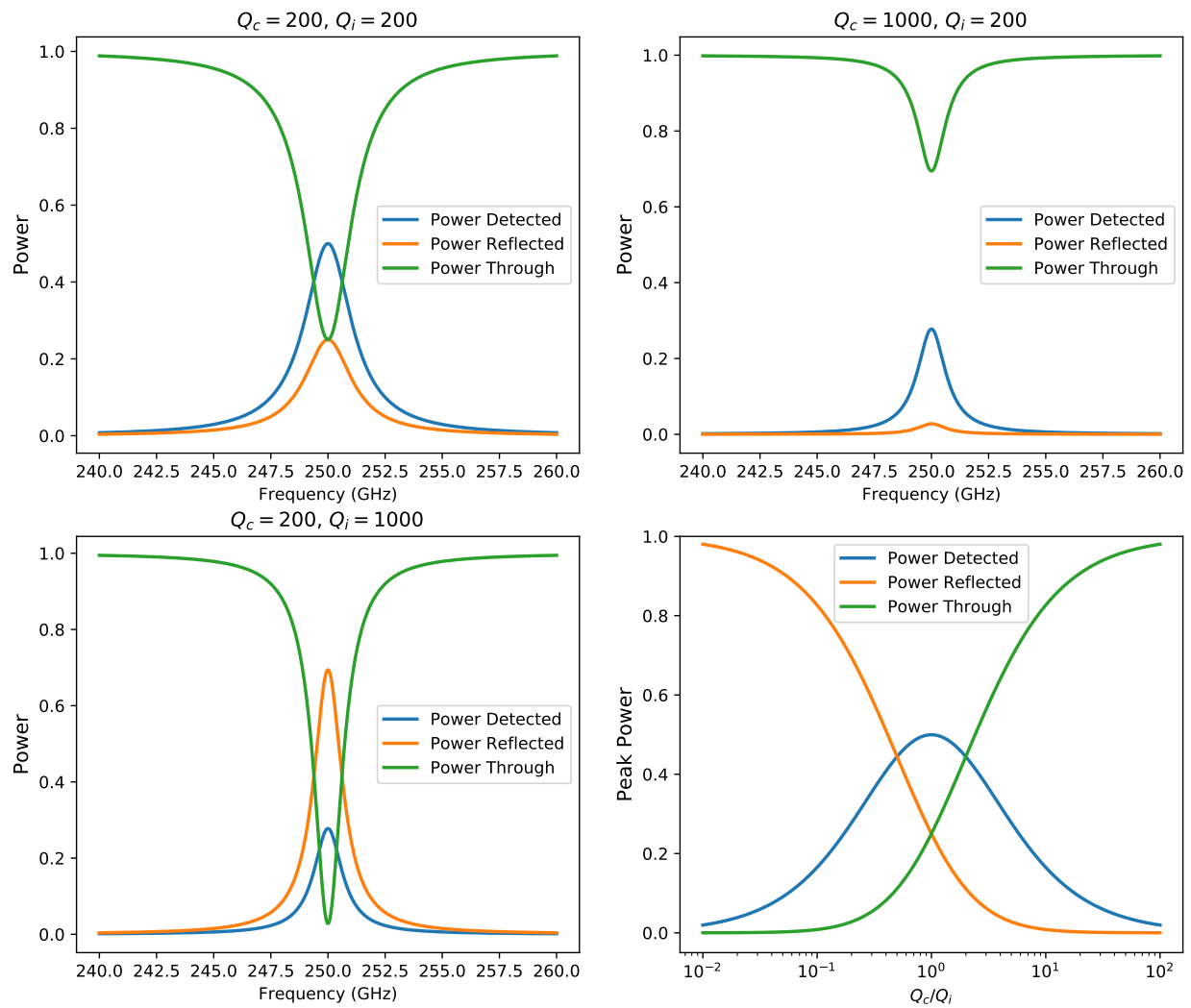


Figure 2.6: The response of a single filterbank channel for different values of Q_c and Q_i . Q_{loss} is assumed to be infinite i.e. lossless. Bottom Right: Peak power detected, reflected, and transmitted over a large range of Q_c/Q_i values. Maximum detection efficiency of 50% for a single channel occurs when $Q_c = Q_i$.

and scaling each adjacent channel using the geometric progression: $f_u, x f_u, x^2 f_u, \dots, x^{N_c-1} f_u$, with x given by the following equation (Shirokoff et al., 2012).

$$x = \exp\left(-\frac{\ln(f_u) - \ln(f_l)}{N_c - 1}\right). \quad (2.5)$$

For higher oversampling factors, more of the total light entering the filterbank is absorbed, increasing the efficiency of the filterbank above the 50% level for a single channel, see Figure 2.7. This does, however, reduce the total radiation coupled into any one given channel.

2.2.3 Kinetic Inductance Detectors

SuperSpec employs kinetic inductance detectors (KIDs) to detect radiation in each of the mm-wave resonators. KIDs have attracted great interest in the submillimeter detector community because of their ability to be easily constructed and read out in large arrays. They are superconducting circuits in which the charge carriers are electrons bound in Cooper pairs. Cooper pairs transmit superconducting DC current without resistance, but AC circuits have nonzero inductance due to the inertia of Cooper pairs, known as kinetic inductance. When submillimeter energy $> \Delta$, where Δ is the superconducting gap energy, is absorbed by the superconductor, Cooper pairs are broken creating quasiparticles. The additional quasiparticles change the kinetic inductance fraction of the circuit. By constructing KIDs as high quality factor (Q factor) resonating LC circuits, one can detect this change by measuring a change in the resonant frequency of the circuit through the absorption of a transmitted microwave probe signal.

SuperSpec's KIDs are fabricated using titanium nitride (TiN). TiN, as a KID material, has attracted interest because the theoretical floor of the noise equivalent power (NEP) falls well below $10^{-19} \text{ WHz}^{0.5}$ (Leduc et al., 2010). Such sensitive detectors could potentially enable background limited performance even in the very low background conditions on-board

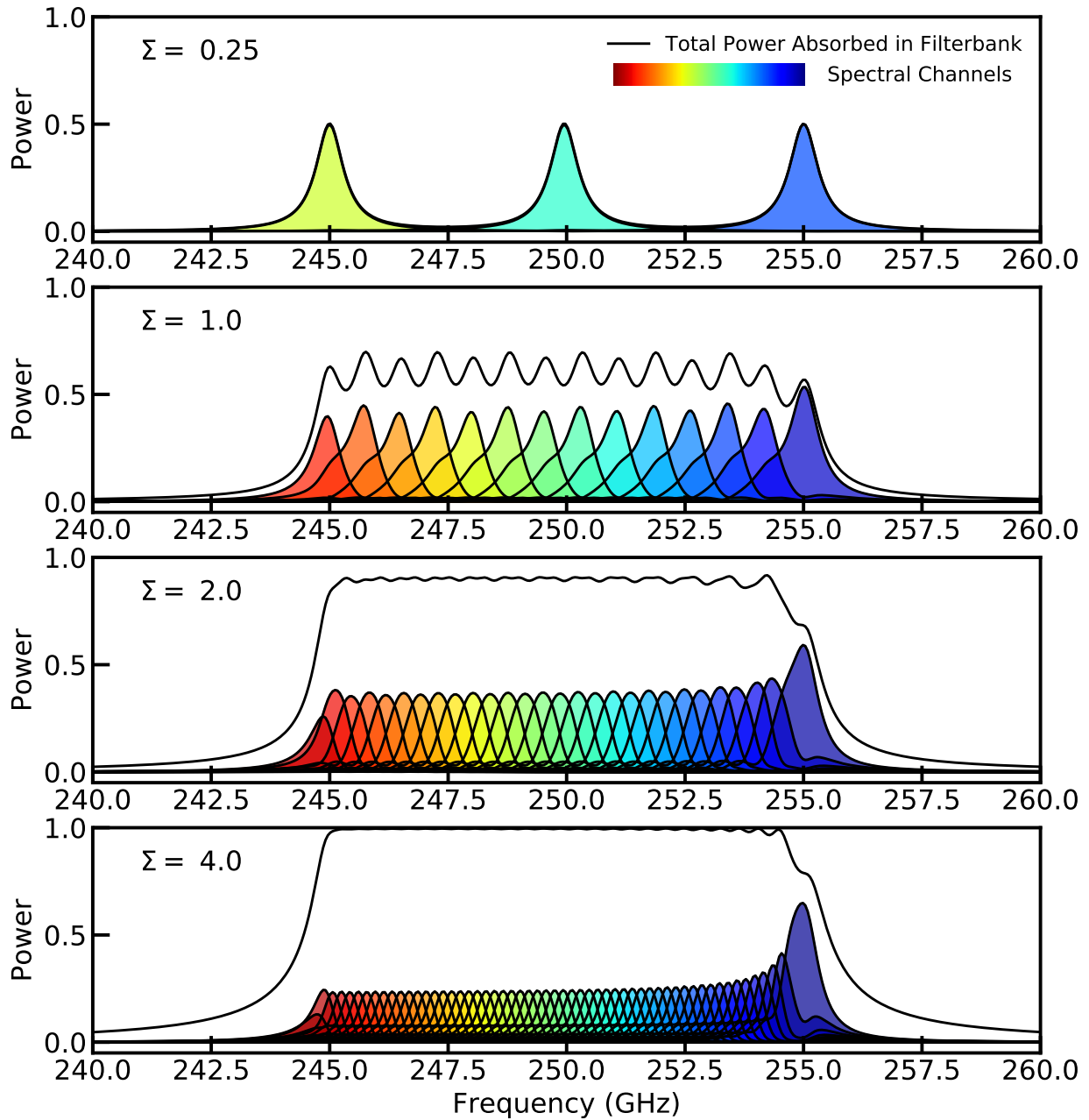


Figure 2.7: Several filterbanks from 245 to 255 GHz for different oversampling factors, Σ . Filterbank parameters are $Q_c = Q_i = 700$, $Q_{loss} = \infty$. As Σ is increased the total absorption of light within the filterbank also increases.

a space telescope with a cryogenically cooled primary mirror. This low NEP is in part due to the fact that the T_c of TiN is tuneable. By controlling the flow rate of nitrogen gas in the deposition chamber, a T_c of anywhere from 0.5 to 4.2 K can be achieved. Since a lower T_c equates to more response, very low NEPs can be achieved for the lowest values of T_c .

This thesis won't go into too much detail on the physics of KIDs because it is a subject that could easily compose an entire thesis by itself. In addition, KID physics is already explained better than I would be able to in Jiansong Gao's thesis (Gao, 2008). So for further information regarding KID physics, I refer the reader to the above citation. Instead, I just show in Figure 2.8 a demonstration of how KIDs are practically used to detect signals.

For the detectors, we want the opposite of the microwave feedline. We want radiation at wavelengths of ~ 150 GHz and above to break Cooper pairs creating quasiparticles and thus changing the kinetic inductance of the KID so that absorption of light can be measured. Solving Equation 2.1 given $f_{gap} = 250$ GHz for T_c , yields a $T_c = 2$ K. Thus, the KIDs must have a T_c of 2 K or below. A lower T_c often means more response, so a lower T_c is better until T_c approaches roughly five times that of your cryostat base temperature. At this point, thermal quasiparticles will dominate your achieved resonator Qs and detector noise. For SuperSpec, the current cryostat operates at a temperature of 210 mK. Thus, a ballpark target T_c for the TiN KIDs is around 1.25 K.

The TiN KIDs are implemented with an inductive meander placed inside each resonant staple, Figure 2.9 Panel D. This inductor is attached to a large interdigitated capacitor, Figure 2.9 Panel E. Each KID is then in turn coupled through a second interdigitated capacitor to a CPW microwave readout line. This readout line is then bonded to SMA connectors to allow microwave readout via coax. The resonant frequencies of the SuperSpec resonators are currently in the range of 100 to 400 MHz, relatively low frequencies for KIDs. By operating at these low frequencies two things are accomplished. First, the lower the readout frequencies of the resonators, the more resonators can be packed into the bandwidth of the readout system. This is because the number of resonators one can fit within an octave of frequency

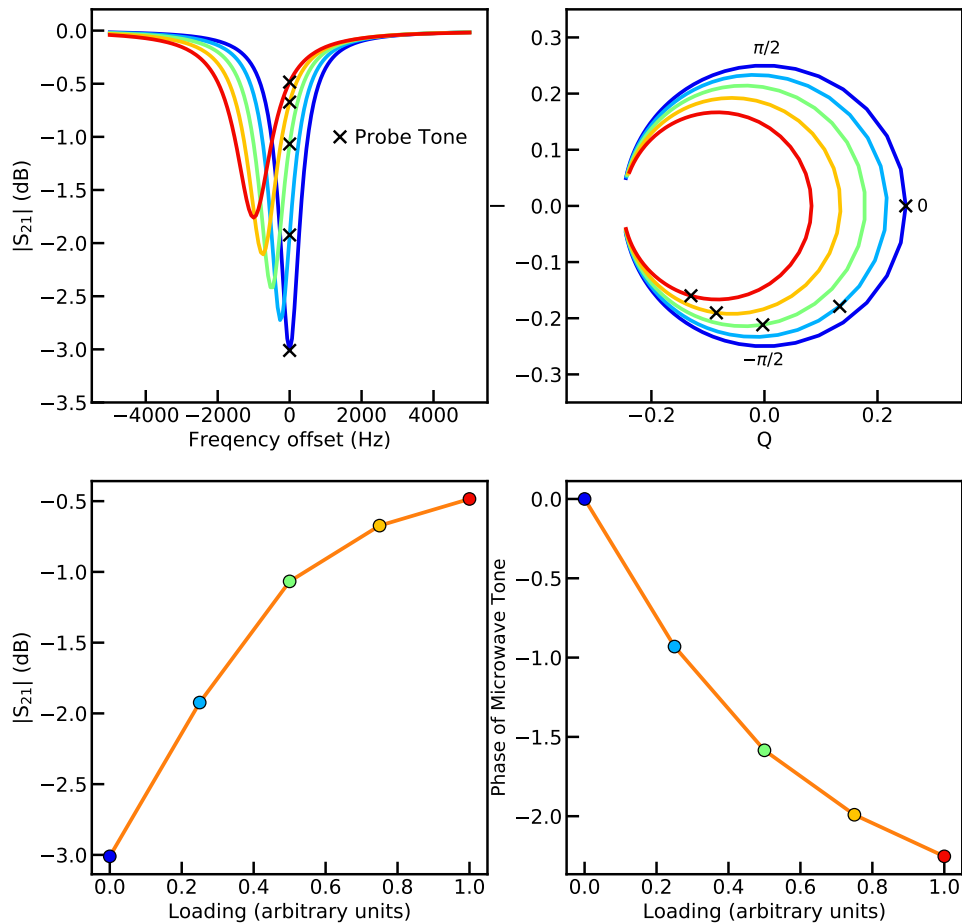


Figure 2.8: Demonstration of how a microwave tone probe signal tracks changes in loading for a kinetic inductance detector. Top Left: Plot showing the transmission through the microwave readout lines in magnitude versus frequency. The resonator absorbs energy at its resonant frequency. Top Right: Plot showing the resonant loop measured as a function of I and Q where different frequencies correspond to different locations around the loop. This measurement is made by mixing a reference signal with a signal that has propagated through the detectors allowing the change in phase of the signal to be measured. As the loading increases, the resonator shifts to lower frequencies and the quality factor of the resonator decreases. Here loading increases as the curves change color from blue to red. As the frequency shifts and the Q changes, this causes a readout tone held at a single frequency to change in both magnitude and phase. In practice, a KID is usually designed so that changes with loading only cause a significant change in the frequency and not the quality factor of the resonator or vice versa.

space is constant, so at these frequencies, only 300 MHz of readout bandwidth is required to read out 2 octaves of resonators, i.e. 100 to 200 GHz and 200 to 400 GHz. In contrast with resonant frequencies at 1 GHz, a readout bandwidth of 300 MHz cannot cover even one octave. At the same time, lower frequencies can help reduce the presence of two-level-systems noise in the detectors (Swenson et al., 2012). However, the disadvantage of operating at low frequencies is that the detectors require larger area capacitors, making it difficult to pack many detectors in close proximity. Thus, in some cases, it may be advantageous to go to higher readout frequencies in order to save space on the wafer.

As mentioned above, the KIDs are coupled to the resonant filters via proximity by placing the inductor inside the resonant staple. It is important to realize that this unique coupling scheme employed by SuperSpec allows for the creation of incredibly low volume, high responsivity, TiN KIDs. The current inductor volumes are $2.6 \mu\text{m}^3$. In comparison, if direct coupling methods are used where the inductor is a direct absorber at the focus of a lens, detectors that scale as λ^2 are required. Since responsivity is proportional to the inverse of quasiparticle-occupied volume, this allows SuperSpec to reach the low NEPs required by moderate resolution spectroscopy to be photon limited from the best ground-based observing sites, i.e. $5 \times 10^{-18} \text{ W/Hz}^{0.5}$ at $R = 300$.

The inverted microstrip geometry enables easy incorporation of the KIDs into the lithographic fabrication process. The layers in a SuperSpec device are shown in Figure 2.9 Panel F. The strip of the microstrip, as well as the TiN that composes the detectors, can be placed directly onto the silicon. The dielectric layer of SiN can then be placed on top of both the Nb microstrip strip and the TiN detectors. The ground plane is then placed on top of the dielectric layer. In order to allow the interdigitated capacitor to work as a lumped element and to reduce the presence of two-level-systems noise caused by two-level-systems in the SiN dielectric, both the ground plane and the SiN are etched away over the KID capacitors. Being able to remove the dielectric above the capacitors is the real power in using an inverted microstrip geometry since two-level-systems noise is often the limiting

factor in achieved sensitivities for KIDs. For further information on two-level-systems noise in KIDs see Gao et al. (2007); Kumar et al. (2008); Gao et al. (2008); Noroozian et al. (2009).

2.3 SuperSpec Test Filterbank

All of these aspects come together to form the SuperSpec filterbanks. This is shown in detail in Figure 2.9 for a 50 channel filterbank. The process starts with a SuperSpec filterbank receiving astrophysical-radiation via a lens-coupled antenna. SuperSpec employs an anti-reflection coated silicon hyper-hemisphere lens. This radiation then propagates down a microstrip transmission line where specific frequencies of radiation are picked off by the proximity-coupled, half-wavelength microstrip resonators. Careful tuning of the proximity of the resonators to the feedline dials in the desired resolving power of the SuperSpec filterbank by tuning the coupling quality factor, Q_c . The half wavelength resonators are coupled in turn to the inductive meander of kinetic inductance detectors, which serve as the power detectors for the SuperSpec filterbank, Figure 2.9 Panel D. The coupling of the detectors are tuned to match the coupling of the mm-wave resonant filters. Altogether, each SuperSpec filterbank can contain hundreds of kinetic inductance detectors, and the KIDs' high quality factors allow for the readout of large numbers of detectors required to readout an entire filterbank on just one transmission line. This culminates in an entire spectrometer that only occupies a few to 10s of cm squared of silicon.

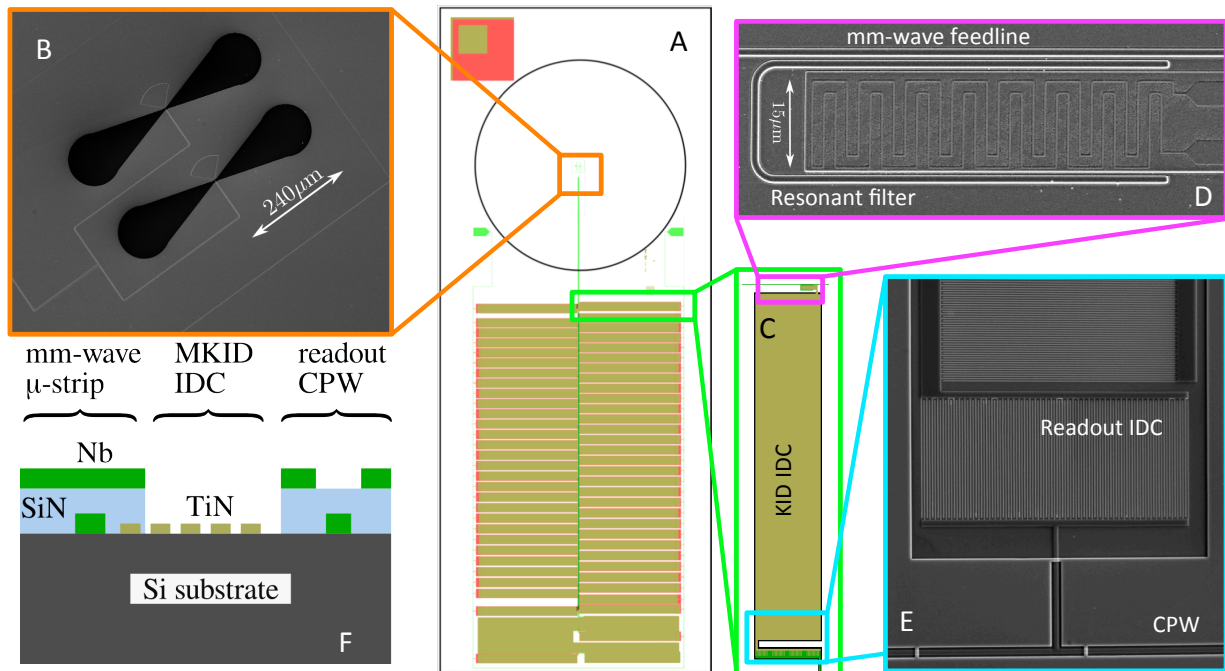


Figure 2.9: (A) A mask with dual bowtie-slot antenna and lens footprint at the top, and feedline running vertically past an array of bandpass filters. (B) Dual bowtie-slot antenna. (C) A single mm-wave filter and KID. (D) The mm-wave resonator and 250 nm line width inductor. (E) The lower portion of the large interdigitated capacitor (IDC), coupling IDC, and readout coplanar waveguide. (F) Cross-section showing the device layers.

Chapter 3

SuperSpec Test Results: Ultra Low Volume TiN Kinetic Inductance Detectors

In this chapter, the performance of the SuperSpec titanium nitride (TiN) kinetic inductance detectors (KIDs) is discussed. The results of the detector characterization are almost entirely independent to the filterbank performance, with the exception of where the detectors are located on a wafer and the small inductor volumes that are enabled by the SuperSpec coupling scheme. As detailed below, this small volume enables the SuperSpec detectors to be some of the most sensitive detectors currently produced. Throughout this chapter a frequency readout scheme is adopted, such that response is only measured in the frequency direction and any response in the dissipation direction is ignored.

3.1 T_c Variations for TiN KIDs: Characterization and Coping Strategy

Variation across a wafer of the critical temperature, T_c , is an important issue for TiN kinetic inductance detectors. Non-uniform nitrogen concentrations in the deposition chamber during Ti sputtering cause variations in the TiN stoichiometry, thereby causing a variation in T_c . A variation in T_c causes a change in the resonator readout frequency, which scales as $\sqrt{T_c}$. This can cause both wafer-level gradients and localized scatter in resonator readout frequencies, which may result in readout collisions for a kinetic inductance detector array. Furthermore, variations in T_c cause variations in responsivity, which scales as $T_c^{-3.5}$, meaning a 10% variation in T_c can cause a 40% variation in responsivity. These effects are so significant that they have encouraged some groups to completely abandon TiN in search

of more uniform T_c materials (Szypryt et al., 2016). However, there are several solutions for how to reduce or compensate for this variation.

One way this problem can be mitigated is by reducing the T_c variation across the wafer. Methods to accomplish this include using a ring-shaped nitrogen emitter, rather than a single source, while sputtering Ti (a method employed for SuperSpec devices), or by using multi-layer films of alternating stoichiometric TiN and Ti (Vissers et al., 2013). Another way to reduce the effects of T_c variation is to place resonators that are near each other in readout space also near each other in physical space on the chip. This means that only the variation on very small scales is important for resonator frequency scatter, and the large scale variation has minimal impact. This method is utilized for SuperSpec as detailed below.

First, in order to estimate T_c for SuperSpec devices, we measure the fractional frequency shift of resonators as a function of array temperature and fit to the following equation (equation 20 from Gao et al. (2008)).

$$\frac{\Delta f}{f}(T, T_c, f, \alpha, \gamma) = -\frac{\alpha\gamma}{2} \frac{\delta\sigma_2}{\sigma_2} = -\frac{\alpha\gamma}{2} \frac{\sigma_2(T) - \sigma_2(T=0)}{\sigma_2(T=0)} = -\frac{\alpha\gamma}{2} \left(\frac{\sigma_2(T)}{\sigma_2(T=0)} - 1 \right). \quad (3.1)$$

Here σ_2 is the imaginary part of the complex conductivity of the resonator calculated from Mattis-Bardeen theory. This equation can be simplified using the following equation (Equation 12 from Gao et al. (2008)) relating σ_2 to the normal-state conductivity σ_n .

$$\frac{\sigma_2(T)}{\sigma_n} = \frac{\pi\Delta_0}{\hbar\omega} \left[1 - \sqrt{\frac{2\pi k_B T}{\Delta_0}} e^{-\frac{\Delta_0}{k_B T}} - 2e^{-\frac{\Delta_0}{k_B T}} e^{-\xi} I_0(\xi) \right]. \quad (3.2)$$

From this, we find that

$$\frac{\sigma_2(T)}{\sigma_2(T=0)} = \left[1 - \sqrt{\frac{2\pi k_B T}{\Delta_0}} e^{-\frac{\Delta_0}{k_B T}} - 2e^{-\frac{\Delta_0}{k_B T}} e^{-\xi} I_0(\xi) \right], \quad (3.3)$$

so equation 3.1 becomes

$$\frac{\Delta f}{f}(T, T_c, f, \alpha, \gamma) = -\frac{\alpha\gamma}{2} \left[1 - \sqrt{\frac{2\pi k_B T}{\Delta_0}} e^{-\frac{\Delta_0}{k_B T}} - 2e^{-\frac{\Delta_0}{k_B T}} e^{-\xi} I_0(\xi) \right], \quad (3.4)$$

where $\Delta_0 = 1.762k_B T_c$ and $\xi = \frac{h \cdot f}{2 \cdot k_B T}$, T is the temperature of the detectors, f is the resonant frequency, and I_0 is the zeroth order Bessel function of the first kind.

γ is a parameter that relates a change in complex conductivity for a resonator to change in the surface impedance of a resonator. It can be analytically calculated in three different limits. For a thick film in the local limit $\gamma = 1/2$. When the electron mean free path is longer than the distance over which the field varies the resonator will be in the extreme anomalous limit, and $\gamma = 1/3$. Finally, when the films are very thin $\gamma = 1$. See Gao (2008); Zmuidzinis (2012) for the derivation of these limits. For SuperSpec devices, the TiN thickness is 20 nm. This places the detectors strongly in the thin film limit implying $\gamma = 1$. α is the ratio of the kinetic inductance from the superconductor to the total inductance of the circuit, which is a combination of the kinetic inductance and the geometrical inductance. For the SuperSpec inductor geometries and given TiN's large kinetic inductance, it can be assumed that $\alpha = 1$. Thus, given a measured resonant frequency, f , at each temperature, T , one can fit for the single variable T_c . Fits presented in this section are completed using a brute force method for a finely sampled range of possible T_c values and an example of these fits is shown in Figure 3.1.

Figure 3.2 shows the T_c variation for four SuperSpec test filterbank devices. What is found is that the variation in T_c across the SuperSpec filterbanks is mostly systematic with relatively small random variations. In Figure 3.3, two filterbanks from the same wafer (Figure 3.2 Top Right and Top Left) are used to fit a 2-dimensional parabolic conic to the T_c variation across an entire wafer. The data is very consistent with such a fit. This is shown

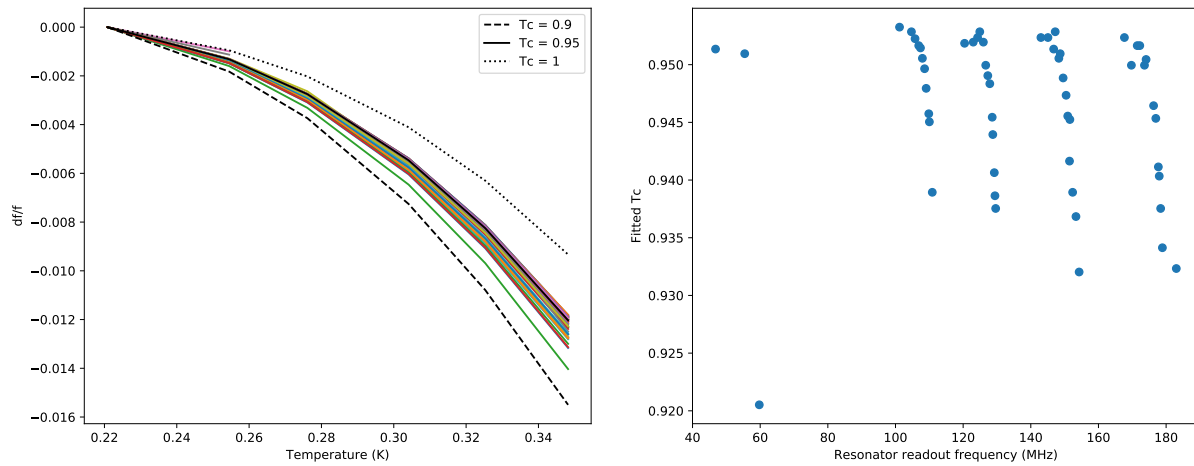


Figure 3.1: An example of how T_c fitting is implemented for SuperSpec prototypes. The resonant frequency of each resonator is recorded for a variety of array temperatures. Left: df/f as a function of array temperature for the resonators, shown in colored lines. These values are then compared to models for the expected shift in df/f with T for different T_c values (black lines). Right: Fitted T_c values. It can be seen that between 100 and 180 MHz there are four banks of resonators, and each bank of resonators shows a similar trend with frequency. This trend reflects a systematic T_c variation with position on the wafer.

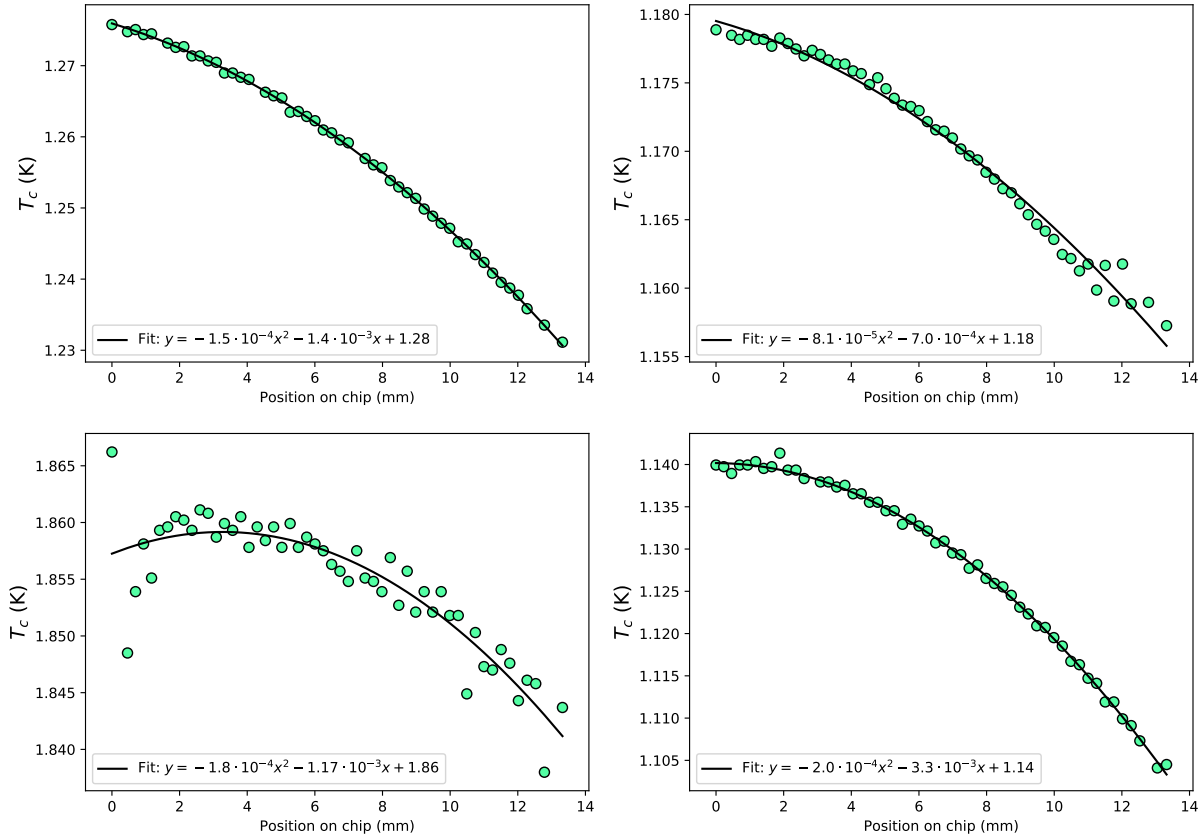


Figure 3.2: A plot of T_c variation across 4 different 50 channel SuperSpec filterbank prototypes. In all cases, the T_c variations are well fit with a parabolic function with respect to the location on the chip.

in Figure 3.3, where the data is shown in blue and the fit is shown as a red wire grid.

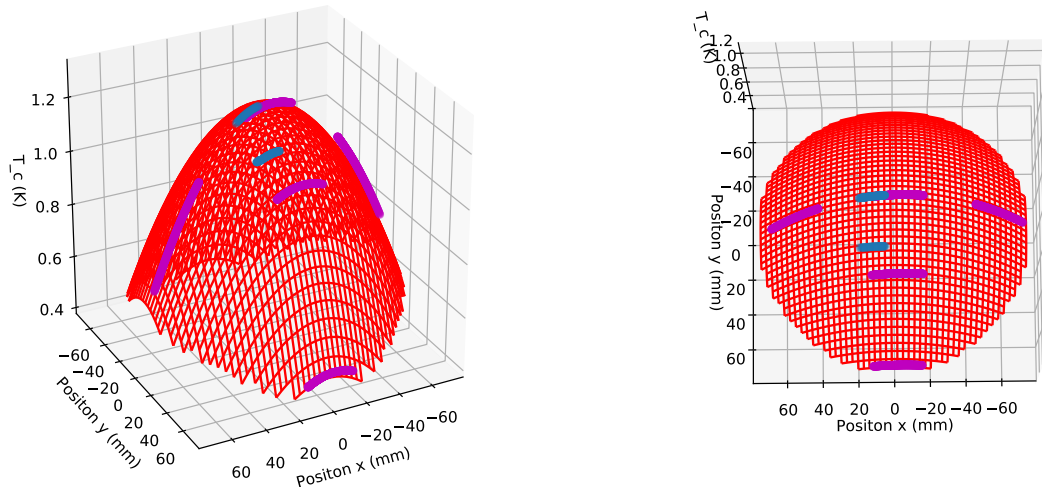


Figure 3.3: 2-dimensional data of T_c versus position for two SuperSpec test devices from the same wafer (blue points). Fit using a parabolic conic is shown as a red wireframe. Then, hypothetical T_c values for 300 channel filterbanks with $\lambda/4$ spacing at different locations along the wafer are shown as purple points.

Given that the T_c variation is well described by a parabolic function, this fit can be used to predict how the placement of the detectors on a wafer will impact the resultant resonant frequencies. This is shown in Figure 3.4. In particular, since many filterbanks are produced on one wafer at a time, how the T_c variation will change the achieved resonant frequencies for different filterbanks on the same wafer is investigated. Examining this figure in detail, it can be seen that the T_c variation has a much more significant impact on filterbanks in the same row rather than the same column. This is because the T_c variation is strongest in the radial direction and, thus, when the filterbank detector placement is aligned with a radial vector the T_c variation is maximum. The central position in the central row of filterbanks has minimum frequency variation, but filterbanks to the left or right in that row have resonators that either collide between banks (left) or have many collisions for each bank (right). Examining the predictions for the filterbanks in the center column show that

this effect is not as substantial. In this case, the filterbanks are now anti-aligned with a radial vector minimizing the difference in T_c across the filterbank. In particular, for all cases of different achieved peak T_c , we see the effect is quite minimal for position 0 and 1 of the column positions. Based on these results, the SuperSpec team decided to fabricate 3 spectrometers per wafer in positions C0, C1, and opposite of C1 but in the same column, minimizing the effect of systematic T_c variation on the detectors.

The local T_c variation minimization strategy can also be applied to imaging arrays. Given this knowledge, we can establish a few best practices for laying out the resonant frequencies for an imaging array. For example, consider two banks in readout frequency of resonators from 250 to 500 MHz and 85 to 170 MHz. Each adjacent detector should alternate between the two readout banks to avoid cross-talk between adjacent resonators, while still maintaining close proximity for similar readout frequency detectors in each of the two banks. Then, one should assign resonant frequencies to the detectors starting in the middle of the wafer and starting with the highest frequency resonators as the detectors spiral out in position. By monotonically assigning readout frequencies while spiraling out, the detectors will be placed mostly in concentric rings, which should have very similar values of T_c for similar readout frequencies. In addition, the T_c will decrease as the detectors are placed further away in radius. This will then only cause the resonant frequencies to decrease with radius, resulting in resonators moving further apart in readout space, avoiding collisions. Leaving a large enough gap between the two banks ensures that the two banks will not collide. In this case, a T_c variation of greater than two would be required to cause the banks to collide. Alternatively, if the T_c variation has been measured for a given fabrication method, all of the resonant frequencies can be scaled appropriately to compensate for a systematic T_c variation.

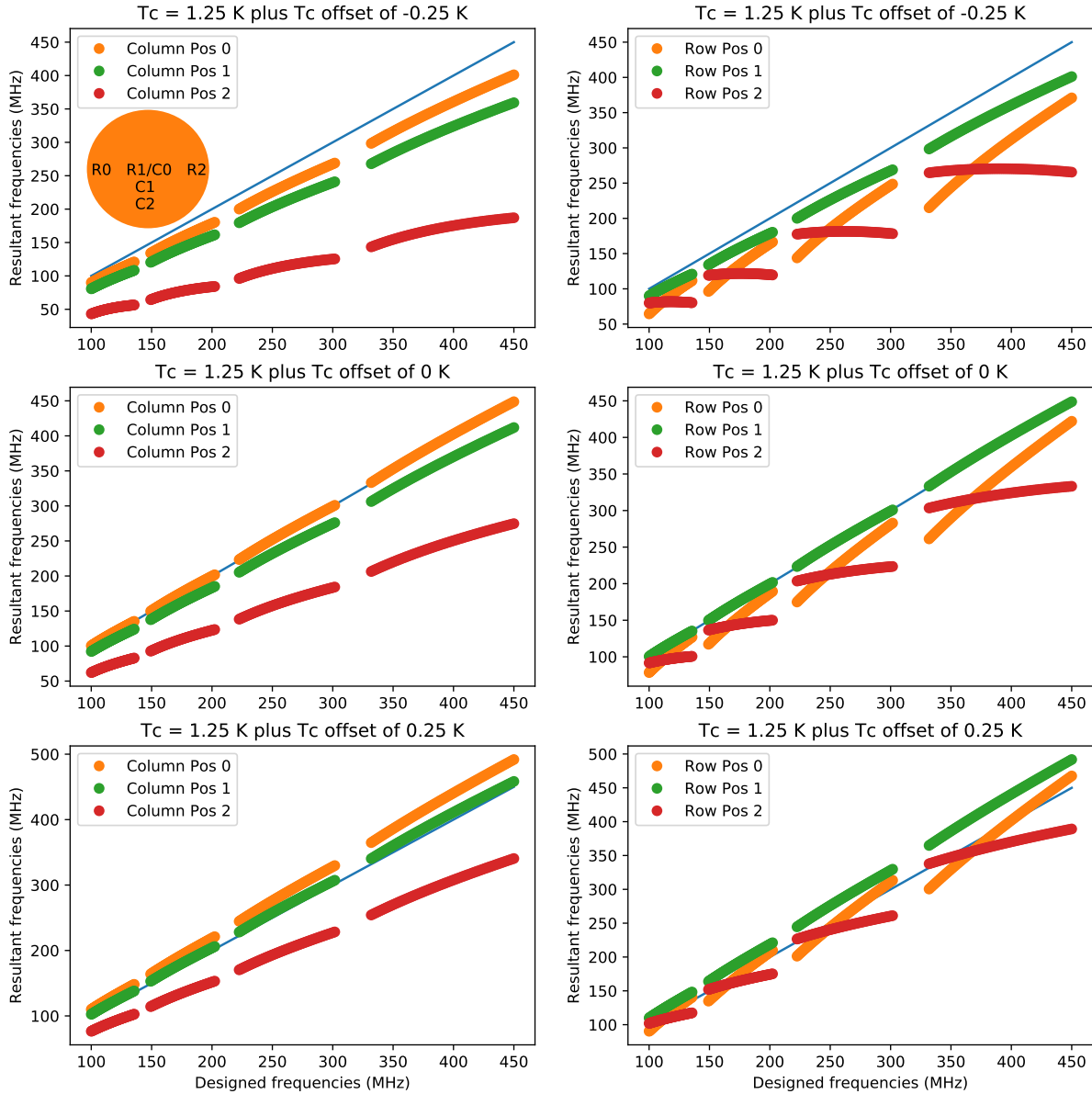


Figure 3.4: Given the T_c fits in Figure 3.3, the systematic T_c variation across the wafer can be predicted. In turn, how much this variation will change the resonator readout frequencies from their designed values can also be predicted. These plots take into account two systematic variations. One is a manufactured T_c that is different from what was intended, represented here as a T_c offset which is different for each row of plots. For example, a target $T_c = 1.25 \text{ K}$ with a fabrication offset of -0.25 K will yield a wafer with a $T_c = 1.0 \text{ K}$. The second variation is the T_c variation across the wafer according to where the filterbank is placed on a wafer. This is shown for three different positions for both the center column of a wafer and the center row for a wafer. The graphical depiction of these placements is shown in the top left plot over a wafer that is shown in orange.

3.2 Readout Frequency Targeting and Predicted Collisions

The readout frequencies of the kinetic inductance detectors exhibit scatter that is not entirely explained by T_c variations. Thus, it is important to examine the scatter in resonant frequencies of the detectors in its entirety. The total resonator readout frequency scatter is important because each science-grade spectrometer requires hundreds of detectors. If the resonators exhibit too much scatter from their targeted values, there will be collisions between resonators in frequency space resulting in unusable channels, lowering the effective yield. Figure 3.5 Left shows the measured readout frequencies versus the designed readout frequencies for a 50 channel filterbank prototype. The measured resonator frequencies came out a factor of ~ 1.25 times greater than the designed values. This is consistent with the 1.55 times increase in T_c measured for this chip. Three diagnostic channels are shown at the lowest frequencies, and the 50 spectral filterbank channels are grouped in four banks in readout frequency space. For each of the four banks, the resonators are monotonically increasing in distance along the filterbank.

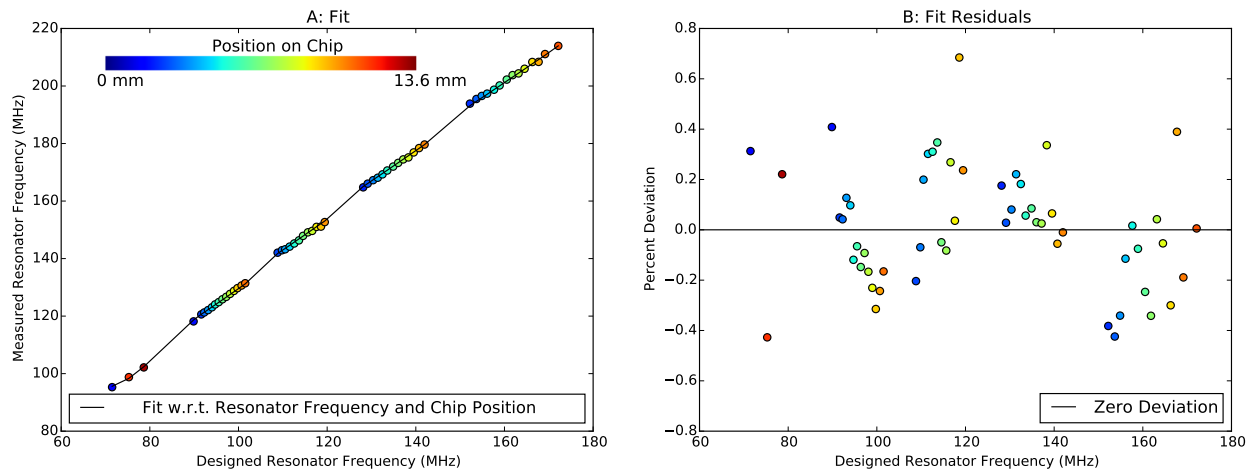


Figure 3.5: Left: Designed resonator frequency versus measured resonator frequency (colored circles) with a fit (black line). The fit is both a second-order polynomial with respect to designed readout frequency and linear fit with respect to the location of the resonator on the chip. Right: Residuals of the fit after the fitted function is removed.

In order to remove systematic trends with readout frequency and position on the chip so that the random scatter can be measured, a second order polynomial function with readout frequency and a linear function with distance along the filterbank is fit simultaneously. The function is then subtracted to obtain the residuals plotted in Figure 3.5 Right, which indicates a $\sigma = 0.23\%$ random scatter. These devices have $Q_r = 10^{4.2}$, while $Q_r = 10^5$ are desired for the full filterbank. With the value of $Q_r = 10^5$ for a full $N = 280$ detector device when using one octave of readout bandwidth, the resonant frequency scatter corresponds to an expected collision rate of 1.5%, where a collision is defined as two resonators being within 5 FWHM of each other. This is shown in blue in Figure 3.6. In the current filterbank design, adjacent spectral channels overlap, so any given optical frequency is sampled by multiple channels. As such, as long as multiple adjacent spectral channels are not simultaneously lost due to collisions, the performance of the filterbank will not be significantly degraded. A loss of up to 1.5% of the channels will, therefore, have a negligible effect on the spectral coverage of the full filterbank. If the Q 's remain at $10^{4.2}$, almost 10% of the resonators will collide. In this case, since this is more than the acceptable number of lost channels, we will pursue fixing the collisions with capacitor trimming. This is a process in which the resonant frequencies are adjusted by lithographically editing the capacitor to change the resonant frequency of targeted resonators. This has been demonstrated by Liu et al. (2017) and also has been used by our collaboration to fix 5 collisions on a 50 channel filterbank.

Systematic scalings to the resonator readout frequencies, with respect to chip position and readout frequency, can also impact the number of collisions. We minimize this effect by placing nearest neighbors in readout space nearly adjacent in physical space; for this filterbank, the spacing was 1 mm on the chip. The systematic scaling of resonator frequency with chip position corresponded to a 150 kHz shift over this same length scale. For a full filterbank, $N = 280$ detectors, using one octave of bandwidth, the spacing is on the order of 360 kHz. So at most, this spacing will be reduced to $(360 - 150) = 210$ kHz. For $Q_r = 10^5$, the FWHM of each resonator is 2 kHz \ll 210 kHz. Thus, a 150 kHz shift between adjacent

resonators will therefore still leave these resonators well-separated and is not expected to generate any collisions.

For the scaling with readout frequency, the fit was dominated by the linear term. Considering the slope of this linear fit, we can approximate the effect of this systematic trend on collisions. A slope greater than unity will drive the resonator frequencies further apart, decreasing collisions and increasing the required bandwidth. A slope that is less than unity will increase the number of collisions and decrease the required bandwidth. For this filterbank the slope was 1.2, increasing the required bandwidth by that factor and decreasing the number of collisions by $1/1.2 = \sim 0.8$. For the dark filterbank, measured previous to this filterbank, a slope of 0.9 was found, which decreased the required bandwidth by that factor and increased the collision probability by a factor of ~ 1.1 . SuperSpec's resonators are read out in the 100 to 450 MHz (2.25 octaves of bandwidth) range with a 500 MSamples/s readout. This means that two full filterbanks could be read out in two octaves of bandwidth, with a single readout system leaving some extra bandwidth in the case of a systematic scaling that increases the required bandwidth. The effect of a $\pm 25\%$ systematic change in the effective bandwidth on the collision probability is shown in grey in Figure 3.6.

3.3 TiN NEP and Noise

The metric that defines the sensitivity of a detector is the noise equivalent power (NEP). It can be understood as a normalized signal-to-noise measurement. Formally, it is defined as the power incident on a detector that gives a signal-to-noise ratio of one with a one hertz readout bandwidth (Richards, 1994). The NEP for kinetic inductance detectors is limited by the generation and recombination of quasiparticles within the detectors. Theoretically, for resonators read out in the frequency domain, NEP can be calculated from the detector

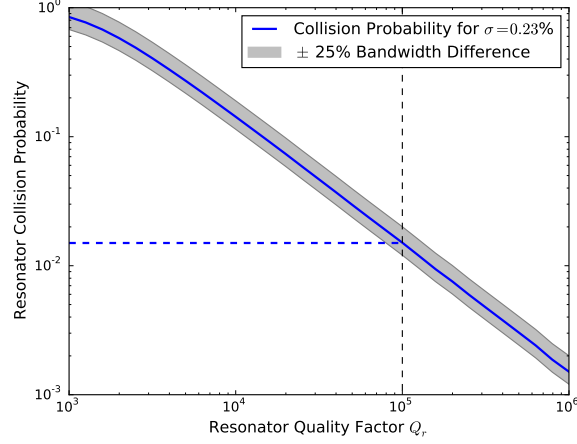


Figure 3.6: Collision probability for a random scatter in resonant frequencies of $\sigma = 0.23\%$ using one octave of readout bandwidth. The effect of increasing or decreasing the readout bandwidth by a factor of 25% is shown in grey. Monte Carlo collision simulations were provided by Dr. Erik Shirokoff.

parameters using the following equation from Zmuidzinas (2012).

$$NEP_{df/f} = 2P_o h\nu(1 + n_0) + \frac{8N_{qp}^2 \Delta_0^2}{\beta^2 \eta_o^2 \chi_c \chi_{qp}^2 \tau_{qp}^2} \frac{kT_a}{P_a} + \frac{4\eta_a \chi_{qp} \Delta_0}{\eta_0^2} P_a + \frac{4\Gamma_{th} \Delta_0^2}{\eta_0^2} + \frac{2N_{qp} \Delta_0^2}{\eta_0^2} (\tau_{max}^{-1} + \tau_{qp}^{-1}). \quad (3.5)$$

The first term is photon noise, the second term is amplifier noise, the third term is shot noise from quasiparticles generated by the readout power, the fourth term is thermal generation noise, and the final term is recombination noise. P_o is the optical power absorbed by the detector, h is the Planck constant, ν is the frequency of the absorbed optical power, n_0 is the occupation number in the detector, N_{qp} is the total number of quasiparticles in the detector equal to $n_{qp}V$ (where V is the volume of the inductor and $n_{qp} = \sqrt{(n_{th} + n^*)^2 + 2\Gamma\tau_{max}n^*/V} - n^*$ where $\Gamma = \eta_o P_o / \Delta_0 + \eta_a P_a / \Delta_0$ is the rate in which quasiparticles are generated by optical and readout photons and $n_{th} = 2N_0 \sqrt{2\pi k_B T \Delta_0} \exp(-\Delta_0 / k_B T)$ with $N_0 = 3.9 \times 10^{10} \text{ eV}^{-1} \mu\text{m}^{-3}$ (Gao et al., 2012)), $\Delta_0 = 1.76 k_B T_c$, β describes the ratio of the response in the frequency direction versus the dissipation direction, η_o is the ef-

efficiency at which optical photons are converted to quasiparticles, η_a is the efficiency at which readout photons are converted to quasiparticles, χ_c is the coupling efficiency factor $\chi_c = 4Q_cQ_i/(Q_c + Q_i)^2$, χ_{qp} is the fraction of the resonator internal dissipation from quasiparticles ($\chi_{qp} = Q_i/Q_{qp}$ where Q_{qp} is the quality factor due to quasiparticle losses, see (Zmuidzinas, 2012) Equation 65), $\tau_{qp} = \tau_{max}(1 + n_{qp}/n^*)^{-1}$ is the quasiparticle lifetime, τ_{max} is the experimentally observed maximum quasiparticle lifetime, n^* is an experimentally observed quasiparticle density above which the quasiparticle time constant τ_{qp} declines, T_a is the noise of the amplifier in temperature units, P_a is the absorbed readout power, and Γ_{th} is the thermal quasiparticle generation rate $\Gamma_{th} = (n_{th}V/2)(\tau_{max}^{-1} + \tau_{th}^{-1})$ where τ_{th} is the quasiparticle lifetime when only thermally generated quasiparticles are present. Here we have neglected TLS noise contributions to the NEP because for SuperSpec detectors, TLS noise has been engineered to be subdominant. For kinetic inductance detectors read out in the frequency domain, the NEP can be calculated from data with the following equation.

$$NEP = \sqrt{S_{xx}}/R. \quad (3.6)$$

In this equation, R is the responsivity with units of W^{-1} , so that R is the response of the detectors in units of x to 1 watt of power. S_{xx} is noise power, where $x = \Delta f/f$ is the normalized frequency shift of the resonator circuit. In practice, S_{xx} is measured by taking a time stream of the detectors when they are exposed to a constant load and held at a constant temperature. This time stream is then converted into the normalized frequency shift units of x and Fourier transformed to show noise power as a function of the readout bandwidth. Given a sample rate f_{sr} and a total number of samples N_{tot} , the equation for S_{xx} is

$$S_{xx} = \frac{2FFT(x)\overline{FFT(x)}}{f_{sr}N_{tot}}. \quad (3.7)$$

Here the convention that is used is the same as Python's Numpy's fast Fourier transform, where the FFT is not scaled and the inverse FFT is scale by $1/N_{tot}$. The resultant units of S_{xx} are Hz^{-1} .

Responsivity is usually measured by exposing the detectors to a known load that is radiating a well-understood power level within the bandwidth of the detectors and measuring the response of the detectors to this load. In order to back out the responsivity of the detector independent of the efficiency of the test setup, i.e. accounting for filter efficiency and the beam filling factor of the load, this method requires careful calculation of the test setup efficiency or an independent measurement of it. As such, this method can introduce some additional uncertainty into a responsivity measurement.

The SuperSpec collaboration has routinely used a different method to measure the responsivity that is independent of the test setup's optical efficiency. The responsivity is found by measuring the change in white, readout frequency independent, S_{xx} photon noise in the detectors as the loading of a coherent local oscillator source is varied. This is possible because a coherent local oscillator source produces purely shot noise without any wave noise. The responsivity, R , can be extracted from the slope of the measurement of S_{xx} versus x using the equation from Hailey-Dunsheath et al. (2016).

$$\frac{dS_{xx}}{dP} = 4R^2 h\nu. \quad (3.8)$$

Since $R = dx/dP \Rightarrow dP = dx/R$ the equation can be written as

$$\frac{dS_{xx}}{dx} = 4Rh\nu \Rightarrow R = \frac{\Delta S_{xx}}{\Delta X} \cdot \frac{1}{4h\nu}. \quad (3.9)$$

Thus, a plot of S_{xx} versus x will have a slope equal to $4Rh\nu$. The validity of this measurement

is dependent on the assumption that one photon will only break one Cooper pair. This should be a good assumption for the SuperSpec detectors because at a T_c of 1.25 K, $h\nu/\Delta_0 \sim 5$, so one photon does not have the energy to produce many quasiparticles. Furthermore, one photon will initially break one Cooper pair and since the films are thin, 20 nm, the escape time for any phonons that are created when those quasiparticles recombine will be much faster than the pair-breaking timescale for those phonons to break further Cooper pairs.

3.3.1 NEP 9 Cubic Micron Detectors

For the previous generation $9 \mu\text{m}^3$ volume detectors, the responsivity was found using the local oscillator source as detailed above. The measurements are shown in Figure 3.7 Left. This responsivity, $R = 1.7 \times 10^8 \text{ W}^{-1}$, along with the measured S_{xx} value for a $T_c = 1.85 \text{ K}$ chip, produces a NEP curve represented by the blue curve in Figure 3.7 Right. This responsivity is not what one would expect for a future SuperSpec filterbank with $T_c = 1.2 \text{ K}$. Thus, in order to estimate the NEP for a $T_c = 1.2 \text{ K}$ chip, the previously measured responsivity for a $T_c = 1.15 \text{ K}$ device, $R = 9.8 \times 10^8 \text{ W}^{-1}$ (Hailey-Dunsheath et al., 2016), is used, along with dark noise data taken on the previous optically dark $T_c = 1.2 \text{ K}$ chip, for which the median white noise level at 100 to 200 Hz was $S_{xx} = 5 \times 10^{-17} \text{ Hz}^{-1}$. This produces a NEP that is $7 \times 10^{-18} \text{ WHz}^{-0.5}$ which is represented by the curve shown in green in Figure 3.7 Right. The fact that the responsivity for the $T_c = 1.85 \text{ K}$ chip was a factor of 5.8 times less than the responsivity of the previous $T_c = 1.15 \text{ K}$ chip is roughly consistent with the 5.3 times decrease expected when comparing T_c values.

This NEP level is sufficient to carry out ground-based spectroscopy at $R = 100$ (red dashed line in Figure 3.7 Right); however, further reduction is required to meet the background limit for $R = 400$ spectroscopy (purple dashed line in Figure 3.7 Right). In order to meet the $R = 400$ requirement, we decided to reduce the inductor volume of the detectors.

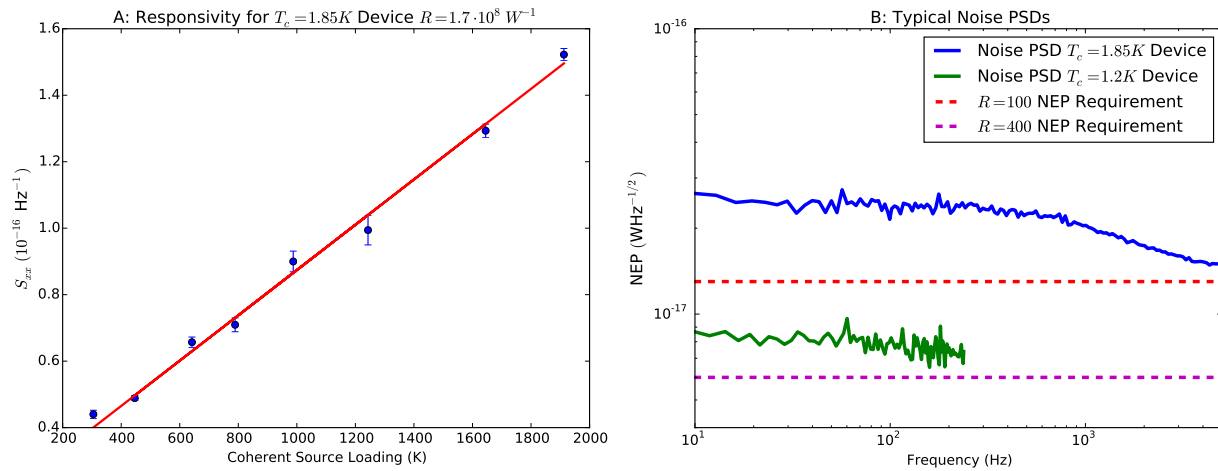


Figure 3.7: Left: Photon noise from a coherent local oscillator source as a function of loading for a $T_c = 1.85 \text{ K}$ $9 \mu\text{m}^3$ chip, yielding a responsivity of $R = 1.7 \times 10^8 \text{ W}^{-1}$. Right: Typical noise PSDs for SuperSpec detectors. Blue indicates the NEP for a $T_c = 1.85 \text{ K}$ chip and green indicates NEP for a $T_c = 1.2 \text{ K}$ chip.

3.3.2 NEP 2.6 Cubic Micron Detectors

To improve the SuperSpec kinetic inductance detector sensitivity, a new ultra-low-volume inductor utilizing 0.25-micron-wide lines was patterned in 20 nm TiN film. The total inductor volume of SuperSpec devices is now $2.6 \mu\text{m}^3$, and these inductors are produced with high yield. Fractional-frequency response to optical loads is calibrated in the usual way, using nitrogen-cooled loads relative to ambient. Additionally, a concave mirror outside the cryostat is utilized to achieve an effective temperature of ~ 15 K, less than expected at the observatory (30 to 60 K).

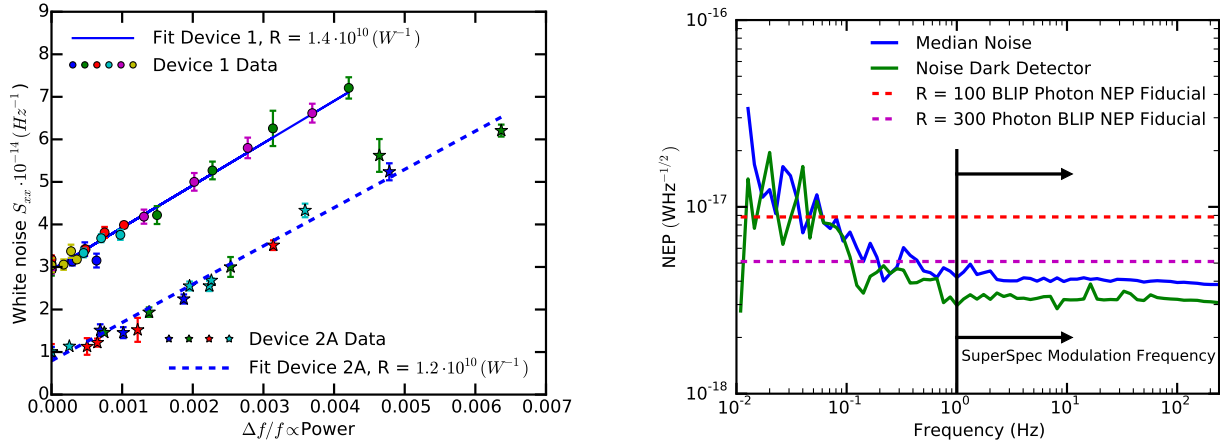


Figure 3.8: Left: Measured responsivities for Device 1 and 2A. Each different color symbol represents a different kinetic inductance detector with resonant frequencies from 100 to 200 MHz. The coherent source was set to a frequency of 265 and 278 GHz respectively. Detectors are assumed to have the same responsivity and similarity of slopes between detectors confirms this assumption. Each detector for each device has been vertically offset to have the same Y-intercept. Right: NEP PSDs for SuperSpec detectors. NEP data shown is for Device 2A; however, absolute levels of the NEP curves are the same for both Device 1 and Device 2A.

Again, the frequency responsivity is obtained from the slope of the photon noise as a function of loading when excited by a coherent local oscillator source. This does assume that the responsivity is constant with changing loading, which has been confirmed for these TiN detectors over the power level range used for this measurement and is further confirmed by the linearity of the data in Figure 3.8 Left.

For Device 1, a responsivity of $1.4 \times 10^{10} \text{ W}^{-1}$ (Figure 3.8 Left) is found, along with a median noise level of $2.7 \times 10^{-15} \text{ Hz}^{-1}$ measured at $T_{det} = 210 \text{ mK}$. These numbers yield a NEP of $4 \times 10^{-18} \text{ W/Hz}^{0.5}$ at 1 Hz. For Device 2A, a responsivity of $1.2 \times 10^{10} \text{ W}^{-1}$ (Figure 3.8 Left) is found, along with a median noise value of $2.1 \times 10^{-15} \text{ Hz}^{-1}$. This also yields a NEP of $4 \times 10^{-18} \text{ W/Hz}^{0.5}$ at 1 Hz. Each SuperSpec die includes a kinetic inductance detector which is not coupled to the filterbank as a way to assess chip-level effects. For this dark channel kinetic inductance detector the noise is slightly lower, $1.3 \times 10^{-15} \text{ Hz}^{-1}$, resulting in a detector NEP of $3 \times 10^{-18} \text{ W/Hz}^{0.5}$. The NEP measurements are shown in Figure 3.8 Right, where it can be seen that the device noise is below the expected photon noise level at the Large Millimeter Telescope. The instrument will be modulated with a chopping mirror for the Large Millimeter Telescope demonstration, and as such, the low-frequency noise will not impact the sensitivity. For all devices the T_c was approximately $\sim 0.93 \text{ K}$. As a result, these devices prefer to be operated at a lower T_{det} to reduce the thermal generation-recombination (G-R) noise. This is demonstrated in McGeehan et al. (2018) where Device 1 was tested at lower T_{det} demonstrating even lower NEP can be achieved.

3.3.3 White Noise

Next, we take an in-depth look into the individual sources of noise that contribute to the detector noise. First, the various contributions to the white, readout frequency independent, noise sources such as photon noise and thermal generation-recombination noise are examined. To determine the various contributions to the noise, noise is measured as a function of detector temperature (Figure 3.9). At high detector temperatures, it is expected that thermal generation-recombination noise becomes significant and dominates the noise levels, while at low temperatures photon noise is expected to come into play. This is supported by the observation that at low temperatures there is a correlation between efficiency on-chip of each detector (measured by the fractional frequency response of each detector when exposed to a cold load at 77 K versus a hot load at 300 K) and the white noise level whereas at high

detector temperatures this correlation disappears (Figure 3.9 Right). The fits to the noise levels are made using the formalism from Zmuidzinas (2012), where $\tau_{qp} = \tau_{max}(1 + n_{qp}/n^*)^{-1}$. This formalism states that the quasiparticle lifetime is limited to a maximum lifetime of τ_{max} and that the quasiparticle lifetime will reduce once the number of quasiparticles exceeds some value n^* . n^* and τ_{max} are experimentally determined. In particular, we use the equation from Hailey-Dunsheath et al. (2018) such that

$$S_{xx} = \left(\frac{\alpha\gamma S_2}{4N_0\Delta_0} \right)^2 \left[\left(\frac{\eta_{pb}\tau_{qp}}{\Delta_0 V} \right)^2 2h\nu P_{abs}(1 + n_\gamma) + \frac{4\tau_{qp}^2}{V^2} (\Gamma_{th} + \Gamma_r) \right] + S_{xx,0}. \quad (3.10)$$

Here α and γ are defined as in Equation 3.4, $N_0 = 3.9 \times 10^{10} \text{ eV}^{-1} \mu\text{m}^{-3}$ (Gao et al., 2012), Δ_0 is the superconducting gap energy, $\Delta_0 = 1.76k_B T_c$, V is the volume of the inductor, η_{pb} is the efficiency of photon pair-breaking in the detectors, τ_{qp} is the quasiparticle lifetime, P_{abs} is the optical power absorbed by the detector, ν is the frequency of the absorbed optical power, n_γ is the photon occupation number in the detector, $S_{xx,0}$ is any extra constant source of noise in the detectors, and S_2 is given by the following equation from Zmuidzinas (2012).

$$S_2(\omega) = 1 + \sqrt{\frac{2\Delta_0}{\pi k_B T}} \exp(-\hbar\omega/2k_B T) I_0(\hbar\omega/2k_B T). \quad (3.11)$$

Here T is the temperature of the detector, ω is the readout frequency, \hbar is the reduced Planck constant, and k_B is the Boltzmann constant. In addition, the thermal quasiparticle generation rate Γ_{th} and recombination rate Γ_r are given by

$$\Gamma_{th} = (n_{th}V/2)(\tau_{max}^{-1} + \tau_{th}^{-1}) \text{ and} \quad (3.12)$$

$$\Gamma_r = (n_{qp}V/2)(\tau_{max}^{-1} + \tau_{qp}^{-1}), \quad (3.13)$$

where τ_{th} is the quasiparticle lifetime when the system is dominated by thermally generated quasiparticles. n_{th} and n_{qp} are the same as in Equation 3.5. The first term within the square brackets in Equation 3.10 is the photon noise from optical loading and the second term is from thermal generation noise and the recombination noise from all sources.

Examining Figure 3.9 Left and the fits within, reveals that the noise at the highest measured temperatures can be almost entirely attributed to thermal generation-recombination noise. However, for the lowest temperature points, noise in excess of the thermal generation-recombination noise for both the optical detectors and the dark channel KID on the optical chip is found. The ratio of the excess noise between the optical devices and the dark channel KID, approximately a factor of four, corresponds to the ratio of the response of these detectors to hot-cold loads outside the cryostat. Thus, this noise seems correlated to chip efficiency and is believed to be photon noise. It should be noted that the response of the dark channel is mostly contributed to by power below the spectral band frequency range (the science band) but above the TiN band gap, that is 75 to 200 GHz. This is currently not filtered in the testbed, and for the telescope run, it will be mitigated by high-pass filtering. For Device 2B (the device in a dark package), the excess white noise is not seen at the lowest temperature and the noise can be entirely attributed to thermal generation-recombination noise. The instrument is expected to be strongly photon noise limited at the observatory because a) loading from the coupling optics, telescope, and sky will be at least double the ~ 15 K level used here, and b) further optimization of the system filtration and antenna/lens coupling are planned, increasing the efficiency of photons delivered to the detector.

For this device, we also examined how the noise changes with loading. In this case, we investigate both the white, frequency independent noise, and $1/f$ noise, noise that increases with slower timescales. At low loading levels, the white noise will be a combination of both photon noise and thermal generation-recombination noise. At high loading levels, the noise will be mostly photon noise. In Figure 3.10 Left, it can be seen that as the loading is

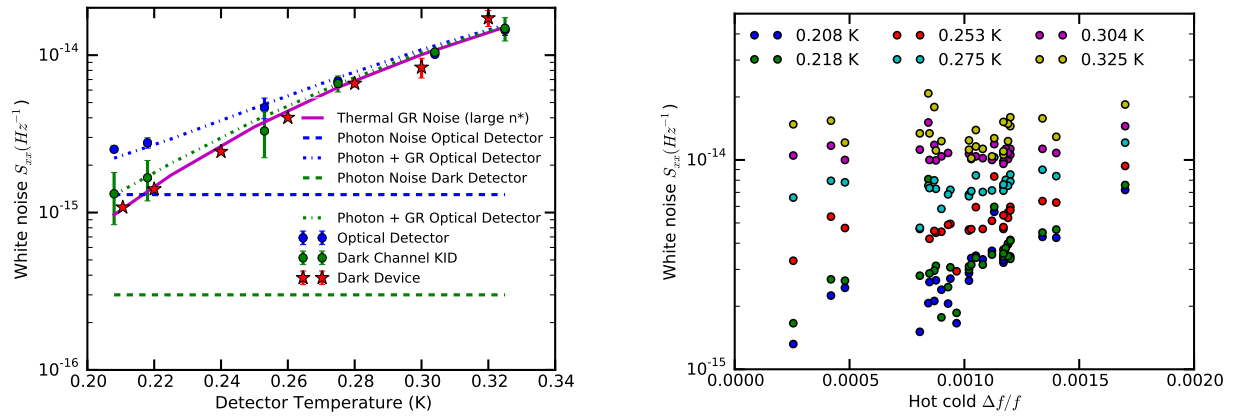


Figure 3.9: Left: Noise versus detector temperature for SuperSpec detectors. Blue (typical optical channel) and green (dark channel) circles are for the optically coupled Device 2A and the red stars are for Device 2B which was kept in a dark box. The fits to thermal G-R noise with and without a constant source of photon noise are also shown. Right: Noise as a function of the hot-cold response of Device 2A for different detector temperatures.

increased the white noise level in the detectors also increases. From this, it can be concluded that at higher loading levels the detectors will be photon noise limited from the emissivity of the sky/telescope mirrors.

3.3.4 1/f Noise

Next, we examine the 1/f noise. This type of noise can originate from several sources. Sources can include: slow fluctuations in the array temperature that causes a slow drift in the resonant frequencies, slow drift in the gain of the readout hardware, or variation in atmospheric opacity while observing on the telescope. These types of 1/f noise will be correlated between detectors. As such, one can use the information from other detectors to remove this signal from a particular detector. We accomplish this using principal component analysis (PCA). PCA finds common mode signal within many detectors, then transforms to a vector space where the common mode signals are orthogonal to other signals. When in this vector space, the common mode signal can be easily subtracted off from all of the detectors at once. The data is then transformed back to the standard time series space, with any undesired common mode signals removed. This common mode signal could be any of the slow fluctuations listed above or it could be the periodic pulse from the cryostat pulse tube cooler. 1/f noise that is common to all of the detectors is generally not concerning because it can be removed with PCA. However, for the SuperSpec TiN kinetic inductance detectors, it is always found that some 1/f noise that is not correlated between detectors still remains after carrying out PCA.

A common source of non-correlated 1/f noise for kinetic inductance detectors is two-level-systems noise or TLS (Gao et al., 2007; Kumar et al., 2008; Gao et al., 2008; Noroozian et al., 2009). This is noise that arises in the capacitor of kinetic inductance detectors. It is caused by two-level-systems in the dielectric which a capacitor is on, or embedded in, that causes fluctuations in the capacitor's capacitance. TLS noise has some signature attributes such as: a slope in $S_{xx}(f)$ that increases as $1/f^{0.5}$, noise that decreases with increasing

readout power (Gao et al., 2008), a dependence on capacitor geometry (Gao et al., 2008), and noise that decreases with increasing detector temperature (Kumar et al., 2008). For the noise observed in the SuperSpec detectors, none of these tell-tale signs are observed (albeit our ability to probe different readout powers is not large due to amplifier noise becoming significant for power levels much lower than the bifurcation power). Thus, it is concluded that this noise arises from some other mechanism; but as of yet, we do not have a physical model for what mechanism that might be. However, we have made some measurements of the empirical scaling of this noise. The first thing noticed is that this noise increases with increasing photon loading. This is demonstrated in Figure 3.10, Middle and Right. Since the noise is dependent on loading, it must arise from a mechanism within the active area of the resonator, i.e. the inductor.

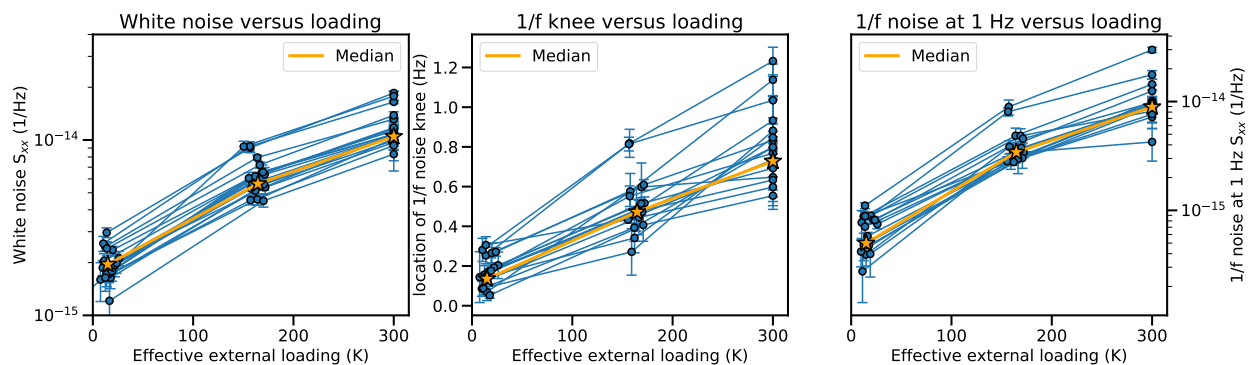


Figure 3.10: The effect of optical loading on the noise levels. Each panel incorporates measurements from 37 detectors. Left: Frequency independent white noise increases with increasing loading outside the cryostat, consistent with photon noise. Middle: The 1/f knee in readout frequency as a function of loading. The 1/f knee is defined as the readout frequency where half of the noise contribution is from white frequency independent noise and half arises from 1/f noise. At higher loading levels, the ability to operate at the low readout frequencies is diminished. Right: The magnitude of the 1/f noise measured at a frequency of 1 Hz as a function of loading. The 1/f noise increases substantially with loading.

Over the years, I have taken noise data on many different devices with a range in values of T_c . When this noise data was compared, an interesting effect was noticed. The noise performance of SuperSpec devices at low readout frequencies was systematically better

for devices with a lower T_c . In particular, the location of the 1/f knee is pushed to a lower frequency on lower T_c devices. This effect is demonstrated by the data in Figure 3.11. In Figure 3.11 Left, it can be observed that the 1/f noise in S_{xx} units seems to be independent of the value of T_c . However, as T_c is decreased and the array operating temperature is kept the same, thermal generation-recombination noise will become more significant. So in Figure 3.11 Left, it can be seen that the white noise level, due to mostly thermal generation-recombination noise, increases while the 1/f noise remains constant. This effect moves the 1/f knee to slower readout frequencies. Decreasing T_c can lead to a more sensitive detector because a lower T_c will yield a higher response. Empirically, we see that responsivity, R , scales as $T_c^{-3.5}$. Decreasing the T_c will not necessarily improve the detector NEP if the operating temperature of an array cannot also be reduced to minimize increased thermal generation-recombination noise that comes with a reduced T_c . Thus, for SuperSpec, which is limited to a base temperature of 210 mK, we find that our NEP at frequencies where white noise dominates is roughly constant for different values of T_c . However, this is not true when it comes to 1/f NEP performance. At slow readout frequencies, where the SuperSpec detector noise is dominated by this 1/f noise, decreasing the T_c will not cause an increase in the noise level. Thus, the NEP will improve linearly with increasing responsivity, R , such that $\text{NEP} \propto T_c^{-3.5}$. This is demonstrated by Figure 3.11 Right where the NEPs based on the noise traces shown in Figure 3.11 Left are scaled assuming a responsivity, $R \propto T_c^{-3.5}$. This result will be applicable to any type of 1/f noise source that does not depend on T_c , including two-level-systems noise.

Lowering the value of T_c is not without consequence. Once the T_c is lowered such that the array operating temperature is no longer less than $T_c/5$, the quality factors of the resonators will decline. This will hurt the multiplexing factors that can be achieved without causing excessive cross-talk between channels due to readout collisions. Decreasing T_c is not a cure-all for improving the 1/f noise in TiN detectors, but it is one parameter that can be adjusted to help. At the same time, the observation that this 1/f noise is independent of T_c

provides an additional clue when trying to understand what mechanism might be causing this anomalous noise.

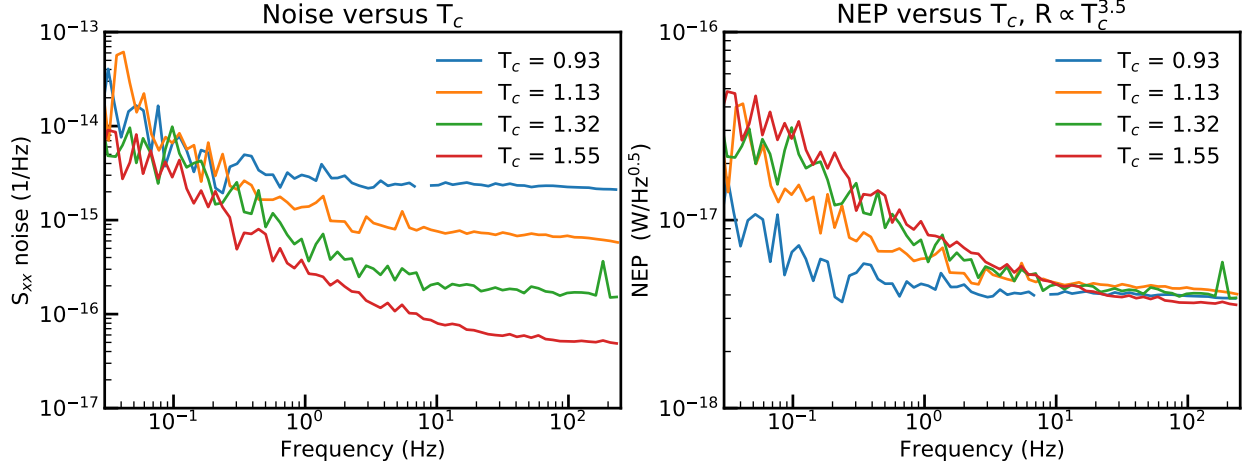


Figure 3.11: Plots showing the effect of T_c on the $1/f$ noise level for SuperSpec detectors. All noise traces shown are for $2.6 \mu\text{m}^3$ volume inductors and all data was taken at an array temperature of 210 mK. Left: The raw noise data in S_{xx} units. Right: Hypothetical NEP achieved assuming that the responsivity of the detectors goes as $T_c^{-3.5}$.

3.4 Time Constants

One more parameter of interest for kinetic inductance detectors is the quasiparticle lifetime of the detectors, τ_{qp} . This is an important characteristic of the detectors because maximizing this quantity will maximize the responsivity of the detectors. This is because responsivity is linearly proportional to the quasiparticle lifetime. In particular, responsivity, R , is given by the equation from Hailey-Dunsheath et al. (2018).

$$R = \frac{\delta x}{\delta P_{abs}} = \frac{\alpha \gamma S_2}{4 N_0 \Delta_0} \frac{\eta_{pb} \tau_{qp}}{\Delta_0 V}. \quad (3.14)$$

Here α and γ are defined as in Equation 3.4, $N_0 = 3.9 \times 10^{10} \text{ eV}^{-1} \mu\text{m}^{-3}$ (Gao et al., 2012), Δ_0 is the superconducting gap energy, $\Delta_0 = 1.76 k_B T_c$, V is the volume of the inductor, η_{pb}

is the efficiency of photon pair-breaking in detectors, and S_2 is Equation 3.11.

The quasiparticle lifetime can be measured as long as it is greater than the resonator ringtime, $\tau_{res} = \frac{Q}{\pi f_0}$, where Q and f_0 are the quality factor of the resonator and the resonator readout frequency respectively (de Visser et al., 2012). From this, it can be seen that measuring the quasiparticle lifetime will be easiest when τ_{res} is minimized. This condition is satisfied when Q is low and f_0 is large. For TiN the time constants are often much shorter than for aluminum detectors, making time constant measurements more difficult. In order to enable this measurement, the latest SuperSpec detectors were fabricated with a few purpose-built time constant kinetic inductance detectors with low quality factors and high frequencies.

There are two ways to measure the time constants of the detectors. The first is to flash the detectors with a fast source, such as an LED, and fit the $x = df/f$ response as the resonance settles back to equilibrium. The second is to take a time stream of data and to fit the roll-off in the noise power spectrum in S_{xx} units with a Lorentzian. This is the method employed here. The four parameter equation used in the fits is

$$S_{xx}(f) = \frac{(S_{xx,white} + S_{xx,1/f}f^n)}{1 + (2\pi f\tau_{qp})^2}. \quad (3.15)$$

The time constant can be measured in this way because the noise will decrease at timescales that are faster than the detector can respond to. This measurement only requires that there is enough clearance over the amplifier noise to see the roll-off in the noise spectrum.

The fits to the Lorentzian noise roll-offs are shown in Figure 3.12 for several different array temperatures. For this detector, the frequency was $f_0 = 550$ MHz and the quality factor was $Q = 3000$. This yields a ringtime of $1.7 \mu s$. The fits find a $\tau_{qp} \sim 10 \mu s$. Since the ringtime is less than the measured time constant, it can be concluded that the quasiparticle time constant, τ_{qp} , of the detector is being measured. This value is a bit shorter than the

time constant of $65 \mu\text{s}$ measured by Gao et al. (2012) for $T_c = 1 \text{ K}$ detectors and $100 \mu\text{s}$ for $T_c = 1.1 \text{ K}$ detectors measured by Leduc et al. (2010). Given that one might expect time constants to scale as T_c^{-2} (Leduc et al., 2010) and this detector has a T_c of 1.55 K , one might expect a $24 \mu\text{s}$ time constant if the T_c was scaled to 1 K . This would still be shorter than those previously measured. This is not entirely surprising because short time constants, and thus lowered responsivity, of TiN detectors has driven many groups to pursue aluminum detectors instead, where 1 ms time constants can be achieved (Baselmans et al., 2017).

Additionally, it is found that the time constant has little dependence on the thermal loading induced by higher array temperatures, Figure 3.12 Right. This is consistent with the very linear response of TiN detectors found previously (Hailey-Dunsheath et al., 2016). A small decrease in the time constant at higher temperatures is seen (Figure 3.12 Right) but this is likely just due to a small degeneracy between the fitting of the $1/f$ noise component and the Lorentzian fall-off.

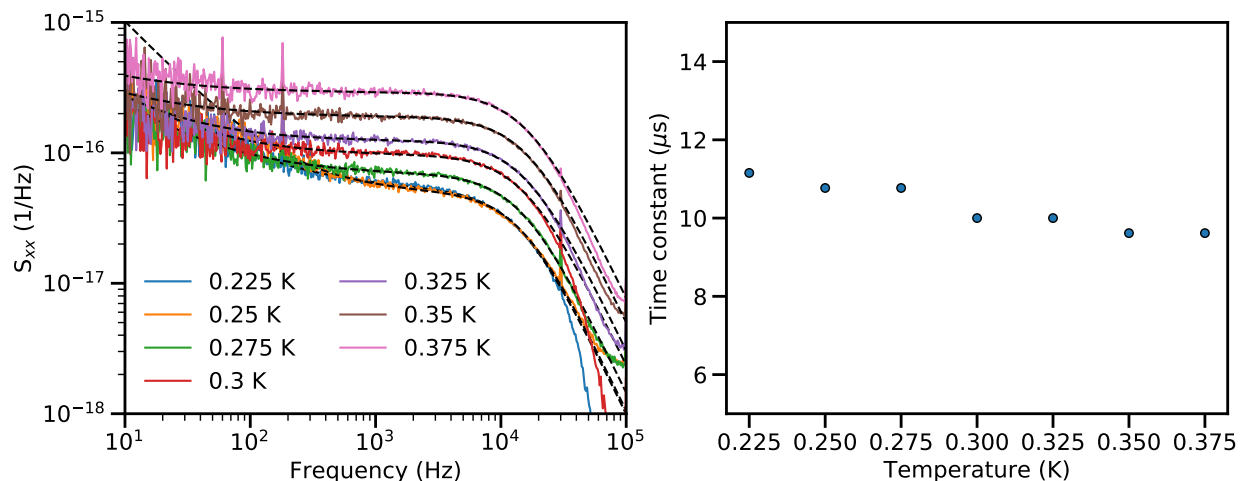


Figure 3.12: Left: Fits to the noise spectrum of a high-frequency low-Q detector. Spectrum is fitted using Equation 3.4 by selecting the minimum of a direct computation of the squared residuals of the model subtracted from the data over a large grid of possible parameters. Right: The extracted τ_{qp} as a function of array temperature. τ_{qp} is found to be roughly independent of the array temperature for the temperatures measured here. The small trend with temperature may be due to degeneracy between parameters in the fit.

3.5 Summary

Improving detector sensitivity is a paramount concern for submillimeter and millimeter detectors. For the previous generation SuperSpec detectors, we found the NEP to be 7×10^{-18} W/Hz^{0.5}. Understanding that this was still above the background limit for our desired resolution on the Large Millimeter Telescope, our collaboration made the decision to reduce the volume of the inductors. This is because responsivity is inversely proportional to the quasiparticle-occupied volume, Equation 3.14. The unique coupling method employed by SuperSpec devices facilitates this ultra low volume design. Along with a lower T_c , we achieved NEPs of 3×10^{-18} W/Hz^{0.5} at an operating temperature of 210 mK and NEPs of 7×10^{-19} W/Hz^{0.5} for colder operating temperatures (McGeehan et al., 2018). This is only slightly more than a factor of 2 from some of the best NEPs measured for kinetic inductance detectors to date, 3×10^{-19} W/Hz^{0.5} (Baselmans et al., 2017). In addition, we found that if the detectors are limited by two-level-system noise or other non-loading dependent 1/f noise, significant NEP gains are achieved by reducing the T_c . For SuperSpec, we took advantage of this regime to achieve arguably the best kinetic inductance detector NEPs measured at slower observing speeds (i.e. 1 Hz). Altogether, the SuperSpec detector architecture demonstrates many aspects of how to build extremely sensitive detectors for millimeter or submillimeter focal planes.

Chapter 4

SuperSpec Test Results: Filterbank Performance

In the previous chapter, we discussed the performance of the kinetic inductance detectors for the SuperSpec filterbanks. In principle, the filterbank architecture could be implemented using several different types of detector technologies. Thus in this chapter, we discuss the testing results as they pertain to the optical performance of the filterbank which could be generalized to be applicable with any detector type. The optical performance of the SuperSpec devices encompasses the performance of antenna/lens, microstrip feedline, and the spectral mm-wave resonant filters.

4.1 Filterbank Testing Procedure

We measure SuperSpec devices' spectral profile responses using either a coherent local oscillator source or by using a Fourier-transform spectrometer. For the coherent local oscillator source, the spectral profiles were determined by scanning the source across the bandwidth of the filterbank while simultaneously reading out all of the resonators. For the coherent source, a large dynamic range is required to simultaneously read out the spectral channels (large response) and broadband channels (small response described below) at the front and end of the line. In order to accomplish this, a comb of tones spanning 90 kHz (10s of FWHMs) to readout each resonator was used. When utilizing this method if a resonator shifts away from one tone by more than its linewidth it can be read out with the adjacent tone. This is a clever readout technique for KIDs to avoid saturation for large loads. Another

possible implementation would be tone tracking. As a result of using this technique, data for two sets of resonators that were within 90 kHz of each other was not obtained and thus four filterbank channels are not shown in Figure 4.2. SuperSpec devices have several test structures included with each filterbank that allow us to complete different measurements. These test structures are shown in Figure 4.1.

The first of these test structures are broadband detectors located at the front and back of the filterbank. We use these broadband detectors in two ways. The first is to remove the effects of the testbed's filtration when comparing to models. We most commonly normalize the spectral response of the filterbank channels to a broadband detector located at the front of the filterbank. This removes any Fabry-Perot fringing due to multiple reflections for optical components not on the chip itself such as low-pass metal mesh filters. One can also normalize the response of the spectral channels to the broadband detector located at the back of the filterbank to the same effect. This works well for isolated resonators where a significant amount of radiation will still make it to the back broadband detector. However, for a filterbank with an oversampling factor $\Sigma = 2$, only a few percent of the total radiation will make it through the filterbank. This makes the normalization by the back broadband detector a more noisy measurement within a highly over-sampled filterbank. Thus, often this measurement is not used. In the case of isolated resonators not part of a large filterbank, the observed profile of a spectral channel normalized by the broadband detectors probes the internal Qs via the following relatively simple analytic equations. These equations are derived in detail in Hailey-Dunsheath (2015). For an isolated spectral channel normalized by the broadband detector at the front of the filterbank (BB_1), the response is given by the following equation.

$$\frac{SC}{BB_1} = \frac{2(Q_r/Q_c)(1 - Q_r/Q_c - Q_r/Q_{loss})}{\epsilon_1(1 + (Q_r/Q_c)^2)} \left[\frac{1}{1 + (2Q'x)^2} \right]. \quad (4.1)$$

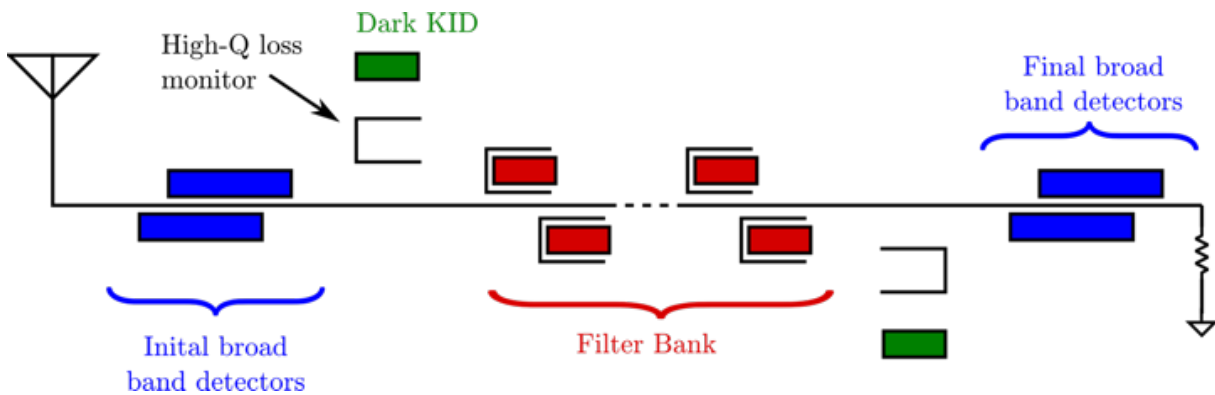


Figure 4.1: Here we show the components of a SuperSpec filterbank. Starting from the left, radiation is received from the on-chip antenna shown here as a triangle. Radiation then propagates down the microstrip feedline where $\sim 0.1\%$ of the light is picked off by frequency independent broadband detectors. Following these detectors, we have both a mm-wave resonator without a detector and a dark detector without a mm-wave resonator. These are located both at the start and end of the filterbank. Following this is the filterbank spectral channels. For the 50 channel test devices, this included 50 closely spaced channels along with 1 channel that is separated in mm-wave frequency from the rest. At the end of the filterbank, we again have frequency independent broadband detectors. Finally, the microstrip feedline is fed into over 20 linear cm of broadband absorbers which completely absorb any remaining radiation that makes it through the filterbank. This is shown as a resistive termination to ground. Figure provided by Dr. Steven Hailey-Dunsheath.

Here x is defined as the fractional frequency detuning away from the resonator center frequency f_0 , $x = \frac{f-f_0}{f_0}$. ϵ_1 and later ϵ_2 are the percentage of power absorbed by the broadband detectors at the front and back of the filterbank respectively. This function is a Lorentzian (the term inside the square brackets) with a Q' defined by the following equation.

$$Q' = \frac{Q_r}{(1 + (\frac{Q_r}{Q_c})^2)^{0.5}}. \quad (4.2)$$

Q_r is given by Equation 2.2. Also, the spectral channel can be normalized by the broadband detector at the back of the line (BB_2). In this case, the profile is given by the function

$$\frac{SC}{BB_2} = \frac{2(Q_r/Q_c)(1 - Q_r/Q_c - Q_r/Q_{loss})}{\epsilon_2(1 - (Q_r/Q_c)(2 - (Q_r/Q_c)))} \left[\frac{1}{1 + (2Q'x)^2} \right]. \quad (4.3)$$

This function is a Lorentzian (the term inside the square brackets) with a Q' defined by the following equation.

$$Q' = \frac{Q_r^2}{[1 - \frac{Q_r}{Q_c}(2 - \frac{Q_r}{Q_c})]} = Q_{diss}. \quad (4.4)$$

Here Q_{diss} is defined as the Q representing the total dissipation in the resonator with $1/Q_{diss} = 1/Q_i + 1/Q_{loss}$. In this way, this measurement directly probes all of the loss in the resonator and for a known Q_{loss} directly yields Q_i .

The second use for the broadband detectors is to normalize the back broadband detector's response by the front broadband detector's response to get a "sock out" measurement. This is effectively a S_{21} measurement and shows the total light that makes it all the way through the filterbank. It is equal to BB_2/BB_1 . This measurement is shown in Figure 4.2 Bottom Left. This measurement provides several useful pieces of information. The first is that the ratio of the power at the front of the filterbank compared to the back of the filter-

bank far away from any spectral channels provides a measurement of the dielectric loss for the microstrip over the distance d that separates these detectors for a given wavelength λ according to the equation

$$\frac{BB_2}{BB_1}(\lambda) = \exp\left(-2\frac{\pi\sqrt{\epsilon_r}}{Q_{loss}\lambda}d\right). \quad (4.5)$$

The second is that it allows for characterizing of another test structure. These are resonant channels that have a high Q_c and no detector ($Q_i = \infty$), High-Q loss monitor Figure 4.1. In addition to the no-KID High-Q loss monitor, two of the spectral channels have a high Q_c and Q_i to act as another loss monitor. For the no-KID resonators, the “sock out” measurement is the only way to measure the power dissipated in them. Both High-Q loss monitor structures act as a separate check on the loss in our dielectric because their total Q is dominated by Q_{loss} as follows:

$$\frac{1}{Q} = \frac{1}{Q_{loss}} + \frac{1}{Q_c} + \frac{1}{Q_i} = \frac{1}{Q_{loss}} + \frac{1}{\gg Q_{loss}} + \frac{1}{\gg Q_{loss}(\infty)} \sim \frac{1}{Q_{loss}}. \quad (4.6)$$

In practice, we fit for both Q_c and Q_{loss} rather than assuming Q_c is negligible. The “sock out” measurement for an isolated mm-wave resonator will have a profile that is defined by the following equation (Hailey-Dunsheath, 2015).

$$\frac{BB_2}{BB_1} = \frac{\epsilon_2}{\epsilon_1} \left(1 - \frac{2Q_r/Q_c}{1 + (Q_r/Q_c)^2} \left[\frac{1}{1 + (2Q'x)^2}\right]\right). \quad (4.7)$$

This is basically 1 minus a Lorentzian (the term inside the square brackets) with an amplitude that is sensitive to (Q_r/Q_c) and with a Q' defined by the following equation.

$$Q' = \frac{Q_r}{(1 + (Q_r/Q_c)^2)^{0.5}}. \quad (4.8)$$

As a quick note, an isolated spectral channel can be fully characterized by this measurement and the depth of this “sock out” measurement can quickly allow you to determine if the resonator is Q_c (deep profile) or Q_i (shallow profile) limited.

The final test structure on the SuperSpec chips is a detector without a resonant filter that is somewhat far away from the feedline, Dark KID in Figure 4.1. These test detectors measure the amount of radiation that is present on the chip but is not coupled to the microstrip feedline, such as stray light that has entered the silicon chip directly, not through the antenna, or radiation that has become decoupled from the microstrip feedline.

4.2 SuperSpec Millimeter-wave Profiles and Model Fitting

The spectral response of the millimeter-wave resonators can be modeled in two ways. The first is by comparing the spectral response to analytical models of the expected response for isolated channels described in the previous section. This works very well for isolated resonances on test devices. However, when many resonators are combined into a filterbank their response becomes too complex to be solved algebraically. This is because as the radiation interacts with each mm-wave resonator there is some amount of reflection and transmission and this reflection and transmission is then reflected and transmitted by all other mm-wave resonators in the filterbank. For this situation, the mm-wave resonators must all be considered simultaneously and the network must be solved in parallel. In order to do this, the spectral response of the mm-wave resonators coupled to the detectors is modeled using an $n+2$ (n is the number of spectral channels) port microwave model. This is implemented using Python’s scikit-rf toolkit and was developed by Dr. George Che (Che, 2018).

I expanded upon this model by wrapping it with Python’s SciPy `curve_fit` function as well as providing some parallelization to the code to provide a fast fitting technique for our measured data. When fitting the data, Q_{loss} for the entire filterbank, a global Q_c and Q_i for all spectral channels and the center frequency of each spectral channel are allowed to

vary. In addition, the Q_c 's and center frequency of each high-Q loss test structure is also allowed to vary. All in all, this totals to a 61 variable fit. However, even with such a large number of variables, the fits end up well-constrained because each spectral channel composes a separate data set sampled at 400 individual frequencies. In addition, most of the variables have little degeneracy with each other, with the exception of Q_i and Q_{loss} for the spectral channel measurements. This degeneracy is broken by the inclusion of the high-Q channels and the “sock out” measurements in the fit. In particular, I simultaneously fit the response of the spectral channels normalized to the response of the broadband detector at the front of the line (Figure 4.2 Top) along with the “sock out” measurement (Figure 4.2 Bottom Left). The fits are shown in Figure 4.2 and the fitted parameters are shown in Table 4.1. Important information from these fits is discussed in the following sections.

4.3 Spectral Profiles

The SuperSpec spectral profile measurements and fits for a 50 channel filterbank prototype are shown in Figure 4.2. In particular, by examining Figure 4.2 Bottom Right we can very clearly see the response of one individual channel from within the filterbank and the fit for that channel. There are a few important things to gather from this data. The first being, far away from the resonator's central frequency we can see a low-level frequency independent response to light. This is not an artifact of measurement noise. It is direct coupling from either the microstrip feedline or from the silicon substrate into the detectors bypassing the mm-wave resonators. This pickup is measured to be at the -30 dB level. We find that this level of direct pickup is perfectly acceptable. This is because in the case that it is radiation from the microwave feedline, at a -30 dB level, a filterbank could contain 1000 individual resonators before 10% of the radiation in the filterbank becomes unwanted out-of-band response. For example, in this situation, the very last channel in a 1000 channel filterbank would have its efficiency in-band reduced by only 10%.

Again looking at Figure 4.2, we can see that the fit does a very good job capturing the

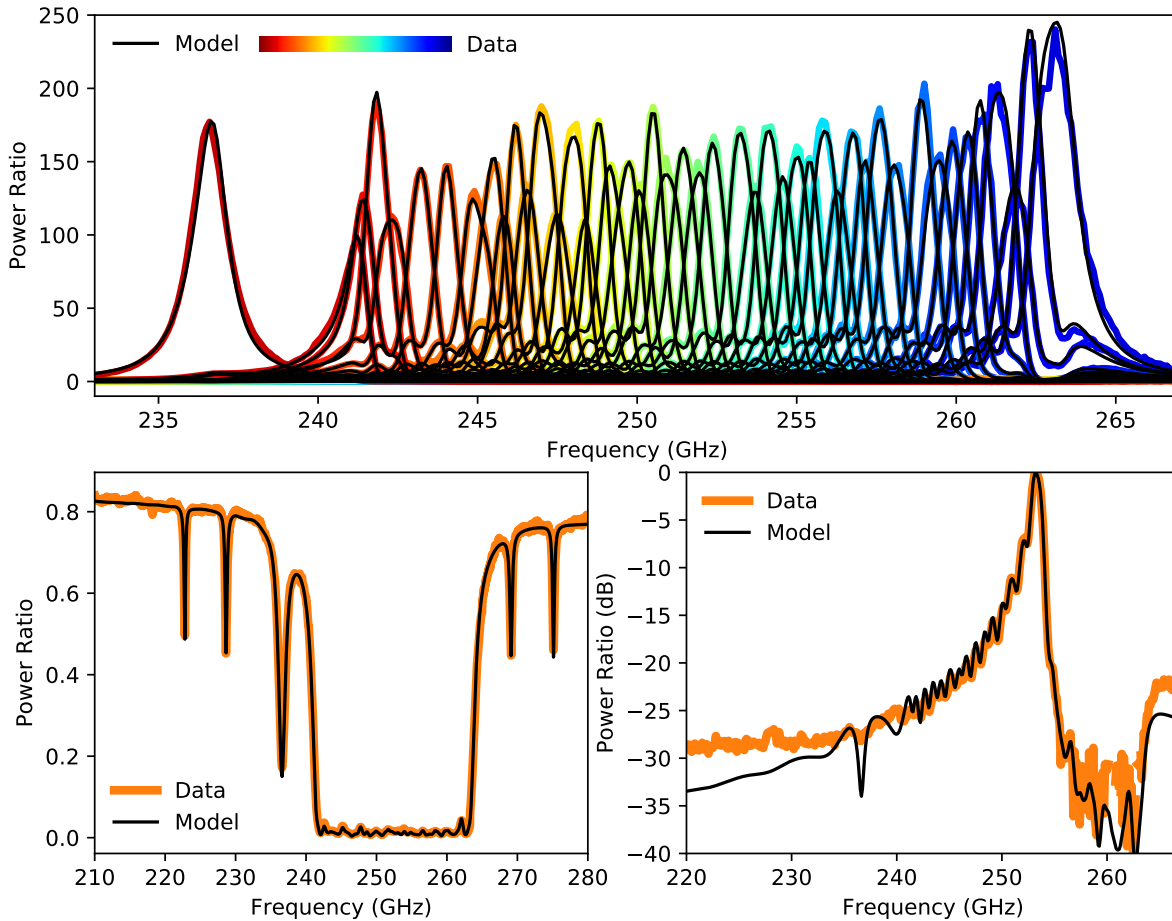


Figure 4.2: Here we show a SuperSpec 50 channel filterbank’s spectral profiles with model fits to the data. Data is shown as colored lines and models as solid black lines. Even though four spectral profiles were omitted from the data provided to the fitter, the fitter is able to fit those channels based on their effect on the surrounding channels. Thus, all 50 channels were fit even though only 46 channels are shown. Top: The response of the spectral channels normalized to the response of a broadband detector at the front of the filterbank. Bottom Left: The response of a broadband detector at the back of the filterbank normalized to a broadband detector at the front of the filterbank (“sock out” measurement). This approximates an S_{21} measurement. Bottom Right: One of the profiles from the top panel plotted in log space.

Table 4.1. Fitted Parameters for SuperSpec Filterbank

Parameter	Value	Range ^a	Designed Value
Spectral Channel Q_c	415	± 1	462
Spectral Channel Q_i	685	± 20	800
Q_{loss}	1260	± 2	–
First No-KID High-Q Channel Q_c	4340	± 20	2000
First High-Q Channel with KID Q_c	3400	± 20	2000
First High-Q Channel with KID Q_i	3500	± 120	2000
Second High-Q Channel with KID Q_c	3600	± 10	2000
Second High-Q Channel with KID Q_i	4500	± 120	2000
Second No-KID High-Q Channel Q_c	4550	± 20	2000
BB coupling strength	0.002	± 0.00002	0.001

^aThe range is a 1σ value calculated from the estimated variance of each parameter determined by a local approximation of the increased cost for varying each parameter near the best-fitted values using errors from measurement uncertainty. In many cases, systematic effects from data acquisition will dominate the true errors on the parameters. The main values of the spectral channels Q_c and Q_i , as well as Q_{loss} , should be accurate to within at least ± 50 .

Note. — Best fit parameters for SuperSpec spectral channel/“sock out” measurement fits. All spectral channels are fitted with a single Q_c and Q_i . The order of the High-Q test structures in this table match their order in ascending frequency. Their profiles are the narrowest four features in Figure 4.2 Bottom Left.

resonator response down to a level of -25 dB on the low-frequency side. The non-smooth profile here in the shoulder of the spectral response is caused by reflection of subsequent filterbank channels after this channel. On the high-frequency side there is a steep drop off in the profile. This is simply because the high-frequency mm-wave resonators are located closer to the front of the filterbank. Therefore, the high-frequency mm-wave resonators before this channel have already absorbed much of that out-of-band (for this channel) response before it reaches this channel. We do notice that the model underestimates the response on this high-frequency side. This is simply because our model has approximated the resonator as a resonator with an impedance that varies with $x = (f - f_0)/f_0$. However, in reality, the impedance doesn't just depend on the detuning from the resonant frequency but has a dependence on the frequency itself. This effect causes an asymmetry from high to low frequency that is observed in realistic electromagnetic simulations using SonnetTM and HFSSTM. However, we find that this resonator approximation is sufficient for our models and fitting procedures.

4.4 Millimeter-Wave Resonator Frequency Scatter

There is some variation in the mm-wave frequencies from their designed values to the values we measure when characterizing our devices. In fact, the variation in peak amplitude from channel to channel seen in Figure 4.2 is actually the effect of slight changes in the mm-wave frequencies of the channels rather than an intrinsic responsivity variation within the detectors themselves. For the mm-wave resonant filters, minimal scatter in frequency is desired so that channels do not overlap or spread apart, opening gaps in the spectral coverage. The fitted values for the center frequency of each mm-wave resonator versus their designed values are shown in Figure 4.3.

A linear function is fit to these data as shown in Figure 4.3 Left. The slope of the fit, 1.05, causes a systematic spreading of the filter channels. However, this 1.05 systematic spreading is a subdominant effect to the random scatter, shown in Figure 4.3 Right. The

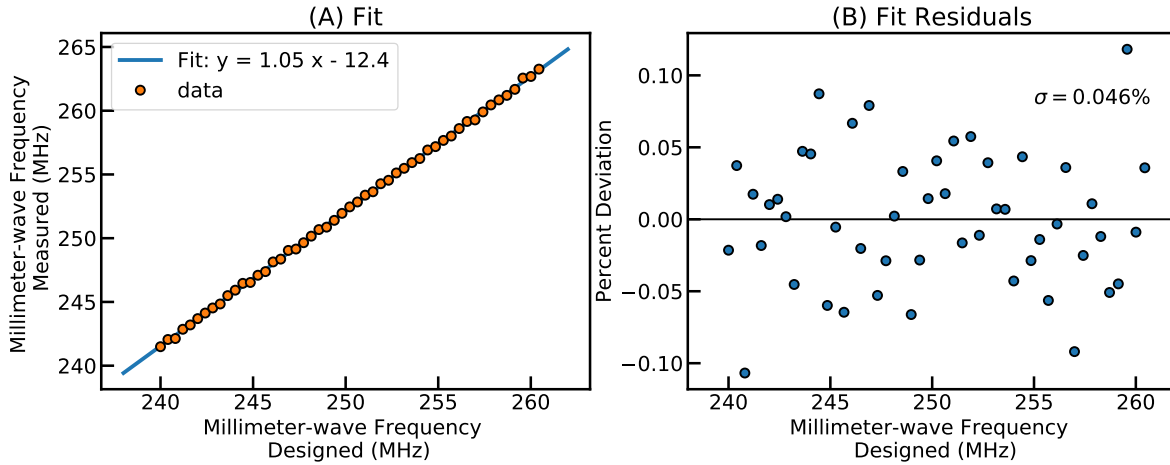


Figure 4.3: Left: Designed mm-wave resonant filter frequencies versus measured mm-wave resonant filter frequencies (circles) with a fit (blue line). Right: Residuals of the fit.

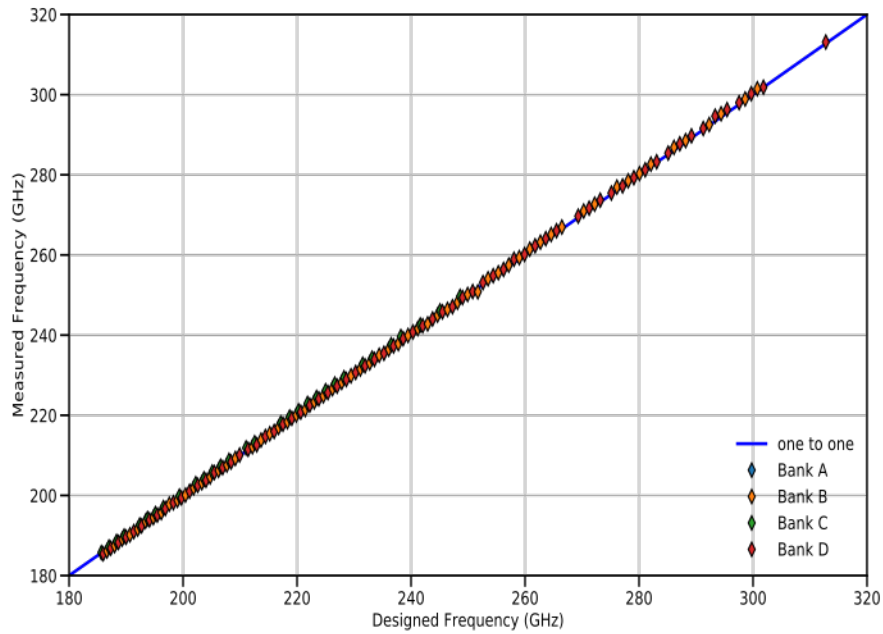


Figure 4.4: Designed mm-wave resonant filter frequencies versus measured mm-wave resonant filter frequencies. In readout space, we separate all of the KIDs into four different banks. The four different banks in readout space are shown as four different symbols. The one-to-one line is shown in blue. Perfect one-to-one mm-wave frequency targeting was achieved for this prototype. Gaps in the data are due to a 60% yield for this prototype that impacted some readout banks more than others.

residual scatter is 0.04% compared to the filter spacing that is 0.17%. This suggests that for a $N \sim 300$ device the mm-wave frequency scatter will have a negligible impact on the spectral coverage. The effect of this scatter on the total NEP of the filterbank is explored in detail in Section 5.1.

The center of the filterbank was shifted by 2 GHz. This means that there is a small systematic shift of the entire filterbank in mm-wave frequency space. An implication of this is that a full filterbank will require additional channels at high and low frequencies so that if there is a systematic shift to higher or lower filter frequencies there will still be complete coverage across the scientific band of interest. In practice, we observed systematic shifts as high as 10 GHz for some test devices but most often of only a few GHz. This is well demonstrated by results for a 300 channel prototype where an exact one-to-one designed versus measured spectral channel targeting was achieved (Figure 4.4).

4.5 Dielectric Loss

Dielectric loss is of paramount concern for on-chip spectrometers. It is the ultimate limiter of the maximum attainable resolution and is an important factor in the total filterbank efficiency. The dielectric loss is extracted from our fitted model shown in Figure 4.2. The dielectric loss can be extracted in several ways. As discussed above we can use the fits to the High Q loss monitor test structures. We can also do this by measuring the power ratio of the broadband channels response far away from the filterbank (i.e. at 210 and 280 GHz in Figure 4.2 Bottom Left). In addition, the loss is measured by a decrease in the response of the spectral channels from the front of the filterbank to the back of the filterbank. For our filterbanks, this is from highest frequency mm-wave spectral channels to the lowest frequency mm-wave spectral channels. All of these aspects are probed and fit simultaneously within the fitting procedure. The result for the dielectric loss for this data set is shown in Table 4.1. Given this measurement and other similar measurements for other test devices, we adopted a slightly conservative value of $Q_{loss} = 1200$ for design optimization of future filterbanks as

discussed in Section 5.1.

4.6 Response

For each test device we measure the response of the detectors by measuring the resonator shift $\Delta f/f$ when exposed to alternating 300 K and 77 K loads. This provides a measure of the total efficiency of the entire system including the filterbank, antenna/lens combination, and testbed filtration. We do this for all SuperSpec test devices and normalize this response to changes in optical coupling and responsivity from different T_c values to keep track of how the total efficiency varies from fabrication run-to-run and cooldown-to-cooldown.

The hot-cold resonator shift as a function of mm-wave resonant frequency for the test device is shown in Figure 4.5. When examining this figure there are a few important takeaways. First, we can see the effect of filterbank order on the hot-cold response in the spectral channels. The first few spectral channels have elevated spectral response compared to the rest of the filterbank channels. This is consistent with the relative amplitude and integral of the spectral channel profiles shown in Figure 4.2. This is expected and is the result of the fact that these spectral channels are the first to see the radiation propagating down the feedline and thus have to share less of this radiation than subsequent channels. In addition, some of the radiation from subsequent channels is reflected back off of them and is then absorbed by these channels. This is why the very first channel has even more response than the isolated channel.

The effect of loss along the filterbank is very clear from looking at the spectral channels response in Figure 4.5. This is seen in the fact that as the mm-wave resonator frequencies decrease, increasing distance along the filterbank, the response decreases due to loss in the microstrip feedline. There is an additional subdominant effect that couples in with this. This effect arises from the fact that lower frequency light, being less energetic, will produce a smaller response than higher frequency light.

The scatter for the spectral channel response in Figure 4.5 matches the scatter in

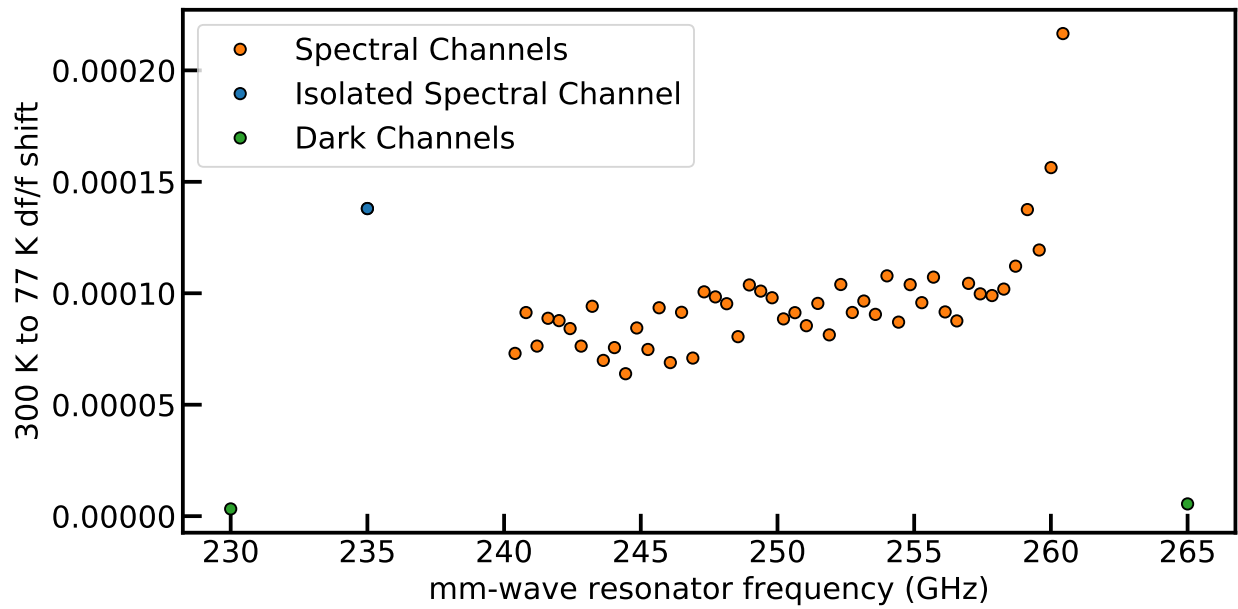


Figure 4.5: Hot-cold response of detectors versus mm-wave resonator frequency for the filterbank shown in Figure 4.2. Note that the highest frequency channels are closest to the antenna along the filterbank. Dark channels shown in blue do not actually have a mm-wave frequency associated with them but have been placed at fiducial frequencies that correspond to their position on the filterbank.

amplitude for the spectral profiles seen in Figure 4.2. This non-uniform response from one channel to the next is not concerning because any astrophysical line is sampled by multiple channels at once so that a non-uniform efficiency between spectral channels does not impact the overall NEP of the entire filterbank. This is discussed in more detail in Section 5.1.

The final thing to note from Figure 4.5 is that the response of the dark channels is 20 times lower than the response of the spectral channels. Thus, we can conclude there is negligible dark pickup when compared to the actual spectral pickup of each channel. In addition, we note that this dark pickup does decrease as you move away from the antenna as seen in the different responses for the two dark detectors.

4.7 Antenna/Lens Performance

SuperSpec uses a lens coupled antenna with a silicon hyper-hemisphere lens. SuperSpec test devices have utilized three different generations of antennas. Before antennas were implemented SuperSpec was horn coupled. The horn coupling scheme required fabrication on SOI wafers. Therefore, in order to enable more rapid prototyping, via reduced fabrication complexity, a lens coupled antenna was adopted. SuperSpec may one day return to horn coupling. In particular, I would like to see a microstrip to finline waveguide transition to enable SuperSpec chips to become end firing devices. This would enable a higher density of spectrometers in a focal plane.

The three SuperSpec antenna types are shown in Figure 4.6. The original dual slot antenna was implemented for early SuperSpec prototypes with smaller bandwidth requirements. The design of such dual-slot antenna's are detailed in Filipovic et al. (1993) and the SuperSpec implementation of this antenna is shown in Figure 4.6 Left. Corwin Shiu extended this antenna design to increase the bandwidth to cover the entire 1 mm atmospheric window by flaring out the slots to produce the first generation dual-bowtie antenna. This antenna had a maximum length of $470 \mu\text{m}$ and the slots are separated by a distance of $180 \mu\text{m}$ with a bowtie flare angle of 34° . The antenna was coupled with a 5 mm diameter hyper-

hemispherical silicon microlens. The design was optimized to work with a 1.25 mm extension length. The dual-bowtie antenna was further refined to increase efficiency and uniformity of the beam across the entire 200-300 GHz band. This optimization was conducted by Maria Alonso of JPL. This antenna also utilized a 5 mm diameter silicon hyper-hemispherical lens but was optimized to work with downstream optics with an extension length of 1.8 mm. This antenna has a maximum length of $400\ \mu\text{m}$ and a flare angle of 46° .

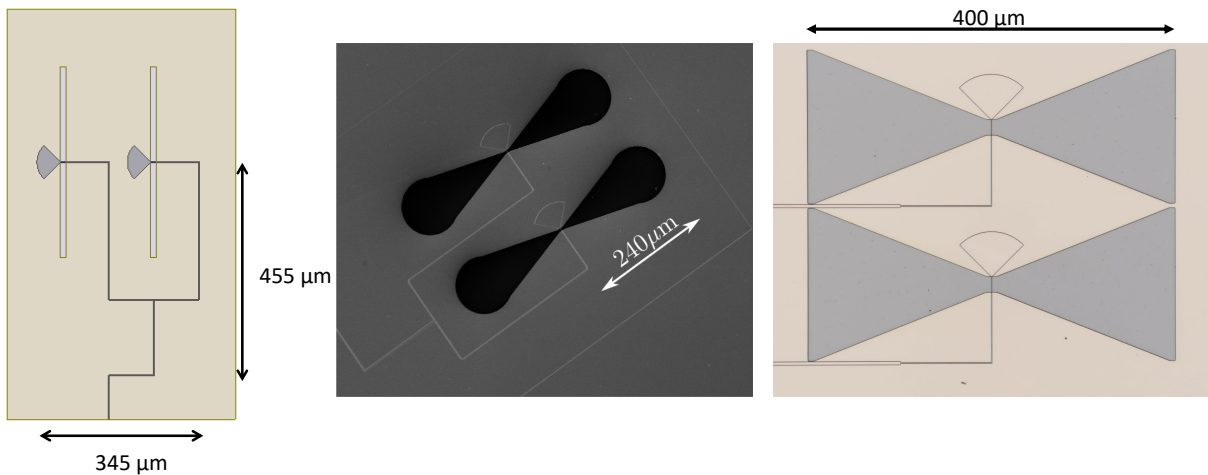


Figure 4.6: The SuperSpec device antennas. Left: Double slot antenna. Middle: First generation dual-bowtie antenna. Right: Second generation dual-bowtie antenna.

4.7.1 First Generation Dual-Bowtie Antenna

In order to characterize the dual-bowtie slot antenna, both the beam and spectral response of the antenna/lens combination were measured. Beam maps for the dual-bowtie antenna were performed by scanning a 77 K cold source that was modulated against a 300 K background with a 1-inch aperture at a distance of 20 inches from the detector. At this distance, the measurements are in the far-field of the lens and the antenna but not the far-field of the limiting filter aperture at the 4 K stage of our testbed. This may cause some low-level beam distortion not captured by the models. The results of the beam maps are shown and compared with HFSSTM models in Figure 4.7. Good agreement between the

measurements and the models was found. The models were run for a single polarization while beam maps were performed with an unpolarized source.

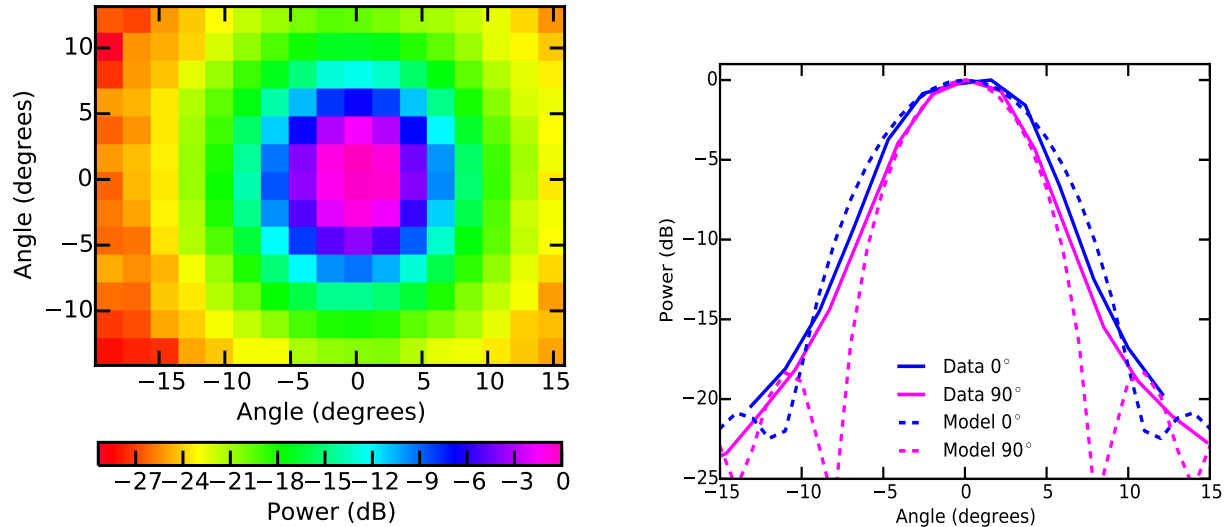


Figure 4.7: Left: Beam map made from coadding all of the spectral channels’ beam responses from a 50 channel SuperSpec test device. Right: Cuts of the beam map are compared with HFSSTM models. The spectral channels have an average frequency of 265 GHz, spanning a range of 20 GHz, and the HFSSTM models were produced for the frequency of 265 GHz.

To determine the relative efficiency across the band, the response of a broadband detector on the feedline before the chip’s spectral channels to a Fourier transform spectrometer was measured. This is compared to the launching efficiency from HFSSTM modeling in Fig 4.8. When the filtering in the testbed is taken into account, good agreement between the measurements and the simulations is found.

4.7.2 Second Generation Dual-Bowtie Antenna

Upon implementation of the second generation dual-bowtie antenna, I performed additional beam maps to confirm its response. These are shown in Figure 4.9. These test results were for a 300 channel filterbank for which we measured a beam map for each of the spectral channels. A few select beams are shown in Figure 4.9 and compared to HFSS simulations. Again, we find good agreement between the measurements and the simulations.

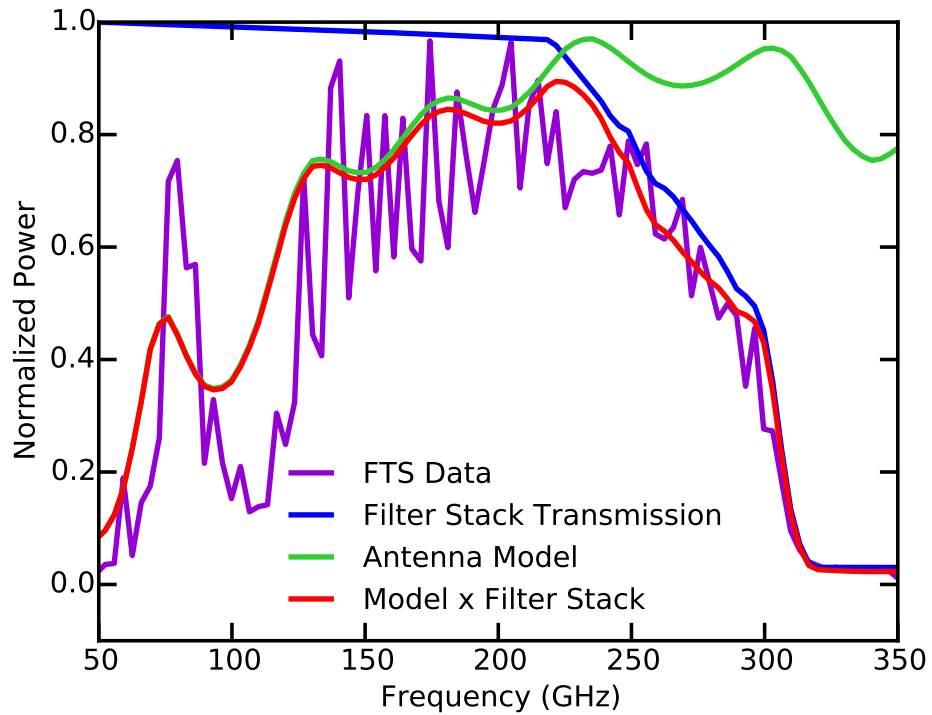


Figure 4.8: Broadband antenna spectral response. Measured power has been normalized. The short-period fringing corresponds to a Fabry-Perot effect with a length scale that is roughly that of the separation between metal mesh filters in the cryostat. Telescope demonstration instrument will have optimized low pass filtering as well as a 185 GHz high pass filter.

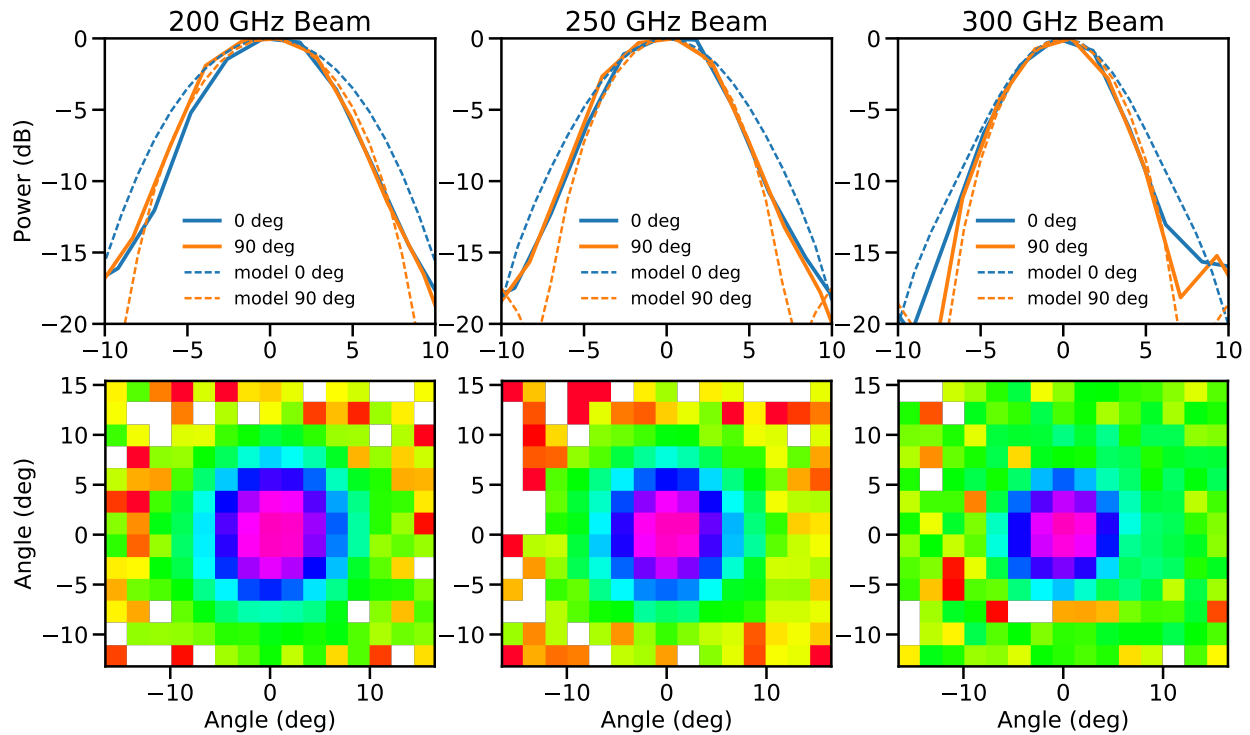


Figure 4.9: Beam maps for the second generation dual-bowtie antenna made from spectral channels' beam responses at 200, 250, and 300 GHz are compared with HFSSTM models. A clear decrease in beam size is seen with increasing frequency.

Chapter 5

SuperSpec Demonstration Instrument

SuperSpec technology is very promising. However, to really build confidence in the viability of this technology, we need to demonstrate the ability of this technology to actually produce meaningful science. In order to accomplish this, the SuperSpec collaboration is working toward a demonstration instrument to show that the SuperSpec technology is as capable as the grating spectrometers that have preceded it. This instrument is designed for single source follow-up of galaxies that have been detected with submillimeter and millimeter imaging instruments but do not yet have spectroscopic measurements. This demonstration instrument will be fielded on the Large Millimeter Telescope outside Puebla, Mexico. Following the scientific success of this instrument, the SuperSpec technology can be extended to more ambitious instruments such as a steerable multi-object spectrometer or an integral-field spectrometer. In this chapter, we discuss how the SuperSpec collaboration has arrived at full scientific spectrometer designs and we discuss the implementation of the full instrument system to house these designs for astronomical observations on the Large Millimeter Telescope. In addition, I present some of the strategies for the identification of potential scientifically interesting targets for this demonstration instrument.

5.1 Design Optimization for a Full Filterbank

Given the measurements detailed in the previous two chapters, the SuperSpec collaboration used our filterbank models to converge on a design for deployment of a pathfinder in-

strument for the Large Millimeter Telescope. The two most important driving factors for our optimization is the detector noise equivalent power, NEP, measured to be $3 \times 10^{-18} \text{W/Hz}^{0.5}$ and our dielectric loss tangent measured to be $Q_{loss} = 1200$. Given these two numbers and the expected photon loading at the Large Millimeter Telescope, we can use the filterbank models channel response to calculate the filterbank performance and achieved NEP for a variety of Q_i , Q_c , and Σ values. In particular, I investigate the optimum filterbank NEP given any choice of Q_i and Q_c incorporating our measured values of Q_{loss} and detector NEP.

The original derivation of this methodology can be found in Hailey-Dunsheath (2016). The NEP of the filterbank is calculated in the following way. First, the power from a partially emissive sky is calculated and then modified by the assumed instrument system efficiency and the frequency dependent channel efficiency from the python filterbank model. The photon noise from this power is used to calculate a frequency dependent NEP for each channel which is then combined with the measured detector NEP to calculate the total frequency dependent NEP for each spectral channel. Since multiple channels simultaneously sample a single astronomical spectral line, the NEP of the entire spectrometer is found by computing a noise weighted average of all of the spectrometer channels, such that

$$\frac{1}{NEP_{sys,net}^2} = \sum_i \frac{1}{NEP_{channel_i}^2}. \quad (5.1)$$

For these models, we assume the system efficiency of the demonstration instrument will be 50%. This includes beam truncation and cryostat filter efficiency. The filterbank efficiency is taken into account separately using the python filterbank models. The photon noise assumed is loading from a 260 K sky temperature and assumed $\tau = 0.1$ for atmospheric optical depth. The results of this modeling are shown in Figure 5.1 and in Figure 5.2.

There are a few important takeaways from this analysis. A higher oversampling means more channels in the filterbank and more of the total light entering the filterbank is absorbed.

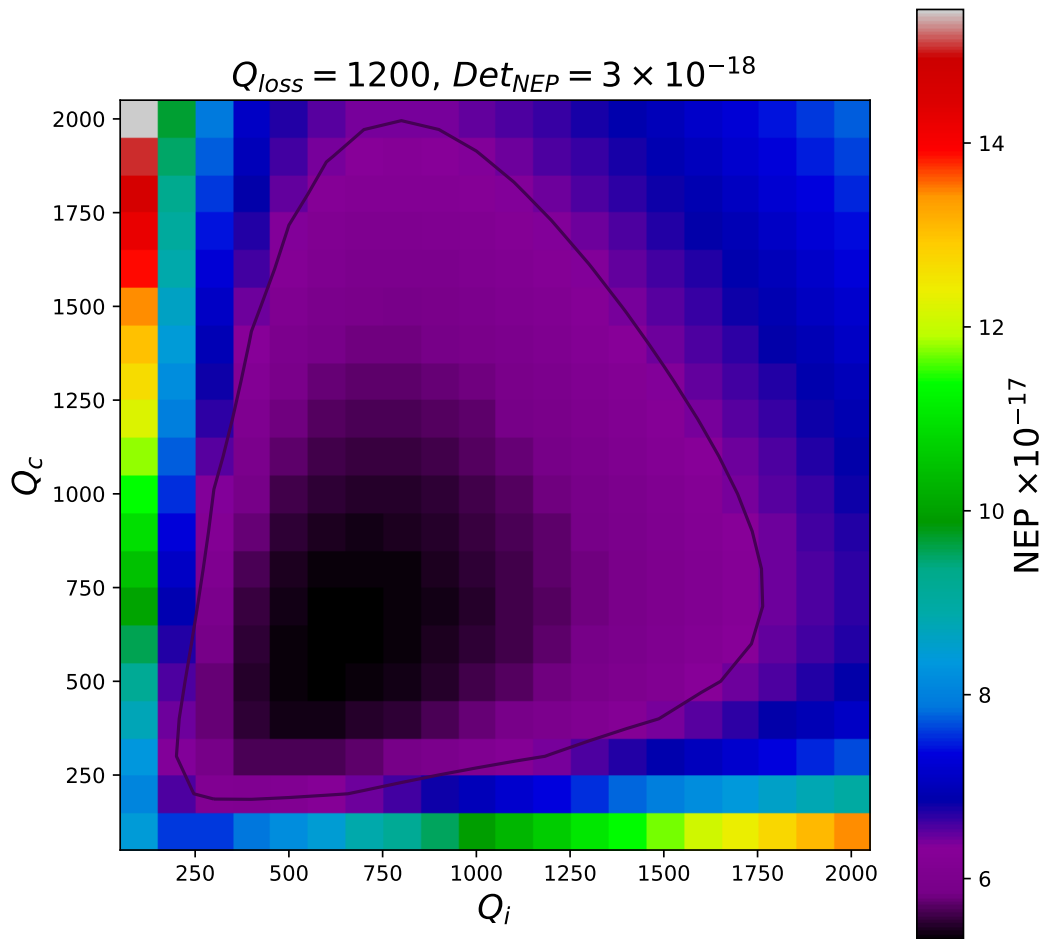


Figure 5.1: NEP achieved for different Q_i and Q_c values given $\Sigma = 2$, $Q_{loss} = 1200$, and detector NEP = 3×10^{-18} W/Hz^{0.5}. The optimum value is $Q_c = Q_i = 700$. The contour shown is for a 20% increase in NEP.

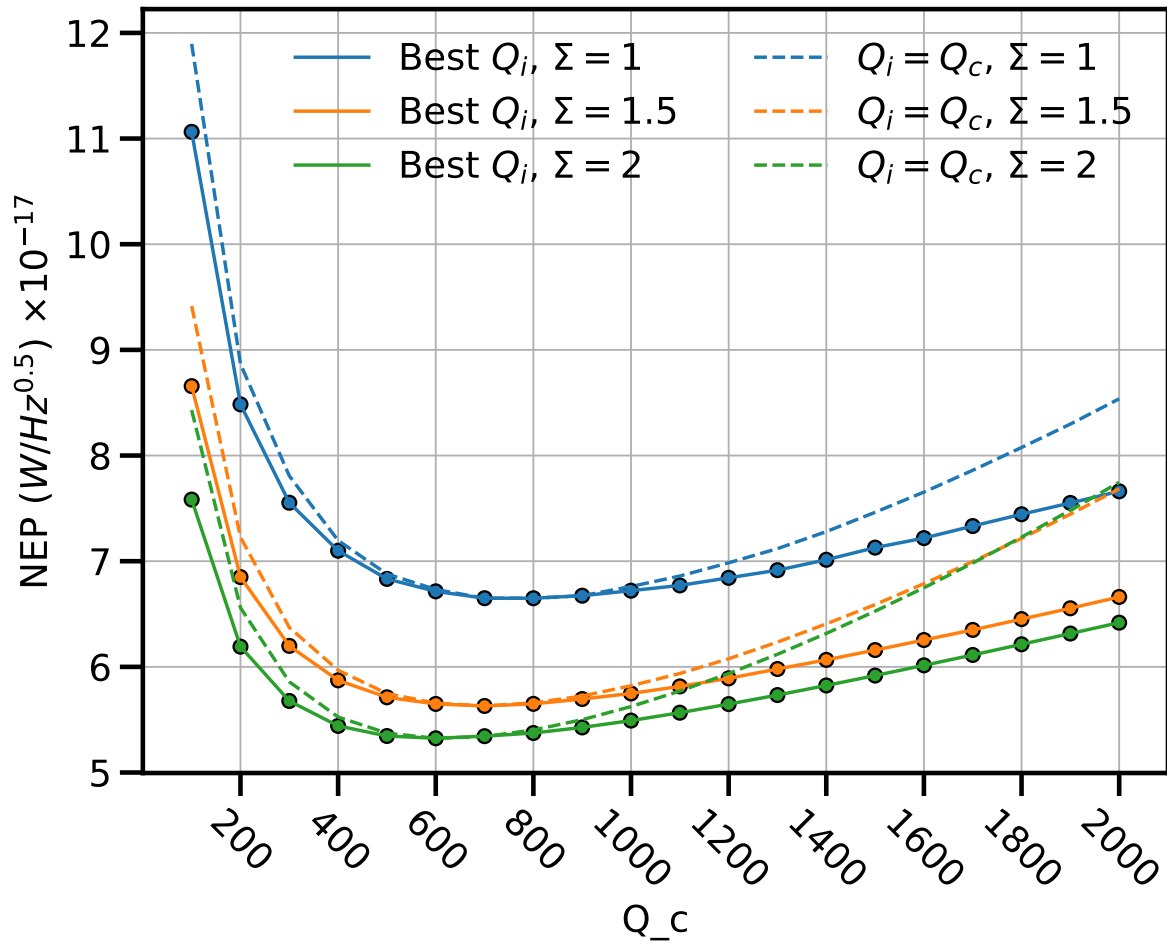


Figure 5.2: NEP as a function of Q_c for both $Q_c = Q_i$ and the best Q_i value given a Q_c choice for different oversampling factors $\Sigma = 1, 1.5, 2$.

This decreases, improves, the NEP up to a point where you pay a penalty for dividing up the power onto too many channels. This effect will be most significant if your detector NEP is not low enough. This is because for more dividing up of the astronomical signal there will be less photon noise per channel making the requirements on the detector NEP stricter. A perfect spectrometer with boxcar spectral channels would thus have the least stringent requirements on detector NEP. In addition, as you increase the oversampling factor you require more detectors. Not only does this cause increased readout complexity because more detectors mean more demand on your readout system in terms of required hardware and noise per channel, but eventually you will also pay a penalty due to loss along a very long filterbank. In practice, we find that increasing the oversampling factor beyond $\Sigma = 2$ pushes the filterbank designs into a regime of diminishing returns.

Next, we examine the shape of each of the curves. We see an increase in NEP at low Q_c , R . This is because as you lower R , more light gets into each channel increasing the photon noise in that channel. At low resolution, the filterbank NEP is dictated by the photon noise from the sky. As you move to higher resolution the NEP also increases. This is due to the dielectric loss as R is increased. The amount of dissipated radiation absorbed by the detector is simply:

$$\epsilon = \frac{1/Q_i}{1/Q_i + 1/Q_{loss}}. \quad (5.2)$$

This means that as Q_i is increased in comparison to Q_{loss} , more and more of the radiation is lost in the dielectric rather than absorbed by the detector hurting the achieved NEP. However, you can gain a little bit of sensitivity back at high resolving powers by tuning Q_i to be slightly less than Q_c (Figure 5.1).

The next important aspect seen in Figure 5.2 is that there is a broad minimum for achieved NEP with respect to Q_c choice in the range of 400 to 1000, $R = 200$ to 500. The

best Q_i in this range is simply $\sim Q_c$. Based on these results, the SuperSpec collaboration arrived at a design targeting a resolution of ~ 300 , $\Sigma = 2$, 300 channel filterbank ($Q_i = Q_c = 700$). The simulation of this filterbank is shown in Figure 5.3 Top and the expected NEP of this filterbank is shown in Figure 5.4.

Inspection of Figure 5.4 might first reveal that the peak power coupled to any individual channel is around 16%. A common misconception would be to assume this means the filterbank efficiency is 16%. Instead, this is the effect of oversampling the filterbank and splitting up the power over many channels. In this case for a reasonably high oversampling factor such as $\Sigma = 2$ (meaning most of the power on the feedline is absorbed) and a reasonably high resolution such as $R = 300$ (meaning the dielectric loss is significant) the filterbank efficiency will be dominantly set by the ratio of power absorbed in the detectors versus dissipated in the dielectric, Equation 5.2. For $Q_i = Q_c = 700$ and $Q_{loss} = 1200$ this factor would be 63%. In addition, increased filterbank efficiency doesn't necessarily make for a more efficient spectrometer as demonstrated in Figure 5.1 and 5.2. So decreasing Q_i won't necessarily result in a more sensitive spectrometer. However, improvements in dielectric loss, i.e. a higher Q_{loss} , would certainly improve filterbank efficiency and spectrometer NEP. As such, an important parallel enabling technology development effort to achieve low-loss dielectrics such as hydrogenated amorphous silicon (a-Si:H) could greatly benefit on-chip spectrometer development.

In Figure 5.3 Top, the model output for an ideal filterbank is shown where each of the mm-wave channels ends up at exactly the frequency at which they were designed. However, it is not expected for this to be the case, it is actually expected to have some scatter in the mm-wave frequency placement of each channel with a $\sigma = 0.046\%$ as measured in Section 4.4. To explore this effect on our 300 channel filterbank design we can add in a random perturbation with $\sigma = 0.046\%$ into the frequency placement of our mm-wave resonators for our model. The result of this is shown in the bottom three panels of Figure 5.3 and the resultant NEP for this simulated filterbank is shown in red in Figure 5.4. We can see from

Figure 5.3 that this scatter does cause significant variations from one channel to the next in terms of channel shape and peak power absorbed. However, upon examination of the NEP of this filterbank in Figure 5.4, we can see that the NEP as a function of frequency is not overly degraded. The mean NEP is the same as it is for the ideal filterbank but the mm-wave scatter does cause some deviations from the ideal filterbank NEP as a function of frequency. These variations do not result in NEP degradation of more than 35% for any given frequency. In addition, 35% is the most extreme deviation rather than the median.

In test devices, we often found that we did not achieve exactly the values of Q_i and Q_c that we designed for (Table 4.1). In addition, we found that this variation changed from fabrication run to fabrication run. Due to this, we did have some concern about how different achieved values of Q_i and Q_c would impact our overall filterbank NEP. In order to examine this, I ran a set of models given our filterbank design to see what effect the variation of the achieved Q_i and Q_c values would have on the NEP performance. This is shown in Figure 5.5. What we find is that even for a Q_i or Q_c variation of a factor of 2 we only pay a 20% NEP penalty. This is because changing your Q's with a set number of channels just permutes how oversampled the channels in the filterbank are. This is a reassuring result that indicates that we do not need to expend additional effort in making sure our fabrication from run to run is extremely consistent.

5.2 Readout Software Development

Kinetic inductance detectors are read out by placing a tone on the resonance and measuring both the change in amplitude and phase of that signal over time. Each resonance requires its own tone, so for large arrays of KIDs, you must have 100s to a 1000 tones on a single readout line. In order to do this, essentially a software defined radio is used to generate and readout many tones at once. These systems consist of a DAC to generate the tones, an ADC to read in the tones after they have gone through the detector arrays, and a FPGA board to process the raw wave-forms of the many simultaneous tones into magnitude and

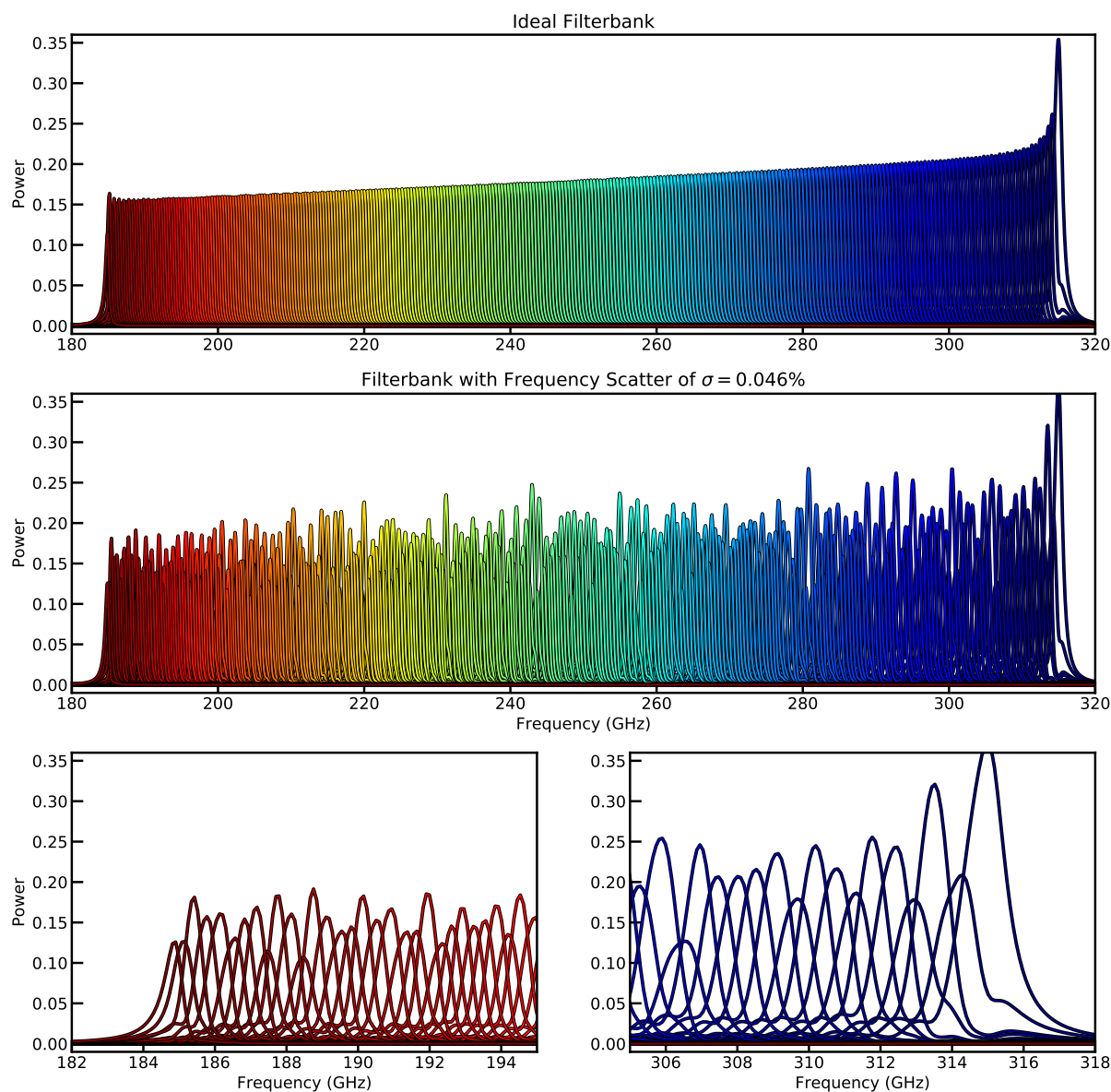


Figure 5.3: The spectral profiles for a $R = 300$, $\Sigma = 2$, 300 channel filterbank design. Y-axis units are the percentage of power that is absorbed by each detector referenced to the power present at the beginning of the filterbank. Top: An ideal filterbank in which every resonator has the optimally designed frequency. Middle: A more realistic filterbank with a scatter in the mm-wave frequencies of $\sigma = 0.046\%$, as measured in Figure 4.3. Bottom: Subsets of the middle panel at the high and low frequency ends.

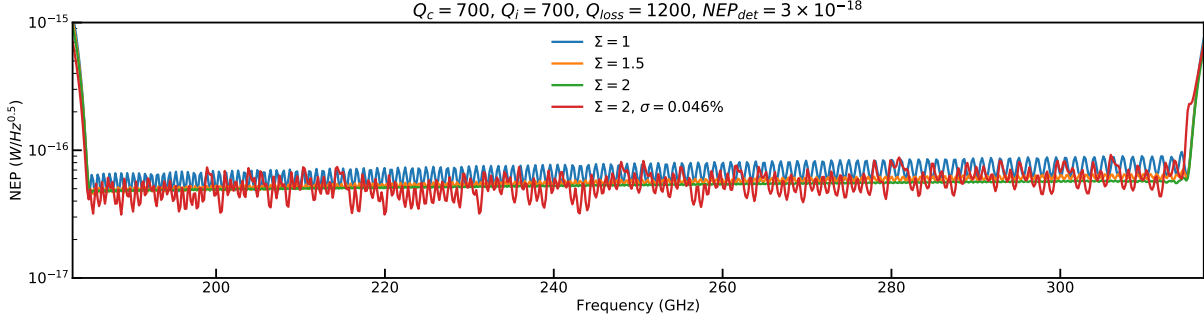


Figure 5.4: NEP as a function of frequency for several oversampling factors Σ . The $\Sigma = 2$ curves correspond to the filterbanks shown in Figure 5.3 Top and Middle.

phase values. In addition, this base readout system is often coupled with RF modulators and demodulators to mix up the signal coming from the DAC and then later downconvert the signal to be received by the ADC to enable readout of higher frequencies as required for many detector architectures. This readout circuit is shown in Figure 5.6. This is a gross oversimplification of a complex and intricate process that composes building a readout system, for more information see Sam Gordon’s thesis (Gordon, 2019).

I have personally used three different multitone readout systems over the course of my graduate career (Duan et al., 2010; Swenson et al., 2012; Gordon et al., 2016) to read out thousands of different resonators. As such I have gained some experience in understanding useful aspects of multitone software for reading out KIDs that makes me uniquely suited to build software improvements for KID readout.

There are two SuperSpec readout development efforts taking place to enable the deployment of a SuperSpec demonstration instrument at the Large Millimeter Telescope. One is to develop a system capable of synchronizing with the telescope while simultaneously reading out 6 individual multitone systems. The second effort for which I have made contributions, is software development for a single readout system that optimizes the experience of acquiring data for test devices in the lab. While much of the same software can be utilized for a deployment grade system, lab software must be highly flexible to be applicable in many different situations as new test devices are produced. Whereas, deployment software

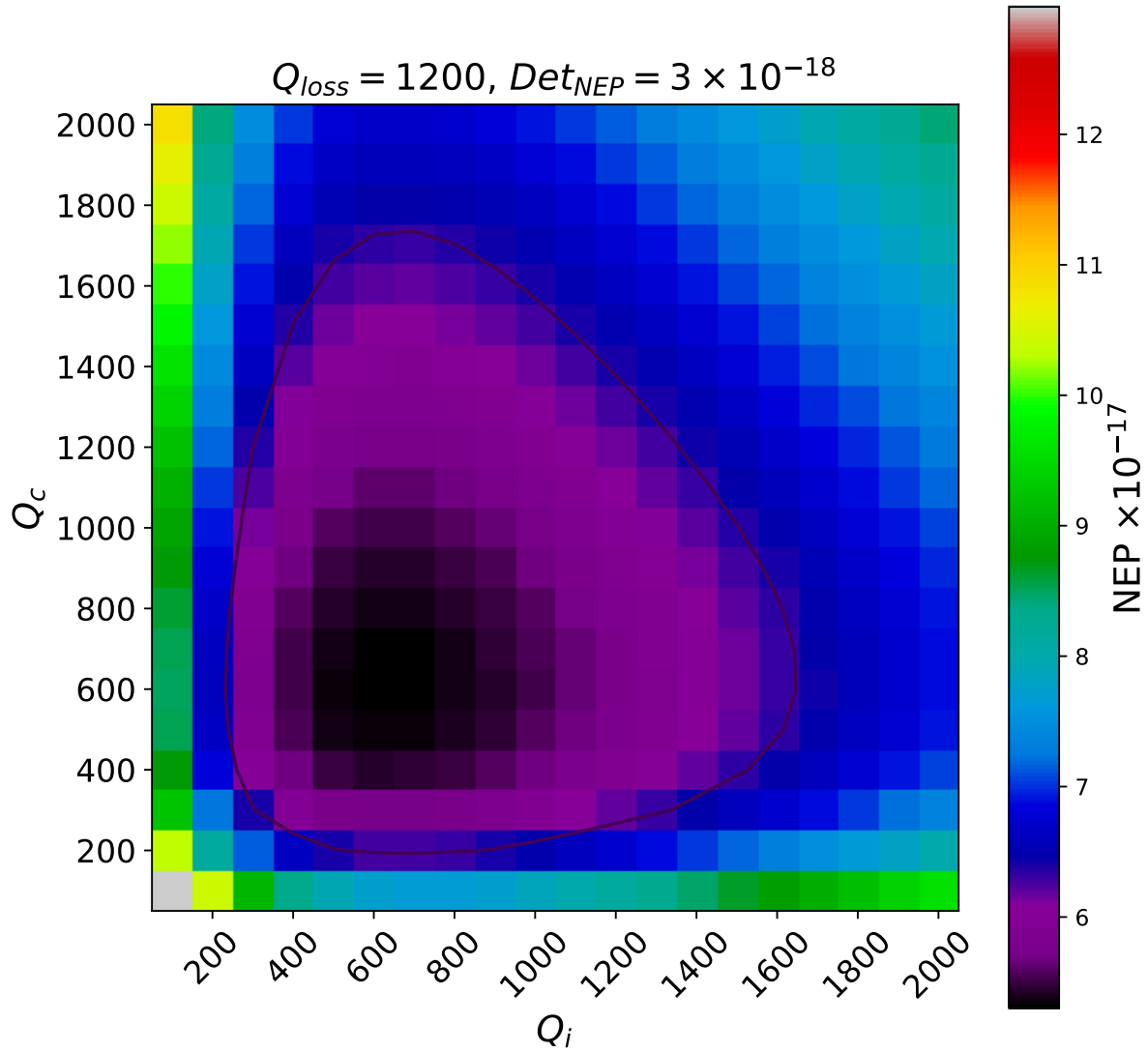


Figure 5.5: NEP achieved if Q_i and Q_c vary in fabrication. The optimum value is about $Q_c = Q_i = 700$, The contour shown is for a 20% increase in NEP.

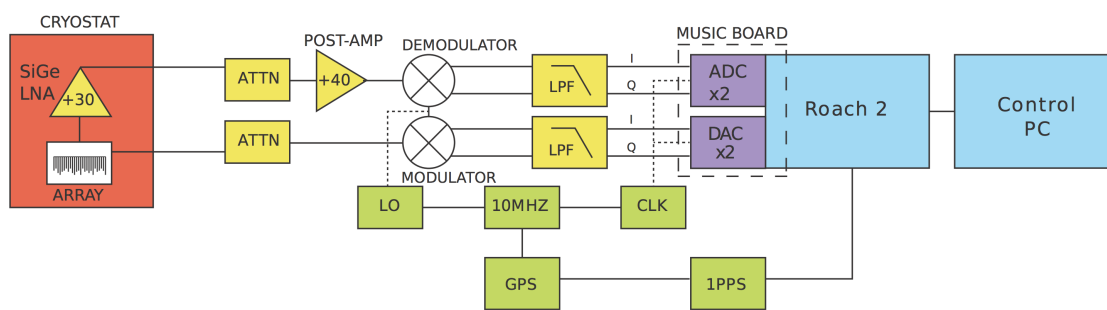


Figure 5.6: Schematic of the readout circuit. Starting with the DAC, a comb of tones is generated corresponding to the downshifted resonant frequencies of the kinetic inductance detectors in the range of -250 to 250 MHz. To cut down on higher frequency aliasing this comb is then fed through 250 MHz low pass filters. Then the baseband comb of tones is mixed up using a modulator to the true frequencies of the detectors. This signal is then attenuated to the appropriate power desired by the detectors and fed through the detector array. At cryogenic temperatures, the signal is then amplified by a low noise amplifier. Some attenuation can then be used to reduce the effects of reflection in between components, but as little as possible is best as to not reduce the signal to noise of the probe tones. Additional amplification is then used at room temperature to achieve the desired power levels for the ADC. The signal is then demodulated back to I and Q signals at frequencies between -250 and 250 MHz and again filtered. This signal is then received by the ADC and digitized. The digitized signal is then processed by the Roach 2 FPGA board to provide I and Q for each of the desired frequencies at some specific sample rate. In addition, at the telescope, synchronization between the telescope and readout system is achieved via a clock signal from a GPS and both a 1 pulse per second (1PPS) and 10 MHz reference signal. Often lab measurements may or may not use these additional systems. Additional filtering in the high-frequency part of the readout chain is also encouraged. Figure from Gordon et al. (2016).

should be streamlined to rely on the previous characterization of arrays and benefit from the repeatability of array parameters from night to night. Such a system could, for instance, rely heavily on look-up tables determined from previous lab characterization.

The software additions I present here benefit from the hard work that created the kidPy software and most importantly the multitone firmware that was developed by Sam Gordon, a graduate student at Arizona State University (Gordon, 2019). Most of the advanced software created is necessitated by the nature of building software for a spectrometer as well as my own obsessiveness. An imaging experiment may be able to accept neglecting to properly readout 20% of their detectors and just take a 20% penalty in mapping speed, but for a spectrometer every resonator is precious. If too many adjacent spectral channels are missing, a gap in spectral coverage will open up and one won't just pay a mapping speed penalty but might completely miss a high-redshift galaxy. At the same time, the software must be efficient so that it doesn't take weeks to characterize a single spectrometer. This aspect was probably driven by the nature of my NSTRF fellowship where I would travel to location for one week at a time and in that short amount of time try to extract every single measurable quantity from a SuperSpec device before returning to Colorado.

5.2.1 KID Resonance Location

Current KID arrays have 100s to 1000 detectors on a single wafer read out using a single input and output microwave line. Given this large number of resonances, users don't want to find each and every resonance by inspection and thus an automated procedure is required. This procedure was developed by Sam Gordon. It takes an effective vector network analyzer (VNA) sweep carried out by the multitone system and uses a filter in Fourier space to remove slow variations in gain across the readout bandwidth. It then detects resonant dips in magnitude space that are below a preset threshold.

I expanded on this procedure to add a user interface to the plot. This includes letting the user change the threshold value and instantly updating the plot so the user can see

real-time what will and will not be flagged as a resonator. Following the automated flagging of resonators, the user will be provided with an interactive plot of the VNA sweep with all of the found resonators shown including a displayed index. The user can then utilize this interactive plot to update the resonator list in real-time by either adding new resonances or deleting resonators that were flagged but should not be included in the resonator list. This interactive program allows for a user to correctly and exhaustively identify all of the hundreds of resonators in a matter of only minutes. The idea of this software upgrade is relatively simple but the increase in efficiency for using KID arrays is substantial.

Likewise, to when finding resonances, it is often necessary to retune the frequencies of the tones used to readout the resonators as they change frequency with changing loading or array temperature. When retuning tones there are two natural choices for how to tune the resonators. The first is simply to tune the tones to be on the minimum of the magnitude plot of each resonator. This is good for taking frequency sweeps to characterize the resonances. The second is to retune the tones to be at the frequency where there is the greatest distance in IQ space between adjacent frequency points. This maximizes the change in signal in IQ space for a given change in frequency for a resonator. This helps maximize S/N in situations where amplifier or any kind of isotropic noise in IQ space is significant. This should be the default when taking any kind of streaming data such as astrophysical observations.

Given a calibration sweep, it is relatively straight forward to find the minimum in magnitude space or the maximum in IQ space. Complications mostly only arise for very closely spaced resonators/collided resonators when there are multiple minimums or maximums for a single calibrations sweep because the sweep contains two resonances. To aid in these situations I implemented a tuning function with several aspects. The first is that the function allows the user to specify how far to look around the old tone frequencies. Thus the user can try to find an optimum frequency range to search for a min or max while not increasing the range so much that it falls on adjacent resonators. In addition, the tuning function can be implemented in an interactive mode that allows the user to quickly scan through a plot for

each resonator observing the automated chosen frequencies and allows the user to override the automated choice by clicking on the plot.

This function also aids in the reading out of collided resonators. This could be by allowing the user to cleverly place a single tone right between two resonances to readout both resonators at once via cross talk. Alternatively, the user can place two tones on two closely spaced resonators in a way that minimizes the contribution of cross talk but is still sensitive to the frequency shifts of each of the individual resonators. For example, the user could choose to put one tone in the high-frequency wing of the higher frequency resonator and another tone in the low-frequency wing of the lower frequency resonator. I have regularly utilized this software to readout collided resonators. In fact, I have read out collided resonators to determine their mm-wave spectral frequencies so that each resonator in readout space can be identified to the physical resonator on the chip as designed. Then using this information, the SuperSpec collaboration led by Chicago has post-processed the capacitors of the KIDs to change their resonant frequencies to fix the collisions. The ability to do this characterization depends on having flexible lab software.

5.2.2 Tone Power Optimization

One of the most important aspects of using a KID array in the lab or at the telescope is proper optimization of the tone powers used to readout resonators. For KIDs, often you want to operate them at the maximum readout power allowable or close to it. This can be either to maximize clearance over amplifier noise or to saturate TLS noise (Gao et al., 2008). The maximum drive power for a KID is determined by when the KID becomes substantially non-linear, characterized by non-linearity parameter $a = 0.77$. This non-linearity occurs because the kinetic inductance increases with increasing readout current in the circuit. The increased kinetic inductance will then detune the resonator to lower frequencies. This effect is demonstrated in Figure 5.7 and the formalism for analytically describing this effect is derived in Swenson et al. (2013); Zmuidzinas (2012).

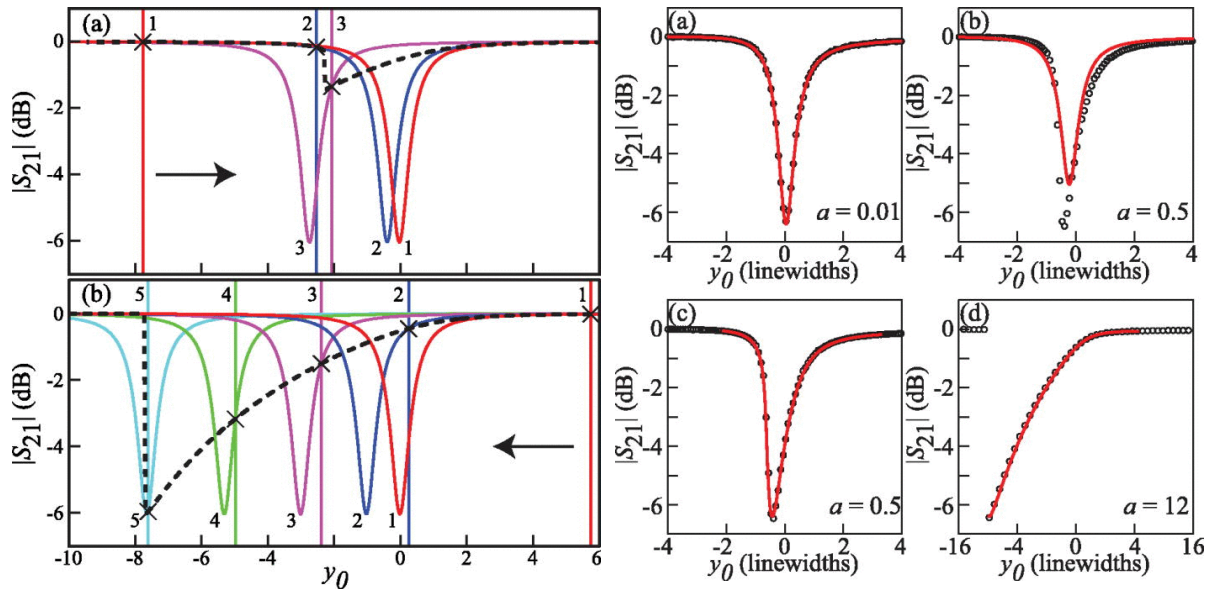


Figure 5.7: Demonstration of non-linearity with readout power in kinetic inductance detectors. Left: Depiction of non-linearity with readout power for resonators operated at a non-linearity parameter $a > 0.77$. In each case, the readout tones at different frequencies are shown as X's and the position of the resonator for each readout tone are correspondingly numbered. Top Left: The dashed black line shows the measured resonator profile when completing a frequency sweep from low to high frequency. At position 1, the resonator is not perturbed by the readout tone. As the tone is swept closer to the resonator, the amount of power dissipated in the resonator increases. This then increases the kinetic inductance and decreases the readout frequency. This is demonstrated as the tone is moved to position 2. As the tone approaches the point of maximum absorption, the resonator very quickly moves to lower frequencies causing a quick (in frequency space) “snap” of the resonator to lower frequencies as the tone is varied from position 2 to 3. Bottom Left: The dashed black line shows the measured resonator profile when completing a frequency sweep from high to low frequency. In this case, as the tone is swept to lower frequencies, more energy is absorbed, and the resonator is also pushed to lower frequencies. This continues until the tone passes the maximum absorption point of the resonator where the power absorbed starts to decrease. This then causes the resonator to rapidly increase in frequency sending the resonator back toward position 1. Right: The result of frequency sweeps for different non-linearity parameters. (a) Low readout power will result in almost no perturbation of the resonant frequency. (b) At higher non-linearity parameter, $a = 0.5$, the resonator cannot be fit well without introducing the non-linearity term. (c) Demonstration of fitting in the case where the non-linearity is accounted for. (d) When the non-linearity parameter a is greater than 0.77 the frequency sweep exhibits discontinuous jumps. SuperSpec kinetic inductance detectors are only operated at non-linearity parameters less than 0.77. Figures from (Swenson et al., 2013).

In order to determine the optimal power at which to operate each individual KID, we conduct a power sweep with a digital attenuator to measure the KID resonances for a range of different power levels. At each power level, we fit the resonator and determine the non-linearity parameter a . We fit the resonators both in magnitude space and IQ space. For magnitude space, we use the following formula from Siegel (2016).

$$|S_{21}|^2 = (b_0 + b_1 x) \left(1 - \frac{Ae^{j\phi}}{1 + 2jy} + \frac{A(e^{j\phi} - 1)}{2} \right)^2. \quad (5.3)$$

Here $A = Q_r/Q_c$, b_0 and b_1 are normalization factors describing the gain of the system off resonance, ϕ represents a rotation of the IQ loop caused by extra inductance in the readout circuit, and y is the non-linearity of the resonator detuning with readout power described by the equation:

$$Q_r x = y + \frac{a}{1 + y^2}. \quad (5.4)$$

In this equation, x is the fractional detuning of the resonator $x = \frac{f-f_0}{f_0}$. The roots of the above equation are solved for numerically. In IQ space we use the following equation to fit the resonances.

$$z_{res} = (I_0 + jQ_0)e^{-j2\pi(f-f_0)\tau} \left(1 - \frac{Ae^{j\phi}}{1 + 2jy} + \frac{A(e^{j\phi} - 1)}{2} \right)^2. \quad (5.5)$$

Again, y is given by Equation 5.4, $A = Q_r/Q_c$, I_0 and Q_0 are normalization factors describing the gain of the system off resonance, ϕ represents a rotation of the IQ loop caused by extra inductance in the readout circuit, and τ is a phase shift with frequency caused by cable delay from unequal coax lengths when mixing the signal with the reference signal.

We fit in both magnitude and IQ space because in different situations the different

types of fits are less or more likely to be successful. For the magnitude fit, there are 7 free parameters and the IQ fit has 8 free parameters. Since there are so many free parameters we use a steepest descent method for fitting rather than a more robust brute force or Monte-Carlo methodology. At the same time to improve the fitting success and to avoid becoming trapped in a local minimum during optimization, I developed a smart initial value guessing program. The result of this is successful fits for isolated resonators over a large range of different variable conditions > 90% of the time.

Once the resonances are fitted at all power levels, we solve for the power at which the non-linearity parameter is a specific value such as 0.5. This is shown in the bottom plot of Figure 5.8. We again use an interactive plotting program that allows the user to see the automated power choice corresponding to a specific non-linearity parameter. At the same time, the user can use this program to flip through all of the resonators and power levels. The user can then decide to override the power choice for a given resonator. This is imperative for if the fitting has failed which will often be the case if there are for instance two close resonances that have collided in readout space. Following the users' acceptance of the chosen power levels, this program will produce a digital transfer function that can be loaded into the multitone readout system to change all of the tone powers.

Once this transfer function is loaded into the multitone readout system all of the resonators will have the same non-linearity parameter for a given digital attenuator power setting. Thus, all of the resonators will be optimized to be read out at their maximum, or close to it, allowed readout power for specific digital attenuator power level. As demonstrated in Figure 5.9 there can be large variations in the ideal tone power from one tone to the next. In this case, if the tone powers were not normalized properly there would be many resonators whose noise would be completely dominated by amplifier noise. On the telescope, this would result in many resonators for which no science quality data could be produced.

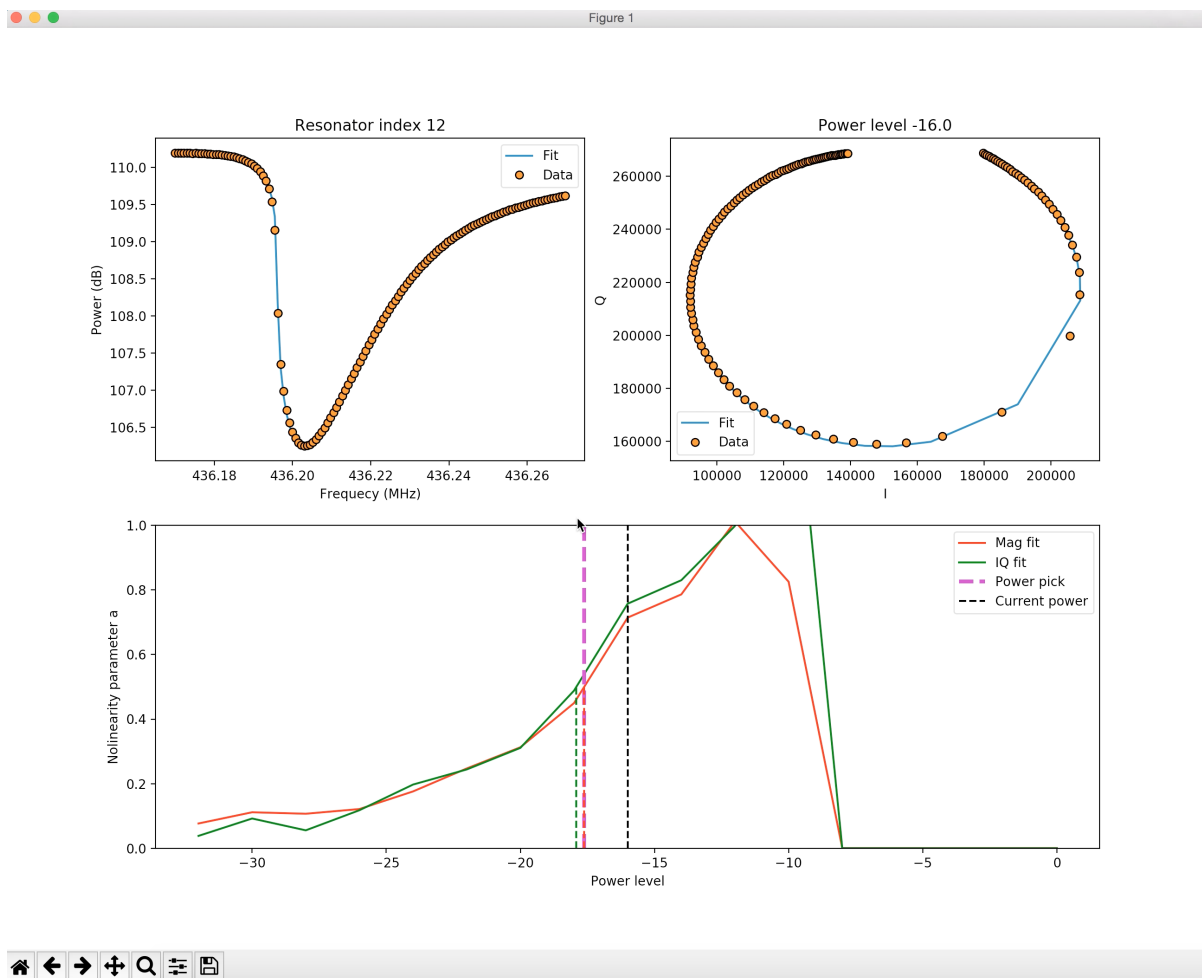


Figure 5.8: Interactive power tuning software for tone power optimization. For the current power level shown (power level indicated by the dashed black line on the bottom plot) in this figure, the resonator (top panels) is at a non-linearity parameter $a \sim 0.77$, right where it becomes non-linear and cannot be read out properly. The bottom panel plots the fitted non-linearity parameters as a function of the digital attenuator power setting (red and green lines). The automated fitting picked a power of -17.5 dB to achieve a non-linearity parameter of 0.5 (purple dashed line).

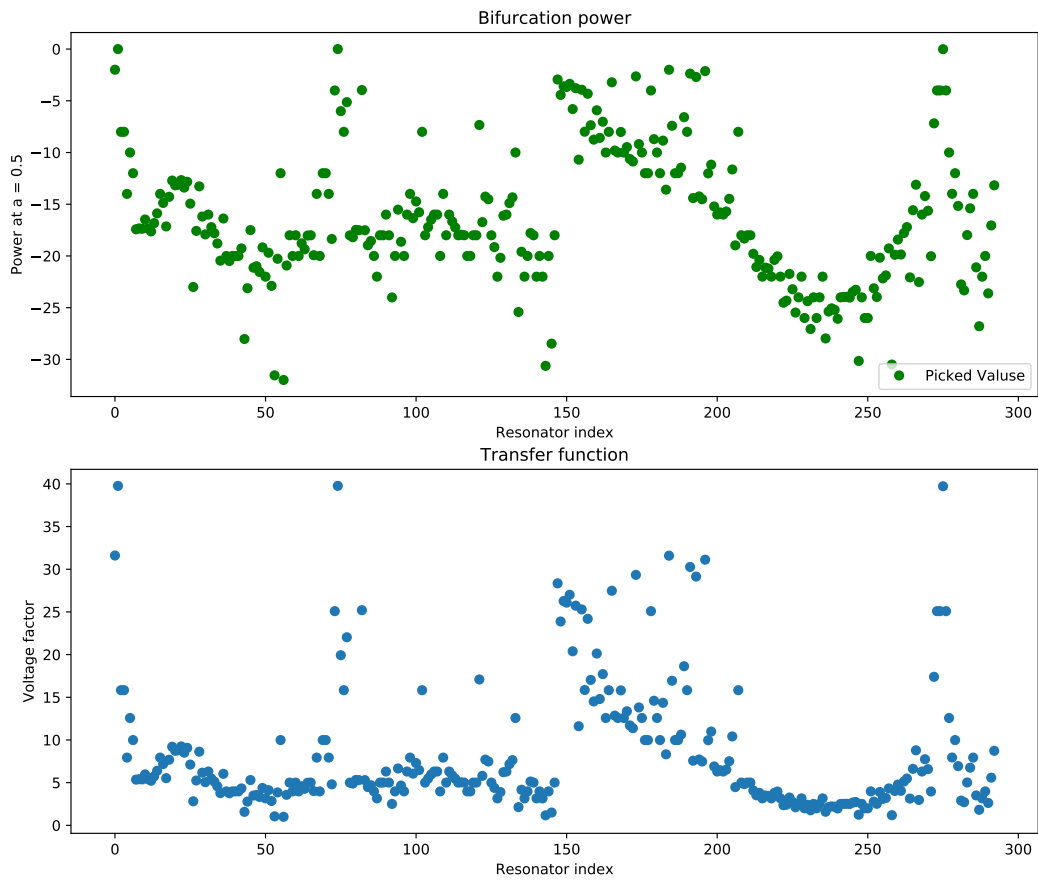


Figure 5.9: Interactive power tuning software output. Top: The digital attenuator power level at which each resonator had a non-linearity parameter $a = 0.5$ as determined by the interactive power fitting software from Figure 5.8. Bottom: A digital transfer function for the multitone DAC to weight each resonator tone to increase or decrease each tones' power relative to the other tones. Following this optimization, all resonators will simultaneously have approximately the same non-linearity parameter for any given digital attenuator power level.

5.3 SuperSpec on the Large Millimeter Telescope

The Large Millimeter Telescope (LMT) is a 50 m in size millimeter and submillimeter telescope on top of the extinct volcano Sierra Negra outside of Puebla, Mexico. At an altitude of 15,030 feet, the LMT has quality of observing conditions on par with that of other submillimeter sites such as Mauna Kea in Hawaii and the Atacama in Chile. The LMT has been completing science observations since 2014 and has recently upgraded from utilizing only the central 32 m of the telescope to utilizing the entire 50 m of available real estate for the primary dish. This makes the LMT the largest such single dish telescope for these wavebands, and as a result, the LMT is quite sensitive.

SuperSpec has spent the last year preparing for a telescope demonstration instrument run. This demonstration instrument will consist of 6 spectrometer chips making up three total on-sky pixels each with two polarizations, Figure 5.10. SuperSpec will follow-up point source observations made by imaging cameras. To modulate the detectors at speeds above the $1/f$ noise, SuperSpec will chop on and off source between the three pixels always keeping one pixel on-source. The third pixel will aid in the modeling and removal of atmospheric variations.

The effort to prepare for this telescope run has included designing optics to interface with the LMT (Figure 5.11), developing readout software (discussed in the above section), and upgrading the SuperSpec lab testbed into a 6-chip spectrometer instrument. Caltech graduate student Joseph Redford and I were the primary responsible party for updating the testbed hardware. In particular, I was responsible for designing new shield extensions as well as the hardware to hold optical components at cryostat stage temperatures of 1 K and above. In addition, I was responsible for the upgrade of the cold microwave readout to increase the cryostat throughput to handle additional input and output lines to accommodate 6 different readout lines at once.

We extended the length of the Caltech testbed to accommodate additional optics and

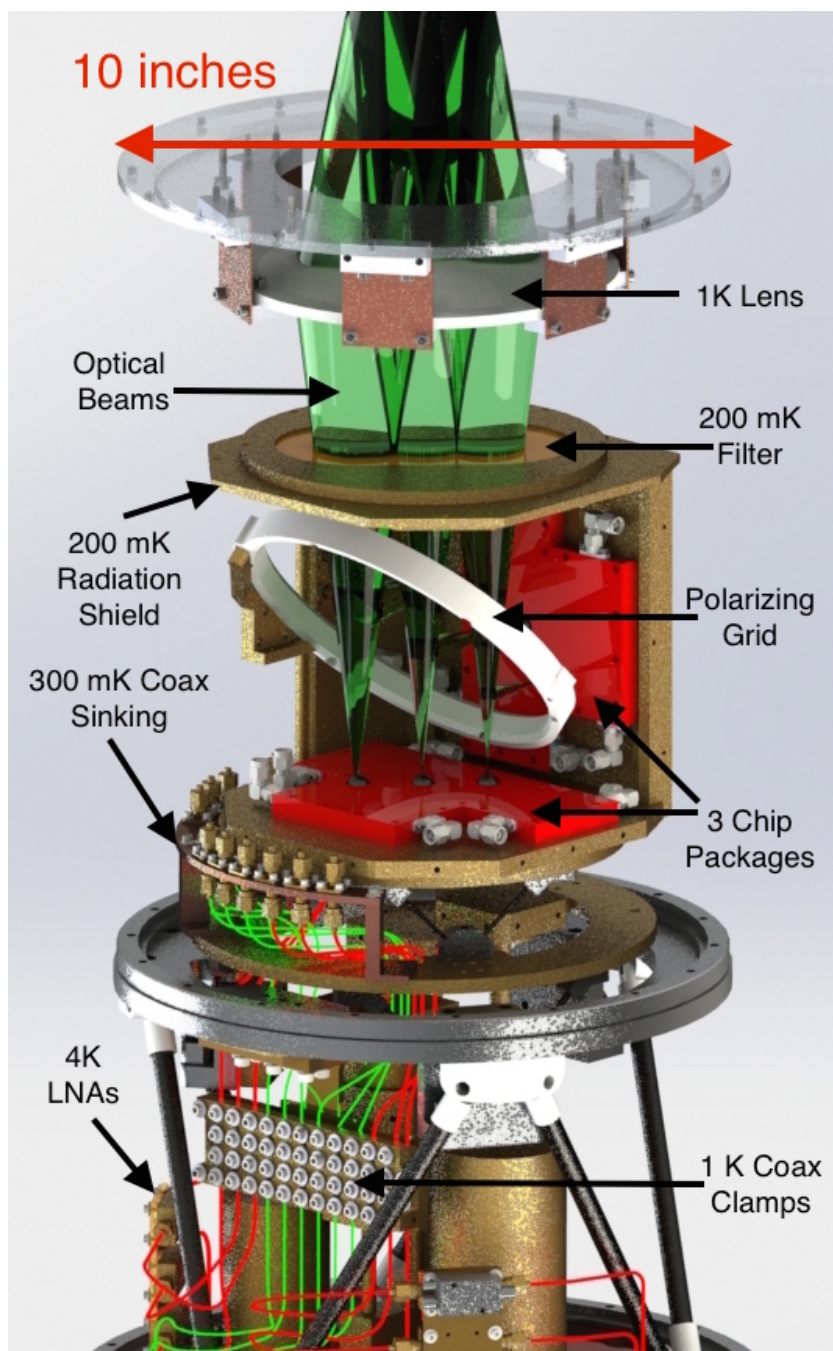


Figure 5.10: CAD rendering of the SuperSpec demonstration instrument focal plane. There are 6 SuperSpec spectrometers, 3 mounted horizontally and 3 mounted vertically, to form 3 on-sky pixels with two polarizations each. Polarizations are divided by a polarizing grid for which the frame is shown in white. Beams pass through a HDPE lens at 1 K, also white.

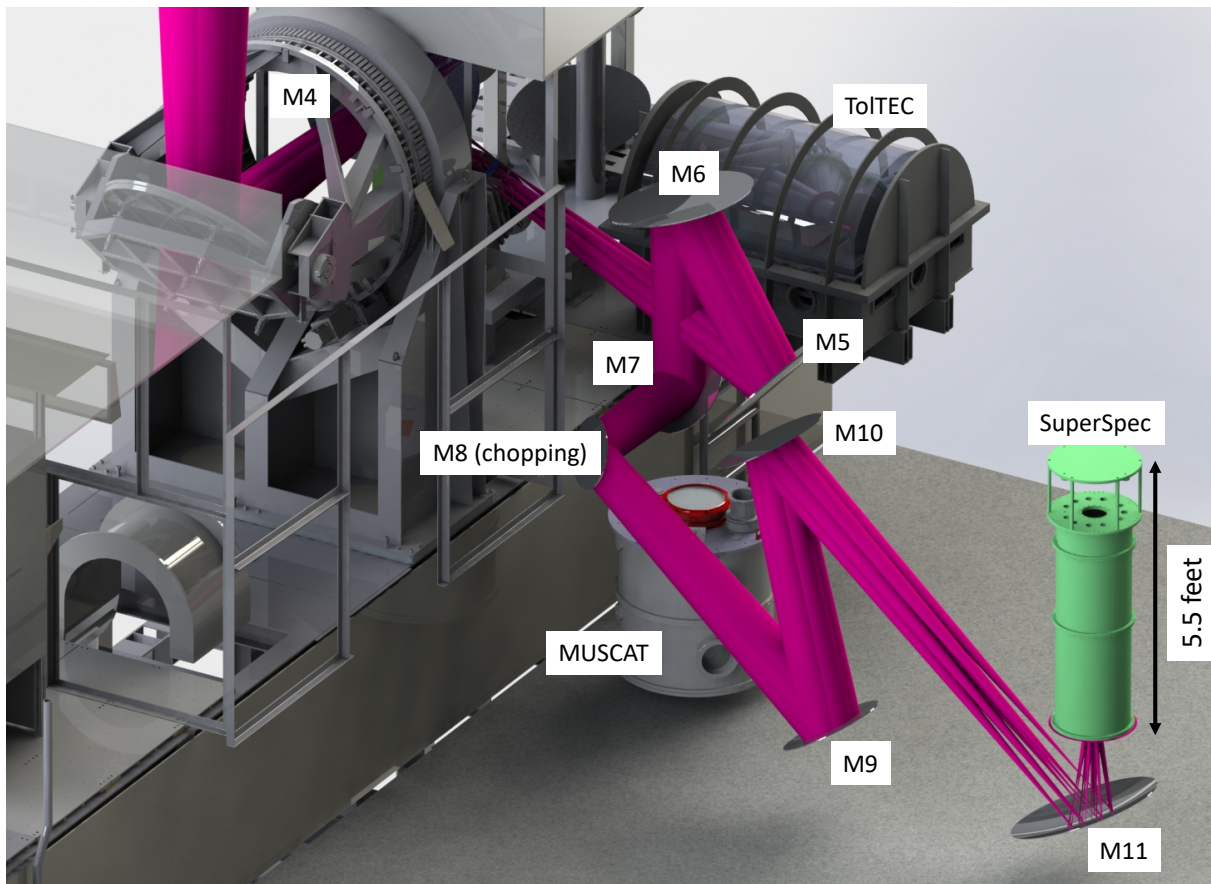


Figure 5.11: CAD rendering of the SuperSpec cryostat and optics inside the receiver cabin at the Large Millimeter Telescope. M8 is located at a pupil and is modulated to chop the individual pixel beams on and off source.

provide a greater cold path length to accommodate baffling. Extensive baffling is a necessity for millimeter and submillimeter cameras because stray light is prolific for such instruments and if not mitigated with extreme prejudice stray light will result in reduced performance. My baffling and shield designs are shown in Figure 5.12. Each baffle is coated with stycast loaded with carbon lampblack and stainless steel powder to make the surfaces black to millimeter-wave radiation.

5.3.1 SuperSpec Cold Readout Optimization

Cryogenic readout is an optimization of tolerable heat load, acceptable microwave loss, and cost. The optimization is easy if one of the three can be neglected. The most obvious is cost, if one is able to spend large quantities of money expensive lossless superconducting coax that has very small thermal conduction can be purchased. On the other hand, if an experiment has an extremely powerful dilution refrigerator cryostat, relatively low loss large diameter silver plated stainless coax can be easily used even with the extra heat loads. Finally, if one doesn't care about the loss on the lines, pure stainless coax can be used throughout the cryostat.

Of course, the SuperSpec cryostat required optimization of all three of the aspects described above. In particular, the heat load is of paramount concern for the SuperSpec system because it uses a He10 closed cycle fridge system (one ^4He stage and two ^3He stages). For these fridges the ultra-cold stage can handle several μW of heat load, however, any heat load over even $0.1 \mu\text{W}$ will result in a higher operating temperature. A higher operating temperature would result in reduced performance for the SuperSpec detectors. Thus, it is desirable for there to be almost no heat load on the ultra-cold stage of the SuperSpec cryostat. The previous incarnation of the SuperSpec cryostat minimized the load on the ultra-cold stage by using expensive superconducting NbTi coaxes all the way from the 4 K stage to the ultra-cold stage. Extending this implementation to upgrade to 6 readout lines would have cost \$12,000 in NbTi coax alone. Thus, I completed an optimization of

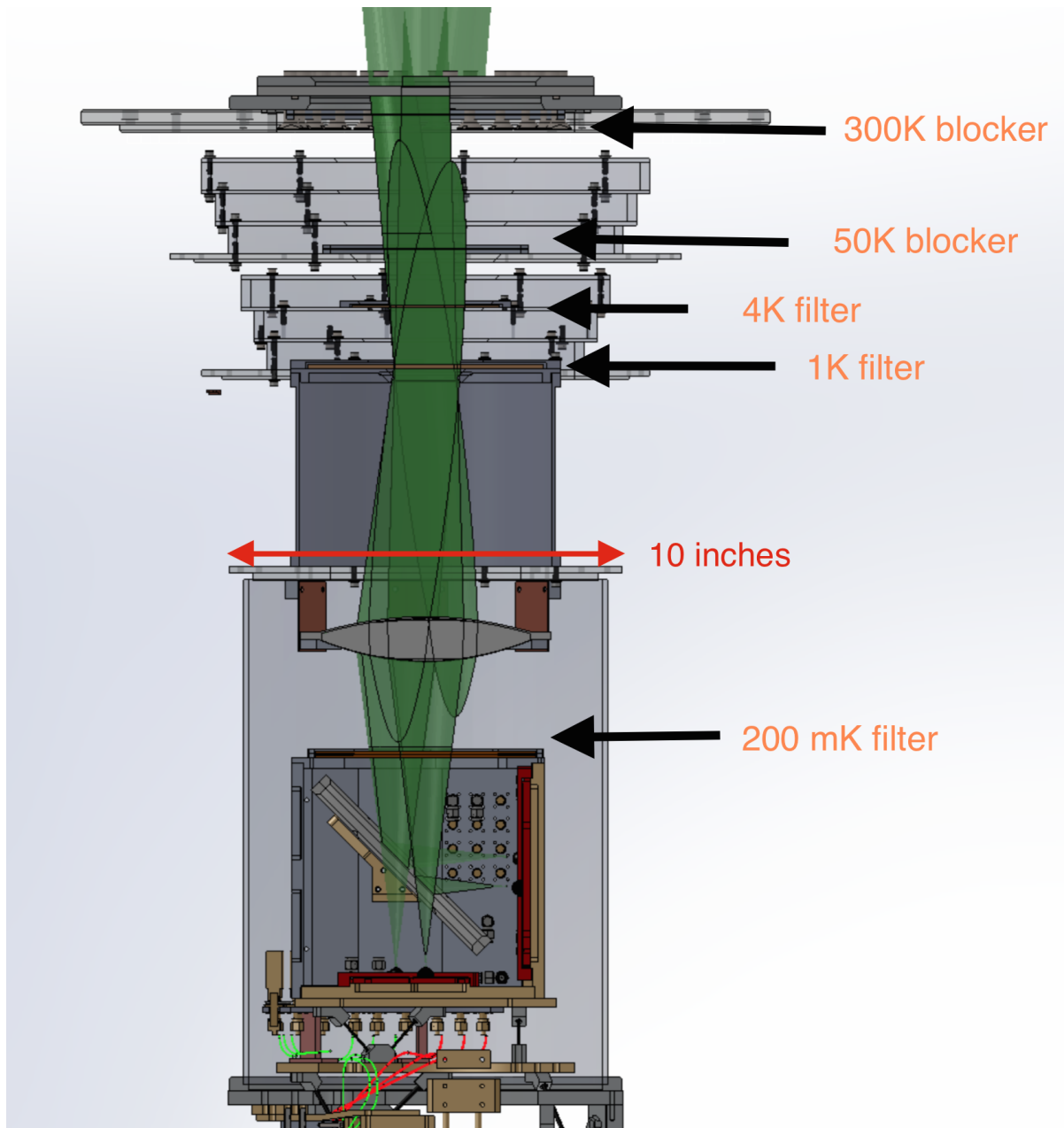


Figure 5.12: Cutaway view of the SuperSpec demonstration instrument. At 300 K and 50 K, thin thermal blockers are used to reflect high frequency out of band radiation. At 4 K, 1 K, and 200 mK multi-layer metal mesh filters are used to block both high and low frequency out of band radiation. The lens is mounted at 1 K and the cold stop is also located at 1 K. In addition to the filters there are three baffles at both 4 K and 50 K.

the cold coax to utilize the existing NbTi coax along with adding in appropriate diameter stainless steel coax. In order to do this, I take advantage of the fact that loss for coax lines is not as important on the input side of our readout lines as it is on the output side. The coax implementation is detailed in Table 5.1 including the cost, microwave attenuation, and resultant heat loads. Heat loads were calculated separately for each of the outer conductor, inner conductor, and dielectric portions of the coax. In order to compute the heat loads we use the following equation.

$$\dot{Q} = \frac{A}{l} \int_{T_{cold}}^{T_{hot}} k(T) dT. \quad (5.6)$$

Here, A is the cross-sectional area of a coax component, l is the length of the coax, T_{hot} is the hotter stage temperature, T_{cold} is the colder stage temperature, and $k(T)$ is the thermal conductivity of the component in units of $W/(m \cdot K)$. Stainless steel and PTFE thermal conductivities are from Kushino et al. (2005), increased by a factor of two for added safety margins. NbTi thermal conductivity is from Olson (1993), also increased by a factor of two for an added safety margin. Implementation of this new coax system resulted in less than a 1 mK increase in the operating temperature of the ultra-cold stage.

5.4 SuperSpec Observational Strategies

The LMT has several active and planned instruments including heterodyne spectrometers as well as imaging instruments. Two of these instruments are of particular interest to SuperSpec instrumentation because of their great synergistic potential. The instruments are the heterodyne instrument known as the Redshift Search Receiver and a planned multi-wavelength imaging polarimeter instrument known as ToI TEC.

The Redshift Search Receiver is a heterodyne spectrometer. It has an instantaneous bandwidth of 40 GHz and covers the 90 GHz atmospheric window (Erickson et al., 2007). In

Table 5.1. SuperSpec Demonstration Instrument Coaxs

Stage	Coax Type	Heat Load	Attenuation ^a	Total Cost
UC to IC (output)	12" 086 SS-SS	0.05 uW	0.6 dB	\$552
UC to IC (input)	12" 047 SS-SS	0.01 uW	1 dB	\$811
IC to 4K clamped @ 1K (output)	12" 064 NbTi	0.73 uW (IC) 16.8 uW (1K)	0 dB	pre-existing.
IC to 4K clamped @ 1K (input)	16" 047 SS-SS	0.86 uW (UC) 7.4 uW (1K)	1.3 dB	\$812
4K to 50K (input and output)	12" 086 SS-SS	4.9 mW (4 coax)	1.0 dB	4 new @ \$ 352
50 to 300K (input and output)	12" 086 SS-SS	8.9 uW (4 coax)	1.0 dB	4 new @ \$ 352

^aAttenuation values from Japan Coax Co. (2019) for 500 MHz signals at temperatures of 4 K for stages at 4 K and below and 300 K for stages at 50 K and above.

Note. — Coax scheme for SuperSpec. SS-SS is stainless steel outer conductor and inner conductor. The UC stage is assumed to sit at a temperature of 210 mK and the IC stage at 350 mK. For the 300K and 4K stages, the heat loads shown are only the additional heat loads from the 4 new coaxs added at each of those stages.

particular, the Redshift Search Receiver has had great success observing CO lines in galaxies (Chung et al., 2009; Snell et al., 2011; Zavala et al., 2015; Harrington et al., 2016). Since it covers a different atmospheric band than the current SuperSpec technology, this allows for the ability to simultaneously obtain multiple CO line transitions for a given source using both instruments. As discussed in Chapter 6, multiple measurements for a single high-redshift galaxy candidate of the CO rotational ladder allows for an observer to distinguish between warm and cold gas components. At the same time high-redshift galaxy candidates for which a CO line is not detected by the Redshift Search Receiver present a potential opportunity for a SuperSpec detection. This is because as the Redshift Search Receiver’s sensitivity falls off at higher redshifts, SuperSpec’s sensitivity to [C II] detection comes into play. The sensitivity landscape of SuperSpec and the Redshift Search Receiver is shown in Figure 5.13. Given the complementary sensitivity landscape, a SuperSpec observation strategy to target high redshift galaxies could be to simply observe all of the Redshift Search Receiver’s null detections.

TolTEC is a planned millimeter-wave camera to be fielded at the Large Millimeter Telescope in 2019 to 2020. It consists of 6,300 detectors in three different wavelength bands, 2 mm, 1.4 mm, and 1.1 mm (Austermann et al., 2018). TolTEC will study a wide variety of astronomical phenomenon from large scale structure to submillimeter galaxies to molecular clouds within our own galaxy (Wilson et al., 2018). In particular, the planned sky surveys with the TolTEC instrument will present interesting high-redshift galaxy candidates for SuperSpec follow-up.

TolTEC will complete a 100 square degree galaxy survey down to a RMS of 0.18 mJy at 2 mm. At a 5σ detection level, the flux density for this survey will be 0.9 mJy. Modeling by Casey et al. (2018) can be used to estimate the number of galaxies at this sensitivity which is shown in Figure 5.14 Left. Assuming the pessimistic (‘Dust-Poor’) model for galaxy number counts, there will be approximately 40 galaxies per square degree, yielding 4000 galaxies for the entire 100 square degree survey. Casey et al. (2018) modeled the redshift distribution

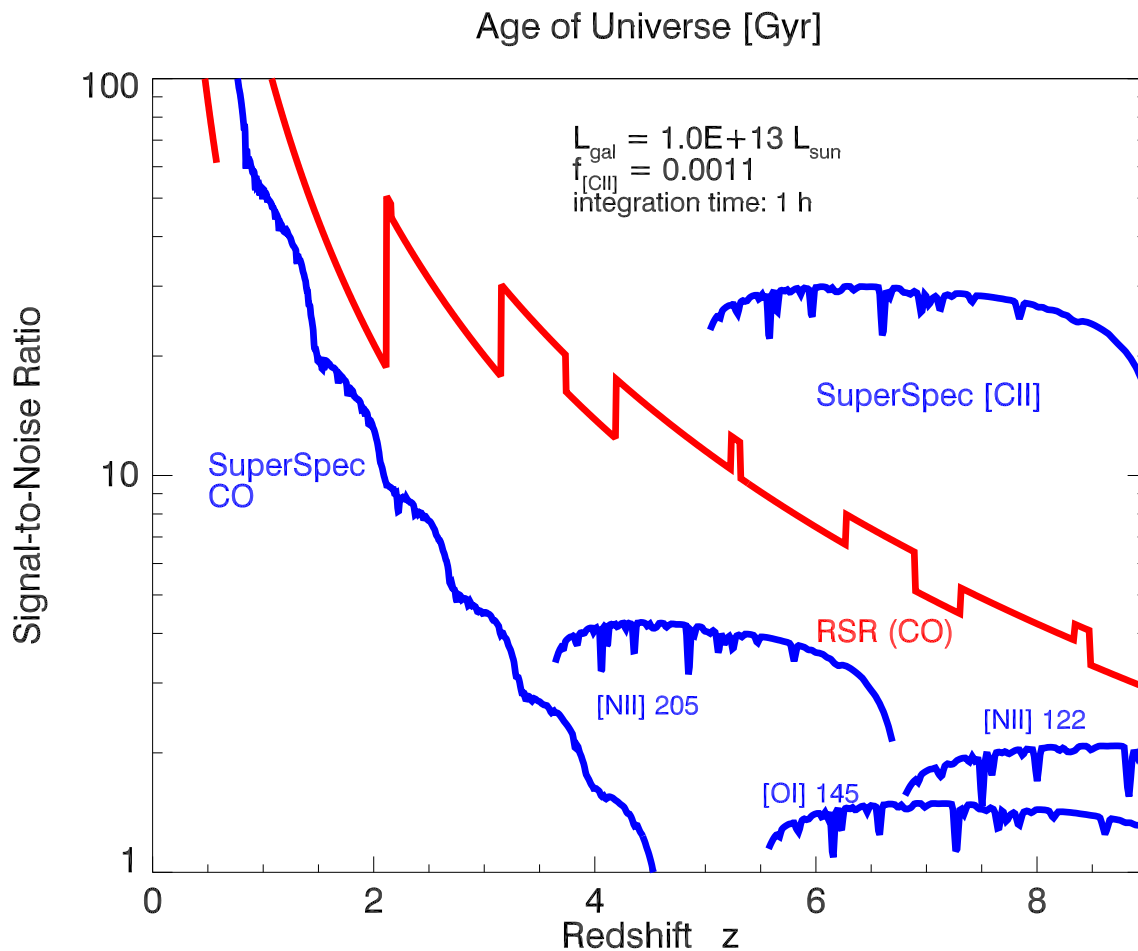


Figure 5.13: Plot showing SuperSpec (blue) and the Redshift Search Receiver (red) S/N versus redshift of several lines after 1 hour of observation time looking at a $10^{13} L_{\odot}$ galaxy using the full 50 m capability at the Large Millimeter Telescope while chopping between two beams and including all of the SuperSpec filterbank efficiency parameters. The structure in the SuperSpec sensitivity curves with redshift comes from non-uniform atmospheric transparency as the lines are redshifted to different frequencies. Figure courtesy of Dr. Matt Bradford.

of the galaxies for the TolTEC $\lambda = 2$ mm band which is shown in Figure 5.14 Middle. At 2 mm, fields are less contaminated by low-redshift galaxies than at shorter wavelengths and between one to two-thirds of the galaxies will be in the redshift range $5 < z < 9$. Using the composite submillimeter galaxy spectral energy distribution (SED) from Pope et al. (2008) scaled to a redshift of $z = 5$, a 2 mm flux density of 0.9 mJy corresponds to a galaxy luminosity of $6 \times 10^{12} L_{\odot}$, with higher redshifts being even brighter because of the negative K-correction. Assuming a [C II] $158 \mu\text{m}$ luminosity fraction of $L_{[\text{C II}]} / L_{\text{FIR}} = 0.0011$, such a galaxy will be detectable at a 12σ level with 1 hour of observation time with SuperSpec on the LMT, Figure 5.13. Since we expect conservatively that one-third of the galaxies observed will lie at $z > 5$, a two-week observing campaign with good 1 mm weather will yield ~ 40 $z > 5$ galaxies. Even a quarter of this initial measurement of the bright high-redshift galaxy candidates will begin to distinguish between the models presented in Casey et al. (2018) and provide a first cut at the dust-obscured star formation rate density at high redshift.

Another similar technique for high-redshift galaxy candidate selection involves selecting candidates from their submillimeter colors. The general idea is that because of negative K-correction, the redder a high-redshift galaxy candidate is, the more likely it is to be at high redshift. This is really just a method of getting a crude photometric redshift from multiple imaging wavebands to put a lower limit on the redshift. This method was utilized very successfully to target $z > 4$ galaxies utilizing the colors from Herschel imaging data at 250, 350, and $500 \mu\text{m}$ (Dowell et al., 2014; Ivison et al., 2016). From the above discussion, it can be seen that utilizing even longer wavelengths such as $850 \mu\text{m}$, 1 mm, and 2 mm observations will improve this selection and help target high-redshift galaxy candidates even greater than $z = 4$. So while 2 mm source selection is very powerful, combining other lower wavelength observations to get rough photo-zs can further increase the likelihood of targeting $z > 5$ galaxies.

It is worth taking a step back from the SuperSpec demonstration instrument capabilities to understand how these observational strategies can be applied to a future multi-object

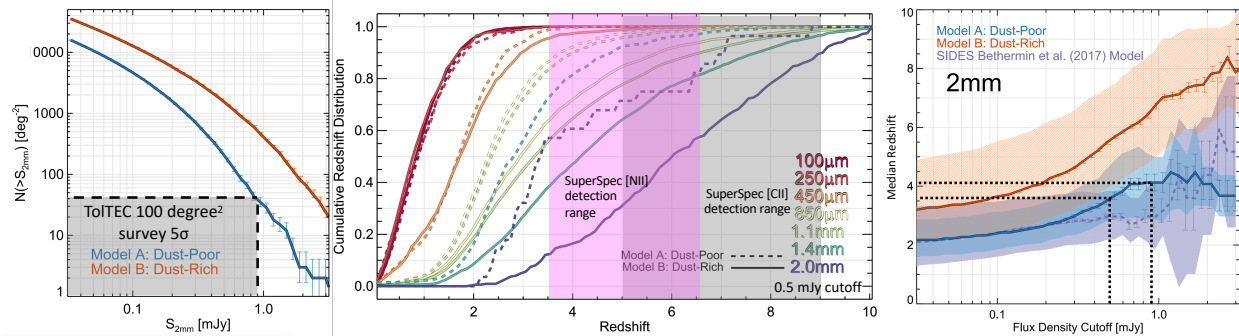


Figure 5.14: At $\lambda = 2$ mm, TolTEC will detect thousands of $z > 3$ galaxy candidates. With SuperSpec we expect to identify tens of $z > 5$ galaxies per 10 day observing campaign from this sample. Left: Expected TolTEC galaxy yield (adapted from Casey et al. (2018), Figure 12). Middle: From $\lambda = 2$ mm selection, 1 to 2 of every 3 galaxies will be $z > 5$, with [C II] falling in SuperSpec’s band. This is for a 0.5 mJy flux density cutoff rather than the 0.9 mJy TolTEC survey cutoff (adapted from Casey et al. (2018), Figure 8.). However, Right: shows that a higher 0.9 mJy cutoff will only increase the median redshift of high-redshift galaxy candidates detected (adapted from Casey et al. (2018), Figure 12).

spectrometer. In this case, the 100 square degree survey will not yield a high enough density of high-redshift galaxy candidates to merit a large multi-object spectrometer. This is because for any one pointing of the Large Millimeter Telescope only one to a few galaxies will fall within the field of view. However, TolTEC will also be completing a 1 square degree survey down to a 10 times lower RMS of 0.018 mJy. At this level, a 5σ detection corresponds to a 0.09 Jy level. Examining Figure 5.14 we see that this should uncover 5000 or more high-redshift galaxy candidates in just 1 square degree. This means that ~ 70 high-redshift galaxy candidates or more will fall in the Large Millimeter Telescope’s field of view (8 arcmin in diameter). The dimmest source, in this case, will be 10 times fainter than the sources discussed above; thus, it will take 100 times longer to detect the spectral lines of these high-redshift galaxy candidates. Due to this, follow-up with a single source instrument is impractical because it could take 300 hours to detect a single high redshift galaxy. However, a multi-object spectrometer could simultaneously measure 70 galaxies at once and in 100 hours reach the required sensitivity to detect these dim, $6 \times 10^{11} L_{\odot}$, galaxies.

We are entering an era where imaging arrays at submillimeter wavelengths will soon map the entire sky to deeper and deeper sensitivities revealing many thousands of galaxies. Spectroscopic follow-up of these sources has been and will remain a bottleneck. In order to accurately constrain the history of the Universe spectroscopic redshifts are required to understand when and where in the Universe these sources are occurring. The small profile of SuperSpec will enable the production of future multi-object spectroscopic instruments that will solve this spectroscopic-bottleneck problem, revolutionizing the field of astrophysics. Even now, with a few pixel instrument, SuperSpec has the potential to uncover 10s to 100s of new high-redshift galaxies. Such an addition of new galaxies would break the submillimeter galaxy field wide open.

Chapter 6

Arp 220: New Observational Insights into the Structure and Kinematics of the Nuclear Molecular Disks and Surrounding Gas

6.1 Introduction

Arp 220 is an ultra-luminous infrared galaxy (ULIRG) in the late stages of a merger between two gas-rich galaxies. At a distance of only 77 Mpc, ALMA's high spatial resolution resolves the emission from the two merging nuclei and provides insight into their gas dynamics in this extreme environment. Arp 220 has very large nuclear star formation rates with $\Sigma_{SFR} = 10^{3.7} \text{ M}_{\odot} \text{ yr}^{-1} \text{ kpc}^{-2}$ for the eastern nucleus and $\Sigma_{SFR} = 10^{4.1} \text{ M}_{\odot} \text{ yr}^{-1} \text{ kpc}^{-2}$ for the western nucleus (Barcos-Muñoz et al., 2015). It shows an unprecedentedly large dust optical depth with $\tau \sim 1$ at $\lambda = 2.6 \text{ mm}$ in the western nucleus (Scoville et al., 2017b). Not only is dust obscuration significant, but molecular absorption features further obscure the center of the disks (Rangwala et al., 2015; Tunnard et al., 2015; Aalto et al., 2015; Martín et al., 2016; Scoville et al., 2017b). In addition, Arp 220 has evidence for molecular outflows from several lines (Sakamoto et al., 2009, 2017; Barcos-Muñoz et al., 2018). Resolved measurements of Arp 220 have revealed complex structure and a wealth of new information that was previously not realizable with single dish measurements. In this way, Arp 220 provides the opportunity to understand how physical conditions such as morphology and kinematics can inform the integrated flux density measurements for sources that cannot be resolved at high redshift.

This chapter first presents the ALMA observations and data reduction in Section 6.2.

Following this, in Sections 6.3, 6.4, and 6.5, the implications of the observations that can be directly observed from the data are discussed. In particular, in Section 6.4 and 6.5 the extended emission morphology and outflowing molecular gas are examined in detail. Finally, in Section 6.6 kinematic non-LTE radiative models for both the eastern and western nuclei are presented and compared with the observations. The implications of the physical parameters derived from these models in regards to the nuclear environments are then considered in Section 6.7 as well as the applicability of Arp 220 as a high-redshift galaxy analog. Finally, we present our conclusions in Section 6.8.

6.2 Observations and Data Reduction

This chapter presents data from two sets of observations: (centered on) $^{12}\text{CO J} = 3 \rightarrow 2$ and $^{13}\text{CO J} = 4 \rightarrow 3$. Arp 220 was observed in CO $\text{J} = 3 \rightarrow 2$ with ALMA's band 7 receivers on August 17th of 2016 (Project 2015.1.00736.S) during cycle-3 in a configuration with baselines ranging from 15 m to 1.4 km. The bands observed were centered on 350.6 GHz (continuum), 352.4 GHz (continuum), 340.6 GHz ($^{12}\text{CO J} = 3 \rightarrow 2$), and 342.4 GHz ($\text{SiO J} = 8 \rightarrow 7$). The total on-source integration time was 4 minutes using 38 antennas. The correlator was configured in low-resolution wide-bandwidth TDM mode to give a spectral resolution of 15.625 MHz. During the observation, the weather was excellent with a median PWV of 0.32 mm. The beam size was $0.244'' \times 0.175''$ with a position angle of 0.34° .

Arp 220 was observed in $^{13}\text{CO J} = 4 \rightarrow 3$ with ALMA's band 8 receivers on July 29th and 30th of 2016 as well as on August 17th and 18th of 2016 (Project 2015.1.00736.S) during cycle-3 in a configuration with baselines ranging from 15 m to 1.4 km. The bands observed were centered on 432.0 GHz ($^{13}\text{CO J} = 4 \rightarrow 3$), 433.8 GHz (HCN $\text{J} = 5 \rightarrow 4/\text{continuum}$), and 421.8 GHz (continuum). The total on-source integration time was 102 minutes using 51 antennas. The correlator was configured in low-resolution wide-bandwidth TDM mode to give a spectral resolution of 15.625 MHz. The median PWV for the observations was 0.65 mm. The beam size was $0.177'' \times 0.125''$ with a position angle of -11.7° .

Imaging and cleaning were carried out using the Common Astronomy Software Applications package CASA (McMullin et al., 2007). The observations were flagged, calibrated, and imaged by ALMA staff prior to delivery. Additional calibration and imaging were performed to verify the quality of the reduced observations. The delivered observations were found to be of high quality and are thus presented here without additional processing. All observations have been corrected for primary beam attenuation. The observations were imaged using Briggs weighting, with robust set to 0.5, resulting in a balance between point source and extended flux density sensitivity. Both observation sets were continuum subtracted using CASA’s `uvcontsub` routine. However, for the non-LTE models discussed in Section 6.6, images were produced rather than UV data. In this case, CASA’s `imcontsub` routine was used for continuum subtraction rather than `uvcontsub`. To confirm that the different continuum subtraction routines do not produce different results, the observations were reanalyzed using both `uvcontsub` and `imcontsub`. The continuum subtracted observations were then compared and it was confirmed that the two routines produce the same line profiles within the noise levels of the observations.

6.3 Observed Morphology and Kinematics

The overall morphology is similar to that described by Sakamoto et al. (1999): two small nuclear disks embedded in a larger extended emission disk. The extended emission disk is well detected in $^{12}\text{CO } J = 3 \rightarrow 2$ but is not in $^{13}\text{CO } J = 4 \rightarrow 3$. Continuum emission morphology for the nuclei is similar in both bands after accounting for the different beam sizes at 365.5 and 427.8 GHz. The continuum flux densities and their Gaussian fits are listed in Table 6.1. The line profiles for the molecular species at the centers of each of the nuclei are shown in Figure 6.1.

Table 6.1: Arp 220 Continuum and Line Measurements

Quantity	Eastern Nucleus	Western Nucleus	Extended Emission	Units
	346.5 GHz Continuum (Beam $0.23'' \times 0.16''$ PA = -0.3°)			
Peak flux location	(15:34:57.294, +23:30:11.34)	(15:34:57.224, +23:30:11.50)	Not detected	J2000
Integrated flux density ($1'' \times 1''$)	220	440	...	mJy
Peak flux density	80.1 ± 2.8	237 ± 6.4	...	Jy/beam
Gaussian FWHM	0.367×0.257 , PA $26.9^\circ \pm 3.8^\circ$	0.265×0.245 , PA $70^\circ \pm 14^\circ$...	arcseconds
Gaussian fit integrated flux density	195.4 ± 7.6	398 ± 16	...	mJy
Deconvolved FWHM	0.298×0.171 , PA $40.7^\circ \pm 5.6^\circ$	0.205×0.076 , PA $85^\circ \pm 14^\circ$...	arcseconds
	427.8 GHz Continuum (Beam $0.18'' \times 0.13''$ PA = -23.2°)			
Peak flux location	(15:34:57.292, +23:30:11.33)	(15:34:57.223, +23:30:11.49)	Not detected	J2000
Integrated flux density ($1'' \times 1''$)	380	680	...	mJy
Peak flux density	93 ± 2.4	237 ± 3	...	Jy/beam
Gaussian FWHM	0.329×0.262 , PA $43.2^\circ \pm 4.3^\circ$	0.268×0.234 , PA $139.7^\circ \pm 3.7^\circ$...	arcseconds
Gaussian fit integrated flux density	342 ± 11	636 ± 11	...	mJy
Deconvolved FWHM	0.299×0.194 , PA $49.9^\circ \pm 4.4^\circ$	0.208×0.183 , PA $105^\circ \pm 12^\circ$...	arcseconds
	$^{12}\text{CO}J = 3 \rightarrow 2$ (Beam $0.23'' \times 0.17''$ PA = -0.34°)			
Peak flux location	(15:34:57.29, +23:30:11.41)	(15:34:57.23, +23:30:11.49)	Not Gaussian	J2000
Integrated flux density ($1'' \times 1''$)	700	800	1800 ($3.5'' \times 3.5''$)	Jy km/s
Peak flux density	54.7 ± 2.8	80.3 ± 4.7	Not Gaussian	Jy/beam km/s

Quantity	Eastern Nucleus	Western Nucleus	Extended Emission	Units
Gaussian FWHM	1.018 x 0.79, PA 30.8° ± 8.1°	0.781 x 0.663, PA 156° ± 14°	Not Gaussian	arcseconds
Gaussian fit integrated flux density	1037 ± 56	977 ± 62	Not Gaussian	Jy km/s
Deconvolved FWHM	0.99 x 0.77 PA 32.7° ± 9.8°	0.745 x 0.636, PA 152° ± 28°	Not Gaussian	arcseconds
L'_{CO}	1.1 × 10 ⁹	1.25 × 10 ⁹	2.8 × 10 ⁹	K km/s pc ²
L_{CO}	1.5 × 10 ⁶	1.7 × 10 ⁶	3.9 × 10 ⁶	L _⊙
L_{CO}/L_{FIR}^a	30 ⁺⁴⁵ _{-21.5} × 10 ⁻⁶	2.6 ^{+18.4} _{-0.9} × 10 ⁻⁶
¹³ CO $J = 4 \rightarrow 3$ (Beam 0.18" x 0.12" PA = -11.7°)				
Peak flux location	(15:34:57.29, +23:30.11.34)	(15:34:57.22, +23:30.11.54)	Not Detected	J2000
Integrated flux density (1" x 1")	110	180	...	mJy km/s
Peak flux density	17.86 ± 0.6	26.3 ± 1.7	...	Jy/beam km/s
Gaussian FWHM	0.427 x 0.285 PA 44.4°	0.408 x 0.368 PA 3.5° ^a	...	arcseconds
Gaussian fit integrated flux density	98.1 ± 3.8	179 ± 13	...	Jy km/s
Deconvolved FWHM	0.403 x 0.233, PA 48.3°	0.371 x 0.343 PA 15° ^b	...	arcseconds
L_{CO}	290	490	...	L _⊙
L_{CO}/L_{FIR}^a	5.8 ^{+9.2} ₋₄ × 10 ⁻⁹	7.8 ^{+54.2} _{-2.9} × 10 ⁻¹⁰
SiO $J = 8 \rightarrow 7$ (Beam 0.24" x 0.18" PA = -1.59°)				
Peak flux location	(15:34:57.30, +23:30.11.36)	(15:34:57. +23:23.30.11.49)	Not Detected	J2000
Integrated flux density (1" x 1")	-13	-26	...	Jy km/s

Quantity	Eastern Nucleus	Western Nucleus	Extended Emission	Units
Peak flux density	-28.7 ± 0.4	-23.0 ± 0.9	...	Jy/beam km/s
Gaussian FWHM	0.431 x 0.381, PA 51°	0.237 x 0.289 PA 12.1°	...	arcseconds
Gaussian fit integrated flux density	-11.0 ± 1.8	24.0 ± 0.9	...	Jy km/s
Deconvolved FWHM	0.385 x 0.304, PA 66°	Not resolved	...	arcseconds
HCN $J = 5 \rightarrow 4$ (Beam 0.18" x 0.13" PA = -26.3°)				
Peak flux location	(15:34:57.29,+23.30.11.39)	(15:34:57.22 +23,23.30.11.53)	Not Detected	J2000
Integrated flux density (1" x 1")	240	490	...	Jy km/s
Peak flux density	21.1 ± 2.0	47.4 ± 5.2	...	Jy/beam km/s
Gaussian FWHM	0.707 x 0.398, PA 126°	0.576 x 0.426, PA 141°	...	arcseconds
Gaussian fit integrated flux density	248 ± 25	488 ± 59	...	Jy km/s
Deconvolved FWHM	0.685 x 0.371, PA 125°	0.547 x 0.406, PA 139°	...	arcseconds

^aUsing the L_{FIR} measured from the ALMA 691 GHz continuum emission from Wilson et al. (2014). The large range in uncertainty in this ratio is from the large systematic uncertainty on the L_{FIR} .

^bThe position angle on ^{13}CO western nucleus is highly uncertain and the profile is not well described by a Gaussian.

Note. — Table showing the measured parameters for the observations. All uncertainties are 1σ .

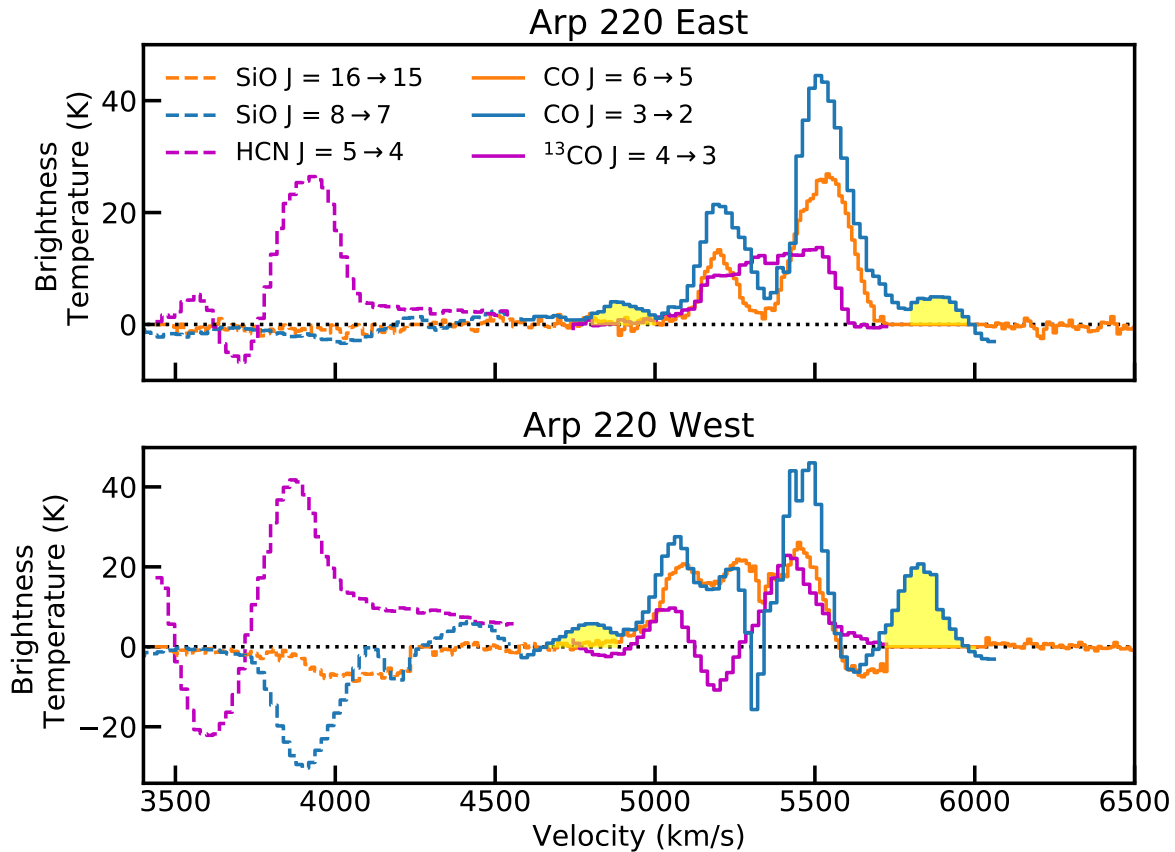


Figure 6.1: Continuum subtracted CO line profiles in the two nuclei. Note the deep absorption features at the centers of the eastern nucleus and western nucleus. High-velocity outflows seen in $^{12}\text{CO } J = 3 \rightarrow 2$ are highlighted in yellow. The line profiles were extracted at the center of the continuum emission at 427.8 GHz (i.e. 15:34:57.292, +23.30.11.33 and 15:34:57.223, +23.30.11.49) for the eastern and western nuclei respectively. This is because each fitted continuum center location is different by 1 to 2 pixels with the 427.8 GHz continuum having the median center location of the 3 data sets. Assumed rest frequency of $^{12}\text{CO } J = 3 \rightarrow 2$ is 345.796 GHz and $^{13}\text{CO } J = 4 \rightarrow 3$ is 440.765 GHz. $^{12}\text{CO } J = 6 \rightarrow 5$ observations are from Rangwala et al. (2015). For $^{12}\text{CO } J = 3 \rightarrow 2$ 1 Jy/beam = 248 K, for $^{13}\text{CO } J = 4 \rightarrow 3$ 1 Jy/beam = 294.5 K, and for $^{12}\text{CO } J = 6 \rightarrow 5$ 1 Jy/beam = 30 K.

6.3.1 $^{12}\text{CO } J = 3 \rightarrow 2$

The spectrometer channel maps for $^{12}\text{CO } J = 3 \rightarrow 2$ are shown in Figure 6.2, and the central velocity kinematic profiles are shown in Figure 6.1. For $^{12}\text{CO } J = 3 \rightarrow 2$, emission can be seen starting at a velocity of 4,919 km/s in both nuclei. At 4,959 km/s the blue

extended emission becomes detectable in the southwest. Progressing from low velocities to high velocities, the emission spirals in toward the eastern nucleus. The extended emission then propagates out from the western nucleus, and the most redshifted emission disappears just slightly north of the eastern nucleus. The strong emission of the western nucleus is evident starting at 5,029 km/s and becomes redder toward the west to a velocity of 5,560 km/s. At 5,360 km/s and 5,640 km/s there is a strong absorption dip. The eastern nucleus emission changes from blue in the southwest to red in the northeast, ranging in velocities from 5,159 km/s to 5,640 km/s.

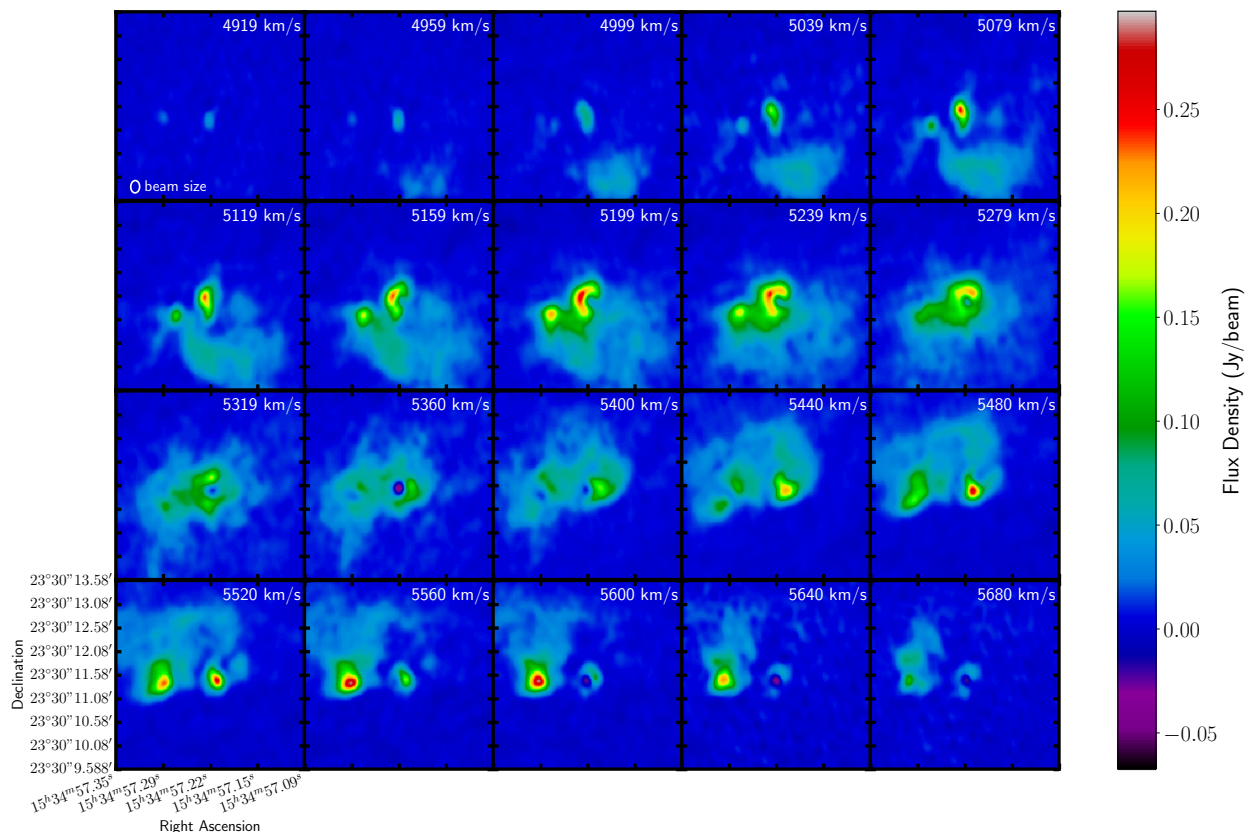


Figure 6.2: Spectrometer channel maps for $^{12}\text{CO } J = 3 \rightarrow 2$. There is a large negative dip (below the continuum level) at 5360 km/s and 5640 km/s. The velocity structure of the extended disk structure of Arp 220 is well resolved.

$^{12}\text{CO } J = 3 \rightarrow 2$ moment 0, 1, and 2 maps are shown in Figure 6.3. Moments 1 and 2 were constructed utilizing only pixels with a signal greater than 4 times the rms of pixels

without signal. Moment 0 clearly shows a large extended emission complex surrounding both nuclei. It also shows an asymmetric brightness for the eastern nucleus with increased flux density for the northeast part of this disk. The central line profile, Figure 6.1, and line profiles throughout the disk also show an asymmetric brightness with the red emission exhibiting enhanced brightness as compared to the blue. For the western nucleus, moment 0 shows a diamond-shaped core with a significant reduction in flux density at the center. Moment 1 shows the velocity gradient for the extended emission and the eastern nucleus is from southwest to northeast and for the western nucleus from west to east. Moment 2 shows that the highest velocity dispersion is located along the rotational axis of the eastern and western nuclei and peaks at 200 and 300 km/s for each respectively. The extended emission has a velocity dispersion of 100 to 150 km/s.

6.3.2 SiO $J = 8 \rightarrow 7$

Moment 0 of SiO $J = 8 \rightarrow 7$ is shown in Figure 6.3. The SiO $J = 8 \rightarrow 7$ absorption in the western nucleus is significant, but only just detectable in the eastern nucleus. The emission is mostly unresolved and coincident with the center of the western nucleus. The absorption in the western nucleus has two distinct velocity components: a very deep blue component and a less so red component. The blue component shows a FWHM velocity of 240 km/s and the red component of only 70 km/s. If this absorption is tracing shocked gas in an outflow in this nucleus, it would be expected that the blue component, which would be in the foreground, potentially would exhibit more absorption than the red component, which is occurring in the background of the disk emitting mass. However, the velocities may be tracing the underlying velocity structure of the rotating disk rather than outflow velocities. Potentially the blue absorption of SiO could be impacted by emission coming from H^{13}CO^+ $J = 4 \rightarrow 3$ line that has a velocity of 4300 km/s on the scale of Figure 6.1. SiO $J = 16 \rightarrow 15$ has also been seen in absorption in the western nucleus (Rangwala et al., 2015) and the $J = 5 \rightarrow 4$ line has been seen in emission (Martín et al., 2011).

Si is known to be depleted in the gas phase throughout the interstellar medium (Haris et al., 2016). This is due to Si's high condensation temperature of ~ 1300 K which causes it to be one of the first elements to be incorporated into silicate dust grains in the atmospheres of AGB stars (Savage and Sembach, 1996). As a result, if Si is observed in the gas phase, a mechanism to extract the Si from silicate dust grains is required. Shocks are the most common mechanism invoked for the destruction of dust grains in interstellar mediums (Draine and Salpeter, 1979). Thus, it is generally accepted that observations of Si in the gas phase are an indicator of the presence of shocks. In particular, Schilke et al. (1997) showed that a shock velocity of 25 km/s and column densities of 10^5 cm $^{-2}$ is sufficient to extract the Si from dust grains creating observable SiO in the gas phase. The presence of SiO absorption features indicates the presence of such shocks within the western nucleus. In the eastern nucleus, a SiO absorption feature is also detectable but the absorption is much less significant. This indicates that shocks, while present in the eastern nucleus, are much less significant than in the western nucleus.

6.3.3 $^{13}\text{CO } J = 4 \rightarrow 3$

The $^{13}\text{CO } J = 4 \rightarrow 3$ observations do not detect the extended emission disk but do resolve the two nuclei with high S/N. The ^{13}CO observations are similar to the ^{12}CO observations for the nuclear disks with a few notable exceptions. For the eastern nucleus, the continuum subtracted line profiles do not exhibit an absorption feature at zero velocity. The profiles are still highly asymmetric from red to blue as in the $^{12}\text{CO } J = 3 \rightarrow 2$ observations. These two properties, along with the modeling in Section 6.6, help to inform the possible sources for this asymmetry. For the western nucleus, similar kinematics as in the $^{12}\text{CO } J = 3 \rightarrow 2$ observations are seen, including a large central absorption feature. In addition, the western nucleus shows a faint high-velocity red wing indicating a potential outflow.

The $^{12}\text{CO } J = 3 \rightarrow 2$ to $^{13}\text{CO } J = 4 \rightarrow 3$ ratio was examined by convolving the ^{13}CO beam to the larger size of the ^{12}CO beam and then dividing each pixel in each spectral

channel by each other. The pixels examined were limited to pixels with a $S/N > 3$ in ^{13}CO and the energy difference between the different transitions, 8:6, was compensated for. For most of the pixels the ratio is small, < 10 , suggesting that at least the ^{12}CO is optically thick in both nuclei. A small number of pixels located in the gaseous bridge between the two nuclei at -80 km/s were found to have a ratio of approximately 40. This suggests a normal abundance ratio between the two species for at least some of the gas. It should be noted that these are different transitions which may reflect different gas components, i.e. cold versus warm gas.

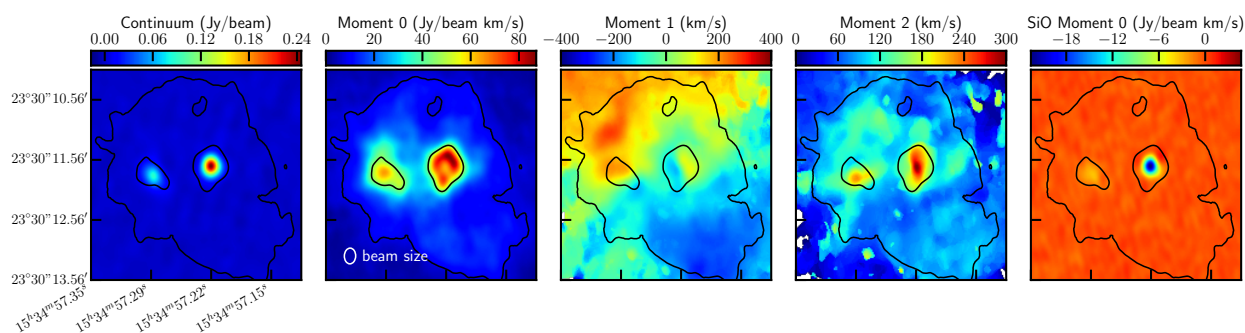


Figure 6.3: 346.5 GHz continuum emission, moments 0, 1, and 2 for ^{12}CO $J = 3 \rightarrow 2$, and moment 0 of SiO $J = 8 \rightarrow 7$. Moment 0 contours of 8, 45 Jy/beam km/s are shown in black for all images to highlight the nuclei and extended emission.

6.3.4 HCN $J = 5 \rightarrow 4$

Bright HCN $J = 5 \rightarrow 4$ emission is seen in both nuclei. Table 6.1 contains the measured properties, Figure 6.1 the line profiles, and Figure 6.5 the moment 0 map. The morphology of the HCN emission has some striking dissimilarities when compared to the CO emission. This is most noticeable in the eastern nucleus where the emission is almost perpendicular in the position angle to the CO emission. Also, in the western nucleus, the emission is most concentrated in the poles of the disk rather than in the plane of the disk. In both nuclei, the HCN feature clearly dips below the zero continuum level. This indicates that the HCN is absorbing some of the dust emission. In the eastern nucleus even more pronounced

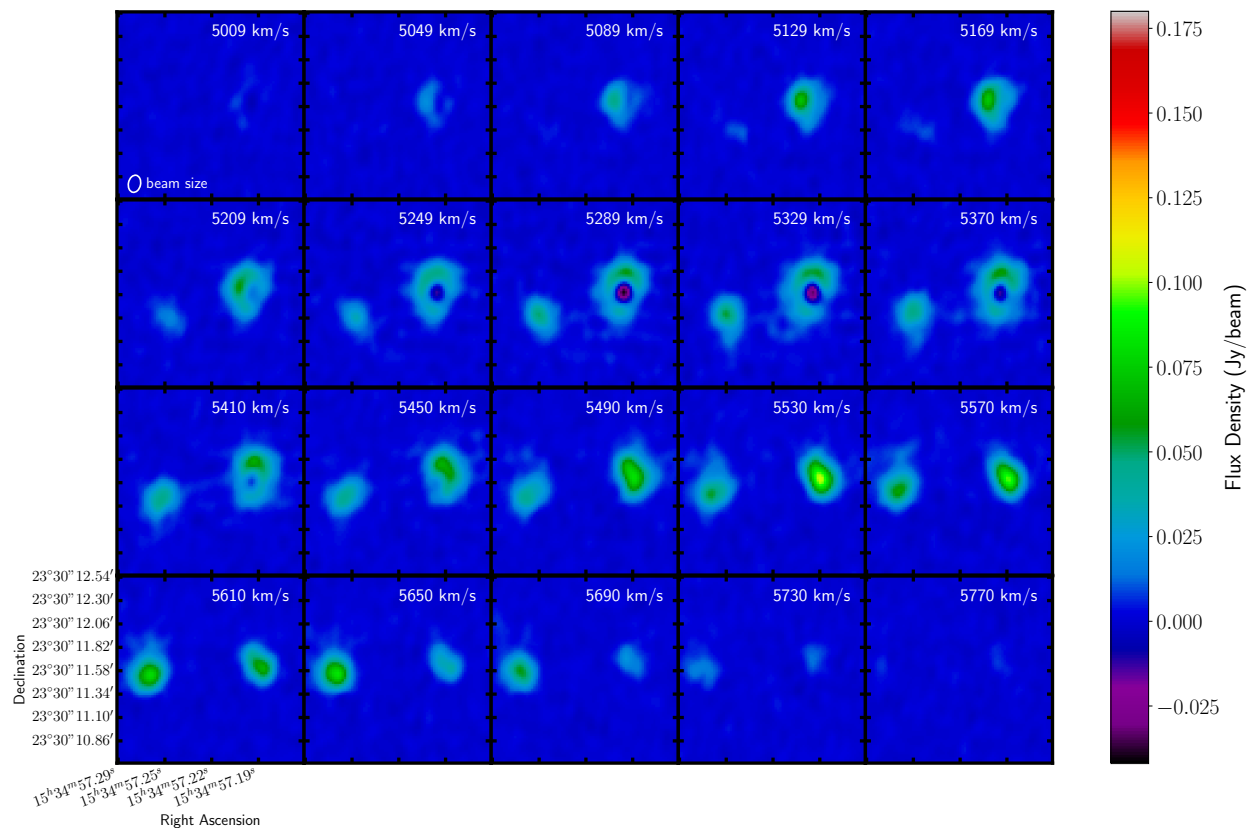


Figure 6.4: Channel maps for $^{13}\text{CO } J = 4 \rightarrow 3$.

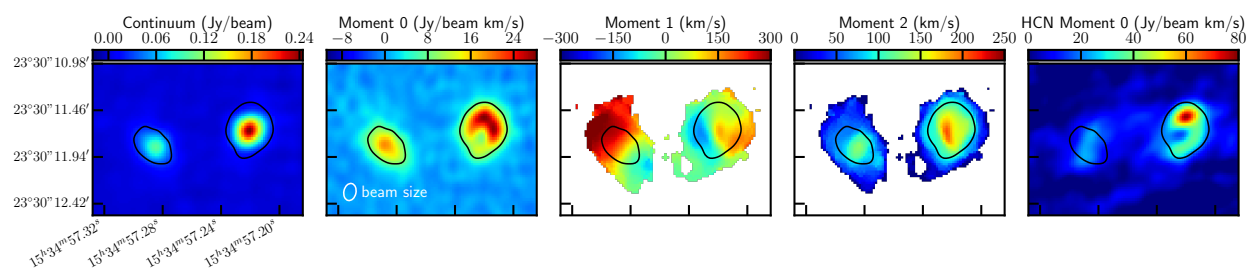


Figure 6.5: 427.8 GHz continuum emission, moments 0, 1, and 2 for $^{13}\text{CO } J = 4 \rightarrow 3$, and moment 0 of $\text{HCN } J = 5 \rightarrow 4$. A moment 0 contour of 8 Jy/beam km/s is shown in black in all images to highlight the nuclei.

asymmetry from blue to red in the central line profiles is seen, as in the CO observations. In the western nucleus, this may also be the case but the blue emission is cut off as it approaches the edge of our observation band. This cutoff also results in the measured flux density for the

western nucleus in Table 6.1 under-measuring the total flux density in HCN for this nucleus.

HCN, because of its large dipole moment, requires a high collision rate to maintain a substantial population above the ground state. Thus, it is often thought of as a tracer of dense gas. However, it can also be vibrationally excited through radiative pumping from 14 μm continuum radiation fields (Aalto et al., 2007; Sakamoto et al., 2010). In order to distinguish between the excitation methods, HCN can be compared with other species such as HNC and HCO^+ or the vibrationally excited $v_2 = 1$ states can be observed directly (Aalto et al., 2007; Sakamoto et al., 2010). The observations in this chapter do not probe HNC or HCO^+ . The vibrationally excited HCN $J = 5 \rightarrow 4$ $v_2 = 1$, $\ell = 1e$ line, is only +35 km/s from the $\nu = 0$ line, making it indistinguishable from the ground state. In addition, the $\ell = 1f$ line is at -1,400 km/s outside our observation band. Since we do not have access to the direct or indirect observations that would allow us to distinguish between excitation methods, we do not attempt to draw any conclusions about the excitation method. However, the fact that the HCN line is as bright as the CO emission probably indicates at least some radiative pumping. For Herschel observations of HCN absorption at high J lines, $J_{\text{upper}} = 12-17$, it was concluded that the primary excitation method was via radiative pumping (Rangwala et al., 2011). Excitation via radiative pumping is also implicated for HCN $J = 3 \rightarrow 2$ because it is found to be over luminous when compared to HNC (Aalto et al., 2007).

HCN emission is potentially seen perpendicular to the disk because 14 μm photons from hot dust are more likely to escape out of the less optically thick poles orthogonal to the disk rather than through the plane of the disk. These photons can then be absorbed and re-emitted in the submillimeter by the HCN molecules. In addition, the HCN in the western nucleus shows a strong central absorption dip below the continuum level. This indicates that the HCN is absorbing the continuum emission which reduces its apparent flux density at the center of the nuclei, Figure 6.1. The apparent flux density reduction also contributes to its polar appearance. A similar preferentially polar morphology is seen the vibrationally excited HCN emission in IC 860 (Aalto et al., 2019). It could be concluded that the HCN is

preferentially tracing the outflowing gas more than the gas in the disk. However, the majority of the gas does not have velocities with large deviations from the systematic velocity that would indicate an outflow.

6.4 Arp 220 Extended Emission

Due to the outstanding S/N in the $^{12}\text{CO } 3 \rightarrow 2$ observations, low-level signal revealing extensive structure in the extended emission surrounding the two nuclei was detected. Significant flux density is seen extending over $3.5''$. The highest velocity blue gas is located far away from the two nuclei in the southwest; whereas, the highest velocity red gas is located just slightly north of the eastern nucleus. Of particular interest, the total emission in this extended region is greater than the total emission of the two nuclei combined, Table 6.1. The extended emission in $J = 3 \rightarrow 2$ comprises more than 50% of the total flux density; whereas, in the $J = 6 \rightarrow 5$ observations from Rangwala et al. (2015) it is responsible for less than 25%. This decrease in flux density ratio at high J indicates that the extended gas is cooler than the gas in the disks. The fractional difference between what components dominate the total emission for different transitions indicates that for single-dish observations different transitions may be probing different physical gas components rather than just different temperature gas.

If a 0.05 Jy/beam contour level is chosen at each velocity, structure is revealed, Figure 6.6. It should be noted, however, if a smaller contour level is taken, i.e. 0.03 Jy/beam, this structure is much harder to discern and the red arm shown in Figure 6.6 merges with the highest velocity red gas north of the eastern nucleus. The structure seen with 0.05 Jy/beam contours is reminiscent of tidal tails caused by the merging of two galaxies such as those predicted by Cox et al. (2006); Johnston et al. (2008); Teyssier et al. (2010); Sparre and Springel (2016). In this case, a $m = 2$ spiral asymmetry is observed. Tidal features are most commonly observed using stars as the tracer medium. but in some cases have been observed in CO (Taylor et al., 2001; Espada et al., 2012). In this case, compared to more

common observations of tidal features as well, as the size scales of the models cited above, these features are quite close to the nuclear disks, no more than a 1 kpc away. The FWHM of these features is 200 km/s on the blue side and 140 km/s on the red side. This $m = 2$ asymmetry could be the result of tidal torques acting on the gas. If so, these torques could provide the mechanism to remove angular momentum of the surrounding gas allowing the gas to push inward (Barnes and Hernquist, 1991) providing the necessary fuel for the intense observed nuclear star formation.

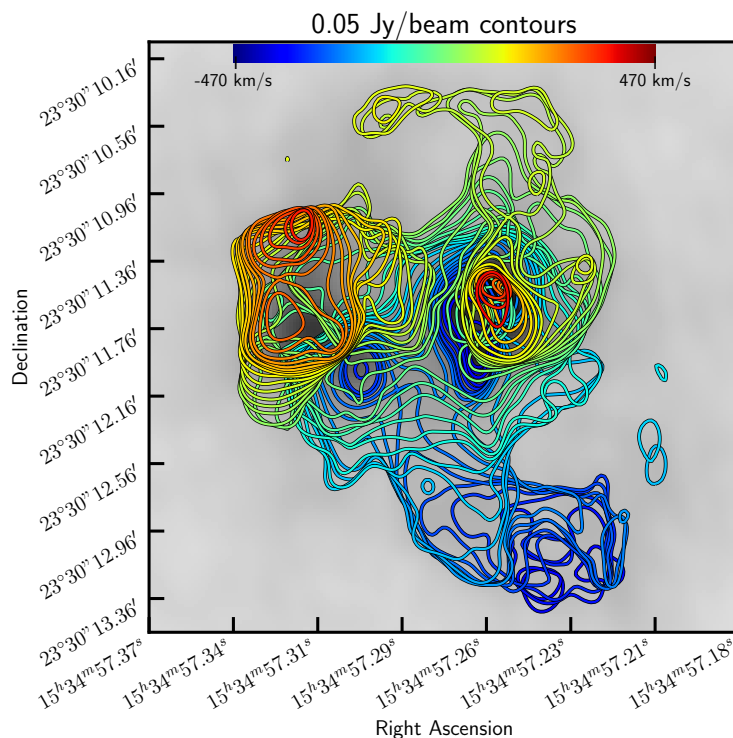


Figure 6.6: 0.05 Jy/beam contours are plotted for each velocity bin from -470km/s to +470km/s. This contour value highlights structure that resembles tidal tails. Moment 0 map is shown in grey scale as the background.

6.5 $^{12}\text{CO } J = 3 \rightarrow 2$ Outflow

In the $^{12}\text{CO } J - 3-2$ observations, significant outflow is detected in both the eastern and western nuclei, Figure 6.7. Significant detection of strong columnated outflows in the

western nucleus have been previously observed; however, this marks the first highly significant detection of an outflow in the eastern nucleus. The outflow shown in Figure 6.7 was constructed by making a moment 0 map for both the red and blue outflows using the high-velocity gas emission highlighted in yellow in Figure 6.1. The orientation and velocity of the outflow detected in the western nucleus match the outflow detected in HCN $J = 1 \rightarrow 0$ and CO $J = 1 \rightarrow 0$ by Barcos-Muñoz et al. (2018). While an examination of Figure 6.7 shows a red outflow that seems to merge with the red portion of the disk, it should be noted that the velocities used to measure the outflow are distinct (much higher velocity) from what seems to be disk related velocities in CO. However, for the red outflow at a velocity of 5700 km/s some of the emission could be from the H¹³CN $J = 4 \rightarrow 3$ line. With this in mind, it is likely that the red outflow is contaminated by H¹³CN emission. In particular, if there is red emission from H¹³CN that is associated with the disk, this would explain why the red outflow seems to merge with the red side of the disk in Figure 6.7.

The western nucleus outflow has a total luminosity for the red component of 32 Jy km/s and the blue component of 3.4 Jy km/s. We can estimate the mass in these outflows by using the conversion factor $0.8 M_{\odot} (\text{K km/s pc}^2)^{-1}$ (Downes and Solomon, 1998). This conversion factor is for ¹²CO $J = 1 \rightarrow 0$. To convert from CO $J = 3 \rightarrow 2$ to CO $J = 1 \rightarrow 0$ we use a scale factor that is the ratio of the CO line luminosity for each of the eastern and western nuclei respectively from CO $J = 3 \rightarrow 2$ to CO $J = 1 \rightarrow 0$. This brightness temperature ratio may be different, however, in the outflowing gas especially if the outflowing gas has different optical depths as compared to the nuclei as a whole. The flux density is converted to a line luminosity using Equation 1.6. To compute the line luminosity scale factors, the measured flux density values from Scoville et al. (2017b) for CO $J = 1 \rightarrow 0$ of 47.3 Jy km/s and 27.8 Jy km/s are used to compute the CO $J = 1 \rightarrow 0$ line luminosities. These values along with $\nu_{obs} = 117.4$ GHz yields $L'_{CO} = 6.3 \times 10^8$ and 3.7×10^8 K km/s pc². L'_{CO} for CO $J = 3 \rightarrow 2$ for the eastern and western nuclei are given in Table 6.1. Together, this yields a conversion factor of 1/2 for the western nucleus and 1/3 for the eastern nucleus. Using this

Table 6.2. Arp 220 Outflow Measurements

Quantity	Eastern Nucleus Red	Eastern Nucleus Blue	Western Nucleus Red ^b	Western Nucleus Blue
Velocity (km/s)	450-610	-(390-590)	390-650	-(470-670)
Flux density (Jy km/s)	8.6	6.4	32	3.4
$L'_{CO3\rightarrow 2}$ (K km/s pc ²)	1.3×10^7	1.0×10^7	5.0×10^7	5.0×10^6
$L'_{CO1\rightarrow 0}$ ^a (K km/s pc ²)	4.3×10^5	3.3×10^6	2.5×10^7	2.5×10^6
$M_{H_2}^b$ (M _⊙)	3.3×10^6	2.7×10^6	$< 2.0 \times 10^7$	2.0×10^6
Size (pc x pc)	$< 129 \times 24$	$< 96 \times 79$	121×50	90×50
Age (yr)	$< 1. \times 10^5$	$< 1.4 \times 10^5$	4.0×10^5	2.5×10^5
\dot{M} (M _⊙ yr ⁻¹)	> 19	> 19	< 50	8

^aDerived by scaling $L'_{CO3\rightarrow 2}$ by 1/2 and 1/3 for the western and eastern nuclei respectively.

^bCalculated using $0.8 M_{\odot} (\text{K km/s pc}^2)^{-1}$.

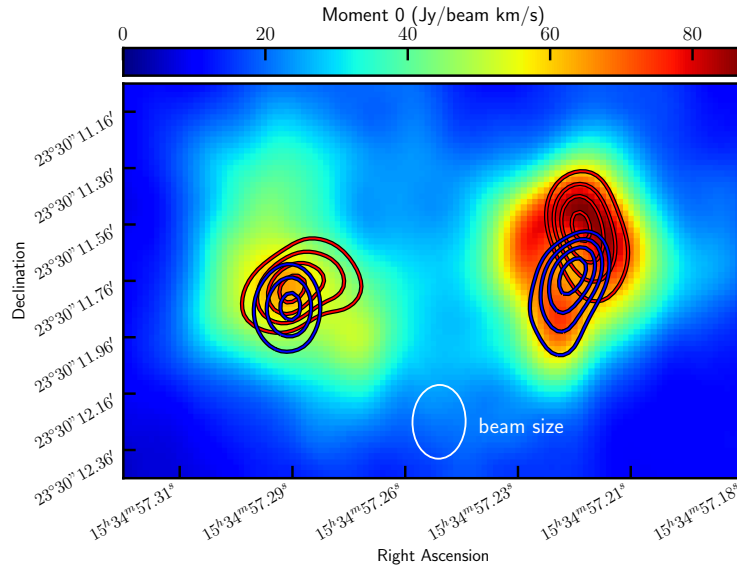


Figure 6.7: ^{12}CO J - 3 \rightarrow 2 red and blue high-velocity gas moment 0 maps tracing outflowing gas are shown as contours. This is overlaid on a ^{12}CO J - 3 \rightarrow 2 moment 0 map that includes gas at all velocities. The velocities used to make the contours are highlighted in yellow in Figure 6.1. The eastern nucleus has 1.5, 2.25, 3.0, and 3.75 Jy/beam km/s contours and the western nucleus has 1.0, 1.75, 2.5, 3.25 Jy/beam km/s contours for the blue outflow and has 6.0, 9.0, 12.0, 15.0 Jy/beam km/s contours for the red outflow.

equation a mass of $2.0 \times 10^7 M_{\odot}$ for the red outflow and $2.0 \times 10^6 M_{\odot}$ for the blue outflow in the western nucleus is derived. This result is 4 times smaller than the blue outflow mass found in CO J = 1 \rightarrow 0 by Barcos-Muñoz et al. (2018) of $8 \times 10^6 M_{\odot}$; yet, the red outflow mass is much more than was previously found, $2.5 \times 10^6 M_{\odot}$. Again, the red mass estimate is potentially contaminated by H^{13}CN emission so it is likely an overestimate of the true mass. The sizes of the outflow were fit using CASA and are shown in Table 6.2. Using these sizes and the outflow average velocities corrected for viewing angle based on the derived inclination angles (Table 6.3, 6.4), mass loss rates of 50 and $8 M_{\odot} \text{ yr}^{-1}$ for the red and blue outflows respectively were obtained. For the blue, outflow this is somewhat smaller than the results of Barcos-Muñoz et al. (2018) of $35 M_{\odot} \text{ yr}^{-1}$. For the red outflow, 3 times more mass than the Barcos-Muñoz et al. (2018) value of $12 M_{\odot} \text{ yr}^{-1}$ was found, possibly from

contamination from H^{13}CN emission.

Similarly, for the eastern nucleus, the outflow has a total luminosity for the red component of 8.6 Jy and the blue component of 6.4 Jy. This yields a mass of $5 \times 10^6 M_{\odot}$ and $4 \times 10^6 M_{\odot}$ for the red and blue outflows respectively. For the eastern nucleus, the outflows are not well resolved so the sizes could be smaller than those fitted. In this case, the sizes in Table 6.2 are taken as upper limits to the true sizes. Using these sizes lower limits for the mass loss rates are found to be $19 M_{\odot} \text{ yr}^{-1}$ for both the red and blue outflow respectively. Given masses of the eastern and western nuclei of $\sim 2 \times 10^9 M_{\odot}$, these mass loss rates yield a depletion time scale of order 10 Myr.

6.6 LIME Modeling

LIME, the Line Modeling Engine (Brinch and Hogerheijde, 2010), is a non-LTE spectral line radiation transfer code for 3D models in arbitrary geometries. LIME carries out radiative transfer in 3 dimensions and after the computationally expensive radiative transfer, the user can choose any viewing angle from which to create an image. This enables simultaneous calculation of several different inclination angles of the disk when searching for a representative model to the observations.

After an image is produced by LIME, CASA is used to convolve the image with a Gaussian representation of the observational beam. CASA's `imcontsub` routine is then used to subtract the dust continuum of the image such that the effects of continuum subtraction will be identical to those in the observations. The spectra are extracted from the model images and the observations at half-beam increments along the plane of the disk as well as orthogonal to it. For both the observations and the model images, the center spectra are taken to be the pixel that is closest to the maximum of the continuum image determined by a Gaussian fit to the continuum emission.

To produce the disk model for LIME a density profile given by the following equation

is assumed.

$$\rho(r, z) = A \cdot e^{r/r_{sh}} \cdot e^{-|z|/z_{sh}}, \quad (6.1)$$

where $r^2 = x^2 + y^2$ and A is such that the integral of equation 6.1 is the total gas mass, M_{gas} . The abundance of ^{12}CO to H_2 is assumed to be 2×10^{-4} . The gas temperature, dust temperature, and turbulent velocity are taken to be constant throughout the disk. For the models, the integrated intensity in the continuum map that is produced is required to be the same as that measured in the observations. In this way, the continuum and gas emissions are simultaneously modeled. This constrains the dust temperature for a given gas mass as determined by the model; yet, other dust temperatures could result if different disk geometries and orientations are modeled.

6.6.1 Arp 220 Eastern Nucleus

The Arp 220 eastern nucleus exhibits asymmetric line profiles with the red side being brighter by a factor of order two for both ^{12}CO and ^{13}CO . Several possible causes were previously proposed including a strong outflow or a blueshifted absorber (Rangwala et al., 2015). In addition to these two explanations, this chapter explores another, that the asymmetric profiles are produced by an asymmetric temperature distribution throughout the disk. This asymmetric temperature distribution is supported by the very high-resolution images of the eastern nucleus in $^{12}\text{CO } J = 1 \rightarrow 0$ where the non-uniformity of the eastern nucleus is clearly visible (Scoville et al., 2017b). The spectral profiles of the eastern nucleus's models and observations were sampled along the disk axis taken to be 45° , as well as perpendicular to this axis.

6.6.1.1 Foreground Absorber Model

In order to reduce the flux on the blue side of the eastern nucleus, a blue shifted foreground absorber can be invoked to preferentially absorb emission from the blue side of

the disk. To simulate the absorption, the approach from Rangwala et al. (2015) was used. A Gaussian absorption profile is invoked with a line center velocity v_{abs} , a velocity dispersion $\sigma_{abs} = 90$ km/s, and a line center optical depth τ_{abs} , which are all allowed to vary with position. By tuning the depth and velocity of such an absorber the line profiles seen in the ^{12}CO $J = 3 \rightarrow 2$ profiles can be easily reproduced. However, if this explanation is correct, it must reproduce all of the line profiles for each of the CO lines including the ^{13}CO line species. For the less abundant species of ^{13}CO , it is expected that the abundance of the absorber should decrease similarly as the abundance ratio of ^{12}CO to ^{13}CO in the disk. If this condition is enforced then less absorption is expected for the ^{13}CO . Examining the model results for ^{13}CO $4 \rightarrow 3$ in Figure 6.8 panel A shows that as the abundance of the absorber is decreased for ^{13}CO by a factor of 40 while keeping the velocity structure the same, asymmetric line profiles are no longer produced. Thus, the asymmetric line profiles observed in ^{13}CO $J = 4 \rightarrow 3$ rule out the possibility of a foreground absorber as the cause of the asymmetry. For this model, all of the ^{12}CO $J = 3 \rightarrow 2$ gas has a temperature of 110 K and the ^{13}CO $J = 4 \rightarrow 3$ gas has a temperature of 950K. With the exception of these two temperatures, all of the rest of the parameters are the same as those listed in Table 6.3 for the asymmetric disk model.

6.6.1.2 Outflow Model

Another way to produce asymmetric line profiles is with a strong outflow. A strong outflow can skew the line profiles for both the ^{12}CO species and the ^{13}CO species as seen in the models in Figure 6.8 panel B. However, in order to produce such a significant perturbation on the line profiles, an outflow of 150 km/s oriented in the plane of the disk pointed directly at the observer with a 120 degree opening angle was required. The requirement that the outflow is oriented in the plane of the disk suggests that this is not a realistic solution. It does, however, reproduce the central line profiles very well for both cases. It fails, though, to capture the asymmetry in brightness from red to blue when moving further away from

the axis of rotation. Thus, it is concluded that an outflow cannot be solely responsible for producing the asymmetry from red to blue observed in the line profiles. This does not rule out the existence of an outflow. This is of particular interest when trying to interpret the results from unresolved emission. If the disk was not resolved and only a single kinematic line profile of a point source was obtained, then an outflow could have reproduced the asymmetric line profiles observed. This provides a word of caution for interpreting unresolved sources, and for resolved sources demonstrates the usefulness of considering the non-centralized line profiles. For this model all of the $^{13}\text{CO } J = 4 \rightarrow 3$ gas has a temperature of 1700 K and a total gas mass of $1.4 \times 10^8 M_{\odot}$. With the exception of these two parameters, all of the rest of the parameters are the same as those listed in Table 6.3 for the asymmetric disk model.

6.6.1.3 Asymmetric Disk Model

An asymmetric temperature distribution will lead to an asymmetric brightness from one side of the disk to the other. In this model, for simplicity, the northeastern side of the disk is simply varied to have a temperature that is 60 percent greater than the southwestern side of the disk in ^{12}CO and 100 percent greater in ^{13}CO . This invokes a sharp discontinuity in the temperature of the model at the center of the disk, but this discontinuity is naturally smoothed by the beam convolution. It is found that the observed line profiles are best reproduced for this model with an asymmetric temperature distribution, Figure 6.8 panel C.

Any asymmetries in this nucleus should be smoothed out as the disk rotates. The fact that the northeastern side of this nucleus is brighter is observationally evident when looking at the $^{12}\text{CO } 3 \rightarrow 2$ moment 0 map in Figure 6.3 and even more so in the high resolution $^{12}\text{CO } J = 1 \rightarrow 0$ observations from Scoville et al. (2017b). Based on the model velocities for this nucleus and the ~ 45 pc radius, the rotation period should be on order 10^5 years. This suggests that the energy source powering this asymmetry must be recent/short-lived. This is too fast in comparison to the typical starburst age of $\sim 10^7 - 10^8$ years for a sustained starburst to be the explanation. A back-of-the-envelope energy calculation for the required

energy to produce a $\Delta T = 45$ K for half of the disk mass, $4 \times 10^8 M_\odot$, using $K = \frac{3}{2} N k_B \Delta T$ yields $K = 4 \times 10^{51}$ ergs or 4 supernovas worth of energy. Likewise, the same calculation for the ^{13}CO yields a bit more energy, 12×10^{51} ergs or 12 supernovae. It seems reasonable, then, to conclude that this brightness asymmetry could be the result of several recent supernovae. Given that the Arp 220 system has a rate of 4 ± 2 supernovae per year (Lonsdale et al., 2006), this seems like a plausible power source.

Considering the preferred fit parameters for this model, shown in Table 6.3, a few conclusions can be drawn. The fitted gas mass of $8 \times 10^8 M_\odot$ is close but lower by a factor of two than the results of the derived dynamical mass from Scoville et al. (2017b) in CO $J = 1 \rightarrow 0$ of $\sim 1.5 \times 10^9 M_\odot$ and Sakamoto et al. (1999) in CO $J = 2 \rightarrow 1$ of $\sim 2 \times 10^9 M_\odot$. The modeling prefers a thick disk with a vertical e-folding distance slightly less than a factor of two compared to the radial e-folding distance. This is consistent with either a thick turbulent disk or launching of gas to high latitudes in the disk through outflows. A turbulent velocity dispersion of $\sigma = 43$ km/s was found, which is smaller than that found in Rangwala et al. (2015) of 85 km/s. It could be that the higher temperature gas probed by ^{12}CO $J = 6 \rightarrow 5$ is more turbulent. Alternatively, the large turbulent velocity derived could be the result of Rangwala et al. (2015)'s assumed edge on geometry which results in narrower line profiles than an inclined disk geometry. For the preferred fit values the temperatures of the $J = 3 \rightarrow 2$ gas and the $J = 4 \rightarrow 3$ gas was found to be dramatically different at 75 K and 475 K. This is not entirely unexpected because these transitions are on the turning point for which the emission of the entire Arp 220 system goes from cold to warm gas dominated (see Figure 5 from Rangwala et al. (2011)). For two such similar transitions, intuitively, the gas is expected to be closer in temperature. As such, it is concluded that the hotter temperature in ^{13}CO may be an effect of the lower optical depth of the ^{13}CO observations. Since ^{13}CO is optically thinner than ^{12}CO , it is probing gas deeper in the nucleus where the gas temperatures are potentially hotter. For the ^{12}CO , much of the hot gas may be shielded by cooler gas in the foreground. This effect for the observed dust temperatures

given optical depth effects in the continuum emission is discussed in detail in Scoville et al. (2017b). Given this, a single temperature gas model may be too simplistic to accurately capture the gas properties in this nucleus. In addition to this, when adopting an abundance ratio between ^{12}CO and ^{13}CO of 40, a lower gas mass for the ^{13}CO species was also required. This is consistent with the warm gas component being less massive (Rangwala et al., 2011). When scaling the gas mass, the dust-to-gas ratio is scaled appropriately so that the total dust mass is kept the same for the two different models.

6.6.2 Arp 220 Western Nucleus

The western nucleus in ^{12}CO $J = 3 \rightarrow 2$ exhibits 3 separate peaks and an extremely narrow absorption feature, Figure 6.1. The narrow absorption dip is believed to be the result of a small-scale velocity-coherent gas complex in the outer envelope of the western nucleus gas. The spectral features observed in ^{12}CO $J = 3 \rightarrow 2$ cannot be reproduced by the smooth disk model approximation used in this chapter. As such, modeling the western nucleus in ^{12}CO $J = 3 \rightarrow 2$ is not attempted. In ^{13}CO $J = 4 \rightarrow 3$ the spectra become smoother, exhibiting only two separate peaks that would be expected for a disk. Thus, it is concluded that the ^{13}CO $J = 4 \rightarrow 3$ is probing the nuclear disk as a whole better than the ^{12}CO $J = 3 \rightarrow 2$ and that the resultant spectra are compatible with the smooth disk model used in this chapter. This does not mean that the ^{13}CO $J = 4 \rightarrow 3$ observations are probing the nucleus in its entirety. Rather, the ^{13}CO line profile (Figure 6.1) exhibits a large central absorption dip, indicating a high optical depth that is absorbing continuum radiation from the nucleus core.

The spectral profiles of the western nucleus were sampled at 3 half-beam distance increments from the center of the continuum along an axis of 30° . 30° is the deconvolved axis derived from the high spatial resolution observations from Scoville et al. (2017b). In addition, the spectral profiles are sampled perpendicular to this axis for two half-beam increments. For the western nucleus, it was found that a constant circular velocity, v_{circ} , captured the

Table 6.3. Parameters for Arp 220 East Asymmetric Disk LIME Model

Parameter	Value	Approximate Range	Description	Defining Spectral Feature(s)
M_{gas}^{13CO}	$8 \cdot 10^8, M_{\odot}$	$4 - 8 \cdot 10^8 M_{\odot}$	Mass of H_2^a	Brightness and depth of absorption
r_{sh}	$2 \cdot 10^8, M_{\odot}$	$1.6 - 2.8 \cdot 10^8 M_{\odot}$	Mass of H_2	Brightness and depth of absorption
z_{sh}	45 Pc	30-52.5 pc	e-folding of density in disk radius	Brightness at large radii
T_{gas}	20 Pc	15-30 pc	e-folding of density in disk height	Absorption depth
T_{gas}^{13CO}	75, 120 K	65-85, 104-136 K	Gas temperature ^a	Brightness
T_{gas}^{13CO}	475, 950 K	375-575, 750-1150 K	Gas temperature ^a	Brightness
T_{dust}	63	50-80 ^b	Dust temperature ^c	Absorption depth, continuum brightness
$^{12}CO/^{13}CO$	40	Not well constrained ^d	Abundance of ^{12}CO to $^{13}CO^a$	Brightness
v_{turb}	43 km/s	38-48 km/s	Turbulent velocity	Line width and doubly peaked lines
v_{circ}	180, 130 ^e	160, 115 - 180, 135 km/s	Circular velocity	Line width and singly peaked lines
gllid	100	Not constrained	Gas to dust ratio	Absorption depth
ϕ	76.5°	72-90°	Disk inclination angle from face-on	Importance of v_{turb} vrs v_{circ} , aspect ratio

^aAll of these parameters are, to some extent, degenerate with each other.

^bDifferent dust temperatures require different M_{gas} to correctly fit the total continuum luminosity and thus, the constraints are not reflected by varying this parameter in the interactive figure.

^cDetermined by integrated continuum emission.

^dBecause ^{13}CO and ^{12}CO are different transitions, abundance variations and temperature variations cannot be distinguished from each other.

^eFirst value is constant out to 40 pc and decreases linearly to the second value at 150 pc.

Note. — The approximate range was found by varying only that parameter while all other parameters were kept the same and then by eye deciding an acceptable range of believability. A more quantitative treatment was computationally too expensive. As such, the reader is invited to use the interactive version of Figure 6.9 (available on-line) to come to his or her own conclusions about which range is believable for a good fit. For parameters that are degenerate, a few multidimensional models are shown in the appendix so that the degeneracies can be explored.

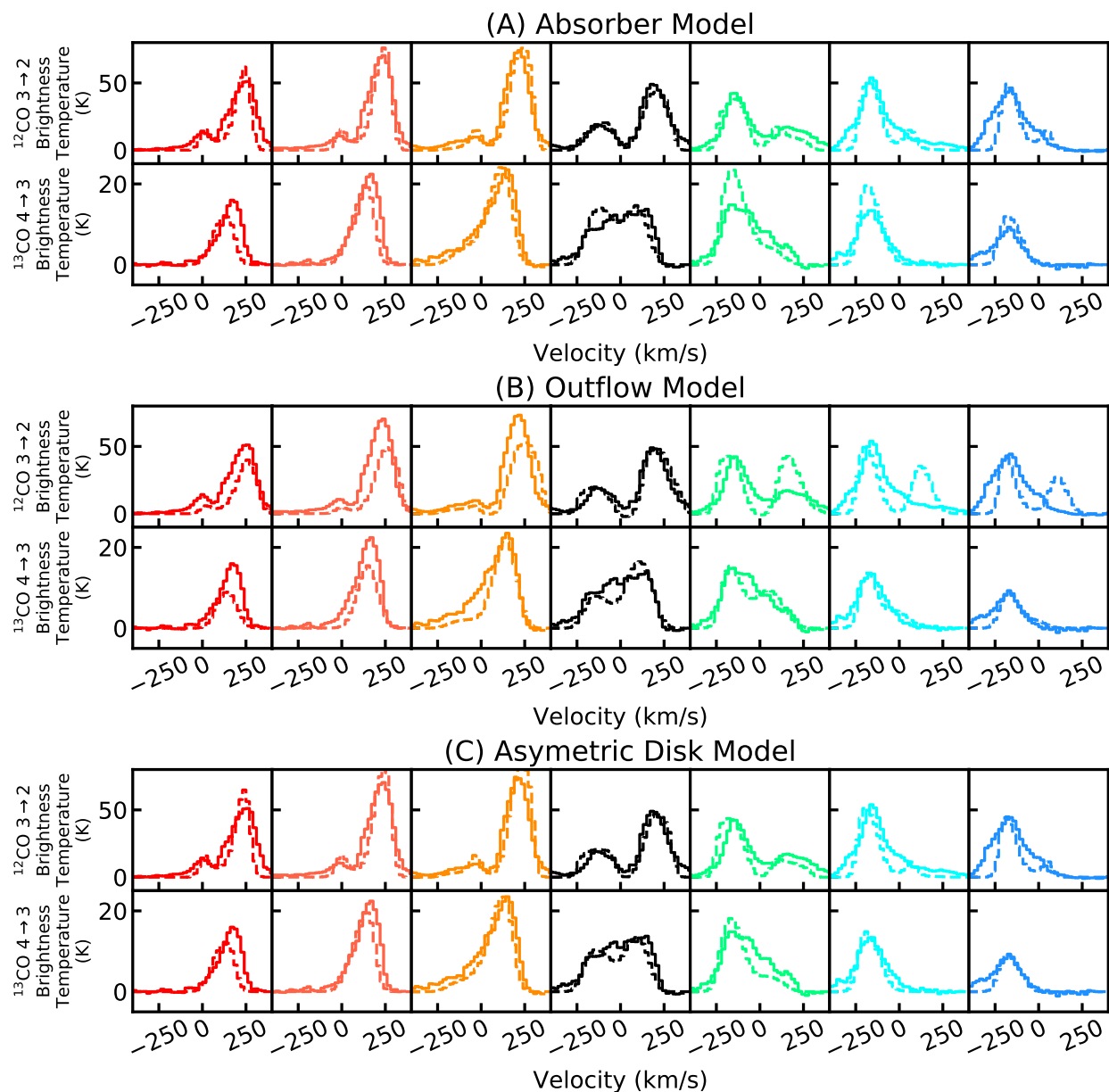


Figure 6.8: Models for Arp 220 east (dashed lines) shown along with the observed line profiles at half-beam increments along the disk axis. $^{12}\text{CO } J = 3 \rightarrow 2$ is shown on top and $^{13}\text{CO } J = 4 \rightarrow 3$ is shown on the bottom of each panel. For $^{12}\text{CO } J = 3 \rightarrow 2$, $1 \text{ Jy/beam} = 248 \text{ K}$ and for $^{13}\text{CO } J = 4 \rightarrow 3$, $1 \text{ Jy/beam} = 294.5 \text{ K}$. Used in the fitting, but not shown here, are several points perpendicular to the axis of the disk that allows for the constraint of the height of the disk. This is shown in detail for the asymmetric disk model in Figure 6.9.

velocity structure of the disk well enough that a velocity that varies with radius was not



Figure 6.9: Models for the Arp 220 eastern nucleus in ^{12}CO $J = 3-2$ (orange lines) and ^{13}CO $J = 4-3$ (purple lines) shown along with the observed line profiles at half-beam increments along the disk axis and perpendicular to the disk axis. For ^{12}CO $J = 3 \rightarrow 2$ 1 Jy/beam = 248 K and for ^{13}CO $J = 4 \rightarrow 3$ 1 Jy/beam = 294.5 K. Interactive figure available on-line (Wheeler et al., 2019 in preparation).

required. A prior was taken that the disk inclination angle is such that the red outflow will be directed to the northwest and the blue outflow toward the southeast, supported by the observed outflow in $^{12}\text{CO } J = 3 \rightarrow 2$ and the outflow seen in HCN (Barcos-Muñoz et al., 2018). The outflow velocity modifies the systematic rotational velocity in the disk within the cone defined by the opening angle, θ_{out} such that the velocity within this cone is a combination of the rotational velocity as well as the outflow velocity. However, for the blue outflow, in order to obtain a narrower absorption feature within the outflow cone, v_{out} is assumed to be the only systematic velocity without any rotational velocity.

The western nucleus is reasonably well modeled by a simple disk with both a red and blue outflow and a few asymmetries. The observations and the model are shown in Figure 6.10 and the derived parameters are shown in Table 6.4. A few notable conclusions from the fitted parameters are drawn below:

1. The fitted gas mass of $1.6 \times 10^9 M_{\odot}$ agrees closely with the results of the derived dynamical mass from Scoville et al. (2017b) in CO $J = 1 \rightarrow 0$ of $\sim 1.5 \times 10^9 M_{\odot}$ and Sakamoto et al. (1999) in CO $J = 2 \rightarrow 1$ of $\sim 2 \times 10^9 M_{\odot}$. This is somewhat surprising because for the $J = 4 \rightarrow 3$ transition one might expect based on the results of single dish experiments (Rangwala et al., 2011) that these observations should be probing a less massive warm gas component. However, as discussed for the eastern nucleus, this may be an effect of the optical depth of the observations. Since the optical depth is large, the $^{13}\text{CO } J = 4 \rightarrow 3$ transition may be just probing a cooler outer envelope of gas in the nucleus. Ultimately, transitions that trace cool, warm, and the combination of cool and warm gas need to be modeled simultaneously for each nucleus to completely understand the significance of cool versus warm gas for different transitions. The derived gas masses are dependent on the $^{12}\text{CO}/^{13}\text{CO}$ ratio, in this case, set to 40, which is a number that cannot be robustly constrained with these observations. It is worth noting that if the observations are probing a lower mass, hotter component of the gas, then the gas-to-dust ratio in the model should be adjusted to be less than 100 in order to reflect the true dust to total gas mass ratio. If this is the case, then

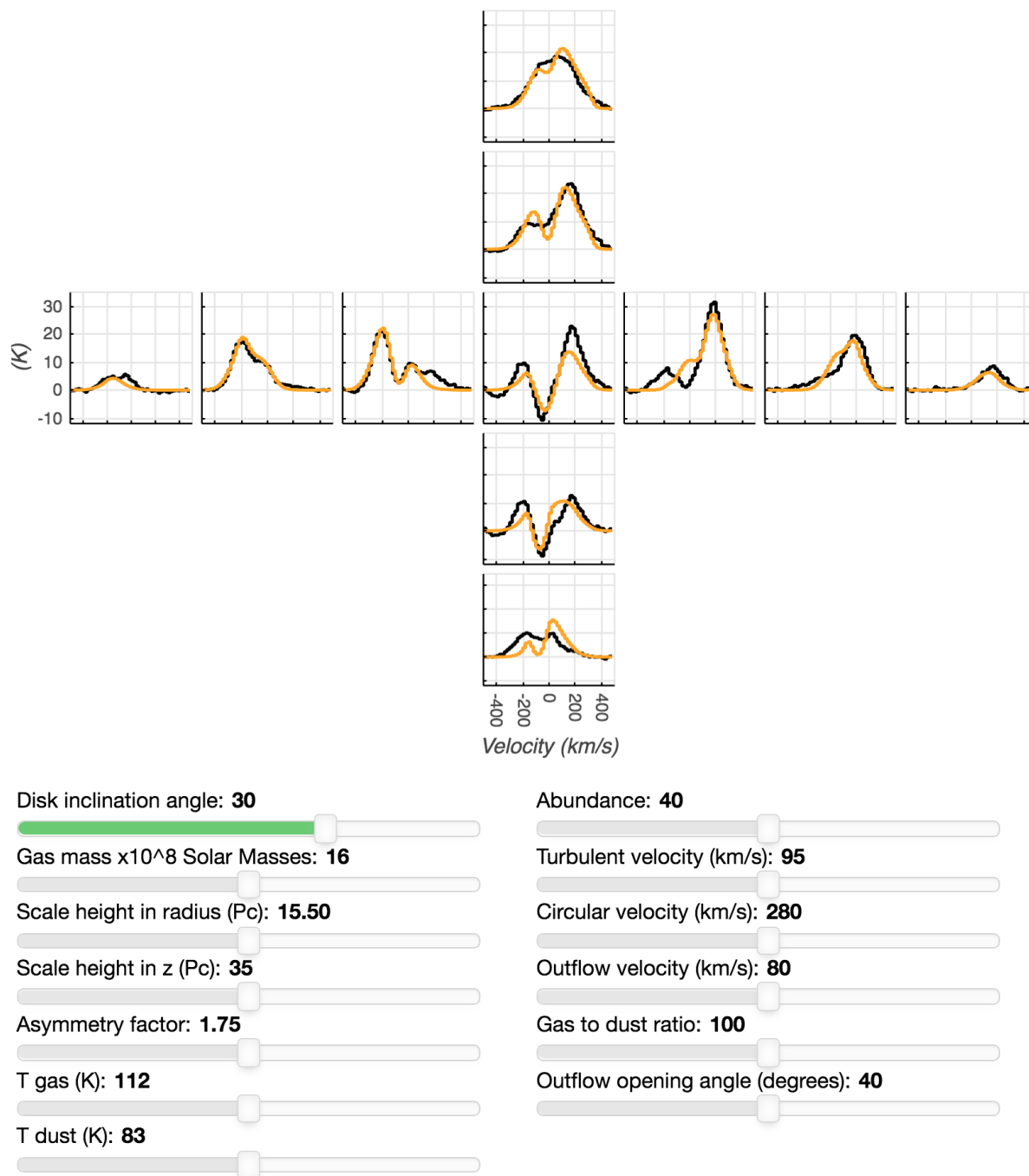


Figure 6.10: Models for the Arp 220 western nucleus in ^{13}CO $J = 4-3$ (orange lines) shown along with the observed line profiles at half-beam increments along the disk axis and perpendicular to the disk axis. $1 \text{ Jy/beam} = 294.5 \text{ K}$. Interactive figure available on-line (Wheeler et al., 2019 in preparation).

the derived dust temperature would be lower than that reported in Table 6.4. However, attempts to produce models with a lower gas-to-dust ratio failed to reproduce the correct continuum flux density while maintaining the strong central absorption feature.

2. $z_{sh} > r_{sh}$: Fitting the western nucleus requires gas at high latitudes in the disk. This is most strongly constrained by the depth of the central absorption. The western nucleus, with an inclination angle of 30° , is much closer to face-on than the eastern nucleus. The result of this is that the observations do not probe the z_{sh} spatially, which degrades the ability to constrain it with the models. However, the parameter z_{sh} is indirectly probed by the depth of the absorption feature. Through the models, it is found that recreating the central absorption dip is best facilitated by having gas at high latitudes in the disk, a larger z_{sh} . However, as discussed in the appendix, when trying to recreate a central absorption dip, z_{sh} is degenerate with the ratio of the gas to dust temperatures, the total gas mass, and the inclination angle. This further degrades the accuracy of the derived z_{sh} . As such, it is possible if the model were modified to have two temperature components with a lower temperature further out from the nuclear core, a smaller z_{sh} might be obtained. With only one transition, invoking a second temperature in the model would overfit the observations without another transition that traces a different temperature component of the gas to constrain a two-temperature model. This does suggest that more transitions would potentially help achieve better constraints for z_{sh} . $z_{sh} > r_{sh}$ invokes an unrealistic aspect ratio, and as such, it can be concluded that the models do not accurately constrain the aspect ratio of the disk. However, the models do indicate that gas at high latitude in the disk is important for recreating the central absorption dip observed in the observations. This potentially indicates the presence of either foreground gas or that outflows are injecting gas into very high latitudes.

3. The narrow absorption dips require a smaller turbulent velocity gas component, as compared to the disk gas, in the foreground to be accurately reproduced. This further indicates that the high latitude gas has different characteristics than the rest of the disk gas. Either

the disk has a parameter gradient with latitude or the central absorption dip traces a gas complex that is distinct from the disk gas. Furthermore, the strong central absorption dip demonstrates that even the ^{13}CO observations are probing gas that is optically thick and absorbing. This leads to the next conclusion.

4. $^{13}\text{CO } J = 4 \rightarrow 3$ is optically thick. Using LIME, an optical depth map for the model shown in Figure 6.10 was produced. In this map, a peak optical depth at the center of the western nucleus is found to be 18 and if the dust is removed from the model a τ of 15 is obtained. Furthermore, changing model parameters within 20 pc of the center of the disk has no effect on the model's produced line profiles, demonstrating an inability to probe to the very center of the disk with these observations. Thus, the absorption is obscuring information from deep inside the western nucleus. In this situation, the modeling would greatly benefit from an even less abundant species such as C^{18}O . However, observations of less abundant tracers will eventually be limited by the optical depth of the dust.

5. The line profiles at the center of the western nucleus dip below zero. Thus, it must be concluded that the ^{13}CO is, in fact, absorbing the dust emission. There is likely also a small amount of CO self-absorption occurring; however, when the dust is removed in the model only a small central dip is observed, suggesting minimal CO self-absorption. These models do suggest that this is not the case for the ^{12}CO species where CO self-absorption does become significant in the western nucleus.

6. The modeled outflows help predict the blue-shifted absorption in the center of the western nucleus and the high-velocity red excess in the northwest of the western nucleus. The outflows derived with this model are more modest than the outflow that is detected in the high-velocity emission in $^{12}\text{CO } J = 3 \rightarrow 2$ observations. It is believed these are all part of the same outflow but the ^{13}CO observations do not have the sensitivity and bandwidth to detect the higher velocity components of the outflow.

Table 6.4. Parameters for Arp 220 West LIME Model

Parameter	Value	Approximate Range	Description	Defining Spectral Feature(s)
M_{gas}	$1.6 \cdot 10^9 M_{\odot}$	$0.8 - 2.4 \cdot 10^9 M_{\odot}$	Mass of H_2^a	Brightness and depth of absorption
r_{sh}	15.5 Pc	12.5-18.5 Pc	e-folding of density in disk radius ^b	Brightness at large radii
z_{sh}	35 Pc	27.5-50 Pc	e-folding of density in disk height	Absorption depth
T_{gas}	112 K	120-210 K	Gas temperature ^{a,c}	Brightness
T_{dust}	83	76-86	Dust temperature ^d	Brightness and depth of absorption
$^{12}CO/^{13}CO$	40	Not constrained	Abundance of ^{12}CO to $^{13}CO^a$	Brightness
v_{turb}	95 km/s	85-105 km/s	Turbulent velocity ^e	Line width and doubly peaked lines
v_{circ}	280 km/s	250-310 km/s	Circular velocity	Line width and singly peaked lines
$v_{out-red}$	150 km/s	75-220 km/s	Outflow velocity	High velocity emission
$v_{out-blue}$	80 km/s	40-120 km/s	Outflow velocity	High velocity absorption
θ_{out}	40°	30-50°	Outflow opening angle	Intensity of high velocity emission
gHd	100	Not constrained	Gas to dust ratio	Absorption depth
ϕ	30°	25-35°	Disk inclination angle from face-on	Importance of v_{turb} vs v_{circ} , aspect ratio

^aParameters somewhat degenerate with each other.

^bValue decreases to 12.5 PC for the southeast corner.

^cValue increases to 196 K for $y > 0$ (north side in image).

^dValue increases to 162 K at $r < 25$ pc.

^eValue decreases to 55 km/s at $|z| > 20$ pc.

Note. — The approximate range was found by varying only that parameter while all other parameters were kept the same and by eye deciding an acceptable range of believability. A more quantitative treatment was computationally too expensive. As such, the reader is invited to use the interactive version of Figure 6.10 (available online) to come to his or her own conclusions about which range is believable for a good fit. For parameters that are degenerate, a few multidimensional models are shown in the appendix so that the degeneracies can be explored.

6.7 Discussion

The results of this analysis reaffirm the results of previous work on Arp 220. The general picture of two counter-rotating disks embedded in an extended emission disk is the same as in Sakamoto et al. (1999). The nuclei masses roughly agree with the dynamical masses from Scoville et al. (2017b); Sakamoto et al. (1999). Thick turbulent disks as seen in Rangwala et al. (2011) are found. The western nucleus outflow observed by Barcos-Muñoz et al. (2018) was confirmed in these observations but an additional outflow in the eastern nucleus was found. The 3-D modeling does allow for a better understanding of the contribution of turbulent velocity, rotational velocity, and disk inclination angle to the observed kinematic line profiles. Though these parameters are somewhat degenerate, these estimates are believed to be relatively accurate to within 20%, although no statistical fitting was carried out. These parameter derivations, along with the observed outflows, allow for the construction of a schematic depicting the rotating disks' orientations. This is shown in Figure 6.11. In addition, structure is found within the extended disk detected by Sakamoto et al. (1999). This structure resembles tidal features suggesting potential inflow of gas to the most central regions of Arp 220. An outstanding question is, does such structure exist in other merging ULIRG systems or is this unique to the Arp 220 system? It is possible that this inflow is required to provide sufficient gas for star formation to be sustained over observable times scales.

Arp 220 has often been used as an analog to understand high-redshift galaxies. Is Arp 220 a good prototype for high-redshift galaxies? Submillimeter galaxies (SMGs) are bright high-redshift galaxies that have continuum detections of ≥ 1 mJy detected in the range from 250 μm to 2 mm (Casey et al., 2014). Historically, SMGs refer to SCUBA detections at 850 μm with flux densities of at least 5 mJy (Hughes et al., 1998; Barger et al., 1998). Due to their high luminosity, $\sim 10^{12.5} L_{\odot}$, astronomers were led to the natural conclusion that these populations represented the equivalent local ULIRGs but at high redshifts. This is supported

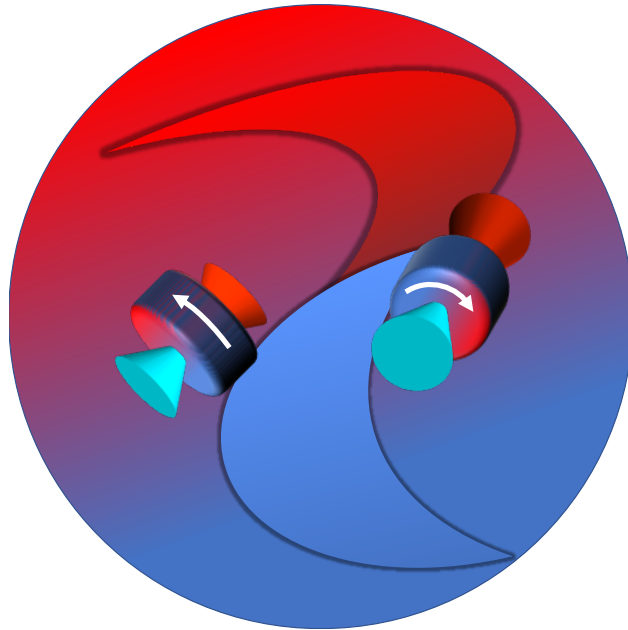


Figure 6.11: Schematic of Arp 220. Thick disks are shown with their inclination angles and outflows indicated. Redshifted and blueshifted gas are shown with red and blue colors. The outer extended emission disk of which the inclination angle is not determined is shown with tidal over density features.

by observational evidence that SMGs often exhibit disturbed morphologies and kinematics (e.g. (Engel et al., 2010; Menéndez-Delmestre et al., 2013)) and that all local ULIRGs are the product of enhanced star formation from major merger events. At the same time, resolved observations found that many SMGs exhibited morphologies that are much larger than local ULIRGs which are in general smaller than 1 kpc. This led to the idea that SMGs may not be merging starburst systems similar to local universe ULIRGs. Rather, these galaxies represent the high-mass end of a normal disk galaxy main sequence that has increased star formation efficiency at high-redshift. This is in stark contrast to Arp 220 which is clearly a merger driven starburst system that cannot be long-lived given the derived gas depletion times, ~ 10 Myr. The depletion time of 10 Myr also suggests that Arp 220 is not a good model for SMGs because the short timescale for which this system exists is not compatible with the number counts of SMGs at high redshift (Davé et al., 2010). Recent simulations and observations

support the conclusion that most SMGs are massive normal disk galaxies rather than Arp 220-like mergers (Narayanan et al., 2015; Koprowski et al., 2016; Michałowski et al., 2017; Scoville et al., 2017a). However, it does seem that $\sim 5\%$ of these galaxies have elevated star formation rates that cause them to lie off the normal galaxy main sequence (Sargent et al., 2012). These systems can be considered high-redshift starburst galaxies. The question that remains now is, are these high-redshift starburst galaxies driven by major mergers like local ULIRG starburst galaxies such as Arp 220 or is their heightened star formation rate driven by increased gas accretion efficiency or minor mergers?

Given this, it is worth considering using knowledge of local starbursts such as Arp 220, what observational characteristics should be searched for in these high-redshift starbursting galaxies that might indicate if they are the product of mergers or not. A natural choice might be to look at the physical size of these galaxies since this is one of the first observational characteristics that suggested SMGs may not be analogs of local ULIRGs. However, the relatively larger extended star formation is in fact predicted for some merger simulations for the high gas masses present in these high-redshift systems (Narayanan et al., 2009). The results from this chapter present an interesting introspective into this idea. In the $^{12}\text{CO } J = 3 \rightarrow 2$ observations, significant extended emission over 1.3 kpc that comprises 50% of the total emission is detected. This is somewhat larger than the typical assumed emission scales for local ULIRGs of < 1 kpc, though still relatively compact. It seems reasonable to suspect that with an increasing gas fraction at high redshift this extended component could be even larger. On the other hand, it is worth considering if these observations completely detect the extended size of Arp 220 or would additional extended gas be revealed by more sensitive lower resolution observations? These results caution careful use of physical size as an indicator of a merging or non-merging system. Ultimately, larger surveys of the most luminous SMGs coupled with resolved spatial kinematic follow-up observations of the gas in these galaxies will unravel whether these systems are mergers or disk galaxies with enhanced gas accretion. Certainly, if sub-kpc resolution with high S/N can be obtained to individually resolve two

different nuclear disks within one SMG, a merger would be unequivocally determined. In addition, the tidal features seen here in Arp 220, though probably difficult to detect, would present another possible identification of a merging system. Detailed understanding of the local ULIRGs, like Arp 220, will aid the community in making this distinction. It is clear that caution is warranted when trying to scale local systems to high-redshift systems that exist in a different environment.

One reason to determine which SMGs are starburst systems, driven by mergers, versus normal galaxies is to obtain accurate gas mass estimates from CO observations. The general practice for determining H_2 gas mass from CO line luminosity is to use a conversion factor of $0.8 M_{\odot} (\text{K km/s pc}^2)^{-1}$ for starburst systems and to use a Milky Way conversion factor of $4.0 M_{\odot} (\text{K km/s pc}^2)^{-1}$ for normal galaxies (Bolatto et al., 2013). While this conversion factor is not measured in this thesis for Arp 220, nor is a conversion factor suggested for SMGs, it is observed from the modeling that physical characteristics of the nuclei can impact the CO line luminosity. The CO line luminosity may, in turn, impact what the CO to H_2 conversion factor value should be. In particular, the observations and modeling show that there can be a significant effect on the line luminosity from the extreme optical depth in the Arp 220 nuclei absorbing continuum radiation. The absorption of the continuum radiation reduces the observed brightness of the CO emission in Arp 220. To be clear, the CO is still emitting at zero velocity, but due to the larger absorption of the continuum emission as compared to the CO emission, it appears in the continuum subtracted spectra that no CO emission is present. This reduced apparent emission is naturally dependent on the dust emission and thus the dust temperature. This effect is demonstrated in Figure 6.12. As such, the CO emission should not be considered without taking into account the possible absorption of the continuum emission. If continuum emission absorption was not taken into account, it might be concluded that there is less gas in the Arp 220 nucleus emitting, leading to underestimates of the gas mass. However, as with other physical factors contributing to the CO to H_2 conversion factor, this effect may be canceled out by another. For instance, a higher dust

temperature leading to reduced CO emission may also always be accompanied by a higher gas temperature leading to more CO emission. The results do show that consideration of continuum absorption in line measurements is warranted for systems with large optical depths when deriving line luminosities.

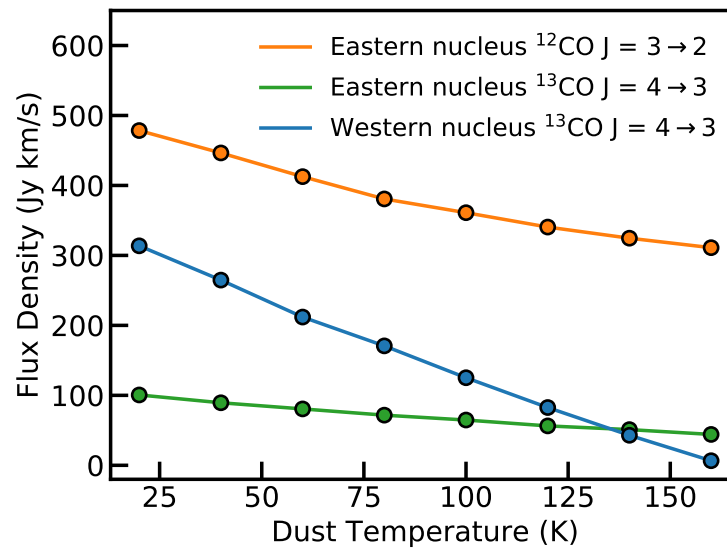


Figure 6.12: Plot showing the dependence of the cumulative flux density of the asymmetric disk model for the eastern nucleus and the model for the western nucleus if the dust temperature is changed. Due to significant continuum absorption in the western nucleus, there is a strong dependence on the CO brightness with dust temperature. A factor of two difference in total flux density is observed as the dust temperature is varied from 20 to 80 K. For the eastern nucleus, this dependence is weaker and is even weaker for the $^{13}\text{CO } J = 4 \rightarrow 3$ line which is not as optically thick.

6.8 Conclusions

The observations of Arp 220 in $^{12}\text{CO } J = 3 \rightarrow 2$, $^{13}\text{CO } J = 4 \rightarrow 3$, HCN $J = 5 \rightarrow 4$, and SiO $J = 8 \rightarrow 7$ reveal incredible amounts of new information into the morphology, kinematics, and internal physics of the Arp 220 nuclei and surrounding material. Extremely bright HCN emission is detected that is spatially different from the CO emission. Extremely deep SiO absorption is detected in the western nucleus but only just detected in the eastern

nucleus, suggesting shocks are significant in the western nucleus but less so for the eastern.

The extended emission detected in $^{12}\text{CO } J = 3 \rightarrow 2$ is significant in both flux, with an integrated emission greater than both nuclei combined, but also in structure. This points to the need for both high-resolution imaging to resolve the nuclear disks and also that lower resolution high sensitivity observations capturing the extended emission are equally important. This will be especially true for understanding flux contributions in unresolved measurements. The extended emission exhibits a $m = 2$ asymmetry which may be indicative of tidal torques that are the signature for gas inflow providing the fuel source for the strong nuclear star formation observed.

Outflows are again observed for the western nucleus in $^{12}\text{CO } J = 3 \rightarrow 2$ and for the first time are also strongly detected in the eastern nucleus. This demonstrates the power of these ALMA observations where outflows can be both kinematically and spatially resolved from the rest of the nuclear disks. Both nuclei's outflows are determined to contain significant mass. These outflows indicate that either star formation or AGN activity is contributing significant feedback, enriching the interstellar medium of Arp 220 with substantial amounts of gas. In addition, the depletion time scales of these outflows suggest that the massive amount of star formation in the Arp 220 system only represents a short time scale event in Arp 220's evolution.

The kinematic models of the eastern nucleus suggest a highly asymmetric disk in temperature as the best explanation for the asymmetric line profiles observed. Also, the inclusion of the less abundant ^{13}CO species in the models allows for ruling out the possibility of a foreground absorber as the cause of the asymmetric line profiles. This suggests fast time scale energetic events are present in the eastern nucleus with supernova as a plausible power source. In fact, given the frequency of supernova in the Arp 220 system, it seems remarkable that the nuclei are not more perturbed. It was also found that the line profiles of the eastern nucleus cannot be reproduced simply by adding in an outflow. Asymmetric line profiles may not always indicate the presence of an outflow.

The modeling of the western nucleus suggests the presence of high latitude absorbing gas in the disk. Furthermore, it demonstrates that the disk is highly optically thick, where even the ^{13}CO species is absorbing significant amounts of continuum radiation. In addition, modeling in both nuclei suggests that the inferred gas temperatures may have a dependence on the optical depth of the observed species. The extreme optical depth of Arp 220 demonstrates that the optical depth, the depth to which observations probe within a gas complex, must be considered when deriving the physical characteristics of the gas such as temperature. So much so, that observations of different abundance tracers of the same transition will not necessarily be probing the same component of gas. The continuum absorption by the molecular gas lines will reduce the total apparent emission from these lines.

Finally, it is concluded that a better understanding of the gas kinematics and physical characteristics of the nuclear disks could be obtained by incorporating a less abundant species such as C^{18}O to probe deeper into the nuclei. In addition, simultaneous modeling of multiple CO transitions that trace cold gas, warm gas, and a combination of both the cold and warm gas is needed to develop the best understanding of the gas temperatures both in value and in physical distribution within each nucleus.

Chapter 7

The Path Forward

In this thesis, we have demonstrated the advancement of millimeter and submillimeter spectroscopy in two different regimes: low-resolution spectrometer technology development and high-resolution observational data analysis. Both of these regimes are continuously developing and growing over time, and with this growth, our understanding of star formation and galaxy evolution will continue to flourish. As such, I will conclude this thesis with a brief discussion of how the aspects of this thesis will continue to evolve beyond that which has been presented.

7.1 Future of SuperSpec Technology

The basic functionality of SuperSpec technology for ground-based observations of high-redshift galaxies has been proven in the laboratory. Soon the SuperSpec technology will be demonstrated on the telescope, proving its ability to make important scientific measurements of the redshifts of submillimeter and millimeter continuum-detected galaxies. While the scientific observations that can be made with a several pixel demonstration instrument will be significant, it will not greatly surpass the ability of standard grating spectrometers to make the same measurements. Ultimately, the power of the SuperSpec technology is to multiplex many spectrometers into a single instrument, as discussed in Section 2.1.1 and 2.1.2.

Given the success of a SuperSpec demonstration instrument, a multi-object spectrom-

eter for a ground-based telescope with a large instantaneous viewing angle on the sky will be well motivated. Given an observation campaign on the order of a year, over 1,000 high-redshift galaxies could be observed, probing down to $6 \times 10^{11} L_{\odot}$ galaxies (Section 5.4). This would provide us with some of the best constraints of star formation in the high-redshift universe to date.

If an integral-field spectrometer is produced, the total [C II] emission from high-redshift galaxy populations can be measured. This measurement would yield the [C II] power spectrum, and thus measure the linear clustering signal. This, in turn, will probe the total [C II] intensity of all galaxies. Such a measurement would probe the faint emission from low-luminosity galaxies in a way that cannot otherwise be achieved. Furthermore, these measurements probe the mechanisms responsible for the re-ionization of the Universe. Both of these instruments could be produced with only minimal modification to the current SuperSpec architecture. However, significant effort would still be required to produce such instruments, as they would represent some of the most ambitious millimeter or submillimeter focal planes to ever be produced.

This does not mean that the technology development for SuperSpec is complete. There is still significant possibilities to improve and extend the technology to more astronomical applications. In particular, as discussed in Section 5.1, improved spectrometer NEP can be obtained by research into low-loss dielectric materials. In addition, low-loss dielectrics will also enable the SuperSpec technology to achieve higher resolution, which will yield improved redshift determination accuracy. At high enough resolution the lines will begin to be resolved, which will allow for some rough kinematic measurements of the gas in spectroscopic targets. Finally, increasing the bandwidth of SuperSpec spectrometers to include the 850 μm atmospheric window would allow for more detections over a broader range of redshifts.

7.1.1 SuperSpec for Orbital Platforms

Beyond ground-based instruments, the SuperSpec technology has inherent advantages for space-based or balloon-borne missions. This is because SuperSpec’s reduced size both decreases the weight and coolant requirements for such missions. All of the same instruments that are envisioned for ground-based observatories can be built for orbital platforms as well. In space, the background light levels are lower, especially if the telescope is actively cooled to cryogenic temperatures. This will allow for more sensitive measurements for the current SuperSpec bands and observations at shorter wavelengths that are not permitted from the ground, due to atmospheric absorption. While the idea of SuperSpec for orbital platforms is exciting, more technology development is required before this can be realized. In particular, as discussed in Section 2.2.1, to enable shorter wavelength observations, higher T_c transmission lines will need to be developed. Additionally, the SuperSpec detector technology has been shown to be background limited for ground-based spectroscopy (Section 3.3.2), but the current detector sensitivity will require substantial improvement to meet the requirements of orbital platforms.

The Origins Space Telescope (OST) is a NASA far-infrared flagship concept study designed to understand the origin and evolution of galaxies and habitable worlds that would launch in the 2030s. OST will require spectroscopic detectors with NEPs of 3×10^{-20} W/Hz^{0.5}. Some improvement in detector sensitivity can be made by further reducing the volume of the SuperSpec detectors, but the current size is not far from fabrication limits. Aluminum, as a kinetic inductance detector material, shows great promise for enabling these sensitive detectors, with NEPs of 3×10^{-19} W/Hz^{0.5} currently achieved (Baselmans et al., 2017). This is enabled by aluminum’s comparatively much larger quasiparticle time constants than TiN’s (Section 3.4). The above NEPs were achieved for detectors with volumes of $\sim 1000 \mu\text{m}^3$, a factor of almost 400 times larger than SuperSpec’s current detector volumes. Since we have seen that NEP improves with reduced volume, Section 3.3.1

and 3.3.2, it is not hard to imagine that an aluminum-based SuperSpec might be able to meet these requirements. The difficulty with switching to aluminum is achieving sufficient coupling between the resonant staple and the detectors because of aluminum's lower resistivity. None the less, tackling this technological challenge is an ongoing endeavor within the SuperSpec collaboration, for which progress is currently being made. That, however, is a subject for a future thesis. Given time and money, there is no reason to suspect that a space-based background limited SuperSpec spectrometer cannot be produced. The improved sensitivity on-board a spaced-based actively-cooled telescope would make for the ultimate submillimeter/far-infrared spectroscopic instrument.

7.2 Future ALMA Observations of Arp 220 and High-Redshift Galaxies

From the ALMA observations and modeling of Arp 220, we have shown that the internal physical gas properties can be determined. We found that the conditions and nature of the observed components of Arp 220 substantially impact the emission observed. These implications are important to consider when trying to understand the emission for unresolved sources at high-redshift. While the proper application of low-redshift observations of systems, like Arp 220, to higher redshift galaxies is unclear (Section 1.5 and 6.7); further study of both will help us to better understand the two populations and their context to each other.

Our studies of Arp 220 could be improved by obtaining additional observations of other CO transitions and species with different abundances, along with careful modeling of these lines. Some of these observations already exist and are waiting to be analyzed with the methodology described in Chapter 6. Yet, some still require new observations to be conducted. For example, additional lines at low and high J transitions will enable us to make important distinctions about the physical state of the nuclear gas, such as determining the contributions of different temperature gas to each line's emission. More specifically, the gas in the disks of both nuclei as well as the surrounding extended gas, including both the warm and cold components, need to be modeled separately and internally self consistently.

Because transitions of the dominant isotope are optically thick, which hampered our ability to model the western nucleus and to derive disk physical parameters, additional ^{13}CO and C^{18}O data could improve our physical constraints. Furthermore, observations of ^{12}CO $J = 4 - 3$ are also needed, to measure the $^{12}\text{CO}/^{13}\text{CO}$ isotope ratio to improve the molecular gas mass measurements we have made. There are limited opportunities to observe ^{13}CO (or C^{18}O) mid- J transitions in galaxies and Arp 220 is one of them. Thus, Arp 220 is an invaluable laboratory to study these isotopes.

Altogether, this data will provide a comprehensive understanding of the bulk molecular gas that is strongly affected by star formation, AGN, and dynamical processes in an iconic and nearby ultraluminous infrared galaxy (ULIRG). These observations and models will both inform theory of low-redshift galaxy mergers and provide context for unresolved observations of high-redshift galaxies. An important aspect of this is understanding the processes of feedback. Low-redshift merging systems like Arp 220 provide excellent laboratories for studying the feedback mechanisms in galaxies. The Arp 220 observations resolve significant outflows driven by star formation or AGN feedback. At high redshift, the systems may or may not be merging but the substantial star formation observed must be driving at least some feedback in the form of supernova-driven winds. These observations would be best coupled with similar spatially resolved observations of high-redshift galaxies to determine exactly what similarities are seen in the high-redshift systems. Unfortunately, such observations are expensive in terms of required time; yet, the catalog of spatially resolved observations of high-redshift galaxies is continuously growing (e.g. (Iono et al., 2016; Gullberg et al., 2018; Hodge et al., 2019)). Preliminary spectroscopic redshift determination with instruments like SuperSpec will help improve the efficiency of ALMA observations, which will enhance the growth of these observations. As discussed in Chapter 1, these detailed observations will prove invaluable for understanding what physical conditions and situations give rise to the emission that is indicative of star formation and AGN activity.

7.3 Outlook of Future Millimeter and Submillimeter Spectroscopy

Future survey spectroscopy instrumentation enabled by the SuperSpec technology will allow for the ultimate statistical constraint of the star formation history of the Universe at high redshift. A redshift search survey instrument would perfectly accompany ALMA's high spatially and kinematically resolved observations by identifying interesting candidates for ALMA follow-up. This would result in the most efficient use of ALMA's highly valuable time. The spatially and kinematically resolved observations will then allow astronomers to understand exactly what physical mechanisms and characteristics of these high-redshift galaxies lead to their observed star formation and AGN activity. It is clear that without an investment of the astrophysical community in millimeter and submillimeter spectroscopy, our understanding of star formation and galaxy evolution will be incomplete. Altogether, submillimeter and millimeter spectroscopic observations, alongside other multi-wavelength studies, of high-redshift galaxies will allow astronomers to unravel the mysteries of the early universe.

Bibliography

- S. Aalto, M. Spaans, M. C. Wiedner, and S. Hüttemeister. Overluminous HNC line emission in Arp 220, NGC 4418 and Mrk 231. Global IR pumping or XDRs? *A&A*, 464(1):193–200, Mar 2007. doi: 10.1051/0004-6361/20066473.
- S. Aalto, S. Martín, F. Costagliola, E. González-Alfonso, S. Muller, K. Sakamoto, G. A. Fuller, S. García-Burillo, P. van der Werf, and R. Neri. Probing highly obscured, self-absorbed galaxy nuclei with vibrationally excited HCN. *A&A*, 584:A42, Dec 2015. doi: 10.1051/0004-6361/201526410.
- S. Aalto, S. Muller, S. König, N. Falstad, J. Mangum, K. Sakamoto, G. C. Privon, J. Gallagher, F. Combes, S. García-Burillo, S. Martín, S. Viti, P. van der Werf, A. S. Evans, J. H. Black, E. Varenus, R. Beswick, G. Fuller, C. Henkel, K. Kohno, K. Alatalo, and S. Mühle. The hidden heart of the luminous infrared galaxy IC 860 I. A molecular inflow feeding opaque, extreme nuclear activity. *arXiv e-prints*, art. arXiv:1905.07275, May 2019.
- J. E. Austermann, J. S. Dunlop, T. A. Perera, K. S. Scott, G. W. Wilson, I. Aretxaga, D. H. Hughes, O. Almaini, E. L. Chapin, S. C. Chapman, M. Cirasuolo, D. L. Clements, K. E. K. Coppin, L. Dunne, S. Dye, S. A. Eales, E. Egami, D. Farrah, D. Ferrusca, S. Flynn, D. Haig, M. Halpern, E. Ibar, R. J. Ivison, E. van Kampen, Y. Kang, S. Kim, C. Lacey, J. D. Lowenthal, P. D. Mauskopf, R. J. McLure, A. M. J. Mortier, M. Negrello, S. Oliver, J. A. Peacock, A. Pope, S. Rawlings, G. Rieke, I. Roseboom, M. Rowan-Robinson, D. Scott, S. Serjeant, I. Smail, A. M. Swinbank, J. A. Stevens, M. Velazquez, J. Wagg, and M. S. Yun. AzTEC half square degree survey of the SHADES fields - I. Maps, catalogues and source counts. *MNRAS*, 401:160–176, Jan. 2010. doi: 10.1111/j.1365-2966.2009.15620.x.
- J. E. Austermann, J. A. Beall, S. A. Bryan, B. Dober, J. Gao, G. Hilton, J. Hubmayr, P. Mauskopf, C. M. McKenney, S. M. Simon, J. N. Ullom, M. R. Vissers, and G. W. Wilson. Millimeter-Wave Polarimeters Using Kinetic Inductance Detectors for TolTEC and Beyond. *Journal of Low Temperature Physics*, 193(3-4):120–127, Nov 2018. doi: 10.1007/s10909-018-1949-5.
- L. Barcos-Muñoz, A. K. Leroy, A. S. Evans, G. C. Privon, L. Armus, J. Condon, J. M. Mazzarella, D. S. Meier, E. Momjian, E. J. Murphy, J. Ott, A. Reichardt, K. Sakamoto, D. B. Sanders, E. Schinnerer, S. Stierwalt, J. A. Surace, T. A. Thompson, and F. Walter.

- High-resolution Radio Continuum Measurements of the Nuclear Disks of Arp 220. *ApJ*, 799:10, Jan. 2015. doi: 10.1088/0004-637X/799/1/10.
- L. Barcos-Muñoz, S. Aalto, T. A. Thompson, K. Sakamoto, S. Martín, A. K. Leroy, G. C. Privon, A. S. Evans, and A. Kepley. Fast, Collimated Outflow in the Western Nucleus of Arp 220. *ApJ*, 853(2):L28, Feb 2018. doi: 10.3847/2041-8213/aaa28d.
- A. J. Barger, L. L. Cowie, D. B. Sanders, E. Fulton, Y. Taniguchi, Y. Sato, K. Kawara, and H. Okuda. Submillimetre-wavelength detection of dusty star-forming galaxies at high redshift. *Nature*, 394:248–251, July 1998. doi: 10.1038/28338.
- J. E. Barnes and L. E. Hernquist. Fueling starburst galaxies with gas-rich mergers. *ApJ*, 370:L65–L68, Apr. 1991. doi: 10.1086/185978.
- P. S. Barry, E. Shirokoff, A. Kovács, T. J. Reck, S. Hailey-Dunsheath, C. M. McKenney, L. J. Swenson, M. I. Hollister, H. G. Leduc, S. Doyle, R. O’Brien, N. Llombart, D. Marrone, G. Chattopadhyay, P. K. Day, S. Padin, C. M. Bradford, P. D. Maukopf, and J. Zmuidzinas. Electromagnetic design for SuperSpec: a lithographically-patterned millimetre-wave spectrograph. In *Millimeter, Submillimeter, and Far-Infrared Detectors and Instrumentation for Astronomy VI*, volume 8452 of *Proc. SPIE*, page 84522F, Sept. 2012. doi: 10.1117/12.927089.
- J. J. A. Baselmans, J. Bueno, S. J. C. Yates, O. Yurduseven, N. Llombart, K. Karatsu, A. M. Baryshev, L. Ferrari, A. Endo, D. J. Thoen, P. J. de Visser, R. M. J. Janssen, V. Murugesan, E. F. C. Driessen, G. Coiffard, J. Martin-Pintado, P. Hargrave, and M. Griffin. A kilopixel imaging system for future space based far-infrared observatories using microwave kinetic inductance detectors. *A&A*, 601:A89, May 2017. doi: 10.1051/0004-6361/201629653.
- M. Béthermin, C. De Breuck, B. Gullberg, M. Aravena, M. S. Bothwell, S. C. Chapman, A. H. Gonzalez, T. R. Greve, K. Litke, J. Ma, M. Malkan, D. P. Marrone, E. J. Murphy, J. S. Spilker, A. A. Stark, M. Strandet, J. D. Vieira, A. Weiß, and N. Welikala. An ALMA view of the interstellar medium of the $z = 4.77$ lensed starburst SPT-S J213242-5802.9. *A&A*, 586:L7, Feb. 2016. doi: 10.1051/0004-6361/201527739.
- A. D. Bolatto, M. Wolfire, and A. K. Leroy. The CO-to-H₂ Conversion Factor. *ARA&A*, 51(1):207–268, Aug 2013. doi: 10.1146/annurev-astro-082812-140944.
- C. M. Bradford, P. A. R. Ade, J. E. Aguirre, J. J. Bock, M. Dragovan, L. Duband, L. Earle, J. Glenn, H. Matsuhara, B. J. Naylor, H. T. Nguyen, M. Yun, and J. Zmuidzinas. Z-Spec: a broadband millimeter-wave grating spectrometer: design, construction, and first cryogenic measurements. In C. M. Bradford, P. A. R. Ade, J. E. Aguirre, J. J. Bock, M. Dragovan, L. Duband, L. Earle, J. Glenn, H. Matsuhara, B. J. Naylor, H. T. Nguyen, M. Yun, and J. Zmuidzinas, editors, *Z-Spec: a broadband millimeter-wave grating spectrometer: design, construction, and first cryogenic measurements*, volume 5498 of *Proc. SPIE*, page 257, Oct. 2004. doi: 10.1117/12.552182.

- C. M. Bradford, S. Hailey-Dunsheath, E. Shirokoff, M. Hollister, C. M. McKenney, H. G. LeDuc, T. Reck, S. C. Chapman, A. Tikhomirov, T. Nikola, and J. Zmuidzinas. X-Spec: a multi-object trans-millimeter-wave spectrometer for CCAT. In Millimeter, Submillimeter, and Far-Infrared Detectors and Instrumentation for Astronomy VII, volume 9153 of Proc. SPIE, page 91531Y, Aug. 2014. doi: 10.1117/12.2056750.
- M. Bradford, A. Crites, J. Hunacek, S. Hailey-Dunsheath, M. B. Zemcov, J. Bock, A. R. Cooray, T.-C. Chang, C.-T. Li, B. Bumble, E. Shirokoff, Z. Staniszewski, R. O'Brient, C. Shiu, Y.-T. Cheng, and B. Uzgil. Probing the Epoch of Reionization via CII Tomography with TIME-Pilot. In American Astronomical Society Meeting Abstracts #227, volume 227 of American Astronomical Society Meeting Abstracts, page 426.07, Jan. 2016.
- C. Brinch and M. R. Hogerheijde. LIME - a flexible, non-LTE line excitation and radiation transfer method for millimeter and far-infrared wavelengths. A&A, 523:A25, Nov. 2010. doi: 10.1051/0004-6361/201015333.
- C. L. Carilli and F. Walter. Cool Gas in High-Redshift Galaxies. ARA&A, 51(1):105–161, Aug 2013. doi: 10.1146/annurev-astro-082812-140953.
- S. Carniani, R. Maiolino, R. Amorin, L. Pentericci, A. Pallottini, A. Ferrara, C. J. Willott, R. Smit, J. Matthee, D. Sobral, P. Santini, M. Castellano, S. De Barros, A. Fontana, A. Grazian, and L. Guaita. Kiloparsec-scale gaseous clumps and star formation at $z = 5-7$. MNRAS, 478:1170–1184, July 2018. doi: 10.1093/mnras/sty1088.
- C. M. Casey, D. Narayanan, and A. Cooray. Dusty star-forming galaxies at high redshift. Phys. Rep., 541(2):45–161, Aug 2014. doi: 10.1016/j.physrep.2014.02.009.
- C. M. Casey, J. A. Zavala, J. Spilker, E. da Cunha, J. Hodge, C.-L. Hung, J. Staguhn, S. L. Finkelstein, and P. Drew. The Brightest Galaxies in the Dark Ages: Galaxies Dust Continuum Emission during the Reionization Era. Astrophysical Journal, 862:77, July 2018. doi: 10.3847/1538-4357/aac82d.
- G. Cataldo, J. A. Beall, H.-M. Cho, B. McAndrew, M. D. Niemack, and E. J. Wollack. Infrared dielectric properties of low-stress silicon nitride. Optics Letters, 37(20):4200, Oct 2012. doi: 10.1364/OL.37.004200.
- S. C. Chapman, A. W. Blain, I. Smail, and R. J. Ivison. A Redshift Survey of the Submillimeter Galaxy Population. ApJ, 622:772–796, Apr. 2005. doi: 10.1086/428082.
- G. Che. Advancements in Kinetic Inductance Detector, Spectrometer, and Amplifier Technologies for Millimeter-Wave Astronomy. PhD thesis, Arizona State University, 2018.
- A. Chung, G. Narayanan, M. S. Yun, M. Heyer, and N. R. Erickson. The Redshift Search Receiver Observations of $^{12}\text{CO } J = 1 \rightarrow 0$ in 29 Ultraluminous Infrared Galaxies. AJ, 138: 858–872, Sept. 2009. doi: 10.1088/0004-6256/138/3/858.
- C. J. Conselice. The Evolution of Galaxy Structure Over Cosmic Time. ARA&A, 52:291–337, Aug 2014. doi: 10.1146/annurev-astro-081913-040037.

- K. Coppin, E. L. Chapin, A. M. J. Mortier, S. E. Scott, C. Borys, J. S. Dunlop, M. Halpern, D. H. Hughes, A. Pope, D. Scott, S. Serjeant, J. Wagg, D. M. Alexander, O. Almaini, I. Aretxaga, T. Babbedge, P. N. Best, A. Blain, S. Chapman, D. L. Clements, M. Crawford, L. Dunne, S. A. Eales, A. C. Edge, D. Farrah, E. Gaztañaga, W. K. Gear, G. L. Granato, T. R. Greve, M. Fox, R. J. Ivison, M. J. Jarvis, T. Jenness, C. Lacey, K. Lepage, R. G. Mann, G. Marsden, A. Martinez-Sansigre, S. Oliver, M. J. Page, J. A. Peacock, C. P. Pearson, W. J. Percival, R. S. Priddey, S. Rawlings, M. Rowan-Robinson, R. S. Savage, M. Seigar, K. Sekiguchi, L. Silva, C. Simpson, I. Smail, J. A. Stevens, T. Takagi, M. Vaccari, E. van Kampen, and C. J. Willott. The SCUBA Half-Degree Extragalactic Survey - II. Submillimetre maps, catalogue and number counts. *MNRAS*, 372:1621–1652, Nov. 2006. doi: 10.1111/j.1365-2966.2006.10961.x.
- T. J. Cox, P. Jonsson, J. R. Primack, and R. S. Somerville. Feedback in simulations of disc-galaxy major mergers. *MNRAS*, 373:1013–1038, Dec. 2006. doi: 10.1111/j.1365-2966.2006.11107.x.
- A. T. Crites, J. J. Bock, C. M. Bradford, T. C. Chang, A. R. Cooray, L. Duband, Y. Gong, S. Hailey-Dunsheath, J. Hunacek, P. M. Koch, C. T. Li, R. C. O’Brien, T. Prouve, E. Shirokoff, M. B. Silva, Z. Staniszewski, B. Uzglil, and M. Zemcov. The TIME-Pilot intensity mapping experiment. In *Millimeter, Submillimeter, and Far-Infrared Detectors and Instrumentation for Astronomy VII*, volume 9153 of *Proc. SPIE*, page 91531W, Aug. 2014. doi: 10.1117/12.2057207.
- D. A. Dale, J. D. T. Smith, E. A. Schlawin, L. Armus, B. A. Buckalew, S. A. Cohen, G. Helou, T. H. Jarrett, L. C. Johnson, J. Moustakas, E. J. Murphy, H. Roussel, K. Sheth, S. Staudaher, C. Bot, D. Calzetti, C. W. Engelbracht, K. D. Gordon, D. J. Hollenbach, R. C. Kennicutt, and S. Malhotra. The Spitzer Infrared Nearby Galaxies Survey: A High-Resolution Spectroscopy Anthology. *ApJ*, 693:1821–1834, Mar. 2009. doi: 10.1088/0004-637X/693/2/1821.
- R. Davé, K. Finlator, B. D. Oppenheimer, M. Fardal, N. Katz, D. Kereš, and D. H. Weinberg. The nature of submillimetre galaxies in cosmological hydrodynamic simulations. *MNRAS*, 404:1355–1368, May 2010. doi: 10.1111/j.1365-2966.2010.16395.x.
- I. De Looze, M. Baes, G. J. Bendo, L. Cortese, and J. Fritz. The reliability of [C II] as an indicator of the star formation rate. *MNRAS*, 416(4):2712–2724, Oct 2011. doi: 10.1111/j.1365-2966.2011.19223.x.
- P. J. de Visser, J. J. A. Baselmans, P. Diener, S. J. C. Yates, A. Endo, and T. M. Klapwijk. Generation-recombination noise: The fundamental sensitivity limit for kinetic inductance detectors. *Journal of Low Temperature Physics*, 167(3):335–340, May 2012. ISSN 1573-7357. doi: 10.1007/s10909-012-0519-5. URL <https://doi.org/10.1007/s10909-012-0519-5>.
- R. Decarli, F. Walter, R. Neri, F. Bertoldi, C. Carilli, P. Cox, J. P. Kneib, J. F. Lestrade, R. Maiolino, A. Omont, J. Richard, D. Riechers, K. Thanjavur, and A. Weiss. Ionized Nitrogen at High Redshift. *ApJ*, 752:2, June 2012. doi: 10.1088/0004-637X/752/1/2.

- R. Decarli, F. Walter, C. Carilli, F. Bertoldi, P. Cox, C. Ferkinhoff, B. Groves, R. Maiolino, R. Neri, D. Riechers, and A. Weiss. Varying [C II]/[N II] Line Ratios in the Interacting System BR1202-0725 at $z = 4.7$. *ApJ*, 782(2):L17, Feb 2014. doi: 10.1088/2041-8205/782/2/L17.
- H. Dole, G. Lagache, J. L. Puget, K. I. Caputi, N. Fernández-Conde, E. Le Floch, C. Papovich, P. G. Pérez-González, G. H. Rieke, and M. Blaylock. The cosmic infrared background resolved by Spitzer. Contributions of mid-infrared galaxies to the far-infrared background. *A&A*, 451:417–429, May 2006. doi: 10.1051/0004-6361:20054446.
- C. D. Dowell, A. Conley, J. Glenn, V. Arumugam, V. Asboth, H. Aussel, F. Bertoldi, M. Béthermin, J. Bock, A. Boselli, C. Bridge, V. Buat, D. Burgarella, A. Cabrera-Lavers, C. M. Casey, S. C. Chapman, D. L. Clements, L. Conversi, A. Cooray, H. Dannerbauer, F. De Bernardis, T. P. Ellsworth-Bowers, D. Farrah, A. Franceschini, M. Griffin, M. A. Gurwell, M. Halpern, E. Hatziminaoglou, S. Heinis, E. Ibar, R. J. Ivison, N. Laporte, L. Marchetti, P. Martínez-Navajas, G. Marsden, G. E. Morrison, H. T. Nguyen, B. O’Halloran, S. J. Oliver, A. Omont, M. J. Page, A. Papageorgiou, C. P. Pearson, G. Petitpas, I. Pérez-Fournon, M. Pohlen, D. Riechers, D. Rigopoulou, I. G. Roseboom, M. Rowan-Robinson, J. Sayers, B. Schulz, D. Scott, N. Seymour, D. L. Shupe, A. J. Smith, A. Streblyanska, M. Symeonidis, M. Vaccari, I. Valtchanov, J. D. Vieira, M. Viero, L. Wang, J. Wardlow, C. K. Xu, and M. Zemcov. HerMES: Candidate High-redshift Galaxies Discovered with Herschel/SPIRE. *Astrophysical Journal*, 780:75, Jan. 2014. doi: 10.1088/0004-637X/780/1/75.
- D. Downes and P. M. Solomon. Rotating Nuclear Rings and Extreme Starbursts in Ultraluminous Galaxies. *ApJ*, 507:615–654, Nov. 1998. doi: 10.1086/306339.
- B. T. Draine and E. E. Salpeter. On the physics of dust grains in hot gas. *ApJ*, 231:77–94, July 1979. doi: 10.1086/157165.
- R. Duan, S. McHugh, B. Serfass, B. A. Mazin, A. Merrill, S. R. Golwala, T. P. Downes, N. Czakon, P. Day, J. Gao, J. Glenn, M. Hollister, H. Leduc, P. R. Maloney, O. Noroozian, H. Nguyen, J. Sayers, J. A. Schlaerth, S. Siegel, and J. Zmuidzinas. An open-source readout for mkids. *Proceedings of SPIE - The International Society for Optical Engineering*, 7741, 07 2010. doi: 10.1117/12.856832.
- A. Endo, K. Karatsu, A. P. Laguna, B. Mirzaei, R. Huiting, D. J. Thoen, V. Murugesan, S. J. C. Yates, J. Bueno, N. van Marrewijk, S. Bosma, O. Yurduseven, N. Llombart, J. Suzuki, M. Naruse, P. J. de Visser, P. P. van der Werf, T. M. Klapwijk, and J. J. A. Baselmans. Wideband on-chip terahertz spectrometer based on a superconducting filterbank. *arXiv e-prints*, art. arXiv:1901.06934, Jan 2019.
- H. Engel, L. J. Tacconi, R. I. Davies, R. Neri, I. Smail, S. C. Chapman, R. Genzel, P. Cox, T. R. Greve, R. J. Ivison, A. Blain, F. Bertoldi, and A. Omont. MOST SUBMILLIMETER GALAXIES ARE MAJOR MERGERS. *The Astrophysical Journal*, 724(1):233–243, nov 2010. doi: 10.1088/0004-637x/724/1/233. URL <https://doi.org/10.1088/0004-637x/724/1/233>.

- N. Erickson, G. Narayanan, R. Goeller, and R. Grosslein. An Ultra-Wideband Receiver and Spectrometer for 74–110 GHz. In A. J. Baker, J. Glenn, A. I. Harris, J. G. Mangum, and M. S. Yun, editors, From Z-Machines to ALMA: (Sub)Millimeter Spectroscopy of Galaxies, volume 375 of Astronomical Society of the Pacific Conference Series, page 71, Oct. 2007.
- D. Espada, S. Komugi, E. Muller, K. Nakanishi, M. Saito, K. Tatematsu, S. Iguchi, T. Hasegawa, N. Mizuno, and D. Iono. Giant Molecular Clouds and Star Formation in the Tidal Molecular Arm of NGC 4039. ApJ, 760(2):L25, Dec 2012. doi: 10.1088/2041-8205/760/2/L25.
- C.-A. Faucher-Giguère, D. Kereš, and C.-P. Ma. The baryonic assembly of dark matter haloes. MNRAS, 417:2982–2999, Nov. 2011. doi: 10.1111/j.1365-2966.2011.19457.x.
- C. Ferkinhoff, D. Brisbin, T. Nikola, S. C. Parshley, G. J. Stacey, T. G. Phillips, E. Falgarone, D. J. Benford, J. G. Staguhn, and C. E. Tucker. First Detections of the [N II] 122 μm Line at High Redshift: Demonstrating the Utility of the Line for Studying Galaxies in the Early Universe. ApJ, 740:L29, Oct. 2011. doi: 10.1088/2041-8205/740/1/L29.
- C. Ferkinhoff, D. Brisbin, T. Nikola, G. J. Stacey, K. Sheth, S. Hailey-Dunsheath, and E. Falgarone. Band-9 ALMA Observations of the [N II] 122 μm Line and FIR Continuum in Two High- z galaxies. ApJ, 806(2):260, Jun 2015. doi: 10.1088/0004-637X/806/2/260.
- J. A. Fernández-Ontiveros, L. Spinoglio, M. Pereira-Santaella, M. A. Malkan, P. Andreani, and K. M. Dasyra. Far-infrared Line Spectra of Active Galaxies from the Herschel/PACS Spectrometer: The Complete Database. ApJS, 226:19, Oct. 2016. doi: 10.3847/0067-0049/226/2/19.
- L. Ferrarese and D. Merritt. A Fundamental Relation between Supermassive Black Holes and Their Host Galaxies. ApJ, 539:L9–L12, Aug. 2000. doi: 10.1086/312838.
- D. F. Filipovic, S. S. Gearhart, and G. M. Rebeiz. Double-slot antennas on extended hemispherical and elliptical silicon dielectric lenses. IEEE Transactions on Microwave Theory Techniques, 41:1738–1749, Oct. 1993. doi: 10.1109/22.247919.
- J. Gao. The Physics of Superconducting Microwave Resonators. PhD thesis, California Institute of Technology, 2008.
- J. Gao, J. Zmuidzinas, B. A. Mazin, H. G. LeDuc, and P. K. Day. Noise properties of superconducting coplanar waveguide microwave resonators. Applied Physics Letters, 90(10):102507, Mar 2007. doi: 10.1063/1.2711770.
- J. Gao, M. Daal, J. M. Martinis, A. Vayonakis, J. Zmuidzinas, B. Sadoulet, B. A. Mazin, P. K. Day, and H. G. Leduc. A semiempirical model for two-level system noise in superconducting microresonators. Applied Physics Letters, 92(21):212504, May 2008. doi: 10.1063/1.2937855.

- J. Gao, J. Zmuidzinas, A. Vayonakis, P. Day, B. Mazin, and H. Leduc. Equivalence of the effects on the complex conductivity of superconductor due to temperature change and external pair breaking. *Journal of Low Temperature Physics*, 151(1):557–563, Apr 2008. ISSN 1573-7357. doi: 10.1007/s10909-007-9688-z. URL <https://doi.org/10.1007/s10909-007-9688-z>.
- J. Gao, A. Vayonakis, O. Noroozian, J. Zmuidzinas, P. K. Day, and H. G. Leduc. Measurement of loss in superconducting microstrip at millimeter-wave frequencies. In B. Young, B. Cabrera, and A. Miller, editors, *American Institute of Physics Conference Series*, volume 1185 of *American Institute of Physics Conference Series*, pages 164–167, Dec. 2009. doi: 10.1063/1.3292306.
- J. Gao, M. R. Vissers, M. O. Sandberg, F. C. S. da Silva, S. W. Nam, D. P. Pappas, D. S. Wisbey, E. C. Langman, S. R. Meeker, B. A. Mazin, H. G. Leduc, J. Zmuidzinas, and K. D. Irwin. A titanium-nitride near-infrared kinetic inductance photon-counting detector and its anomalous electrodynamic. *Applied Physics Letters*, 101(14):142602, Oct. 2012. doi: 10.1063/1.4756916.
- J. Glenn, R. Aikin, J. Aguirre, L. Earle, P. Maloney, J. J. Bock, C. M. Bradford, M. Dragan, H. Nguyen, B. Naylor, J. Zmuidzinas, L. Duband, H. Matsuhara, and P. A. R. Ade. Z-Spec: A Dispersive Millimeter-Wave Spectrometer. In A. J. Baker, J. Glenn, A. I. Harris, J. G. Mangum, and M. S. Yun, editors, *From Z-Machines to ALMA: (Sub)Millimeter Spectroscopy of Galaxies*, volume 375 of *Astronomical Society of the Pacific Conference Series*, page 63, Oct. 2007.
- J. Glenn, A. Conley, M. Béthermin, B. Altieri, A. Amblard, V. Arumugam, H. Aussel, T. Babbedge, A. Blain, J. Bock, A. Boselli, V. Buat, N. Castro-Rodríguez, A. Cava, P. Chaniai, D. L. Clements, L. Conversi, A. Cooray, C. D. Dowell, E. Dwek, S. Eales, D. Elbaz, T. P. Ellsworth-Bowers, M. Fox, A. Franceschini, W. Gear, M. Griffin, M. Halpern, E. Hatziminaoglou, E. Ibar, K. Isaak, R. J. Ivison, G. Lagache, G. Laurent, L. Levenson, N. Lu, S. Madden, B. Maffei, G. Mainetti, L. Marchetti, G. Marsden, H. T. Nguyen, B. O’Halloran, S. J. Oliver, A. Omont, M. J. Page, P. Panuzzo, A. Papa-georgiou, C. P. Pearson, I. Pérez-Fournon, M. Pohlen, D. Rigopoulou, D. Rizzo, I. G. Roseboom, M. Rowan-Robinson, M. S. Portal, B. Schulz, D. Scott, N. Seymour, D. L. Shupe, A. J. Smith, J. A. Stevens, M. Symeonidis, M. Trichas, K. E. Tugwell, M. Vaccari, I. Valtchanov, J. D. Vieira, L. Vigroux, L. Wang, R. Ward, G. Wright, C. K. Xu, and M. Zemcov. HerMES: deep galaxy number counts from a P(D) fluctuation analysis of SPIRE Science Demonstration Phase observations. *MNRAS*, 409(1):109–121, Nov 2010. doi: 10.1111/j.1365-2966.2010.17781.x.
- P. F. Goldsmith, U. A. Yıldız, W. D. Langer, and J. L. Pineda. Herschel Galactic Plane Survey of [NII] Fine Structure Emission. *ApJ*, 814(2):133, Dec 2015. doi: 10.1088/0004-637X/814/2/133.
- S. Gordon. *Highly Multiplexed Superconducting Detectors and Readout Electronics for Balloon-Borne and Ground-Based Far-Infrared Imaging and Polarimetry*. PhD thesis, Arizona State University, 2019.

- S. Gordon, B. Dober, A. Sinclair, S. Rowe, S. Bryan, P. Mauskopf, J. Austermann, M. Devlin, S. Dicker, J. Gao, G. C. Hilton, J. Hubmayr, G. Jones, J. Klein, N. P. Lourie, C. McKenney, F. Nati, J. D. Soler, M. Strader, and M. Vissers. An Open Source, FPGA-Based LeKID Readout for BLAST-TNG: Pre-Flight Results. Journal of Astronomical Instrumentation, 5(4):1641003, Dec 2016. doi: 10.1142/S2251171716410038.
- T. R. Greve, A. Pope, D. Scott, R. J. Ivison, C. Borys, C. J. Conselice, and F. Bertoldi. A 1200- μm MAMBO survey of the GOODS-N field: a significant population of submillimetre dropout galaxies. MNRAS, 389(4):1489–1506, Oct 2008. doi: 10.1111/j.1365-2966.2008.13631.x.
- B. A. Groves, M. A. Dopita, and R. S. Sutherland. Dusty, Radiation Pressure-Dominated Photoionization. II. Multiwavelength Emission Line Diagnostics for Narrow-Line Regions. ApJS, 153:75–91, July 2004. doi: 10.1086/421114.
- B. Gullberg, C. De Breuck, J. D. Vieira, A. Weiß, J. E. Aguirre, M. Aravena, M. Béthermin, C. M. Bradford, M. S. Bothwell, J. E. Carlstrom, S. C. Chapman, C. D. Fassnacht, A. H. Gonzalez, T. R. Greve, Y. Hezaveh, W. L. Holzapfel, K. Husband, J. Ma, M. Malkan, D. P. Marrone, K. Menten, E. J. Murphy, C. L. Reichardt, J. S. Spilker, A. A. Stark, M. Strand et, and N. Welikala. The nature of the [C II] emission in dusty star-forming galaxies from the SPT survey. MNRAS, 449(3):2883–2900, May 2015. doi: 10.1093/mnras/stv372.
- B. Gullberg, A. M. Swinbank, I. Smail, A. D. Biggs, F. Bertoldi, C. De Breuck, S. C. Chapman, C.-C. Chen, E. A. Cooke, K. E. K. Coppin, P. Cox, H. Dannerbauer, J. S. Dunlop, A. C. Edge, D. Farrah, J. E. Geach, T. R. Greve, J. Hodge, E. Ibar, R. J. Ivison, A. Karim, E. Schinnerer, D. Scott, J. M. Simpson, S. M. Stach, A. P. Thomson, P. van der Werf, F. Walter, J. L. Wardlow, and A. Weiss. The Dust and [C II] Morphologies of Redshift ~ 4.5 Sub-millimeter Galaxies at ~ 200 pc Resolution: The Absence of Large Clumps in the Interstellar Medium at High-redshift. ApJ, 859:12, May 2018. doi: 10.3847/1538-4357/aabe8c.
- S. Hailey-Dunsheath. SuperSpec Spectral Profiles. Internal Memorandum, 2015.
- S. Hailey-Dunsheath. Log-Spaced Filterbank Optimization. Internal Memorandum, 2016.
- S. Hailey-Dunsheath, E. Shirokoff, P. S. Barry, C. M. Bradford, S. Chapman, G. Che, J. Glenn, M. Hollister, A. Kovács, H. G. LeDuc, P. Mauskopf, C. McKenney, R. O’Brien, S. Padin, T. Reck, C. Shiu, C. E. Tucker, J. Wheeler, R. Williamson, and J. Zmuidzinas. Low Noise Titanium Nitride KIDs for SuperSpec: A Millimeter-Wave On-Chip Spectrometer. Journal of Low Temperature Physics, 184(1-2):180–187, Jul 2016. doi: 10.1007/s10909-015-1375-x.
- S. Hailey-Dunsheath, A. C. M. Barlis, J. E. Aguirre, C. M. Bradford, J. G. Redford, T. S. Billings, H. G. LeDuc, C. M. McKenney, and M. I. Hollister. Development of aluminum lekids for balloon-borne far-ir spectroscopy. Journal of Low Temperature Physics, 193(5):968–975, Dec 2018. ISSN 1573-7357. doi: 10.1007/s10909-018-1927-y. URL <https://doi.org/10.1007/s10909-018-1927-y>.

- U. Haris, V. S. Parvathi, S. B. Gudennavar, S. G. Bubbly, J. Murthy, and U. J. Sofia. Silicon Depletion in the Interstellar Medium. *AJ*, 151:143, June 2016. doi: 10.3847/0004-6256/151/6/143.
- K. C. Harrington, M. S. Yun, R. Cybulski, G. W. Wilson, I. Aretxaga, M. Chavez, V. De la Luz, N. Erickson, D. Ferrusca, A. D. Gallup, D. H. Hughes, A. Montaña, G. Narayanan, D. Sánchez-Argüelles, F. P. Schloerb, K. Souccar, E. Terlevich, R. Terlevich, M. Zeballos, and J. A. Zavala. Early science with the Large Millimeter Telescope: observations of extremely luminous high- z sources identified by Planck. *MNRAS*, 458:4383–4399, June 2016. doi: 10.1093/mnras/stw614.
- M. G. Hauser and E. Dwek. The Cosmic Infrared Background: Measurements and Implications. *Annual Review of Astronomy and Astrophysics*, 39:249–307, Jan 2001. doi: 10.1146/annurev.astro.39.1.249.
- C. C. Hayward, P. Jonsson, D. Kereš, B. Magnelli, L. Hernquist, and T. J. Cox. How to distinguish starbursts and quiescently star-forming galaxies: the ‘bimodal’ submillimetre galaxy population as a case study. *MNRAS*, 424:951–970, Aug. 2012. doi: 10.1111/j.1365-2966.2012.21254.x.
- T. M. Heckman and P. N. Best. The Coevolution of Galaxies and Supermassive Black Holes: Insights from Surveys of the Contemporary Universe. *ARA&A*, 52:589–660, Aug 2014. doi: 10.1146/annurev-astro-081913-035722.
- L. C. Ho and E. Keto. The Mid-Infrared Fine-Structure Lines of Neon as an Indicator of Star Formation Rate in Galaxies. *ApJ*, 658(1):314–318, Mar 2007. doi: 10.1086/511260.
- J. A. Hodge, I. Smail, F. Walter, E. da Cunha, A. M. Swinbank, M. Rybak, B. Venemans, W. N. Brandt, G. Calistro Rivera, and S. C. Chapman. ALMA Reveals Potential Evidence for Spiral Arms, Bars, and Rings in High-redshift Submillimeter Galaxies. *ApJ*, 876(2): 130, May 2019. doi: 10.3847/1538-4357/ab1846.
- D. J. Hollenbach and A. G. G. M. Tielens. Photodissociation regions in the interstellar medium of galaxies. *Reviews of Modern Physics*, 71:173–230, Jan. 1999. doi: 10.1103/RevModPhys.71.173.
- D. H. Hughes, S. Serjeant, J. Dunlop, M. Rowan-Robinson, A. Blain, R. G. Mann, R. Ivison, J. Peacock, A. Efstathiou, W. Gear, S. Oliver, A. Lawrence, M. Longair, P. Goldschmidt, and T. Jenness. High-redshift star formation in the Hubble Deep Field revealed by a submillimetre-wavelength survey. *Nature*, 394:241–247, July 1998. doi: 10.1038/28328.
- J. Hunacek, J. Bock, C. M. Bradford, B. Bumble, T.-C. Chang, Y.-T. Cheng, A. Cooray, A. Crites, S. Hailey-Dunsheath, Y. Gong, M. Kenyon, P. Koch, C.-T. Li, R. O’Brien, E. Shirokoff, C. Shiu, Z. Staniszewski, B. Uzgil, and M. Zemcov. Design and Fabrication of TES Detector Modules for the TIME-Pilot [CII] Intensity Mapping Experiment. *Journal of Low Temperature Physics*, 184:733–738, Aug. 2016a. doi: 10.1007/s10909-015-1359-x.

- J. Hunacek, J. Bock, C. M. Bradford, B. Bumble, T.-C. Chang, Y.-T. Cheng, A. Cooray, A. Crites, S. Hailey-Dunsheath, Y. Gong, C.-T. Li, R. O'Brien, E. Shirokoff, C. Shiu, J. Sun, Z. Staniszewski, B. Uzgil, and M. Zemcov. Detector modules and spectrometers for the TIME-Pilot [CII] intensity mapping experiment. In Millimeter, Submillimeter, and Far-Infrared Detectors and Instrumentation for Astronomy VIII, volume 9914 of Proc. SPIE, page 99140L, July 2016b. doi: 10.1117/12.2233762.
- J. Hunacek, J. Bock, C. M. Bradford, V. Butler, T.-C. Chang, Y.-T. Cheng, A. Cooray, A. Crites, C. Frez, S. Hailey-Dunsheath, B. Hoscheit, D. W. Kim, C.-T. Li, D. Marrone, L. Moncelsi, E. Shirokoff, B. Steinbach, G. Sun, I. Trumper, A. Turner, B. Uzgil, A. Weber, and M. Zemcov. Hafnium Films and Magnetic Shielding for TIME, A mm-Wavelength Spectrometer Array. Journal of Low Temperature Physics, 193:893–900, Dec. 2018. doi: 10.1007/s10909-018-1906-3.
- D. Iono, M. S. Yun, I. Aretxaga, B. Hatsukade, D. Hughes, S. Ikarashi, T. Izumi, R. Kawabe, K. Kohno, M. Lee, Y. Matsuda, K. Nakanishi, T. Saito, Y. Tamura, J. Ueda, H. Umehata, G. Wilson, T. Michiyama, and M. Ando. Clumpy and Extended Starbursts in the Brightest Unlensed Submillimeter Galaxies. ApJ, 829:L10, Sept. 2016. doi: 10.3847/2041-8205/829/1/L10.
- R. J. Ivison, A. J. R. Lewis, A. Weiss, V. Arumugam, J. M. Simpson, W. S. Holland, S. Maddox, L. Dunne, E. Valiante, P. van der Werf, A. Omont, H. Dannerbauer, I. Smail, F. Bertoldi, M. Bremer, R. S. Bussmann, Z.-Y. Cai, D. L. Clements, A. Cooray, G. De Zotti, S. A. Eales, C. Fuller, J. Gonzalez-Nuevo, E. Ibar, M. Negrello, I. Oteo, I. Pérez-Fournon, D. Riechers, J. A. Stevens, A. M. Swinbank, and J. Wardlow. The Space Density of Luminous Dusty Star-forming Galaxies at $z > 4$: SCUBA-2 and LABOCA Imaging of Ultrared Galaxies from Herschel-ATLAS. Astrophysical Journal, 832:78, Nov. 2016. doi: 10.3847/0004-637X/832/1/78.
- L. Japan Coax Co. Cryogenic cables, 2019. URL <http://www.coax.co.jp/en/cryogenic>.
- K. V. Johnston, J. S. Bullock, S. Sharma, A. Font, B. E. Robertson, and S. N. Leitner. Tracing Galaxy Formation with Stellar Halos. II. Relating Substructure in Phase and Abundance Space to Accretion Histories. ApJ, 689(2):936–957, Dec 2008. doi: 10.1086/592228.
- J. Kamenetzky, N. Rangwala, and J. Glenn. Warm and cold molecular gas conditions modelled in 87 galaxies observed by the Herschel SPIRE Fourier transform spectrometer. MNRAS, 471(3):2917–2931, Nov 2017. doi: 10.1093/mnras/stx1595.
- A. King and K. Pounds. Powerful Outflows and Feedback from Active Galactic Nuclei. ARA&A, 53:115–154, Aug 2015. doi: 10.1146/annurev-astro-082214-122316.
- M. P. Koprowski, J. S. Dunlop, M. J. Michałowski, I. Roseboom, J. E. Geach, M. Cirasuolo, I. Aretxaga, R. A. A. Bowler, M. Banerji, N. Bourne, K. E. K. Coppin, S. Chapman,

- D. H. Hughes, T. Jenness, R. J. McLure, M. Symeonidis, and P. v. d. Werf. The SCUBA-2 Cosmology Legacy Survey: galaxies in the deep 850 μm survey, and the star-forming ‘main sequence’. *MNRAS*, 458:4321–4344, June 2016. doi: 10.1093/mnras/stw564.
- A. Kovács, P. S. Barry, C. M. Bradford, G. Chattopadhyay, P. Day, S. Doyle, S. Hailey-Dunsheath, M. Hollister, C. McKenney, H. G. LeDuc, N. Llombart, D. P. Marrone, P. Mauskopf, R. C. O’Brien, S. Padin, L. J. Swenson, and J. Zmuidzinas. SuperSpec: design concept and circuit simulations. In *Millimeter, Submillimeter, and Far-Infrared Detectors and Instrumentation for Astronomy VI*, volume 8452 of *Society of Photo-Optical Instrumentation Engineers (SPIE) Conference Series*, page 84522G, Sep 2012. doi: 10.1117/12.927160.
- S. Kumar, J. Gao, J. Zmuidzinas, B. A. Mazin, H. G. LeDuc, and P. K. Day. Temperature dependence of the frequency and noise of superconducting coplanar waveguide resonators. *Applied Physics Letters*, 92(12):123503, Mar 2008. doi: 10.1063/1.2894584.
- A. Kushino, M. Ohkubo, and K. Fujioka. Thermal conduction measurement of miniature coaxial cables between 0.3 and 4.5k for the wiring of superconducting detectors. *Cryogenics*, 45(9):637 – 640, 2005. ISSN 0011-2275. doi: <https://doi.org/10.1016/j.cryogenics.2005.07.002>. URL <http://www.sciencedirect.com/science/article/pii/S0011227505001001>.
- G. Lagache, M. Cousin, and M. Chatzikos. The [CII] 158 μm line emission in high-redshift galaxies. *A&A*, 609:A130, Feb. 2018. doi: 10.1051/0004-6361/201732019.
- S. M. LaMassa, T. M. Heckman, A. Ptak, D. Schiminovich, M. O’Dowd, and B. Bertincourt. Exploring the Connection between Star Formation and Active Galactic Nucleus Activity in the Local Universe. *ApJ*, 758:1, Oct. 2012. doi: 10.1088/0004-637X/758/1/1.
- R. B. Larson. Turbulence and star formation in molecular clouds. *MNRAS*, 194:809–826, Mar 1981. doi: 10.1093/mnras/194.4.809.
- H. G. Leduc, B. Bumble, P. K. Day, B. H. Eom, J. Gao, S. Golwala, B. A. Mazin, S. McHugh, A. Merrill, D. C. Moore, O. Noroozian, A. D. Turner, and J. Zmuidzinas. Titanium nitride films for ultrasensitive microresonator detectors. *Applied Physics Letters*, 97(10):102509, Sep 2010. doi: 10.1063/1.3480420.
- X. Liu, W. Guo, Y. Wang, M. Dai, L. F. Wei, B. Dober, C. McKenney, G. C. Hilton, J. Hubmayr, and J. E. Austermann. Superconducting micro-resonator arrays with ideal frequency spacing and extremely low frequency collision rate. *arXiv e-prints*, art. arXiv:1711.07914, Nov 2017.
- C. J. Lonsdale, P. J. Diamond, H. Thrall, H. E. Smith, and C. J. Lonsdale. VLBI Images of 49 Radio Supernovae in Arp 220. *ApJ*, 647:185–193, Aug. 2006. doi: 10.1086/505193.
- N. Lu, Y. Zhao, T. Díaz-Santos, C. K. Xu, V. Charmandaris, Y. Gao, P. P. van der Werf, G. C. Privon, H. Inami, D. Rigopoulou, D. B. Sanders, and L. Zhu. ALMA [N II] 205 μm

- Imaging Spectroscopy of the Interacting Galaxy System BRI 1202-0725 at Redshift 4.7. *ApJ*, 842(2):L16, Jun 2017. doi: 10.3847/2041-8213/aa77fc.
- N. Lu, T. Cao, T. Díaz-Santos, Y. Zhao, G. C. Privon, C. Cheng, Y. Gao, C. K. Xu, V. Charmandaris, D. Rigopoulou, P. P. van der Werf, J. Huang, Z. Wang, A. S. Evans, and D. B. Sanders. CO (7-6), [C I] 370 μm , and [N II] 205 μm Line Emission of the QSO BRI 1335-0417 at Redshift 4.407. *ApJ*, 864(1):38, Sep 2018. doi: 10.3847/1538-4357/aad3c9.
- P. Madau and M. Dickinson. Cosmic Star-Formation History. *Annual Review of Astronomy and Astrophysics*, 52:415–486, Aug 2014. doi: 10.1146/annurev-astro-081811-125615.
- S. Martín, M. Krips, J. Martín-Pintado, S. Aalto, J. H. Zhao, A. B. Peck, G. R. Petitpas, R. Monje, T. R. Greve, and T. An. The Submillimeter Array 1.3 mm line survey of Arp 220. *A&A*, 527:A36, Mar 2011. doi: 10.1051/0004-6361/201015855.
- S. Martín, S. Aalto, K. Sakamoto, E. González-Alfonso, S. Muller, C. Henkel, S. García-Burillo, R. Aladro, F. Costagliola, N. Harada, M. Krips, J. Martín-Pintado, S. Mühle, P. van der Werf, and S. Viti. The unbearable opaqueness of Arp220. *A&A*, 590:A25, May 2016. doi: 10.1051/0004-6361/201528064.
- R. McGeehan, P. S. Barry, E. Shirokoff, C. M. Bradford, G. Che, J. Glenn, S. Gordon, S. Hailey-Dunsheath, M. Hollister, A. Kovács, H. G. LeDuc, P. Mauskopf, C. McKenney, T. Reck, J. Redford, C. Tucker, J. Turner, S. Walker, J. Wheeler, and J. Zmuidzinas. Low-temperature noise performance of superspec and other developments on the path to deployment. *Journal of Low Temperature Physics*, 193(5):1024–1032, Dec 2018. ISSN 1573-7357. doi: 10.1007/s10909-018-2061-6. URL <https://doi.org/10.1007/s10909-018-2061-6>.
- J. P. McMullin, B. Waters, D. Schiebel, W. Young, and K. Golap. CASA Architecture and Applications. In R. A. Shaw, F. Hill, and D. J. Bell, editors, *Astronomical Data Analysis Software and Systems XVI*, volume 376 of *Astronomical Society of the Pacific Conference Series*, page 127, Oct. 2007.
- K. Menéndez-Delmestre, A. W. Blain, M. Swinbank, I. Smail, R. J. Ivison, S. C. Chapman, and T. S. Gonçalves. Mapping the Clumpy Structures within Submillimeter Galaxies Using Laser-Guide Star Adaptive Optics Spectroscopy. *ApJ*, 767(2):151, Apr 2013. doi: 10.1088/0004-637X/767/2/151.
- M. J. Michałowski, J. S. Dunlop, M. P. Koprowski, M. Cirasuolo, J. E. Geach, R. A. A. Bowler, A. Mortlock, K. I. Caputi, I. Aretxaga, V. Arumugam, C.-C. Chen, R. J. McLure, M. Birkinshaw, N. Bourne, D. Farrah, E. Ibar, P. van der Werf, and M. Zemcov. The SCUBA-2 Cosmology Legacy Survey: the nature of bright submm galaxies from 2 deg² of 850- μm imaging. *MNRAS*, 469:492–515, July 2017. doi: 10.1093/mnras/stx861.
- C. Mihos. Dynamics of Mergers. *Ap&SS*, 266:195–205, 1999.
- T. Naab and J. P. Ostriker. Theoretical Challenges in Galaxy Formation. *ARA&A*, 55(1): 59–109, Aug 2017. doi: 10.1146/annurev-astro-081913-040019.

- D. Narayanan, T. J. Cox, C. C. Hayward, J. D. Younger, and L. Hernquist. The star-forming molecular gas in high-redshift Submillimetre Galaxies. *MNRAS*, 400(4):1919–1935, Dec 2009. doi: 10.1111/j.1365-2966.2009.15581.x.
- D. Narayanan, M. Turk, R. Feldmann, T. Robitaille, P. Hopkins, R. Thompson, C. Hayward, D. Ball, C.-A. Faucher-Giguère, and D. Kereš. The formation of submillimetre-bright galaxies from gas infall over a billion years. *Nature*, 525:496–499, Sept. 2015. doi: 10.1038/nature15383.
- K. G. Noeske, B. J. Weiner, S. M. Faber, C. Papovich, D. C. Koo, R. S. Somerville, K. Bundy, C. J. Conselice, J. A. Newman, D. Schiminovich, E. Le Floch, A. L. Coil, G. H. Rieke, J. M. Lotz, J. R. Primack, P. Barmby, M. C. Cooper, M. Davis, R. S. Ellis, G. G. Fazio, P. Guhathakurta, J. Huang, S. A. Kassin, D. C. Martin, A. C. Phillips, R. M. Rich, T. A. Small, C. N. A. Willmer, and G. Wilson. Star Formation in AEGIS Field Galaxies since $z=1.1$: The Dominance of Gradually Declining Star Formation, and the Main Sequence of Star-forming Galaxies. *ApJ*, 660:L43–L46, May 2007. doi: 10.1086/517926.
- O. Noroozian, J. Gao, J. Zmuidzinas, H. G. LeDuc, and B. A. Mazin. Two-level system noise reduction for Microwave Kinetic Inductance Detectors. In B. Young, B. Cabrera, and A. Miller, editors, *American Institute of Physics Conference Series*, volume 1185 of *American Institute of Physics Conference Series*, pages 148–151, Dec 2009. doi: 10.1063/1.3292302.
- T. E. Oberst, S. C. Parshley, G. J. Stacey, T. Nikola, A. Löhr, J. I. Harnett, N. F. H. Tothill, A. P. Lane, A. A. Stark, and C. E. Tucker. Detection of the 205 μm [N II] Line from the Carina Nebula. *ApJ*, 652(2):L125–L128, Dec 2006. doi: 10.1086/510289.
- S. J. Oliver, L. Wang, A. J. Smith, B. Altieri, A. Amblard, V. Arumugam, R. Auld, H. Aussel, T. Babbedge, A. Blain, J. Bock, A. Boselli, V. Buat, D. Burgarella, N. Castro-Rodríguez, A. Cava, P. Chanial, D. L. Clements, A. Conley, L. Conversi, A. Cooray, C. D. Dowell, E. Dwek, S. Eales, D. Elbaz, M. Fox, A. Franceschini, W. Gear, J. Glenn, M. Griffin, M. Halpern, E. Hatziminaoglou, E. Ibar, K. Isaak, R. J. Ivison, G. Lagache, L. Levenson, N. Lu, S. Madden, B. Maffei, G. Mainetti, L. Marchetti, K. Mitchell-Wynne, A. M. J. Mortier, H. T. Nguyen, B. O’Halloran, A. Omont, M. J. Page, P. Panuzzo, A. Papageorgiou, C. P. Pearson, I. Pérez-Fournon, M. Pohlen, J. I. Rawlings, G. Raymond, D. Rigopoulou, D. Rizzo, I. G. Roseboom, M. Rowan-Robinson, M. Sánchez Portal, R. Savage, B. Schulz, D. Scott, N. Seymour, D. L. Shupe, J. A. Stevens, M. Symeonidis, M. Trichas, K. E. Tugwell, M. Vaccari, E. Valiante, I. Valtchanov, J. D. Vieira, L. Vigroux, R. Ward, G. Wright, C. K. Xu, and M. Zemcov. HerMES: SPIRE galaxy number counts at 250, 350, and 500 μm . *A&A*, 518:L21, Jul 2010. doi: 10.1051/0004-6361/201014697.
- J. Olson. Thermal conductivity of some common cryostat materials between 0.05 and 2 k. *Cryogenics*, 33(7):729 – 731, 1993. ISSN 0011-2275. doi: [https://doi.org/10.1016/0011-2275\(93\)90027-L](https://doi.org/10.1016/0011-2275(93)90027-L). URL <http://www.sciencedirect.com/science/article/pii/001122759390027L>.

- R. Pavesi, D. A. Riechers, P. L. Capak, C. L. Carilli, C. E. Sharon, G. J. Stacey, A. Karim, N. Z. Scoville, and V. Smolčić. ALMA Reveals Weak [N II] Emission in “Typical” Galaxies and Intense Starbursts at $z = 5-6$. *ApJ*, 832(2):151, Dec 2016. doi: 10.3847/0004-637X/832/2/151.
- A. Pope, R. S. Bussmann, A. Dey, N. Meger, D. M. Alexander, M. Brodwin, R.-R. Chary, M. E. Dickinson, D. T. Frayer, T. R. Greve, M. Huynh, L. Lin, G. Morrison, D. Scott, and C.-H. Yan. The Nature of Faint Spitzer-selected Dust-obscured Galaxies. *Astrophysical Journal*, 689:127–133, Dec. 2008. doi: 10.1086/592739.
- N. Rangwala, P. R. Maloney, J. Glenn, C. D. Wilson, A. Rykala, K. Isaak, M. Baes, G. J. Bendo, A. Boselli, and C. M. Bradford. Observations of Arp 220 Using Herschel-SPIRE: An Unprecedented View of the Molecular Gas in an Extreme Star Formation Environment. *ApJ*, 743(1):94, Dec 2011. doi: 10.1088/0004-637X/743/1/94.
- N. Rangwala, P. R. Maloney, C. D. Wilson, J. Glenn, J. Kamenetzky, and L. Spinoglio. Morphology and Kinematics of Warm Molecular Gas in the Nuclear Region of Arp 220 as Revealed by ALMA. *ApJ*, 806(1):17, Jun 2015. doi: 10.1088/0004-637X/806/1/17.
- P. L. Richards. Bolometers for infrared and millimeter waves. *Journal of Applied Physics*, 76(1):1–24, 1994. doi: 10.1063/1.357128. URL <https://doi.org/10.1063/1.357128>.
- K. Sakamoto, N. Z. Scoville, M. S. Yun, M. Crosas, R. Genzel, and L. J. Tacconi. Counter-rotating Nuclear Disks in ARP 220. *ApJ*, 514(1):68–76, Mar 1999. doi: 10.1086/306951.
- K. Sakamoto, S. Aalto, D. J. Wilner, J. H. Black, J. E. Conway, F. Costagliola, A. B. Peck, M. Spaans, J. Wang, and M. C. Wiedner. P Cygni Profiles of Molecular Lines Toward Arp 220 Nuclei. *ApJ*, 700(2):L104–L108, Aug 2009. doi: 10.1088/0004-637X/700/2/L104.
- K. Sakamoto, S. Aalto, A. S. Evans, M. C. Wiedner, and D. J. Wilner. Vibrationally Excited HCN in the Luminous Infrared Galaxy NGC 4418. *ApJ*, 725(2):L228–L233, Dec 2010. doi: 10.1088/2041-8205/725/2/L228.
- K. Sakamoto, S. Aalto, L. Barcos-Muñoz, F. Costagliola, A. S. Evans, N. Harada, S. Martín, M. Wiedner, and D. Wilner. Resolved Structure of the Arp 220 Nuclei at $\lambda \approx 3$ mm. *ApJ*, 849(1):14, Nov 2017. doi: 10.3847/1538-4357/aa8f4b.
- M. T. Sargent, M. Béthermin, E. Daddi, and D. Elbaz. The Contribution of Starbursts and Normal Galaxies to Infrared Luminosity Functions at $z < 2$. *ApJ*, 747(2):L31, Mar 2012. doi: 10.1088/2041-8205/747/2/L31.
- B. D. Savage and K. R. Sembach. Interstellar Abundances from Absorption-Line Observations with the Hubble Space Telescope. *ARA&A*, 34:279–330, 1996. doi: 10.1146/annurev.astro.34.1.279.
- P. Schilke, C. M. Walmsley, G. Pineau des Forets, and D. R. Flower. SiO production in interstellar shocks. *A&A*, 321:293–304, May 1997.

- N. Scoville, N. Lee, P. Vanden Bout, T. Diaz-Santos, D. Sanders, B. Darvish, A. Bongiorno, C. M. Casey, L. Murchikova, J. Koda, P. Capak, C. Vlahakis, O. Ilbert, K. Sheth, K. Morokuma-Matsui, R. J. Ivison, H. Aussel, C. Laigle, H. J. McCracken, L. Armus, A. Pope, S. Toft, and D. Masters. Evolution of Interstellar Medium, Star Formation, and Accretion at High Redshift. *ApJ*, 837(2):150, Mar 2017a. doi: 10.3847/1538-4357/aa61a0.
- N. Scoville, L. Murchikova, F. Walter, C. Vlahakis, J. Koda, P. Vanden Bout, J. Barnes, L. Hernquist, K. Sheth, and M. Yun. ALMA Resolves the Nuclear Disks of Arp 220. *ApJ*, 836(1):66, Feb 2017b. doi: 10.3847/1538-4357/836/1/66.
- S. Serjeant and L. Marchetti. Constraints on the galaxy ‘main sequence’ at $z > 5$: the stellar mass of HDF850.1. *MNRAS*, 443(4):3118–3126, Oct 2014. doi: 10.1093/mnras/stu1266.
- E. Shirokoff, P. S. Barry, C. M. Bradford, G. Chattopadhyay, P. Day, S. Doyle, S. Hailey-Dunsheath, M. I. Hollister, A. Kovács, C. McKenney, H. G. Leduc, N. Llombart, D. P. Marrone, P. Mauskopf, R. O’Brien, S. Padin, T. Reck, L. J. Swenson, and J. Zmuidzinas. MKID development for SuperSpec: an on-chip, mm-wave, filter-bank spectrometer. In *Millimeter, Submillimeter, and Far-Infrared Detectors and Instrumentation for Astronomy VI*, volume 8452 of *Society of Photo-Optical Instrumentation Engineers (SPIE) Conference Series*, page 84520R, Sep 2012. doi: 10.1117/12.927070.
- C. Shiu. Design considerations to improving sensitivity in superspec: an onchip kid-based, mm-wave spectrometer, 2015.
- S. R. Siegel. *A Multiwavelength Study of the Intracluster Medium and the Characterization of the Multiwavelength Sub/millimeter Inductance Camera*. PhD thesis, California Institute of Technology, 2016.
- R. L. Snell, G. Narayanan, M. S. Yun, M. Heyer, A. Chung, W. M. Irvine, N. R. Erickson, and G. Liu. The Redshift Search Receiver 3 mm Wavelength Spectra of 10 Galaxies. *AJ*, 141:38, Feb. 2011. doi: 10.1088/0004-6256/141/2/38.
- P. M. Solomon, D. Downes, and S. J. E. Radford. Warm Molecular Gas in the Primeval Galaxy IRAS 10214+4724. *ApJ*, 398:L29, Oct 1992. doi: 10.1086/186569.
- M. Sparre and V. Springel. Zooming in on major mergers: dense, starbursting gas in cosmological simulations. *MNRAS*, 462(3):2418–2430, Nov 2016. doi: 10.1093/mnras/stw1793.
- G. J. Stacey, N. Geis, R. Genzel, J. B. Lugten, A. Poglitsch, A. Sternberg, and C. H. Townes. The 158 micron C II line - A measure of global star formation activity in galaxies. *ApJ*, 373:423–444, June 1991. doi: 10.1086/170062.
- G. J. Stacey, S. Hailey-Dunsheath, C. Ferkinhoff, T. Nikola, S. C. Parshley, D. J. Benford, J. G. Staguhn, and N. Fiolet. A 158 μm [C II] Line Survey of Galaxies at $z \sim 1-2$: An Indicator of Star Formation in the Early Universe. *ApJ*, 724:957–974, Dec. 2010. doi: 10.1088/0004-637X/724/2/957.

- Z. Staniszewski, J. J. Bock, C. M. Bradford, J. Brevik, A. Cooray, Y. Gong, S. Hailey-Dunsheath, R. O'Brient, M. Santos, E. Shirokoff, M. Silva, and M. Zemcov. The Tomographic Ionized-Carbon Mapping Experiment (TIME) CII Imaging Spectrometer. Journal of Low Temperature Physics, 176:767–772, Sept. 2014. doi: 10.1007/s10909-014-1126-4.
- L. J. Swenson, P. K. Day, C. D. Dowell, B. H. Eom, M. I. Hollister, R. Jarnot, A. Kovács, H. G. Leduc, C. M. McKenney, R. Monroe, T. Mroczkowski, H. T. Nguyen, and J. Zmuidzinas. MAKO: a pathfinder instrument for on-sky demonstration of low-cost 350 micron imaging arrays. In Millimeter, Submillimeter, and Far-Infrared Detectors and Instrumentation for Astronomy VI, volume 8452 of Proc. SPIE, page 84520P, Sept. 2012. doi: 10.1117/12.926223.
- L. J. Swenson, P. K. Day, B. H. Eom, H. G. Leduc, N. Llombart, C. M. McKenney, O. Noroozian, and J. Zmuidzinas. Operation of a titanium nitride superconducting microresonator detector in the nonlinear regime. Journal of Applied Physics, 113(10):104501-104501-9, Mar 2013. doi: 10.1063/1.4794808.
- P. Szypryt, B. A. Mazin, G. Ulbricht, B. Bumble, S. R. Meeker, C. Bockstiegel, and A. B. Walter. High quality factor platinum silicide microwave kinetic inductance detectors. Applied Physics Letters, 109:151102, Oct 2016. doi: 10.1063/1.4964665.
- C. L. Taylor, F. Walter, and M. S. Yun. Discovery of Molecular Gas in the Outflow and Tidal Arms around M82. ApJ, 562:L43–L46, Nov. 2001. doi: 10.1086/338048.
- R. Teyssier, D. Chapon, and F. Bournaud. The Driving Mechanism of Starbursts in Galaxy Mergers. ApJ, 720:L149–L154, Sept. 2010. doi: 10.1088/2041-8205/720/2/L149.
- J. Tumlinson, M. S. Peeples, and J. K. Werk. The Circumgalactic Medium. ARA&A, 55(1):389–432, Aug 2017. doi: 10.1146/annurev-astro-091916-055240.
- R. Tunnard, T. R. Greve, S. Garcia-Burillo, J. Graciá Carpio, J. Fischer, A. Fuente, E. González-Alfonso, S. Hailey-Dunsheath, R. Neri, and E. Sturm. Chemically Distinct Nuclei and Outflowing Shocked Molecular Gas in Arp 220. ApJ, 800(1):25, Feb 2015. doi: 10.1088/0004-637X/800/1/25.
- M. P. Viero, L. Wang, M. Zemcov, G. Addison, A. Amblard, V. Arumugam, H. Aussel, M. Béthermin, J. Bock, A. Boselli, V. Buat, D. Burgarella, C. M. Casey, D. L. Clements, A. Conley, L. Conversi, A. Cooray, G. De Zotti, C. D. Dowell, D. Farrah, A. Franceschini, J. Glenn, M. Griffin, E. Hatziminaoglou, S. Heinis, E. Ibar, R. J. Ivison, G. Lagache, L. Levenson, L. Marchetti, G. Marsden, H. T. Nguyen, B. O'Halloran, S. J. Oliver, A. Omont, M. J. Page, A. Papageorgiou, C. P. Pearson, I. Pérez-Fournon, M. Pohlen, D. Rigopoulou, I. G. Roseboom, M. Rowan-Robinson, B. Schulz, D. Scott, N. Seymour, D. L. Shupe, A. J. Smith, M. Symeonidis, M. Vaccari, I. Valtchanov, J. D. Vieira, J. Wardlow, and C. K. Xu. HerMES: Cosmic Infrared Background Anisotropies and the Clustering of Dusty Star-forming Galaxies. ApJ, 772(1):77, Jul 2013. doi: 10.1088/0004-637X/772/1/77.

- M. R. Vissers, J. Gao, M. Sandberg, S. M. Duff, D. S. Wisbey, K. D. Irwin, and D. P. Pappas. Proximity-coupled Ti/TiN multilayers for use in kinetic inductance detectors. *Applied Physics Letters*, 102:232603, Jun 2013. doi: 10.1063/1.4804286.
- A. Weiß, A. Kovács, K. Coppin, T. R. Greve, F. Walter, I. Smail, J. S. Dunlop, K. K. Knudsen, D. M. Alexander, F. Bertoldi, W. N. Brandt, S. C. Chapman, P. Cox, H. Dannerbauer, C. De Breuck, E. Gawiser, R. J. Ivison, D. Lutz, K. M. Menten, A. M. Koekemoer, E. Kreysa, P. Kurczynski, H.-W. Rix, E. Schinnerer, and P. P. van der Werf. The Large Apex Bolometer Camera Survey of the Extended Chandra Deep Field South. *ApJ*, 707:1201–1216, Dec. 2009. doi: 10.1088/0004-637X/707/2/1201.
- J. Wheeler, N. Rangwala, A. Fyhrie, and J. Glenn. New Observational Insights on the Structure and Kinematics of the Nuclear Molecular Disks and Surrounding Gas. *ApJ*, 2019 in preparation.
- C. D. Wilson, N. Rangwala, J. Glenn, P. R. Maloney, L. Spinoglio, and M. Pereira-Santaella. Extreme Dust Disks in Arp 220 as Revealed by ALMA. *ApJ*, 789(2):L36, Jul 2014. doi: 10.1088/2041-8205/789/2/L36.
- G. Wilson, P. Ade, I. Aretxaga, Aretxaga, J. E. Austermann, J. Bardin, P. Barry, J. Beall, M. Berthoud, A. Braeley, S. A. Bryan, A. Burkott, J. Bussan, E. Castillo, M. Chavez, N. DeNigris, S. Doyle, M. Eiben, D. Ferrusca, L. Fissel, J. Gao, W. Gear, V. Gmez, S. Gordon, C. Groppi, R. Gutermuth, M. Heyer, S. Kuczarski, M. Hosseini, S. Offner, A. Pope, F. P. Schloerb, K. Souccar, Y. Tang, G. Wallace, M. S. Yun, P. Maukopf, R. Kelso, J. Knapp, E. Lunde, H. Mani, J. Mathewson, E. Scannapieco, M. Underhill, J. Hubmayr, M. Vissers, D. H. Hughes, I. R. Montoya, D. Sanchez, M. Velazquez, S. Ventura, E. Pascale, S. Rowe, C. Tucker, G. Novak, J. McMahon, and S. Simon. The toltec project: a millimeter wavelength imaging polarimeter (conference presentation), 2018. URL <https://doi.org/10.1117/12.2313347>.
- J. A. Zavala, M. S. Yun, I. Aretxaga, D. H. Hughes, G. W. Wilson, J. E. Geach, E. Egami, M. A. Gurwell, D. J. Wilner, I. Smail, A. W. Blain, S. C. Chapman, K. E. K. Coppin, M. Dessauges-Zavadsky, A. C. Edge, A. Montaña, K. Nakajima, T. D. Rawle, D. Sánchez-Argüelles, A. M. Swinbank, T. M. A. Webb, and M. Zeballos. Early Science with the Large Millimeter Telescope: observations of dust continuum and CO emission lines of cluster-lensed submillimetre galaxies at $z=2.0-4.7$. *MNRAS*, 452:1140–1151, Sept. 2015. doi: 10.1093/mnras/stv1351.
- J. Zmuidzinas. Superconducting microresonators: Physics and applications. *Annual Review of Condensed Matter Physics*, 3(1):169–214, 2012. doi: 10.1146/annurev-conmatphys-020911-125022. URL <https://doi.org/10.1146/annurev-conmatphys-020911-125022>.

Appendix A

LIME Parameter Dependencies

LIME is somewhat computationally expensive. This makes producing Monte Carlo simulations to determine error bars for the derived best-fit quantities difficult without the aid of a supercomputer. However, with a few targeted simulations scaling some of the input variables, one can build up an understanding of how changing a particular variable in LIME effects the output line profiles. This helps build intuition for how to interpret observed line profiles and gives insights into the confidence for the derived parameters.

Here some of the parameters for the western nucleus are varied to demonstrate how they impact the line profiles. This is a hands-on experiment where the reader needs to interact with the plots in order to develop his or her own understanding. It should be noted that for disks that are not so extremely optically thick as Arp 220 the effects will vary somewhat.

In Figure A.1 a cube of models varying the turbulent velocity, the circular velocity, and inclination angle of the disk is depicted. As an example of the degeneracy, the reader can select a turbulent velocity of 95 km/s, a circular velocity of 280 km/s, and an inclination angle of 30° versus a turbulent velocity of 105 km/s, a circular velocity of 250 km/s, and an inclination angle of 37.5° . Note that the profiles, while different, are quite similar for the two sets of disparate conditions. The take away is that if the disk is taken to have a different inclination angle different results for the turbulent velocity and circular velocity will be found and vice versa.

In Figure A.2, models varying the gas temperature, the thickness of the disk, total gas

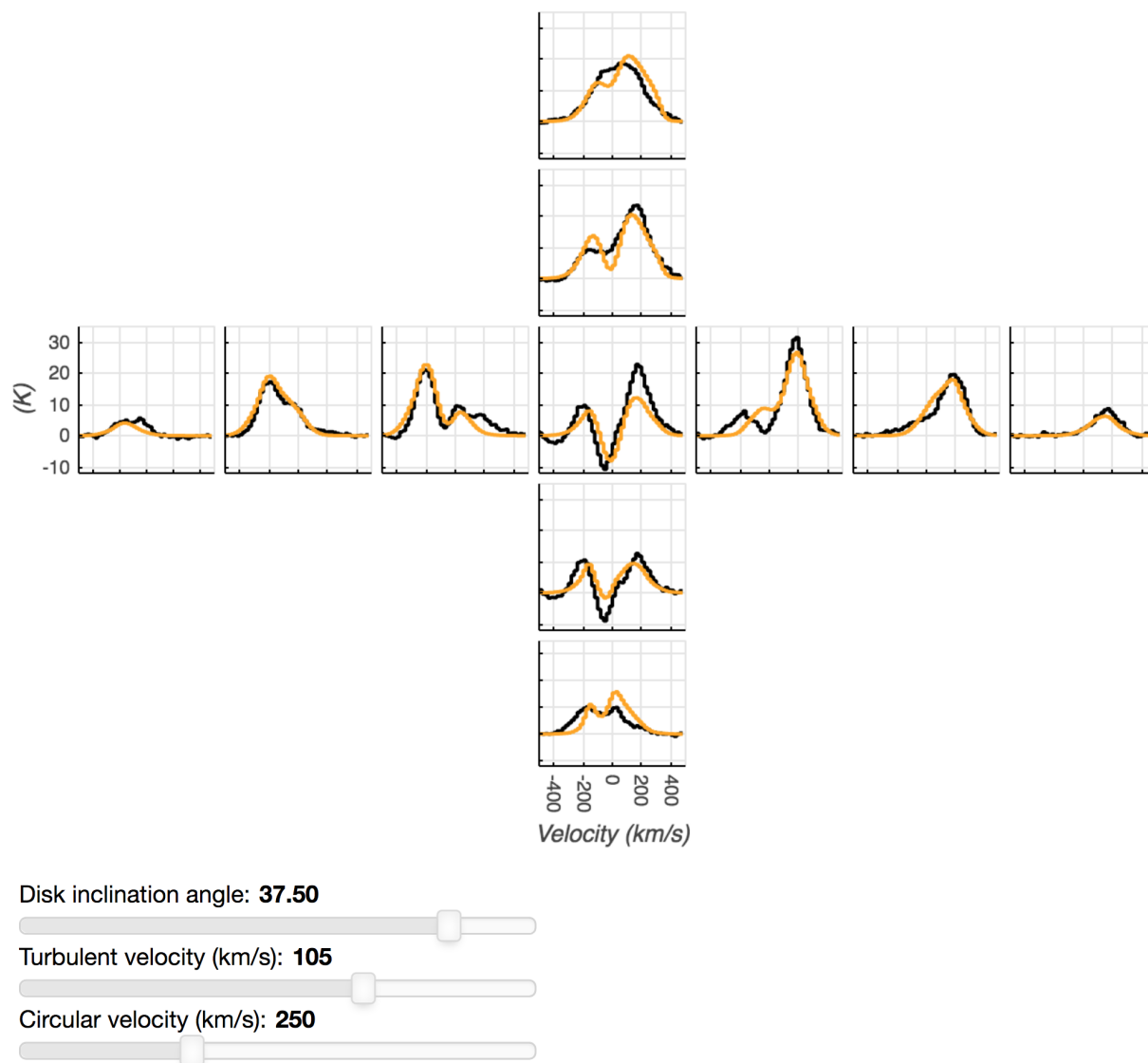


Figure A.1: Models for the Arp 220 western nucleus in $^{13}\text{CO } J = 4 \rightarrow 3$ (orange lines) shown along with the observed line profiles at half-beam increments along the disk axis and perpendicular to the disk axis. $1 \text{ Jy/beam} = 294.5 \text{ K}$. In this figure, any combination of parameters is allowed. Interactive figure available on-line (Wheeler et al., 2019 in preparation).

mass, and inclination angle of the disk are shown. As an example of the degeneracy, the reader can select an inclination angle of 30° , a gas mass of $16 \times 10^8 M_\odot$, a scale height in z of 35 pc, and a gas temperature of 112 K versus an inclination angle of 22.5° , a gas mass of $4 \times 10^8 M_\odot$, a scale height in z of 50 pc, and a gas temperature of 122 K. Notice how

similar the central absorption dip is between these two sets of parameters. For the models in Chapter 6, the dust temperature is partly constrained by the continuum flux density given a total gas mass, therefore not every parameter combination is actually plausible.

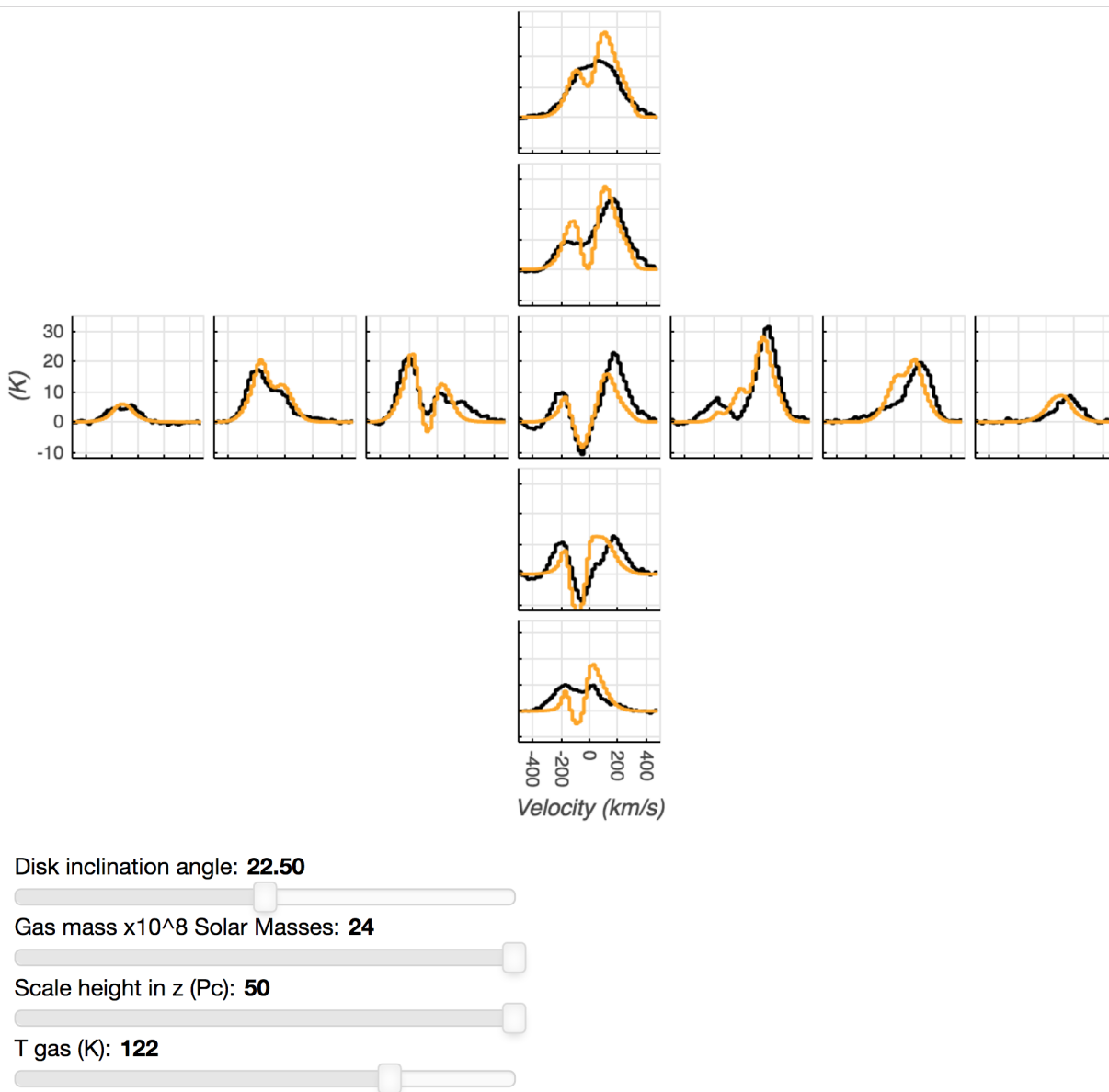


Figure A.2: Models for the Arp 220 western nucleus in ^{13}CO $J = 4-3$ (orange lines) shown along with the observed line profiles at half-beam increments along the disk axis and perpendicular to the disk axis. $1 \text{ Jy/beam} = 294.5 \text{ K}$. In this figure, any combination of parameters is allowed. Interactive figure available on-line (Wheeler et al., 2019 in preparation).